

Design and test of box girder for a large wind turbine blade

Department of
Wind Energy
Report 2012

Per H. Nielsen, Angelo Tesauro, Robert Bitsche, Malcolm McGugan, Christian Lynnov, Flemming Sørensen, Henrik Knudsen, Peter Berring, Kim Branner, Mikkel Lagerbon, Peter Andreasen, Troels Lukassen

DTU Wind Energy E-0010 (EN); ISBN 978-87-92896-16-2

14. September 2012



Author (s): Per H. Nielsen, Angelo Tesauro, Robert Bitsche, Malcolm McGugan, Christian Lynnov, Flemming Sørensen, Henrik Knudsen, Peter Berring, Kim Branner, Mikkel Lagerbon, Peter Andreasen, Troels Lukassen

Summary (max 2000 characters):

This report is covering the structural design and full scale test of a box girder as a part of the project "Demonstration of new blade design using manufacturing process simulations" supported by the EUDP program. A box girder with a predetermined outer geometry was designed using new inventions, which create an inner structure in the box girder. With a combination of advanced FEM analysis and the inventions it was possible to reduce the material thickness of the cap by up to 40%.

The new design of the box girder was manufactured at SSP Technology A/S, where it was demonstrated that the manufacturing process could include the new inventions. Subsequently the box girder was transported to the blade test facility at DTU Wind Energy.

A series of test was performed with the blade to investigate the behaviour during loading, and finally the girder was loaded to ultimate failure.

The report includes the description of the test setup, the test and an overview over the results from the test performed on the box girder.

During the final test the box girder failed at 58 % of the expected ultimate load. Unfortunately, no definite conclusion could be made concerning the failure mechanism.

DTU Wind Energy E-0010 (EN);

ISBN 978-87-92896-16-2

14. September 2012

Technical University of Denmark
Institut for Vindenergi
Frederiksborgvej 399
Bygning 118
4000 Roskilde
Telefon

www.vindenergi.dtu.dk

Content

1.	Introduction	7
2.	Finite Element Analysis and design of box girder	7
3.	Manufacturing of the boxgirder	36
4.	Test setup	39
5.	Measurements	46
6.	Test observations.....	51
7.	Summary.....	67

1. Introduction

In the recent years, extensive research activities have been conducted at DTU Wind Energy including computer simulations (FEM analyses) and experimental test of wind turbine blades. This work has increased the knowledge in how blades collapse structurally and how they can be optimized further. The structural failure mechanisms identified recently are primarily non-linear elastic mechanisms, such as buckling, localized bending and the Brazier effect

The work which is described here is seen as another important contribution in developing the future generation of wind turbine blades. The main idea is to manufacture the load carrying girder of a large blade with the newest technologies in structural design, and include two new patents on internal structural reinforcement.

To demonstrate the capability of the new design the blade is tested at DTU Wind Energy's research full-scale test facility using comprehensive measurement technology to obtain a high degree of understanding of the behaviour of the girder.

2. Finite Element Analysis and design of box girder

Several structural concepts for wind turbine blades exist. The one investigated here consists of a load carrying box girder enclosed by an aerodynamic shell, see Figure 1 and Figure 2. In the present project the aerodynamic shell was omitted and only a box girder was designed, analyzed and tested.

The box girder was manufactured from glass fibre reinforced epoxy composites and sandwich core material by SSP Technology A/S using resin transfer moulding. A previously existing mould for a 42 meter blade was used and only the first 30 meters of the 42 meter box girder were manufactured. As the mould defines the outer geometry of the girder, modifications were limited to the layup and additional internal structure.

A detailed finite element model of the box girder was used to assist the design process and to predict the outcome of the static full-scale test.

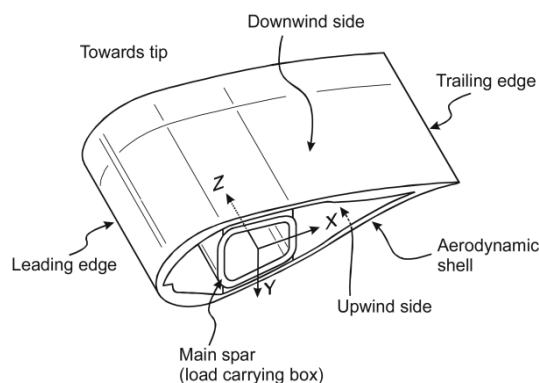


Figure 1: Wind turbine blade with main spar (box girder) and aerodynamic shell.

2.1 Nomenclature for FEM analyses

The box girder consists of two caps (or flanges) and two shear webs as schematically shown in Figure 2.

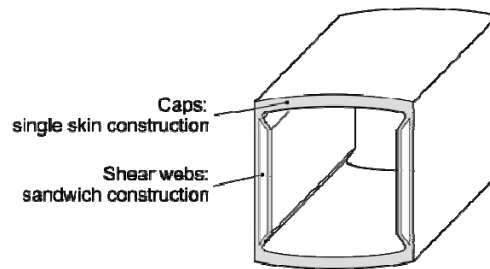


Figure 2: Box girder with two caps and two shear webs.

Figure 3 schematically shows the box girder (solid line) inside the aerodynamic shell (dashed line). The designations “pressure side” and “suction side” refer to aerodynamic pressure and suction. The designations “leading edge” and “trailing edge” refer to the airfoil. The outer geometry of the box girder (the geometry of the mould) is defined in a coordinate system designated “coord 0” in Figure 3. “Coord 2” is obtained by rotating “coord 0” about the x-axis, so that the z-axis of the new coordinate system is parallel to the shear webs. The plus/minus z-direction of “coord 2” is referred to as “flapwise”, the plus/minus y-direction as “edgewise”. In the present report concentrated loads have been applied in plus/minus z-direction of “coord 2” (“flapwise”) in order to achieve a certain bending moment distribution. In terms of load application the z-direction of “coord 2” is referred to as “STP” (suction side to pressure side) and the minus z-direction of “coord 2” is referred to as “PTS” (pressure side to suction side). The x-direction in Figure 3 is also referred to as radial direction (r).

The choice for the direction of load application described above is important as the bending stiffness of the box girder with respect to the z-axis of “coord 2” is considerably smaller than the bending stiffness with respect to the y-axis of “coord 2”. Therefore, even small force components in plus/minus y-direction of “coord 2” lead to large deformations in that direction. Such a mode of deformation is unrealistic for a wind turbine blade including the aerodynamic shell and must therefore be avoided.

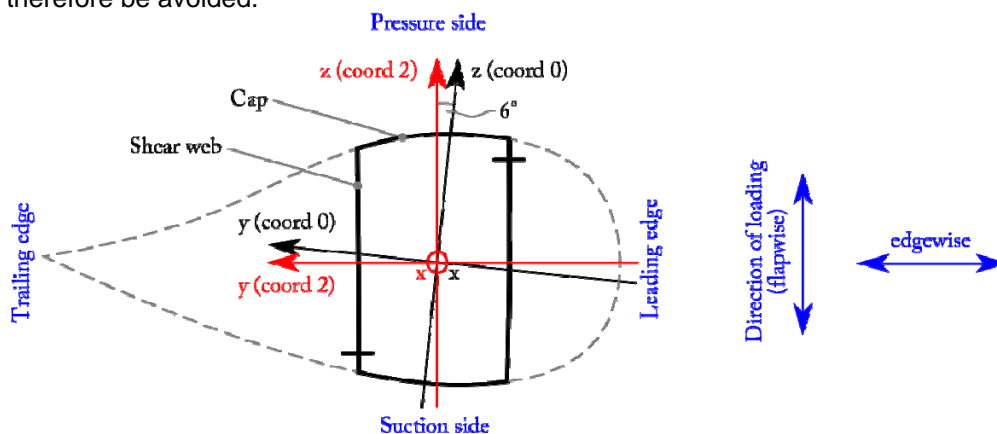


Figure 3: Box girder (solid line) and aerodynamic shell (dashed line); Coordinate systems looking from root to tip (x-direction).

2.2 Design

The girder analyzed in this study is a modification of a girder from a previously existing blade manufactured by SSP Technology A/S. The previously existing girder represents state-of-the-art design and is here referred to as the “original girder”. As the same mould (defining the outer geometry of the girder) was used for production of the new girder, modifications are limited to the layup (thickness) and additional internal structure.

a. Caps and Shear Webs

The box girder consists of two caps and two shear webs as schematically shown in Figure 2. The caps are manufactured from glass fiber reinforced epoxy composites. As the box girder’s main purpose is to carry bending moments, the fibers in the caps are mainly oriented in longitudinal direction. The shear webs are a sandwich construction with face sheets made from glass fiber reinforced epoxy composites with fibers oriented $\pm 45^\circ$. While the box girder corresponds to a 42 meter blade, only the first 30 meters were manufactured and modelled.

b. Longitudinal Stiffeners

The caps of the box girder are considerably thinner as compared to the original design as shown in Figure 4. As a consequence, the caps would buckle when loaded in compression. This is prevented by introducing prefabricated T-profiles which are glued to the caps and act as longitudinal stiffeners, see Figure 6 and Figure 7. Moreover, two prefabricated strips are glued to each side of the T-profile’s web to increase the buckling capacity of the T-profile itself (This is not shown in Figure 7). The T-profiles start at $r=6\text{m}$ and continues to the “tip” at $r=30\text{m}$.

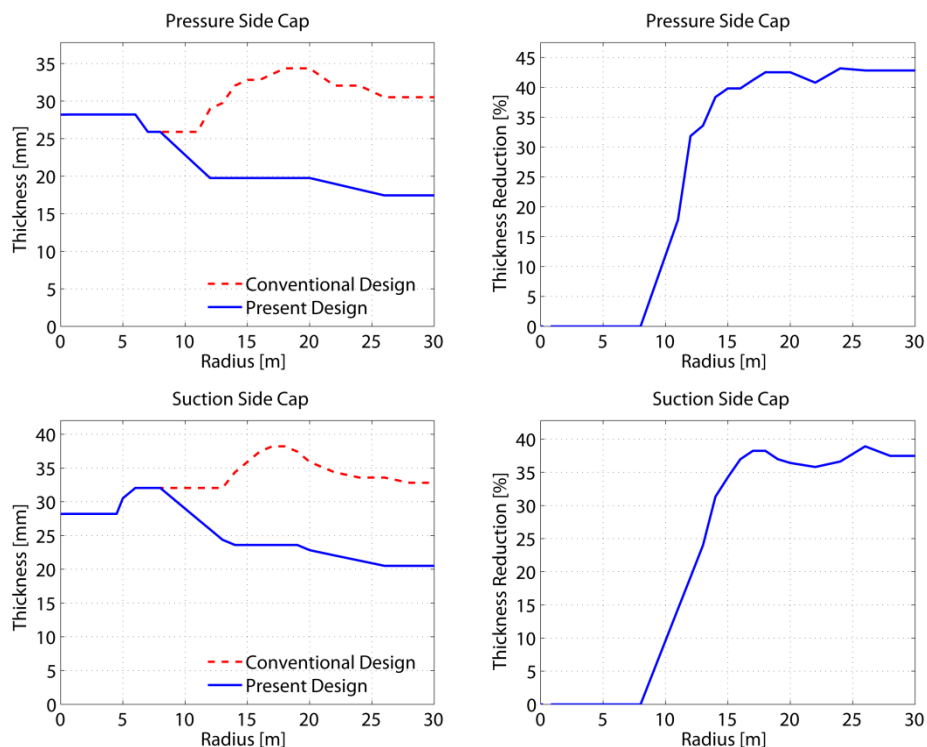


Figure 4: Thickness of the caps as compared to the original design.

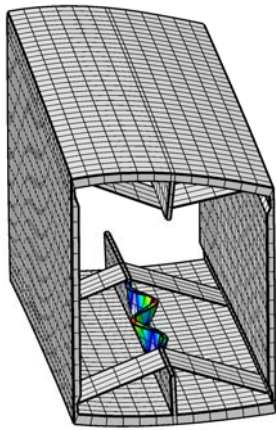


Figure 5: Buckling of the longitudinal stiffener.

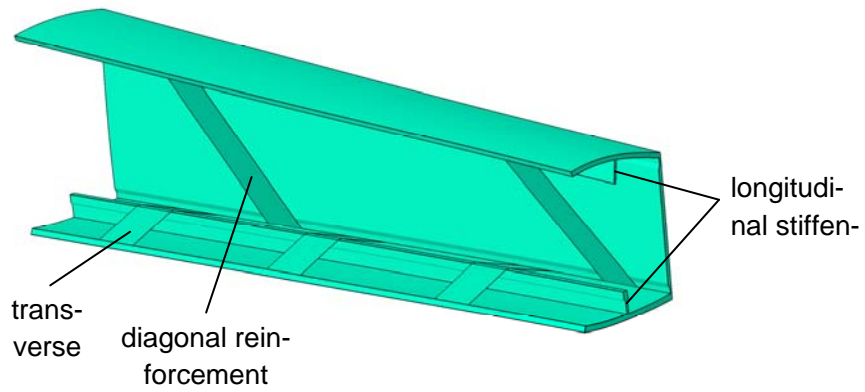


Figure 6: Schematic representation of a section of the box girder. The leading shear web has been removed; the thickness of the diagonals and transverse stiffeners is not shown.

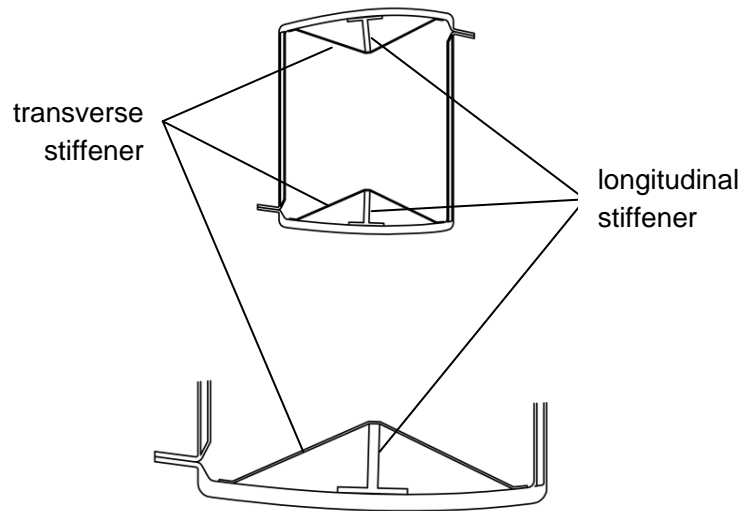


Figure 7: Longitudinal and transverse stiffeners. The two additional strips glued to each side of the T-profile on the suction side are not shown.

c. Transverse Stiffeners

The transverse stiffeners shown in Figure 6 and Figure 7 are meant to counteract the Brazier effect. (The Brazier effect causes a flattening of the box girder's cross-section.)

The transverse stiffeners are approximately 2mm thick and are manufactured from glass fiber reinforced epoxy composites with fibers oriented mainly in transverse direction with respect to the longitudinal direction of the girder. They are glued to the respective cap. Each transverse stiffener is 200mm deep (extension in r-direction) and a stiffener is positioned every meter starting at $r=7.5\text{m}$.

d. Diagonal Reinforcement

The diagonal reinforcements shown in Figure 8 are meant to prevent a distortion of the girder's cross section into a parallelogram-like shape. Due to the absence of the aerodynamic shell, the structure investigated here is sensitive to this kind of distortions.

The diagonal reinforcements must be able to carry tensile as well as compressive loads. In order to prevent buckling of the diagonal reinforcements, they are sandwich constructions. Each diagonal is 200mm deep (extension in r-direction) and a diagonal is positioned every 2 meters starting at $r=6\text{m}$. The sandwich core is generally 20mm thick, except for $r=6\text{m}$ and $r=8\text{m}$, where it is 30mm thick.

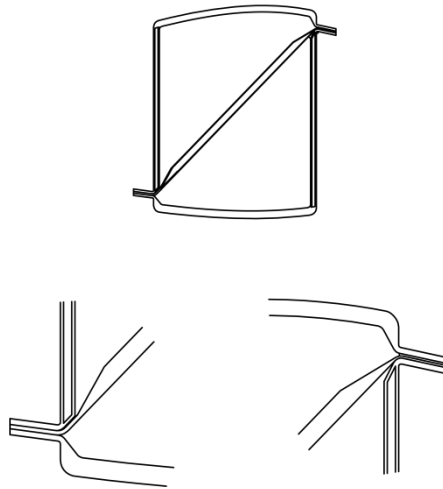


Figure 8: Diagonal reinforcement.

2.3 Modeling

e. Software

The box girder was modeled using the general purpose finite element package ABAQUS (version 6.10-2). MSC Patran together with the in-house software BMT (blade modeling tool) was used for preprocessing.

f. Geometry

As three-dimensional solid elements (see Figure 10) were used to model the girder's main structure, a volume representation of the girder's main geometry was required. This geometry was generated using BMT together with MSC Patran. 30 cross-sections were extracted from a 3D-CAD model of the two moulds provided by SSP Technology A/S. These cross-sections describe the outer geometry of the girder. The curves defining these cross-sections were offset according to the layup definition in order to represent the thickness of the laminates. Finally, the individual cross-sections were connected by spline curves and interpolation surfaces to obtain a volume representation of the girder.

The process described in the previous paragraph was handled automatically by BMT. Finally, custom-made scripts were used to add three-dimensional bodies representing the transverse stiffeners and two-dimensional surfaces representing the mid-surfaces of the transverse stiffeners and diagonal reinforcements as shown in Figure 6. The transverse stiffeners and the diagonal reinforcements are (as opposed to the rest of the structure) modeled using conventional shell elements discretizing only the mid surfaces. The complete model is shown in Figure 9.

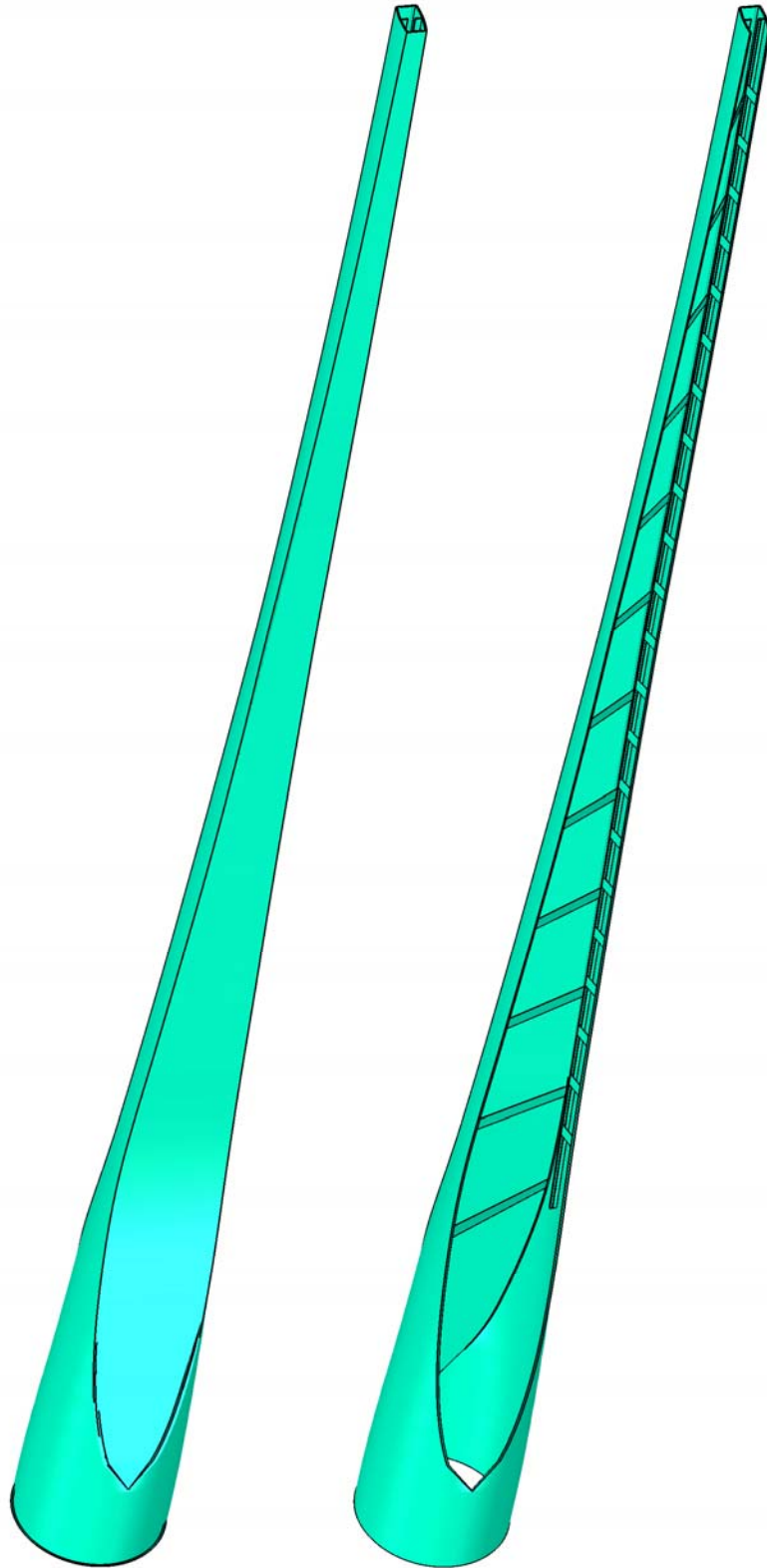


Figure 9: Schematic illustration of the box girder finite element model; left: complete model, right: leading shear web removed.

g. Element Types

The caps, shear webs and longitudinal stiffeners are modeled using a fine mesh of layered, hexahedral continuum shell elements (Abaqus element type SC8R), see Figure 10 and Figure 11.

While continuum shell elements discretize a three-dimensional body like continuum elements, their kinematic and constitutive behavior is similar to conventional shell elements. The effects of transverse shear deformation are included. Unlike conventional shell elements continuum shell elements have only displacement degrees of freedom. The aspect ratio of these elements need not be close to unity.

The transverse stiffeners and diagonal reinforcements are modeled using conventional, 4-noded, layered shell elements (Abaqus element type S4R) as shown in Figure 10 and Figure 11. The individual transverse stiffeners and diagonal reinforcements are “simply supported” at their ends as they share nodes with continuum shell elements which do not have rotational degrees of freedom. This is a well justified assumption as the diagonal reinforcements are very thin in the region where they are connected to the main structure (see Figure 8) and the transverse stiffener are so thin that they have little bending stiffness (see Figure 7).

Connector elements are used to model the cables used for load introduction during the physical test.

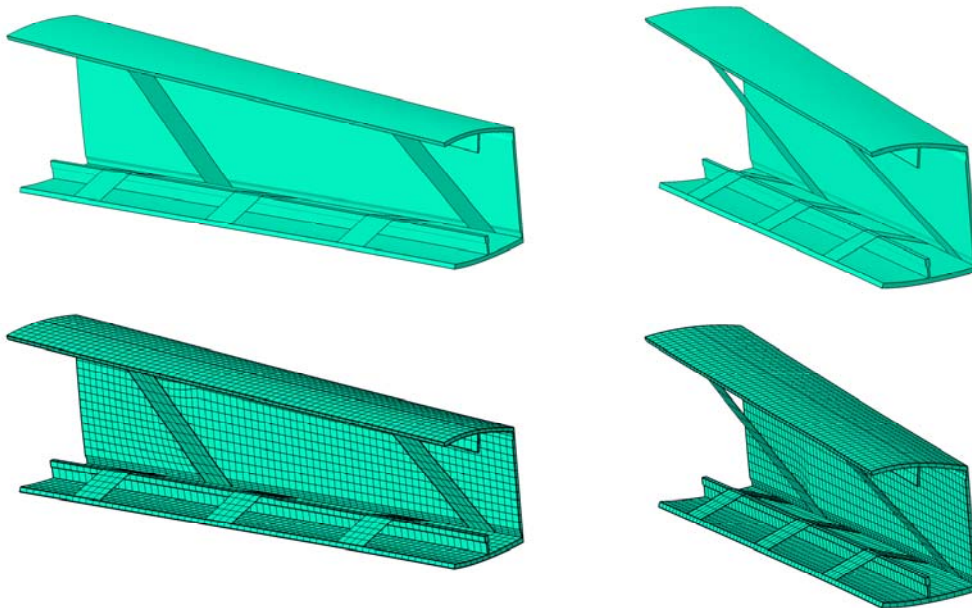


Figure 10: Section of the Finite Element Model; Above: Schematic, Below: Mesh included.

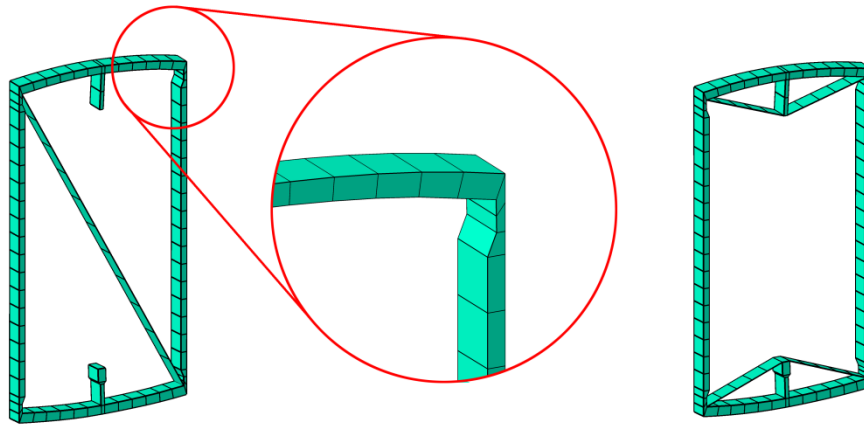


Figure 11: Meshed cross-sections; left: cross-section containing diagonal reinforcement, right: cross-section containing transverse stiffeners.

h. Material Model

All glass fiber reinforced epoxy laminae are assumed linear elastic and orthotropic. As all elements used (continuum shell elements and conventional shell elements) are based on the plane stress assumption, only E_1 , E_2 , ν_{12} and G_{12} are required to define the material behavior (The plane stress condition is $\sigma_{33} = 0$). The shear moduli G_{13} and G_{23} are required to model the transverse shear deformation of the shell. Table 1 reports the effective elastic properties of the laminae used for analysis.

The sandwich core material is assumed linear elastic and isotropic. The elastic properties used for analysis are reported in Table 2.

Table 1: Effective elastic properties of the fiber reinforced epoxy laminates.

Name	Description	Fiber Orientation	Laminate thickness [mm]	E_1 [GPa]	E_2 [GPa]	ν_{12}	G_{12} [GPa]	G_{13} [GPa]	G_{23} [GPa]
SUG 950 (uniaxial composite)	SAERTEX S14EB970-0049-1300-100000	0°	0,769	41,609	10,996	0,3	4,2	4,2	4,2
SBX 800 (biaxial composite)	SAERTEX S32EX010-00811-01270-264000	± 45°	0,648	11,135	11,135	0,55	10,0	5,0	5,0

Table 2: Effective elastic properties of the sandwich core material

(Poisson's ratio ν is computed from Young's modulus E and shear modulus G).

Name	Description	Density	E	G	ν
------	-------------	---------	-----	-----	-------

		[kg/m ³]	[MPa]	[MPa]	
A550	Gurit Corecell	103	84.5	30	0.408
(sandwich core)	A-Foam				

i. Load Introduction and Load Cases

The girder was analyzed in static, flapwise PTS bending. Two load cases are considered, which are here referred to as “design load case” and “test load case”. The design load case was used for designing and optimizing the girder. The test load case simulates the physical, static full-scale test of the girder.

i. Design Load Case

Wind turbine blades are (among other things) designed to carry a certain distribution of bending moments and shear forces. These “design bending moments” are usually obtained from an aeroelastic analysis of the turbine. Figure 13 shows the design bending moment distribution obtained from an aeroelastic analysis of the original blade (compare Section 2.2). This design bending moment distribution has also been used to design the girder analyzed in this study.

In the model an approximation of the design bending moment distribution is generated by applying 29 concentrated forces at $r=2\text{m}$, 3m , ..., 30m (see Table 3) and one moment at $r=30\text{m}$ (see Table 4) as shown in Figure 13. The forces and the moment are computed based on the undeformed geometry. That is, the bending moment distribution actually generated deviates somewhat from the distribution shown in Figure 13 due to the large deformation of the structure.

The loads are applied to the master nodes of coupling constrained defined at each required cross-sections. At the 28 cross-sections from $r=2\text{m}$ to $r=29\text{m}$ so-called “distributing coupling constraints” are used. That is, the force applied at the master node is equally distributed to all nodes lying on the two caps without restraining the ability of the respective cross-section to deform, see Figure 12. At $r=30\text{m}$ a “kinematic coupling constraint” is used instead. That is, all nodes at $r=30\text{m}$ are coupled to the rigid body motion defined by the master node. This prevents the cross-section at $r=30\text{m}$ from deforming.

All concentrated forces are follower loads. That is, the direction of the load rotates with the rotation at the respective master-node. This ensures that the loads remain perpendicular to the deformed axis of the girder as shown in Figure 14.

Table 3: Concentrated forces applied in flapwise (PTS) direction in the design load case.

r [m]	F [kN]	r [m]	F [kN]	r [m]	F [kN]	r [m]	F [kN]
2	4	10	9	18	9	26	11
3	4	11	9	19	8	27	11
4	4	12	9	20	9	28	11
5	5	13	9	21	8	29	11
6	6	14	9	22	9	30	121
7	7	15	9	23	9		
8	7	16	9	24	9		
9	8	17	9	25	10		

Table 4: Bending moment applied at r=30m in the design load case.

r [m]	M [kNm]
30	806

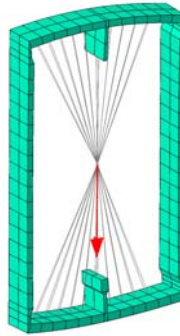


Figure 12: Distributing coupling constraint and load applied to the master node.

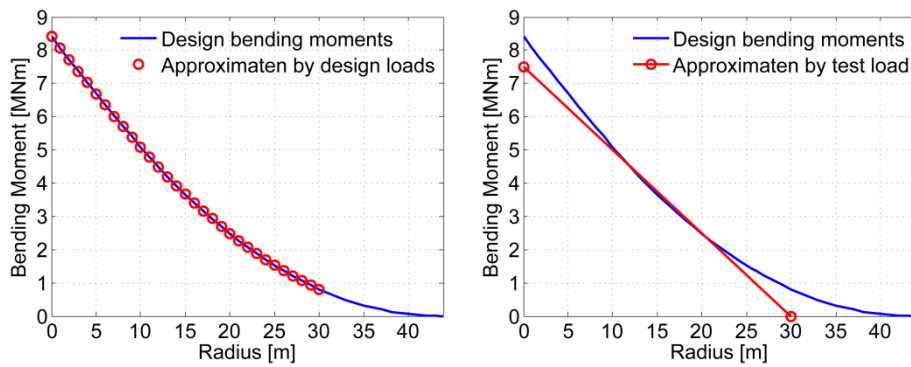


Figure 13: Left: Design bending moment distribution for flapwise PTS bending and approximation by design loads; Right: Design bending moment distribution and approximation by test load (physical test)

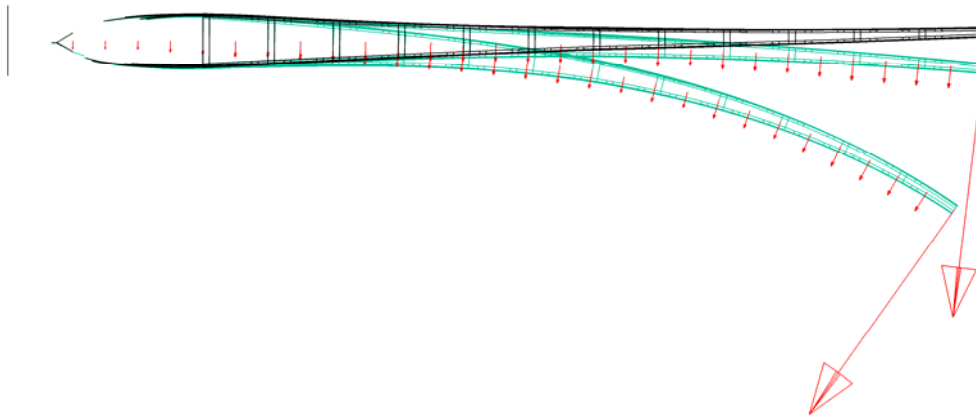


Figure 14: Loads remain perpendicular to the deformed axis of the girder.

ii. Test Load case

The test load case simulates the physical full-scale test of the girder. During physical testing no bending moment is applied at $r=30\text{m}$ (as in the design load case) and a rough approximation of the design bending moment distribution is achieved by applying a single load at $r=30\text{m}$ (see Table 5) as shown in Figure 13. This approximation lies above the design bending moment distribution in the region from $r=11.5\text{m}$ to $r=20.5\text{m}$ and below the design bending moment distribution outside that region. As the region from $r=11.5\text{m}$ to $r=20.5\text{m}$ corresponds to the “region of interest” for the present project, this approximation is appropriate.

Table 5: Force applied in flapwise (PTS) direction in the test load case.

r [m]	F [kN]
30	250

In the design load case follower forces are used to ensure that the forces stay perpendicular to the deformed axis of the girder (see Figure 14). During the physical test the load is applied using a cable. This cable neither has a fixed direction in space, nor does it correspond to a follower force. Therefore, so-called connector elements (type “AXIAL”) are used to model the effect of the cable. These elements provide a connection between two nodes where the relative displacement is along the line separating the two nodes. The connector element is “actuated”, that is, a force is assigned to the element and ramped up during analysis. The force always acts along the line separating the two nodes of the element.

The load application points (the initial arrangement of the cable) has been chosen in such a way that the cable is approximately perpendicular to the deformed axis of the blade when the maximum load level is reached, see Figure 20.

j. Boundary Conditions and Contact

All nodes at $r=0\text{m}$ are fixed.

When the box girder is bent in flapwise direction, an elastic lateral instability occurs which leads to large edgewise deformations. Figure 16 on page 22 shows the results of an eigenvalue buck-

ling analysis. Such a mode of deformation is unrealistic for a wind turbine blade including the aerodynamic shell and must therefore be avoided.

During physical testing lateral deformation was prevented by two steel columns as shown in Figure 15. In the corresponding model (test load case) the steel columns are represented by rigid bodies and frictionless contact between the girder and the rigid bodies is assumed.

In order to prevent the lateral instability in the design load case, lateral boundary conditions are applied to the master nodes of the distributing coupling constraints at $r=10\text{m}$, $r=20\text{m}$ and $r=30\text{m}$.

k. Position of the Suspension Point for Test Load Case

During full-scale testing a single load is applied at $r=30\text{m}$ using a steel cable. During loading the angle between the cable and the girder's neutral axis inevitably changes due to the large deformation.

Preliminary simulation showed that the lower suspension point should be moved 0.41m from the point vertically below the upper suspension point towards the root of the girder. Then, the steel cable is approximately perpendicular to the girder's neutral axis at the critical load level (100% load) as shown in Figure 20.

l. Analysis Procedures

The mechanical behavior of the box girder has been studied using a static, nonlinear, implicit analysis procedures, and eigenvalue buckling analysis. Nonlinear analysis is required due to geometric nonlinearity and (in one case) contact.

When elastic buckling is analyzed by eigenvalue extraction, the buckling loads are obtained as a multiplier of the pattern of perturbation loads, which are added to a set of base state loads. That is, buckling is analyzed relative to a base state that includes the (geometrically) non-linear effect caused by the base state loads.

Moreover a dynamic analysis procedure with implicit time integration was used as an approximation for a static analysis. This was done in order to overcome convergence problems seen during static analysis. The forces are ramped up slowly, so that the total kinetic energy is always negligibly small compared to the total strain energy. A time integration method with significant numerical damping and an "aggressive" time incrementation scheme are used.

Table 6 reports the model configurations, load cases and analysis procedures used. Apart from the standard configuration (as described in Section 2.2), the box girder was analyzed in two more configurations: without transverse stiffeners and without transverse or longitudinal stiffeners.

Table 6: Analysis Procedures.

<i>Model Configuration</i>	<i>Load Case</i>	<i>Analysis Procedure</i>
Standard configuration	PTS design loads	Non-linear static
		Eigenvalue buckling
	PTS test loads and gravity	Dynamic
		Non-linear static
Without transverse stiffeners	PTS design loads	Eigenvalue buckling
		Dynamic
		Non-linear static
Without longitudinal or transverse stiffeners	PTS design loads	Eigenvalue buckling
		Dynamic
		Non-linear static

m. Level of Detail

The corners of the box girder have comparatively little bending stiffness with respect to bending in the plane perpendicular to the girder's axis. This fact is accounted for by thin elements representing the shear webs close to the corners as shown in Figure 11.

The chosen corner bending stiffness affects the buckling load of the caps and shear webs, the level of deformation caused by the Brazier effect and the tendency of the box girder to distort into a parallelogram like shape.

n. Further Assumptions

The transverse stiffeners (see Figure 7) are meant to be loaded in tension, when counteracting the Brazier effect. Therefore, they are only approximately 2mm thick. However, when the girder is loaded in flapwise bending, the cap in tension contracts in transverse direction due to Poisson's effect. For low loads Poisson's effect is stronger than the Brazier effect and the transverse stiffeners attached to the cap in tension are in compression. As they are only 2mm thick they buckle under this compressive loading.

While this behavior may be a problem in terms of the design, it also poses a problem with respect to the finite element analysis. On the one hand the buckling of the transverse stiffeners at low loads causes convergence difficulties during nonlinear static analysis. On the other hand it causes problems during eigenvalue buckling analysis, as many low eigenvalues exist, that correspond to the buckling of the individual transverse stiffeners.

In order to overcome these problems the transverse stiffeners were assumed to be sandwiches with approximately 1mm thick face layers for the sake of analysis. The transverse stiffeners are “simply supported” at their ends as they share nodes with continuum shell elements, which do not have rotational degrees of freedom. Therefore, the sandwich assumption should not influence the outcome of the analysis apart from preventing buckling of the transverse stiffeners at very low loads.

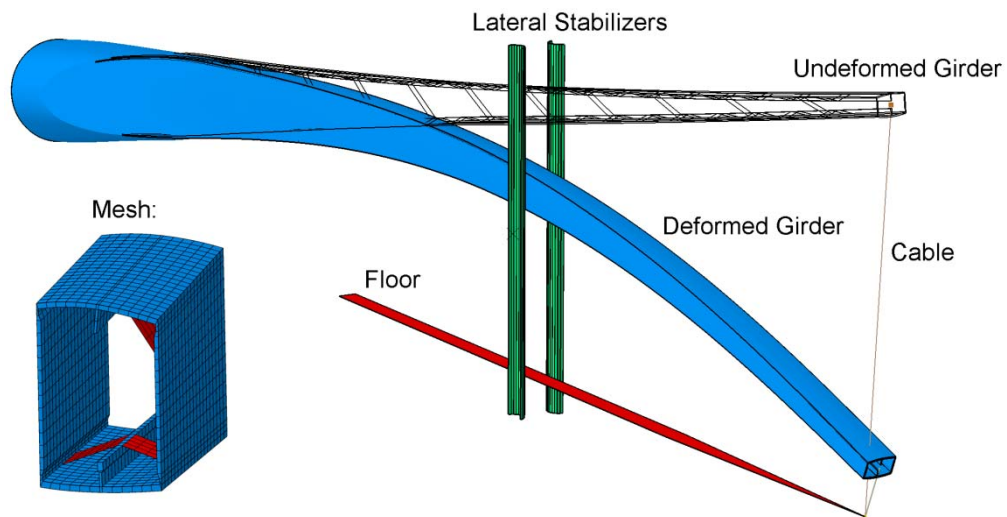


Figure 15: Finite element model including cable and lateral stabilizers; Mesh detail shown bottom left.

2.4 Results

o. Problem Size and Solution Time

The model has approximately 100000 nodes corresponding to approximately 300000 degrees of freedom. About 2GB of main memory are required.

On a HP Proliant BL465c server with two AMD Opteron 2218 dual core CPUs (2.6 GHz), a non-linear static load case (10 increments) took about 30 minutes. A dynamic load case (33 increments) took about 40 minutes. Eigenvalue buckling analysis (first 14 eigenvalues) took about 15 minutes.

p. Lateral Elastic Instability

When the box girder is bent in flapwise direction, an elastic lateral instability occurs which leads to large edgewise deformations and twisting around girder axis. This instability is known as lateral torsional buckling. Figure 16 shows the corresponding mode shapes from an eigenvalue buckling analysis. While Figure 16, left, shows the mode shape for the design load case, Figure 16, right, shows the mode shape for the test load case. The critical load level for the design load case is 75%, while the critical load level for the test load case is 108%. The critical load is higher for the test load case as the cable used for load introduction has a stabilizing effect.

Lateral elastic instabilities of beam-like structures are a well known phenomenon. However, such a mode of deformation is of course unrealistic for a wind turbine blade including the aerodynamic shell. Therefore, suitable boundary conditions are used to prevent this elastic instability, see Section j.

During physical testing lateral deformation is prevented by two steel columns as shown in Figure 15. In the corresponding model (test load case) the steel columns are represented by rigid bodies and frictionless contact between the girder and the rigid bodies is assumed. Figure 17 shows the computed horizontal Force exerted on the right (looking from tip to root) lateral stabilizer. At 100% test load a horizontal force of 1250 N is obtained. The lateral stabilizers were designed to withstand several times this force.

In order to prevent the lateral instability in the design load case, lateral boundary conditions are applied to the master nodes of the distributing coupling constraints at $r=10\text{m}$, $r=20\text{m}$ and $r=30\text{m}$. Figure 18 shows the corresponding reaction forces.

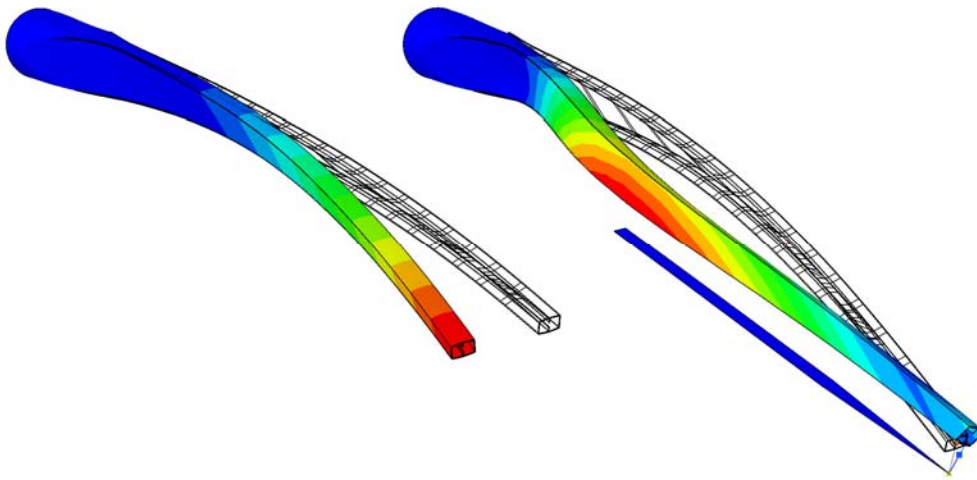


Figure 16: Lateral elastic instability; Left: mode shape for design load case (critical load level: 75%); Right: mode shape for test load case (critical load level: 108%).

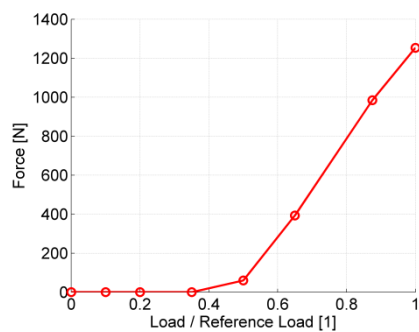


Figure 17: Horizontal force exerted on the right (looking from tip to root) lateral stabilizer; Test load case.

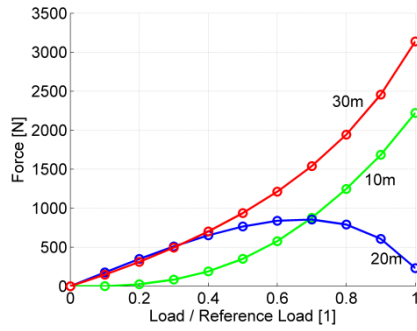


Figure 18: Reaction force at the master nodes of the distributing coupling constraints at $r=10m$, $r=20m$ and $r=30m$; Design load case.

q. Deformation and Global Strain Level

Figure 19 and Figure 20 show the deformed model for 100% design load and 100% test load, respectively. Figure 20 also shows the cable (connector element) used for load introduction and the lateral stabilizers and the floor of the test facility. It can be observed that loading the girder above 100% test load will not be possible in the current test setting, as the tip of the girder hits the floor.

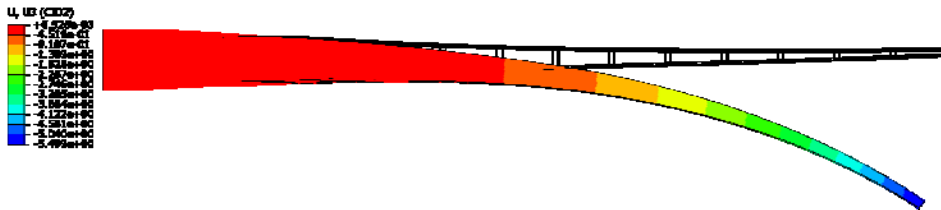


Figure 19: Deformed model, 100% design load.

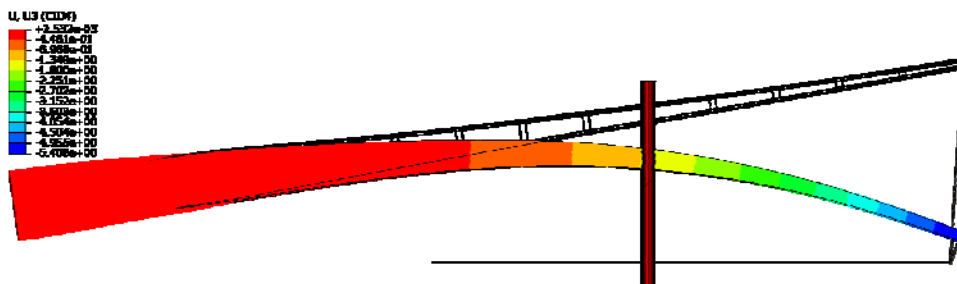


Figure 20: Deformed model, 100% test load.

Figure 21 compares the vertical displacement at $r=30m$ (design load case) obtained from static and dynamic analysis. Both analysis procedures yield the same result. It can be observed that the displacement is a linear function of the applied load.

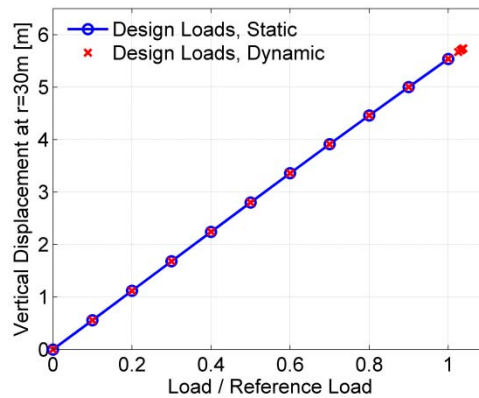


Figure 21: Vertical displacement at $r=30m$; Design load case; Comparison between static and dynamic analysis procedure.

Figure 22 compares the standard model to a model configuration without transverse stiffeners (design load case). It can be observed that the configuration without transverse stiffeners yields slightly higher displacements. This is due to the increased Brazier effect that slightly reduces the bending stiffness.

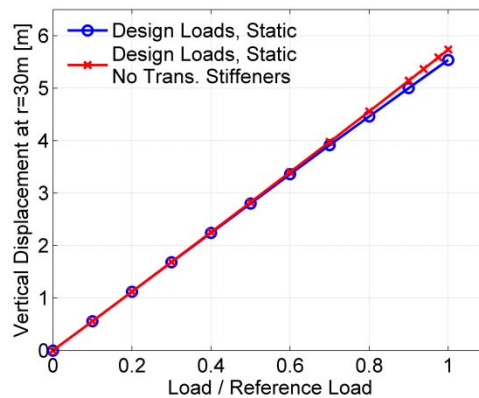


Figure 22: Vertical displacement at $r=30m$; Design load case; Comparison to configuration without transverse stiffeners.

Figure 23 compares the standard model to a model configuration without longitudinal or transverse stiffeners (design load case). It can be observed that the suction side cap buckles at approximately 46% load – see also Figure 31. That is, the presence of the longitudinal stiffener increases the buckling load of the cap by more than a factor two.

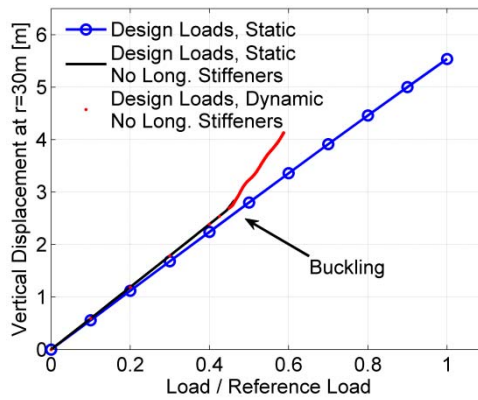


Figure 23: Vertical displacement at $r=30m$; Design load case
Comparison to configuration without longitudinal or transverse stiffeners.

Figure 24 compares the vertical displacement at $r=30m$ (test load case) obtained from static and dynamic analysis. Both analysis procedures yield the same result.

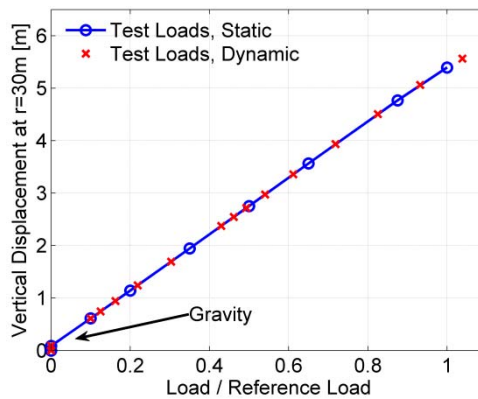


Figure 24: Vertical displacement at $r=30m$; Test load case;
Comparison between static and dynamic analysis procedure.

Figure 25 and Figure 26 present the longitudinal membrane strain in the caps for the design and test load case, respectively. The radial positions of the transverse stiffeners are marked by vertical lines. It can be observed that the absolute value of the longitudinal strain increase at the positions of the transverse stiffeners on the pressure side cap (the cap in tension), but decreases at the positions of the transverse stiffeners on the suction side cap (the cap in compression).

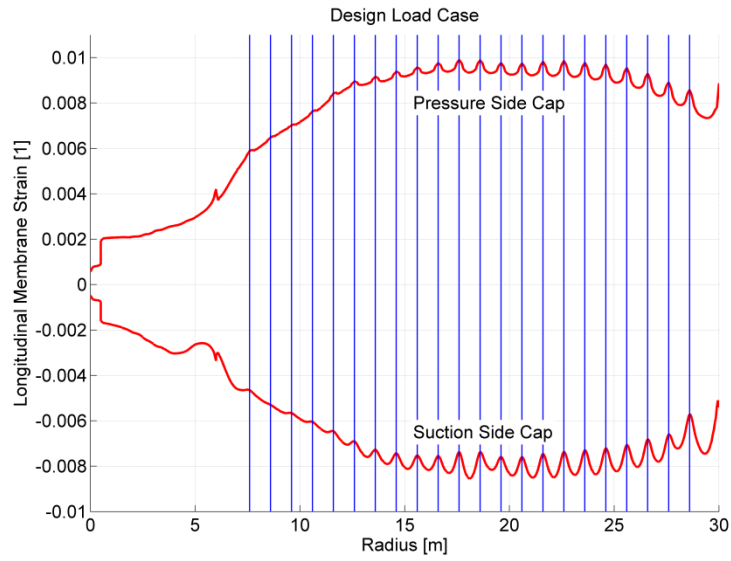


Figure 25: Longitudinal membrane strain; Design load case; Radial position of transverse stiffeners marked by vertical lines.

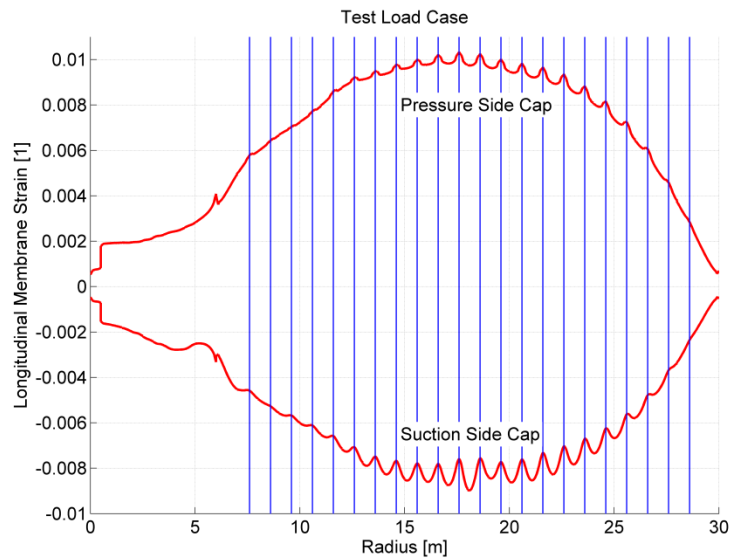


Figure 26: Longitudinal membrane strain; Test load case; Radial position of transverse stiffeners marked by vertical lines.

r. Buckling

Elastic buckling was analyzed using eigenvalue buckling analysis. The buckling loads are obtained as a multiplier of the pattern of perturbation loads, which are added to a set of base state loads. That is, buckling is analyzed relative to a base state that includes the (geometrically) non-linear effect caused by the base state loads.

Figure 27 to Figure 31 show buckling modes computed for three different configurations:

1. Standard configuration
2. Configuration without transverse stiffeners.
3. Configuration without both longitudinal and transverse stiffeners

The buckling loads are given the figure captions.

It can be observed that the transverse stiffeners have little effect on the predicted buckling loads. The longitudinal stiffener, on the contrary, is very important for preventing buckling of the caps in the present design.

s. Standard Configuration

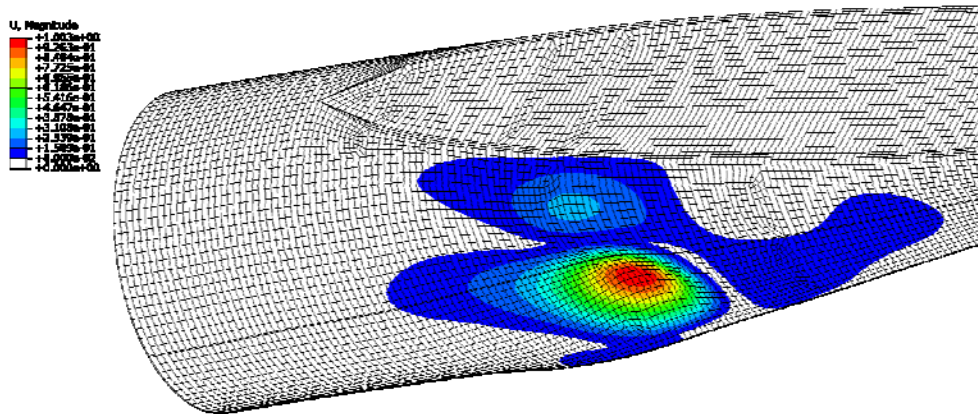


Figure 27: Eigenvalue buckling analysis; Design load case; First buckling mode;
Buckling load: 110% (100% base state load).

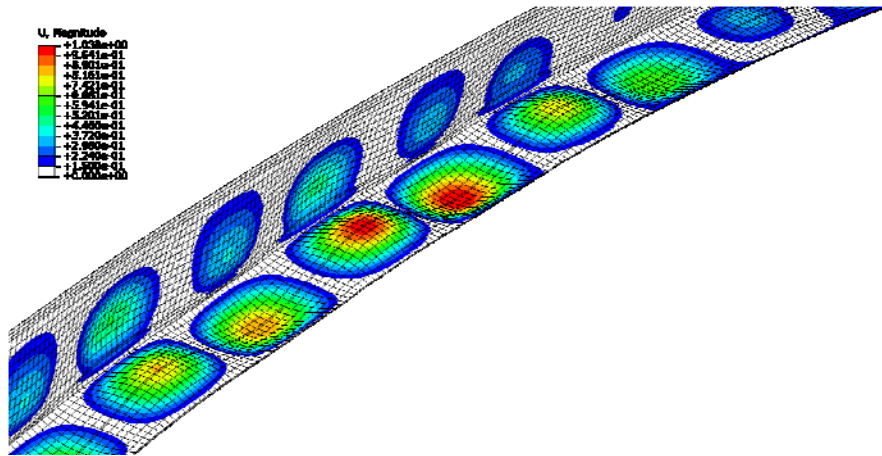


Figure 28: Eigenvalue buckling analysis; Design load case; Third buckling mode;
Buckling load: 128% (100% base state load); Wavelength approx. 2m.

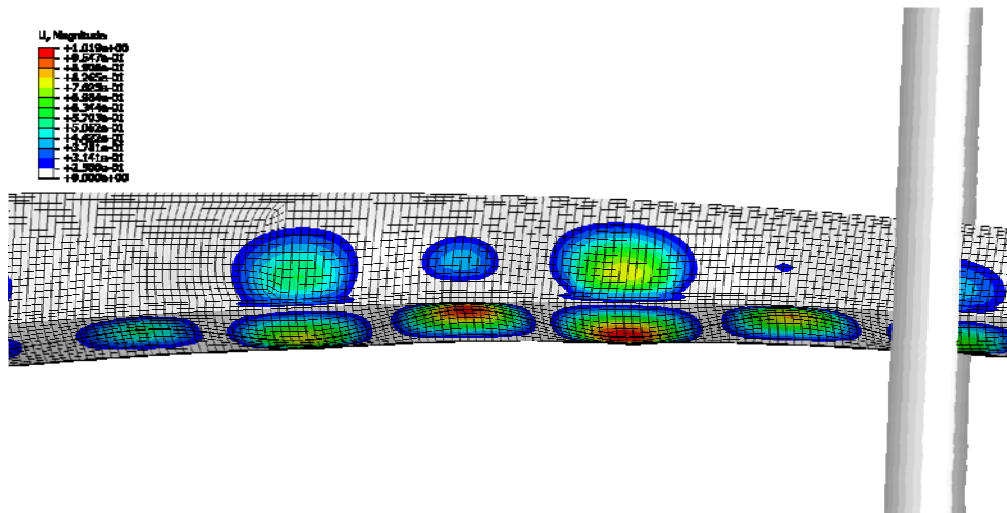


Figure 29: Eigenvalue buckling analysis; Test load case; First buckling mode;
Buckling load 129% (100% base state load); Wavelength approx. 1.3m.

t. Configuration without Transverse Stiffeners

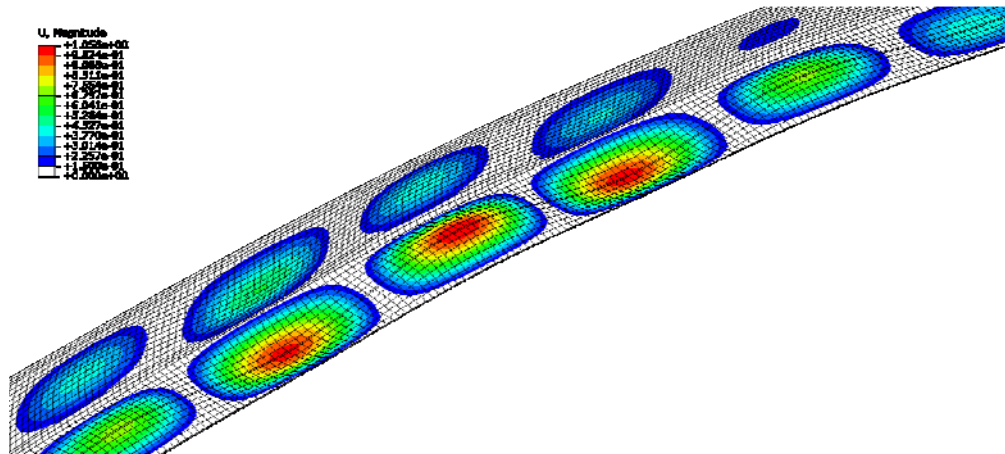


Figure 30: Eigenvalue buckling analysis; Design load case; Without transverse stiffeners; Second buckling mode; Buckling load 114% (100% base state load); Wavelength approx. 2.6m. (Missing transverse stiffeners have no effect on the first buckling mode of course.)

u. Configuration without both Longitudinal and Transverse Stiffeners

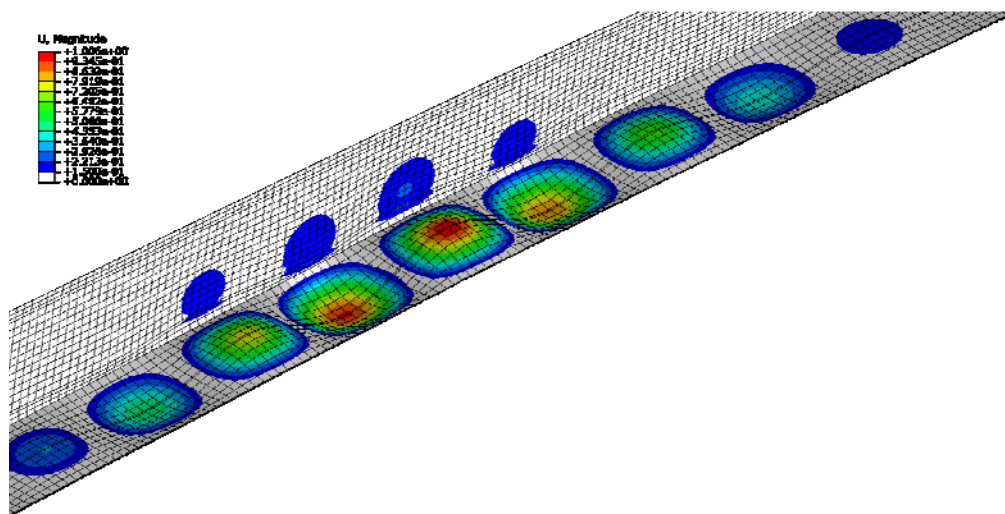


Figure 31: Eigenvalue buckling analysis; Design load case; Without longitudinal or transverse stiffeners; First buckling mode; Buckling load 46% (30% base state load); Wavelength approx. 1.3m

2.5 Effect of the Transverse Stiffeners

In this section the effects of the transverse stiffeners are investigated.

Figure 32 shows the local, vertical deformation of the mid-side point on the caps for a configuration without transverse stiffeners. The mid-side points move up to ~25mm inward, which can also be observed in Figure 34. This deformation is a consequence of the Brazier effect.

Figure 33 shows the local, vertical deformation of the mid-side point on the caps for a configuration with transverse stiffeners. The deformation of the mid-side points is now limited to ~5mm, which can also be observed in Figure 35.

Similar trends can be observed in the transverse normal stress and transverse shear stress in the two caps, see Figure 36 to Figure 39.

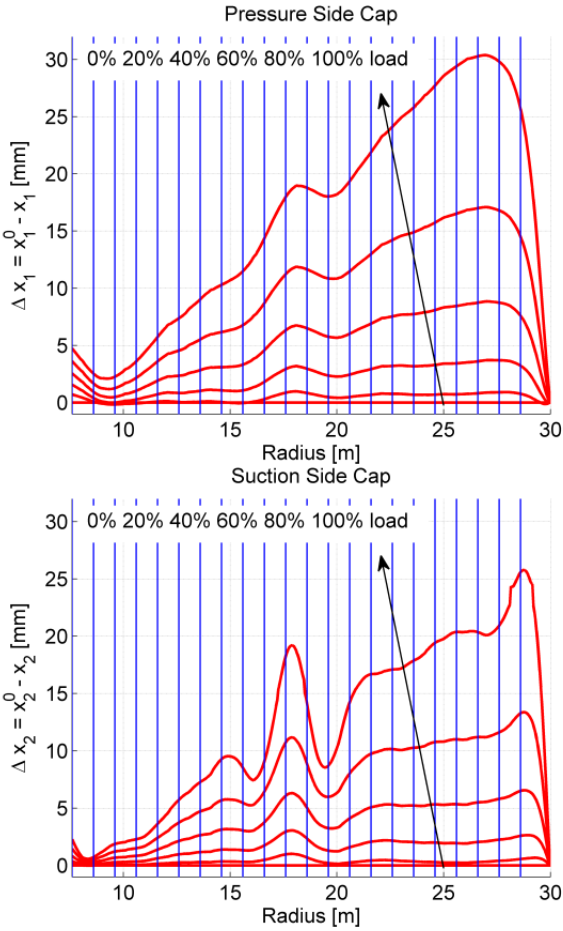


Figure 32: Local deformation of the caps; Design load case; Without transverse stiffeners.

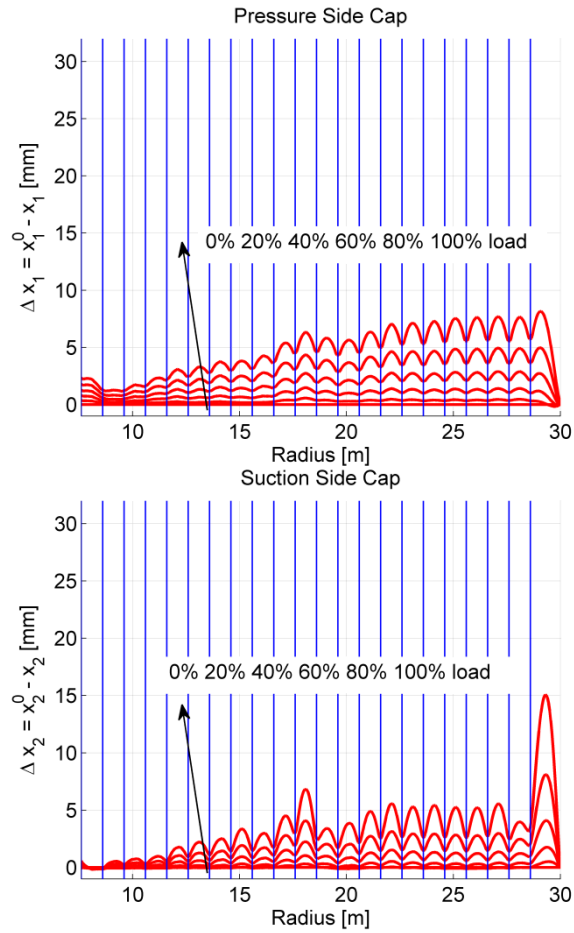


Figure 33: Local deformation of the caps; Design load case; With transverse stiffeners.

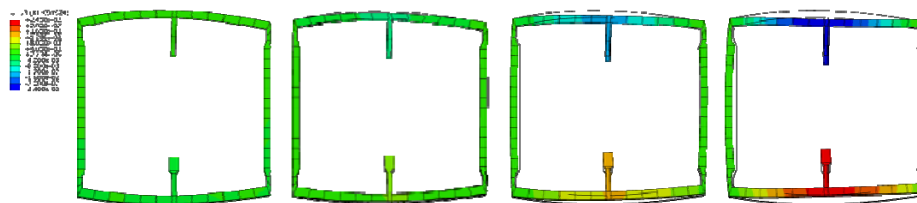


Figure 34: Local deformation of the cross-section at $r=24m$; Configuration without transverse stiffeners; Color indicates vertical displacement; Deformation scale-factor: 1.0; Design load case; Form left to right.; 0% 50% 80% 100% load.

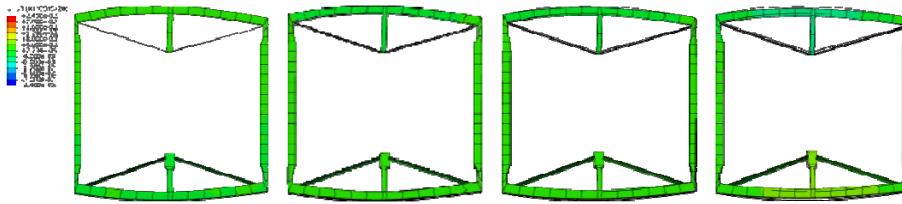


Figure 35: Local deformation of the cross-section at $r=24m$; Configuration with transverse stiffeners; Color indicates displacement; Deformation scale-factor: 1.0; Design load case; From left to right: 0% 50% 80% 100% load;

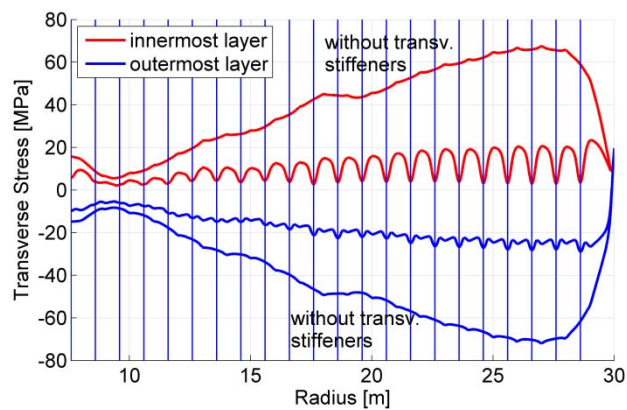


Figure 36: Transverse normal stress in the pressure side cap (innermost layer and outermost layer), with and without transverse stiffeners; Design load case.

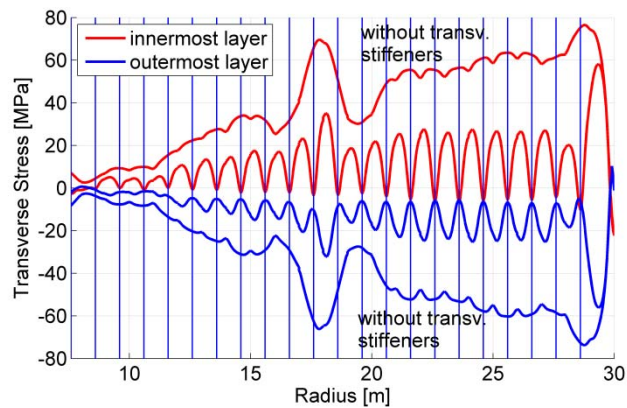


Figure 37: Transverse normal stress in the suction side cap (innermost layer and outermost layer), with and without transverse stiffeners; Design load case.

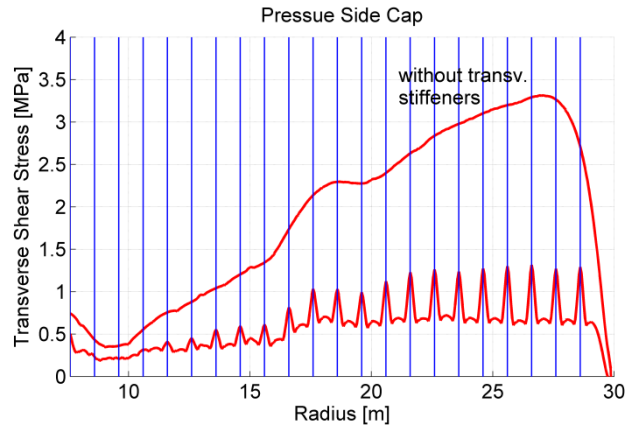


Figure 38: Transverse shear stress (in transverse-normal-plane) in the pressure side cap, with and without transverse stiffeners; Design load case.

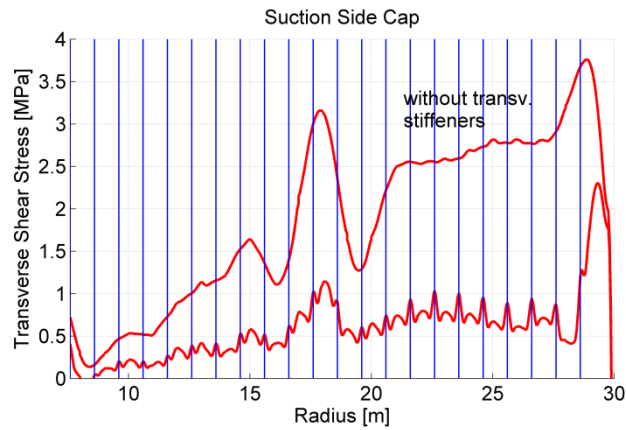


Figure 39: Transverse shear stress (in transverse-normal-plane) in the suction side cap, with and without transverse stiffeners; Design load case.

Figure 40 shows the total (transverse) force carried by one of the two transverse stiffeners on the suction side and pressure side. The Brazier effect suggests that these forces should be tensile (positive). However, on the pressure side, the force is compressive (negative) for a load level below 35%. This is because the pressure side cap is loaded in tension and contracts in transverse direction due to Poisson's effect. For low loads Poisson's effect is stronger than the Brazier effect and the transverse stiffeners are loaded in compression. As they are only 2mm thick, they buckle under this compressive loading. In the FE model this buckling is prevented by assuming the transverse stiffeners to be sandwiches with approximately 1mm thick face layers.

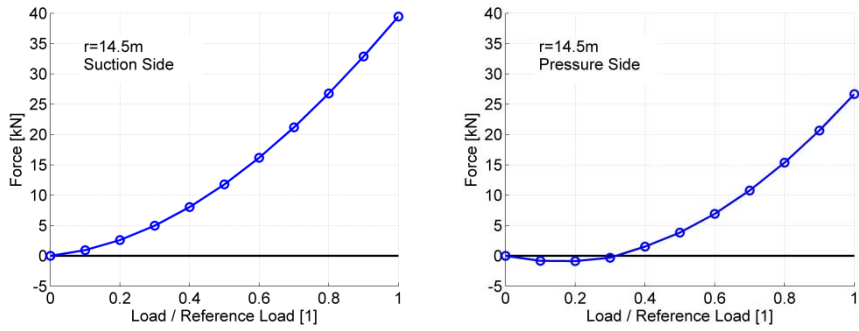


Figure 40: Total (transverse) force carried by one transverse stiffener at $r=14.5m$; Design load case; Left: suction side; Right: pressure side.

2.6 Strain Energy Distribution

In order to estimate how much energy might be transferred to the support structure during catastrophic failure of the girder at a given radial position, the strain energy distribution has been computed – see Figure 41.

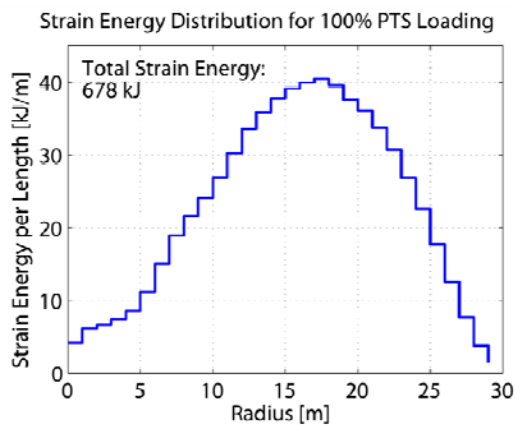


Figure 41: Strain energy distribution; test load case; 100% load.

2.7 Comparison to Measurement Results

In this section data measured during the full-scale test “DMT_2012_05_24_B” are compared to FEM results. The test “DMT_2012_05_24_B” was the last test with a completely intact girder. Figure 42 compares the measured and computed longitudinal normal strain on the suction side cap for a load level of 37.3%. Measured and computed strains are in very good agreement.

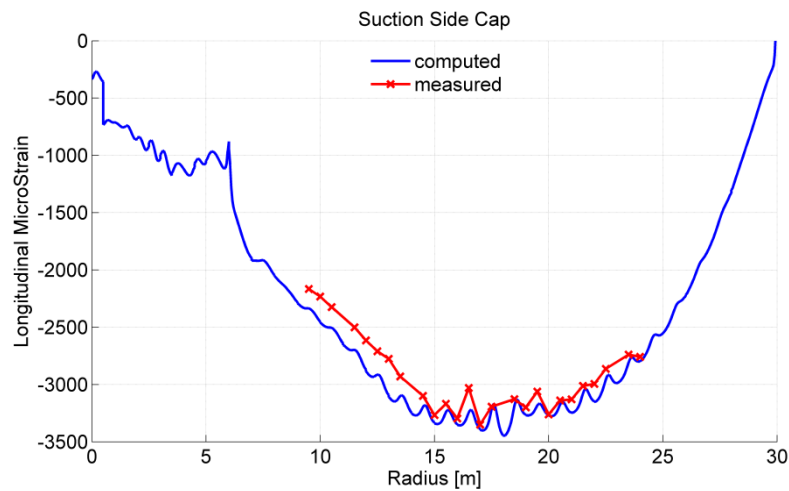


Figure 42: Comparison of measured and computed longitudinal normal strain on the suction side cap; Load level: 37.3%.

Figure 43 and Figure 44 compare the measured and computed strain in the transverse stiffeners at $r=16.5\text{m}$ on the pressure side and suction side, respectively.

It can be observed that the transverse stiffeners on the pressure side show negative strains for low loads. This is due to Poisson's effect, as explained in the “Modeling Section”.

As the transverse stiffeners are only about 2mm thick, they buckle when loaded in compression. In the FEM model the ability of the transverse stiffeners to buckle is suppressed. As the strain gages were mounted on the inner side of the stiffeners, the measured strain contains a component associated with the bending of the stiffener. Therefore, a good match between the measured and computed strains is not to be expected for the stiffeners attached to the pressure side and small loads.

The transverse stiffeners attached to the suction side exhibit tensile strains even for low loads. The numerical analysis over-predicts these strains, as can be seen from Figure 44.

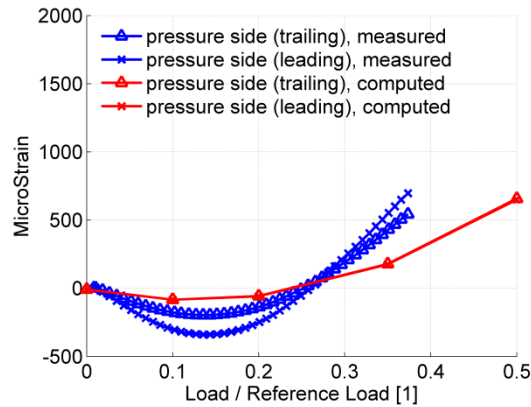


Figure 43: Comparison of measured and computed strain in the transverse stiffeners at $r=16.5m$; Pressure Side.

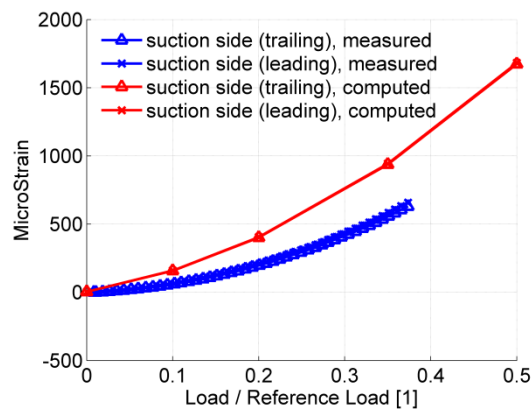


Figure 44: Comparison of measured and computed strain in the transverse stiffeners at $r=16.5m$; Suction Side.

3. Manufacturing of the boxgirder

The basis of the project is an existing 42 m long blade manufactured by SSP Technology. The concept of SSP Technology is a blade with an internal box girder. The concept means that mould is available for the outer shells of the blade as well as for the boxgirder. The box girder is manufactured in two parts using female mould technology. Each part is made separately in its own mould and after the curing the two halves is bonded together by placing one mould on top of the other with the parts still inside. This is often referred to as closing the mould. The materials for the boxgirder are glass fiber reinforcement with epoxy as matrix materials. Sandwich construction is used in webs.

The box girder as well as the outer shells is manufactured using VARTM (Vacuum Assisted Resin Transfer Molding). Due to confidential information a detailed description of the process along with photos is not available.

Both the transverse and the diagonal reinforcements, which is a part of the new design, are manufactured separately before attached to the girder halves. This has to be done before the

moulds are closed and the box girder is bonded together. Also the internal strain gauges and accompanying wiring is attached to the parts before closure of the moulds. The transverse reinforcement is highly stressed when the box girder is loaded, and therefore a test was performed to ensure that the manufacturing method for the reinforcement was capable of sustaining the load. The test is described in detail in appendix F



Figure 45: Test setup for measuring the load capability of the transverse reinforcement.

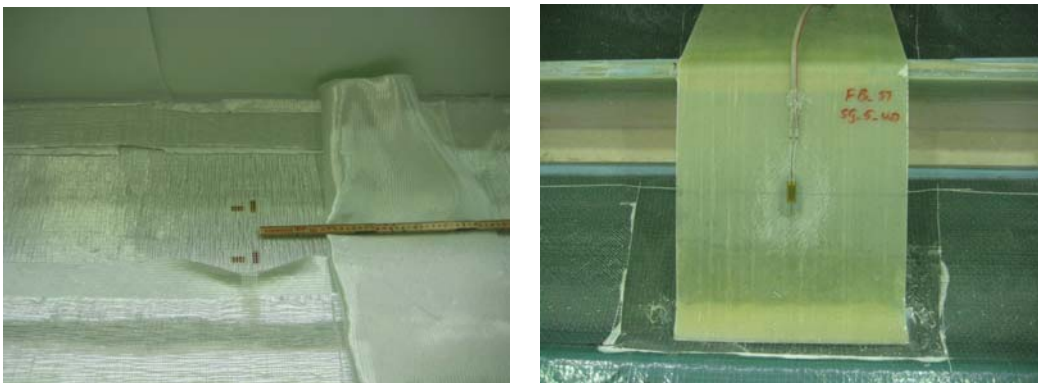


Figure 46: Left.: Strain gauges have been integrated in the laminate to measure internal stresses.
Right: Strain gauges are mounted inside the girder.



Figure 47: Photos of the cured parts with the reinforcements installed



Figure 48: Photos from the inside of the assembled boxgirder.

4. Test setup

As previously described in this report, it was decided to design and manufacture a 30 m section of a 42 m blade, because this part is most critical regarding structural failure, and because this would simplify the full scale test. For the particular concept investigated in this project it is only relevant to test the blade in flapwise direction, because the loads in other directions are managed by other parts of the blade.

The potentially most damaging load to the box girder is the PTS load case. This load case achieves the highest bending moment at the root and at the critical sections of the box girder. The load for this load case was provided by SSP Technology A/S.

In the project it was decided to use a shortened section of the girder. This has several advantages in relation to the test facility, but the main drawback is that the load on the girder cannot achieve the correct value at every section of the girder. This is due to the fact that it is very difficult to introduce bending moments with the load application equipment.

The box girder's root section was unchanged in the design process, and therefore there is no need to test this part at very high loads.

Several moment distributions along the blade were calculated. In the end it turned out that the moment distribution didn't improve a lot but having more load applications it was decided to apply the full load at 30m.

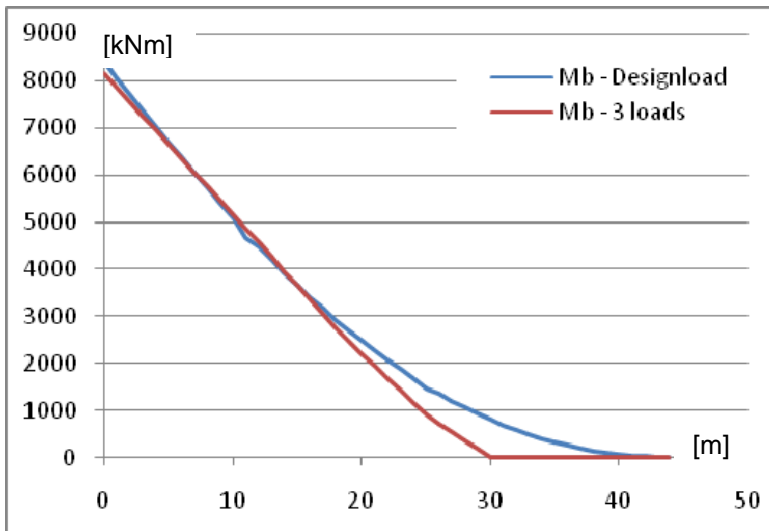


Figure 49: Bending moment along the length of the girder with loads applied at 19, 25 and 30 m.

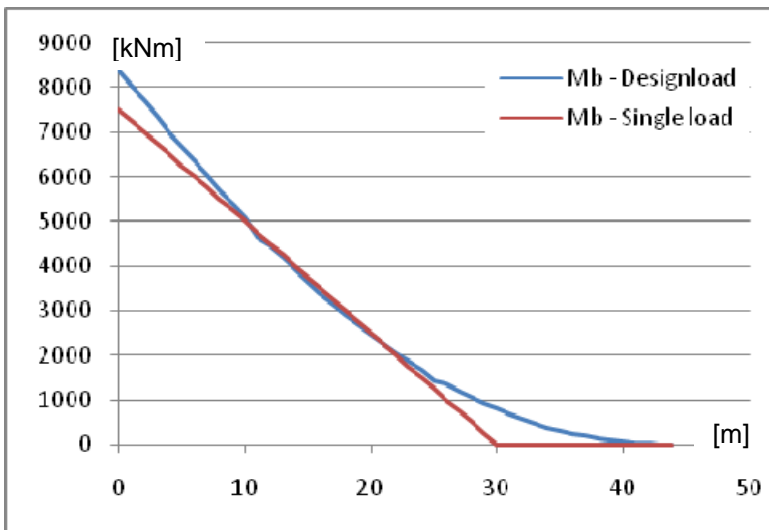


Figure 50: Bending moment along the length of the girder with loads applied 30 m

4.1 Sideways Instability

Detailed finite element analyses, see part 2, have shown that the girder shows unstable behaviour clearly below the certification loads. Non-linear geometric analysis as well as eigenvalue buckling analysis show that the girder starts deforming “sideways”, i.e. in edgewise direction. Such a mode of deformation is unrealistic for a wind turbine blade including the aerodynamic shell and should therefore be avoided.

For instance, Figure 51 shows the first eigenmode obtained from eigenvalue buckling analysis. At the tip the girder’s ability to deform sideways is limited by the load application mechanism. Therefore, the largest sideways deformations are found at a radius of approximately 20m (red color in Figure 51).

This kind of instability is not specific to composite box girders. Any beam whose bending stiffness with respect to the major principal axis is much larger than the bending stiffness with respect to the minor principal axis may show this behaviour when bent about the major principal axis.

In order to prevent the undesirable deformation mode described above, two lateral guides are used in the physical test as shown in Figure 52. Finite element analyses including the guides indicate that these two guided (together with the stabilizing effect of the load application system at the tip) are sufficient to prevent sideways deformations, see Figure 53.

4.2 Load Application

When testing wind turbine blades in bending, one aims at generating a certain distribution of bending moments (and shear forces) by applying concentrated forces at one or several radial positions. In a virtual experiment (a finite element model) this is comparatively simple as “follower forces” can be used. The forces stay perpendicular to the deformed axis of the blade and generate the desired distribution of bending moments and shear forces, see Figure 54.

During the physical test loads are applied using cables. They neither have a fixed direction in space, nor do they correspond to “follower forces”. Therefore, the loads application points (the initial arrangement of the cables) should be chosen in such a way that the cables are approximately perpendicular to the deformed axis of the blade when the critical (or “interesting”) load level is reached. An example of such a choice is shown in Figure 55.

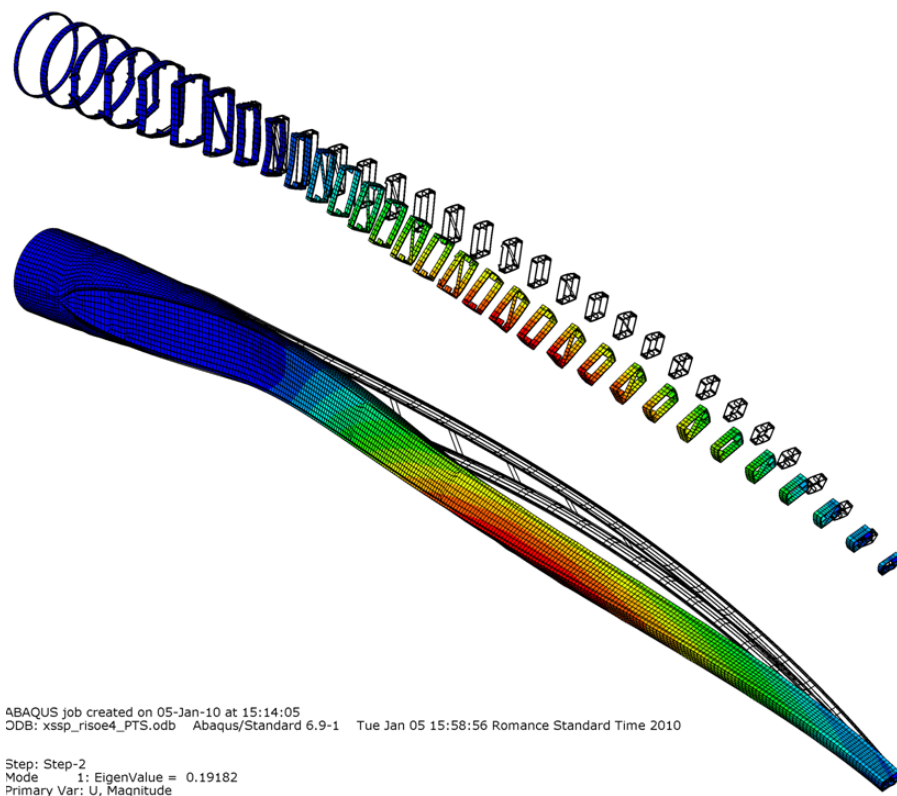


Figure 51: Deformed configuration and first eigenmode corresponding to approximately 65% PTS load; bottom: entire girder; top: selected cross-sections.

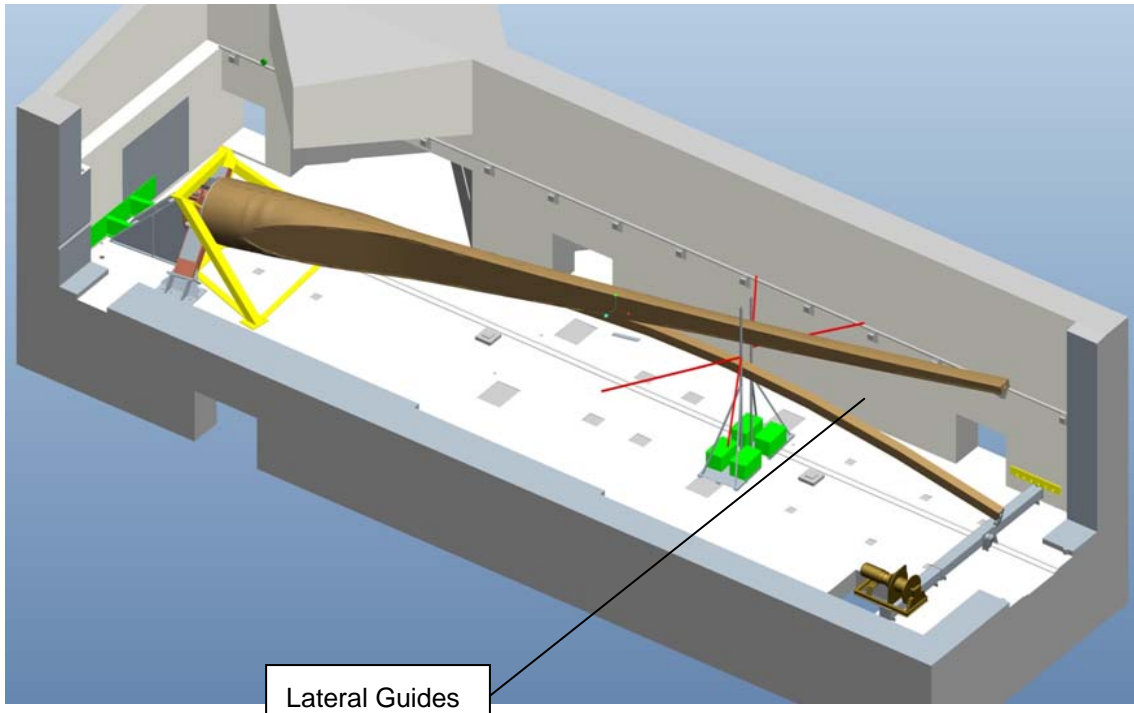


Figure 52: Lateral guides preventing unwanted sideways deformations during the physical test.

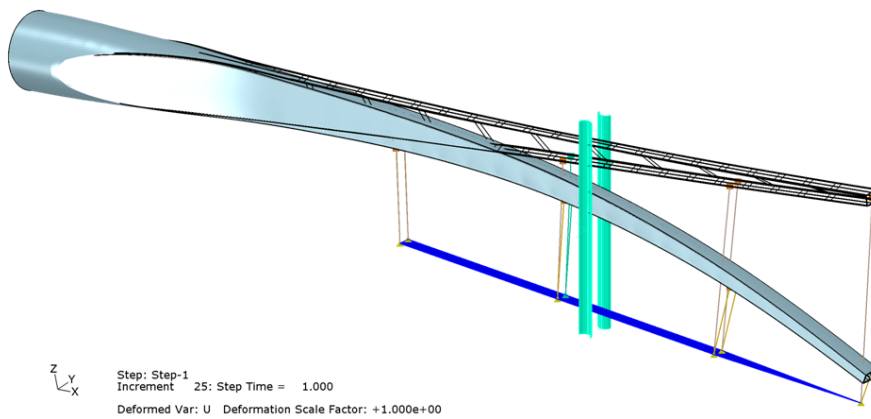


Figure 53: Finite element model including the guides: sideways deformations are prevented.

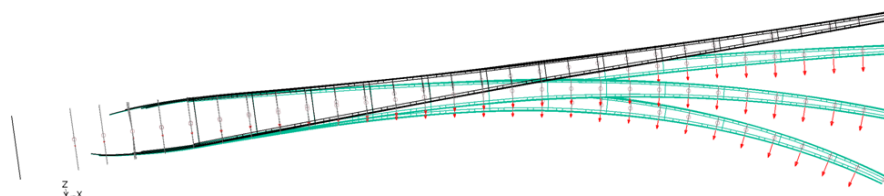


Figure 54: Follower forces stay perpendicular to the deformed axis of the blade.

The loads was tranferes to the boxgirder with at steelinsert in the tip. The steel insert reaches 700 mm inside the girder and is fastened to the girder with adhesives and bolts.

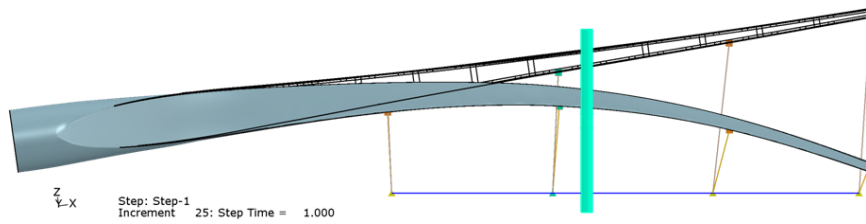


Figure 55: Cables are roughly perpendicular to the deformed axis of the blade when the critical load level is reached.



Figure 56: A view of the test setup from the tip of the girder. The guides is the brown columns in the middle of the picture.



Figure 57: A view of the test setup seen towards the tip.



Figure 58: The loads was tranfered to the boxgirder with at steelinsert in the tip. The steel insert reaches 700 mm inside the girder and is fastened to the girder with adhesives and bolts.



Figure 59: A photo of the steel girder for applying the load. In the back the winch is shown, and in the front, the bracket for guiding the wire to the girder is shown.

5. Measurements

5.1 Terms and definitions for the measurement systems

The blade cross section with the main structural features is presented in Figure 60.

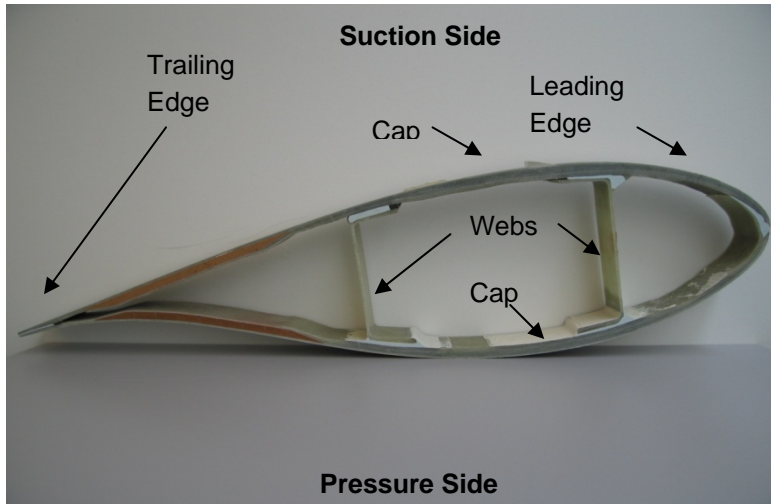


Figure 60. Picture of a blade cross-section indicating construction elements.

Definitions

Blade root:	Part of the wind turbine blade that is closest to the rig
Box girder:	Primary lengthwise structural member of a wind turbine blade
Edgewise:	Direction that is parallel to the local chord of the blade
Flapwise:	Direction that is perpendicular to the surface swept by the non-deformed rotor blade axis
Trailing edge (TE):	Edge of blade pointing opposite travelling direction
Leading edge (LE):	Smooth edge of blade pointing the travelling direction

Table 7 Loading directions with respect to the blade.

Load case
PTS - pressure side towards suction side
STP - suction side towards pressure side
TTL - trailing edge towards leading edge
LTT - leading edge towards trailing edge

The coordinate system

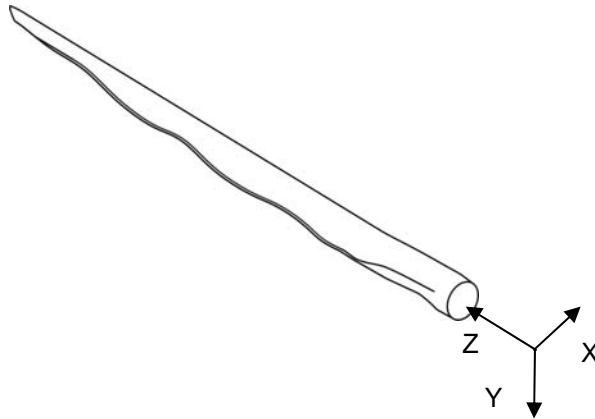


Figure 61. Coordinate system.

The x-axis is directed in edgewise (wind) direction, positive towards leading edge. The y-axis is in flapwise direction, positive in direction from pressure to suction side. The z-axis is along the blade, pointed from the root of the blade, as indicated in Figure 61.

Measurement equipment

Strain gauges (SG)

UD	Uni Directinal (0° in longitudinal direction)
Bx	Biax ($0^\circ/90^\circ$)
Tx	Triax-Rosette ($0^\circ/45^\circ/90^\circ$)
Back to back	One strain gauge on each (inner and outer) side of the blade

Linear transducers (LT)

LT-ASM	Length Transducer from ASM – Cable actuated position sensors
LT-NT	Length Transducer from NovoTechnik

5.2 Description of measurement setup

The box-girder was mounted on a test rig, as shown in the following pictures. It was fastened to the rig through about 50 steel bolts in the root. It was then loaded in vertical direction by means of a hydraulic winch. The load was applied on the tip by means of an additional steel rod fastened to the box-girder between 29,5m and 30m.

Four different data acquisition systems were used (a detailed description of the measurement equipments listed below and their placement is given in the relative appendices).

a. Catman system

The system consists of 1 computer with Catman AP software, one MGC+, 24 canheads, 173 strain gauges, 36 position sensors and 1 force transducers. For further information about this system see Ref [1].

b. Acoustic Emission

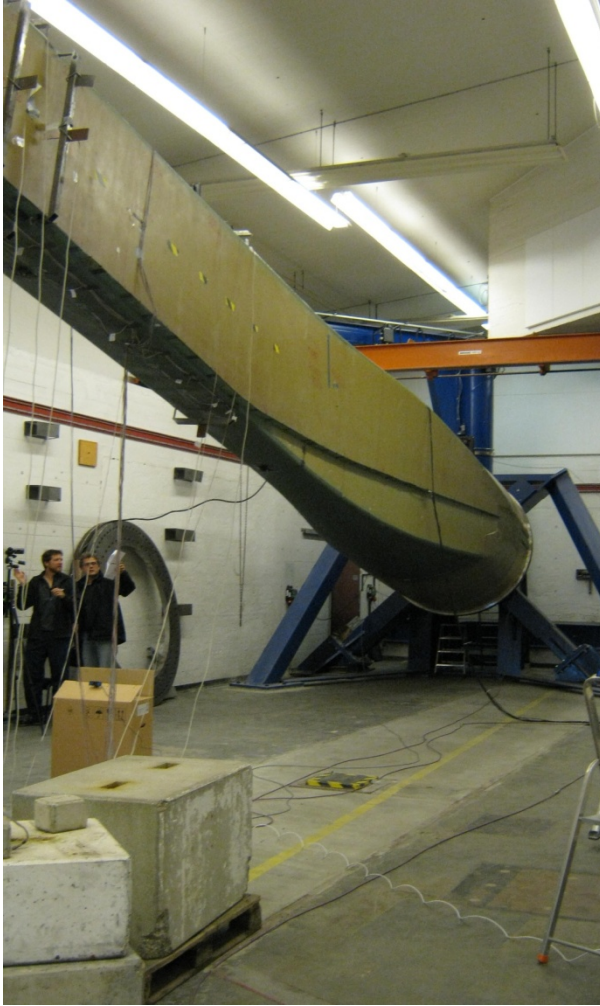
The system consists of 1 computer, a PAC DiSP system and 8 acoustic sensors mounted on the upper and lower cap.

c. Baumer Blade Monitor System

The system used the same computer used for the Catman System, one camera mounted on the test rig, shooting along the blade and two reflectors glued to the upper surface of the box-girder, at 10m and 16m from the root respectively. The description of this system is found in Appendix [E].

d. Video system

Three cameras were used to record videos of the tests. A high definition mounted close to the root, shooting in the along the blade and two low definition cameras for monitoring during the test, the first mounted on the wall behind the test rig and the second one on a tripod around 3m from the root.



The box-girder mounted on the test rig (blue frame)



The box-girder as seen from the root.

Two vertical red beams are visible. These are the lateral stabilizer.



The tip of the box-girder seen from below and the blue rod used to apply the load to the beam.

Figure 62. Photos showing the box girder on the test rig, the lateral stabilizers and the steel construction for applying loads

6. Test observations

6.1 Introduction test

The testing the box-girder was performed in several steps. The first loadings were performed at small load in order to test if all the measurement equipment and everything else worked properly.

Thereafter the load was increased slowly during the different test.

The tests performed were:

DMT_2012_05_10_B,	DMT_2012_05_10_C,	DMT_2012_05_16_A
DMT_2012_05_22_A,	DMT_2012_05_24_A,	DMT_2012_05_24_B
DMT_2012_05_31_A,	DMT_2012_05_31_B,	DMT_2012_06_07_A,
DMT_2012_06_07_B,	DMT_2012_06_07_C.	

For most of the test acoustic emission was carried out In addition to the strain and deflection measurements. The results from this are found in Appendix [D]. Appendix [A] presents the list with measurements equipment and its placement, and Appendix [B] includes the data presented by graph tool, for the two most important tests.

And the last test, DMT_2012_06_07_C, was planned to be carried out to ultimate failure, and as it was planned to be the last boxgirder test, it was also monitored by all most of the available measurement equipment including the Blade Monitoring System which most kindly were placed at our disposal by Baumer A/S.

The structure in the following part describing the test results is that the different events have been described as they appear in time.

Already in the first test, DMT_2012_05_10_B, some peculiar effect is seen at the webs around at around 25m from the root, see section a below. This effect is followed but there is no sure indication of that this later was the cause to failure.

In test DMT_2012_05_31_A the transverse stiffener and T-stiffener at around 16.5 m debonded.

In test DMT_2012_2012_06_07_C the transverse stiffener and T stiffener around 25 m debonded and the boxgirder failed at 58% of the design value.

6.2 Test

e. Test DMT_2012_05_10_B

At the shear web 25m from the root, at the right side seen from the tip and on the outside side, the behaviour of the transverse strain SG-91-Tx-2, see Figure 63, changes suddenly. The curves presented in Figure 64 are strains as a function of the local bending moment. When the test starts, the transverse strain is responding linear with respect to the local bending moment, but when the local bending moment exceed 70kNm, see Figure 64, the strain drops suddenly and becomes seemingly nonlinear.

In the next test the strain follows the new curve, see test DMT_2012_05_16_A in

Figure 64, and here the strains are following this new curve with smaller values. This indicates that indicate that a part of the structure is damaged.

25 meter section

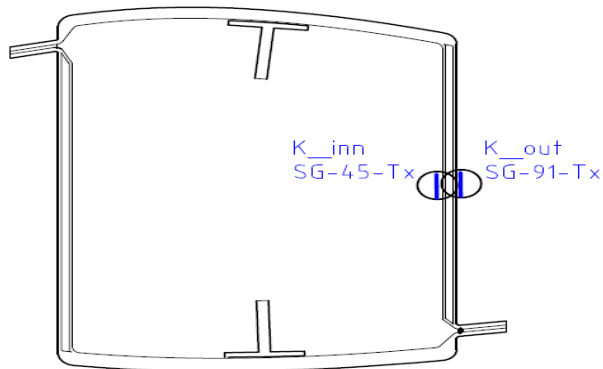
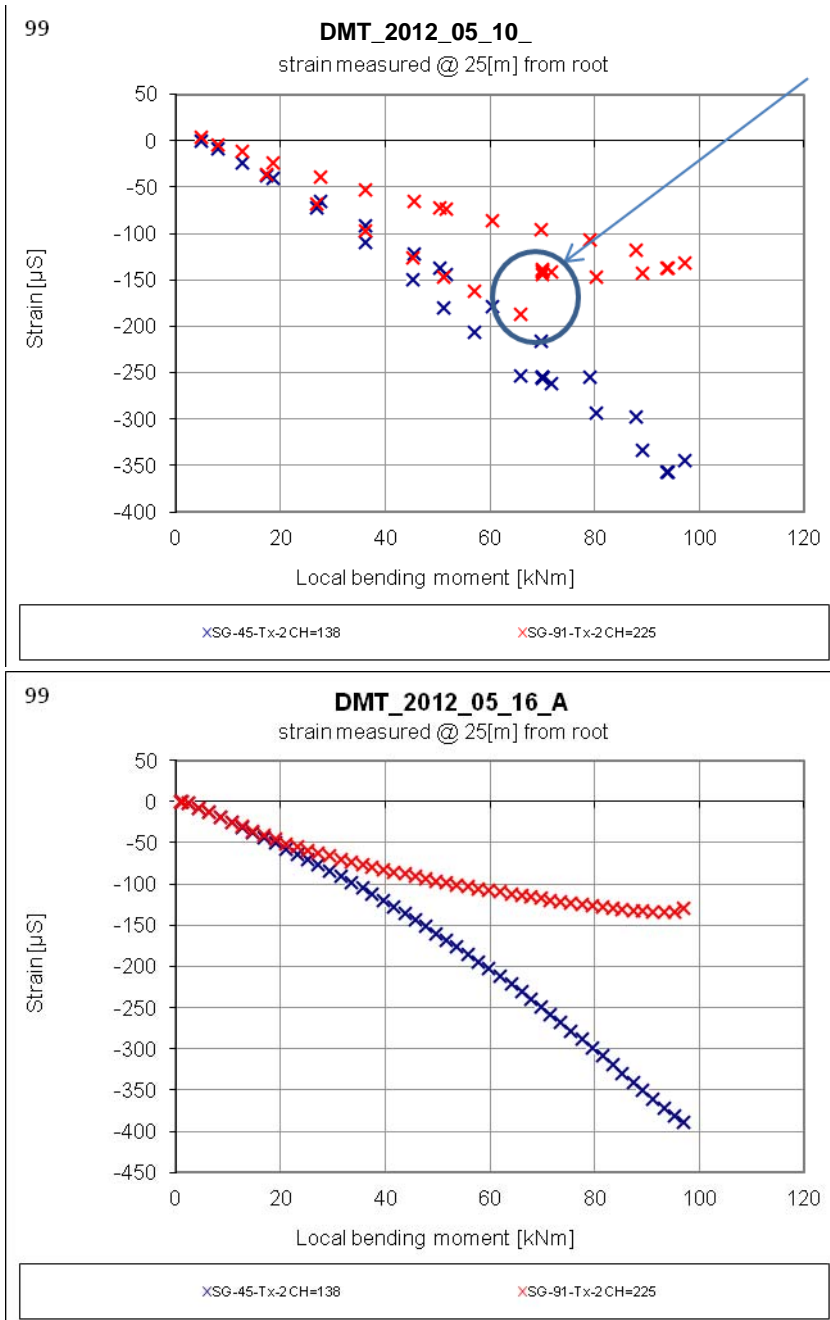


Figure 63: Sketch of the box girder in 25m

Examining the longitudinal strains does not reveal the same behaviour, and in order to exclude measurements error like debonding of strain gauge, the transverse strains in 24.5m and 25,5m are examined.

It is possible to see a change in the longitudinal strains in 24.5 and 25.5 m, even if it is not as pronounced.

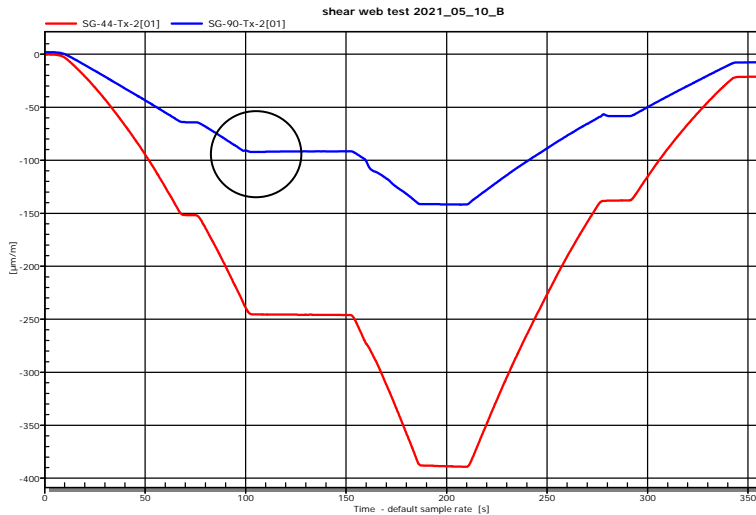
In the graphs in Figure 65 the strains are presented as a function of the time during the test, and they are presented as 24.5m, 25m and 25.5m



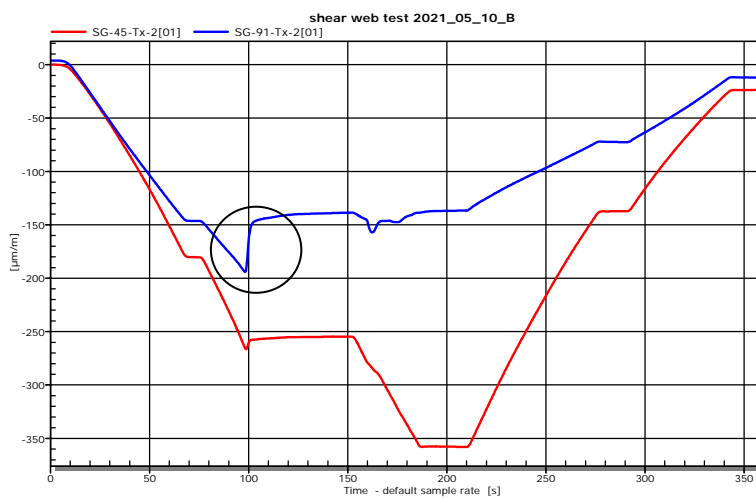
a)
DMT_2012_05_10_B

b)
DMT_2012_05_16_A

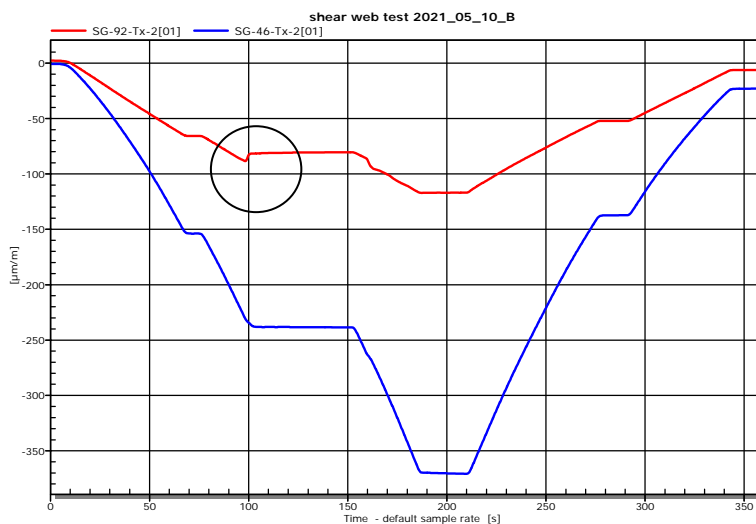
Figure 64 Transverse Strain as a function of the local bending moment in 25m section, from test DMT_2012_05_10_B and DMT_2012_05_16_A. The sudden change in SG-91-Tx-2 in test DMT_2012_05_10_B is placed inside the circle. The measurement points above the circle are from unloading of the girder. In following test, DMT_2012_05_16_A, this strain gauge is following the new curve at the end of the previous test.



a) DMT_2012_05_10_B
 Transverse strain in 24,5m as a function of time during the test. The strains presented are both for measurements outside and inside of the web.



b) DMT_2012_05_10_B
 Transverse strain in 25m as a function of time during the test. This is the event presented in Figure 64.



c) DMT_2012_05_10_B
 Transverse strain in 25,5 m as a function of time during the test.

A change in strains, occur at the same time in 25m and 25,5m, but the change are smaller.

Figure 65 Graphs with transverse strains at the same position on the web in 24,5m, 25m and 25,5m in order to examine if there were similar patterns in the strains.

f. Test DMT_2012_05_31_A

In this test the load were applied to around 40% of the maximum load which it were dimensioned for. At around 35% of the maximum load the upper transverse stiffener (see Figure 66) at 16.5m debonded.

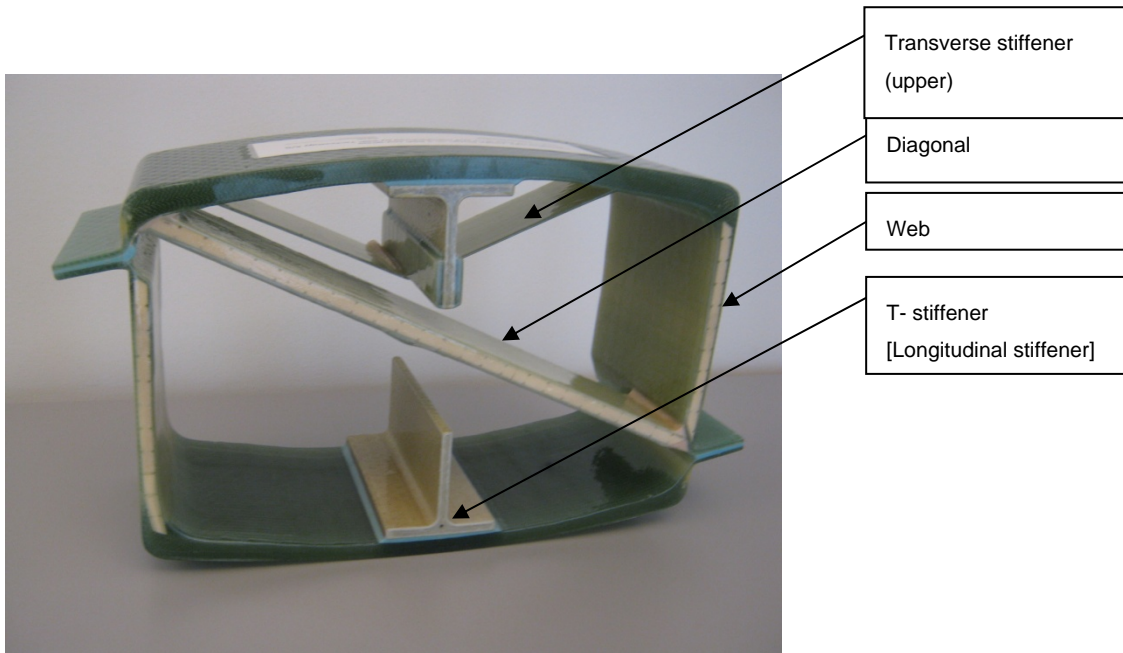


Figure 66. Photo of a section of the DMT-box

This incident was recorded with the strain gauge placed on the transverse stiffener at this place. See Figure 67.

The strains drops suddenly from around 600 μS to 0 μS

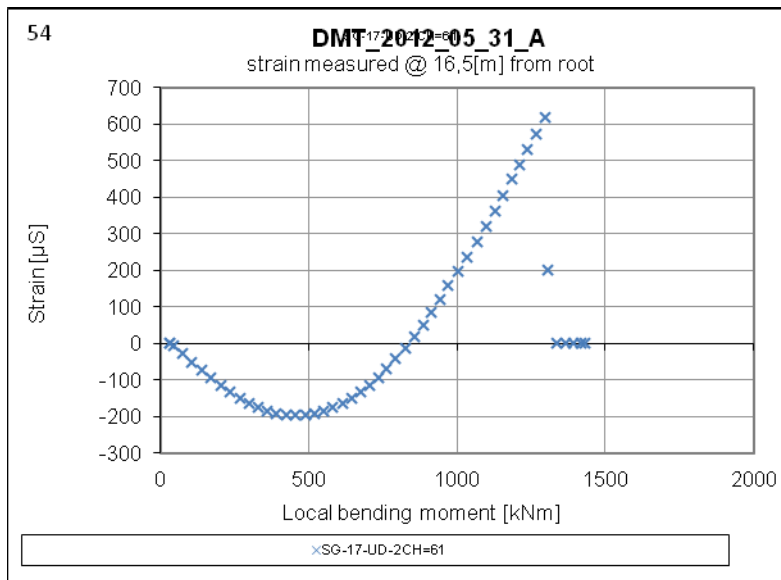


Figure 67 Strain measurements on the left part of the transverse stiffener on the pressure side of the box. The sudden drop in strain is when the adhesive bond between the cap and the transverse stiffener failed.



Figure 68 Photo inside the box after the test DMT_2012_05_31_A. the photo is taken inside the box, as it is difficult to get close to where the damage occurred. But examining it closely at the circle, one of the two transverse stiffener has debonded.

After the test the box was visual inspected inside, and it was revealed that at least one of the transverse stiffeners around 16,5m has debonded. The T-stiffener (Upper cap) has debonded in this area as well.

In Figure 69 the strains on the transverse stiffeners and T-stiffener are followed during the test. The measurements on the T –stiffener are SG-9-UD and SG-10-UD, and on the transverse stiffeners are

SG-17-UD and SG-18-UD. See the position Figure 70

When the upper transverse stiffener SG-17-UD towards trailing edge debonds, the strain on the part of the transverse stiffener towards leading edge change, but doesn't go to zero.

After this event, around half a second later, the T-stiffener debonds.

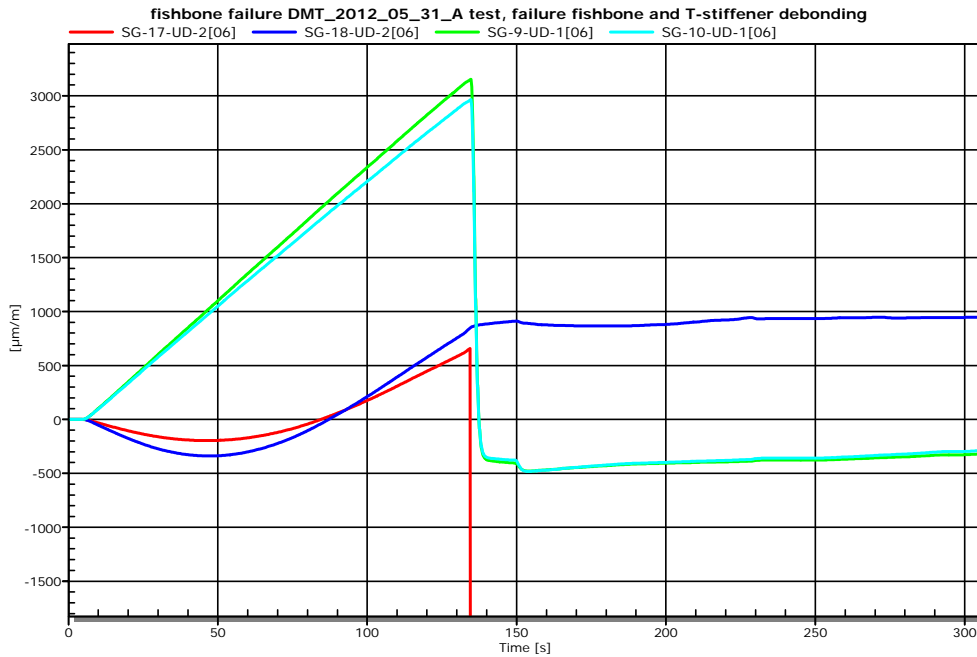


Figure 69 Graphs with the strains on the transverse stiffener and the T-stiffener during test DMT_2012_05_31_A. The transverse stiffener SG-17-UD debonds around half a second before the T-stiffener debonds.

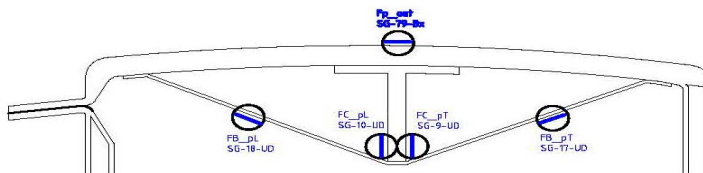


Figure 70 Drawings showing the strain gauge position on the cap at 16.5m section.

g. DMT_2012_06_07

This was the last test where the blade was loaded till failure.

Just before the blade failed there were some indications of failure which can be seen in the measurements and in the following description these incident will be described according to the time when they happened. Figure 71 presents the strain on the diagonals and looking at SG-27-UD-2 it can be seen that the strains jump at the end of the test. This part of the test is performed with continues loading of the girder.

Following was observed during the last part of the test:

- 162,9 sec Small jump downwards
- 167,5 sec Bigger jump upwards
- 181,7 sec Small jump downwards

- 193 sec Ultimate failure

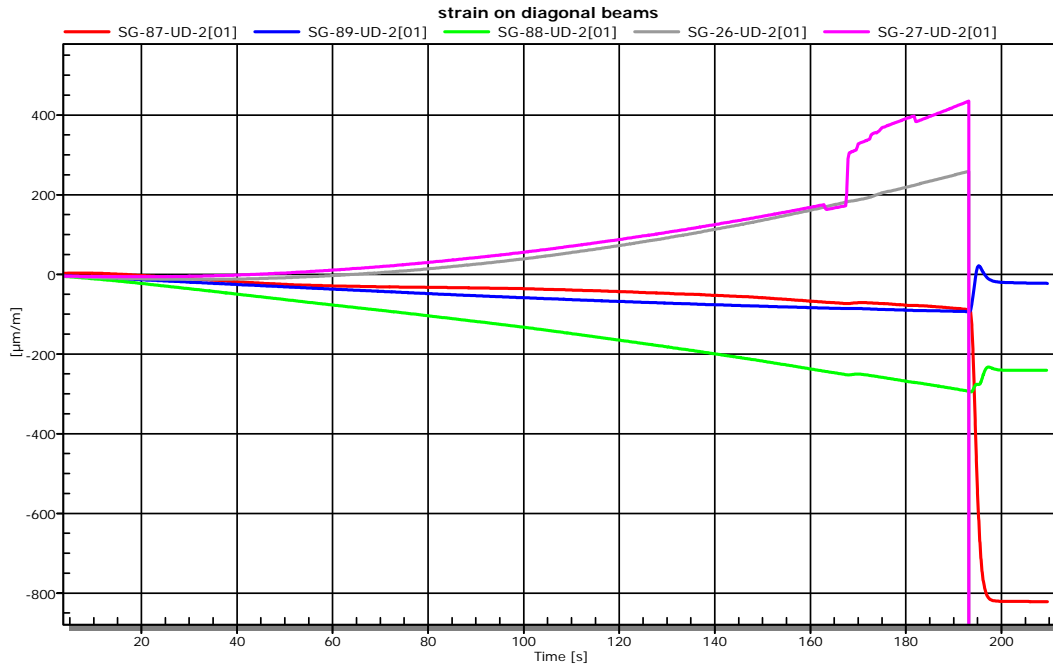


Figure 71 Graph with strain on diagonal from test DMT_2012_06_07. Measurements of strain SG-27-UD-2 on the diagonal in 22m jumps in value before the final failure.

162.9 sec:

The diagonal at 22m and the shear webs between 24.5m and 25.5m have a small jump in strains, see Figure 72 and Figure 73. The jump in strains on the diagonals happens around 0.5 sec. before this happens on the web.

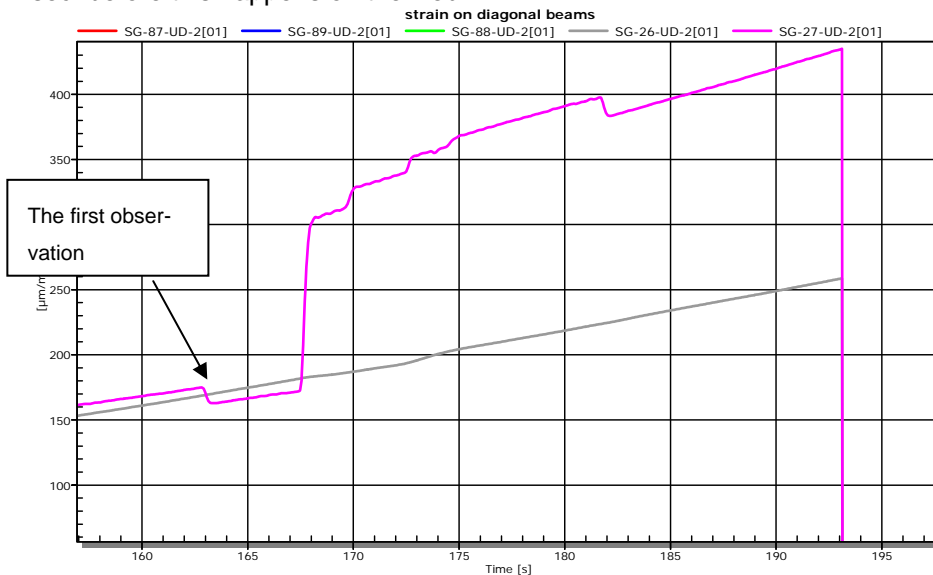


Figure 72. Close up on the graph of strains on the diagonals, following the measurements from SG-27-UD-2 at the time close to the ultimate failure.

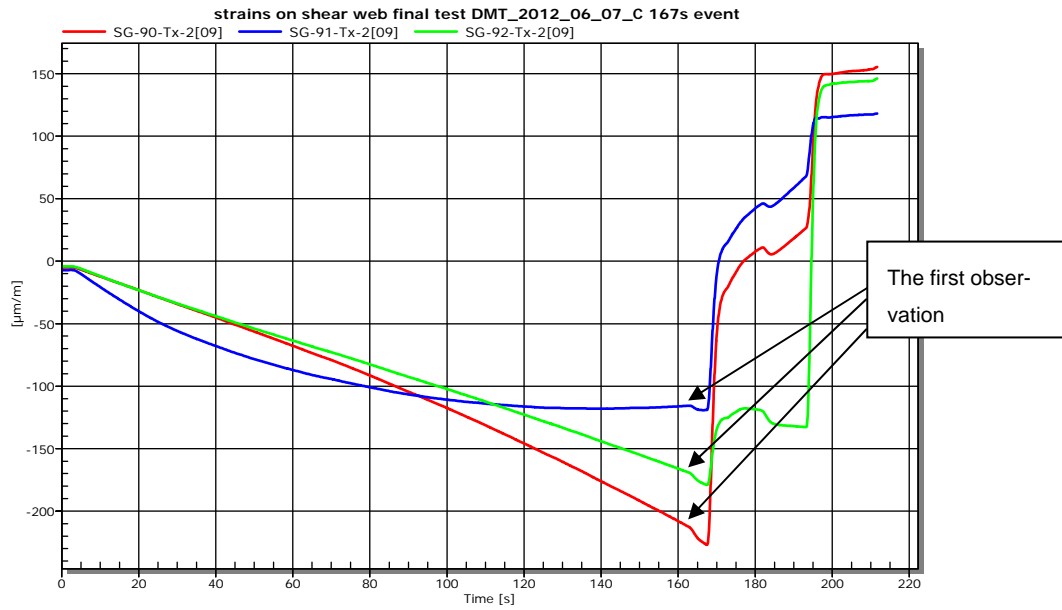


Figure 73 Graphs with the strain on the web in 24.5m 25m, and 25.5m, the first jump in strain are indicated with the arrows.

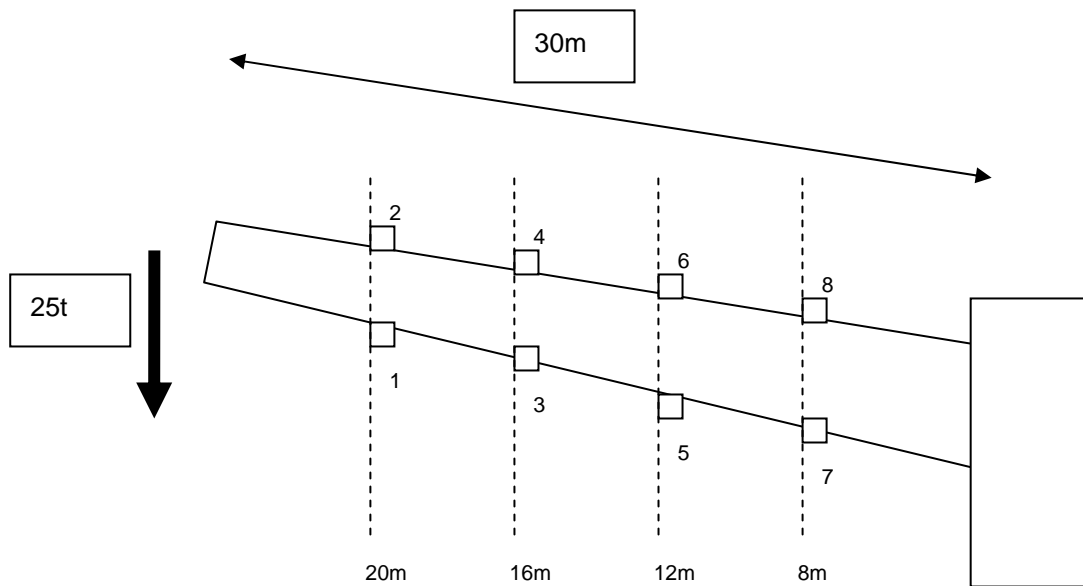
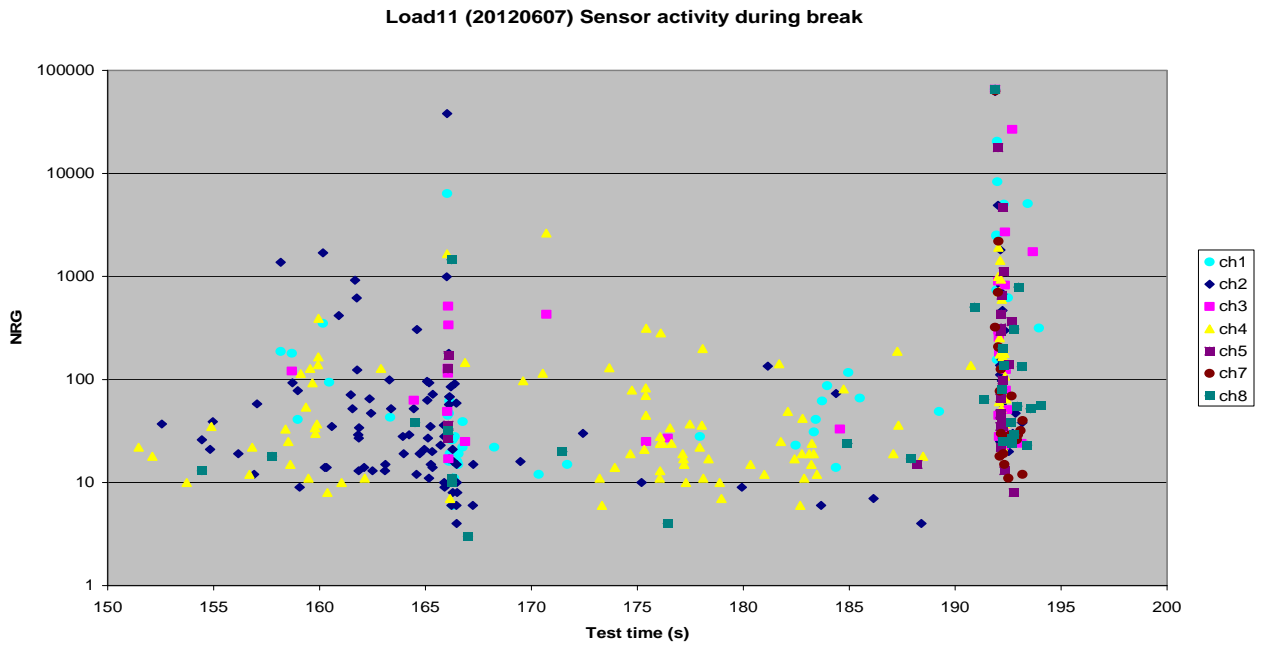


Figure 74 Results from the acoustic emission and the description of where the microphones were placed on the blade

Figure 74 presents the results from the acoustic emissions performed during the final test. The event at 163 sec, is difficult to identify with certainty in the acoustic emission, but the events at 167.5 sec and 193 sec are easy to identify.

167.5 sec:

There is a jump in the applied Force, together with a change in deflection, see Figure 75

The transverse stiffener and T-stiffener at 22,5m debonds, see Figure 76 and Figure 77
 This jump can be seen in a couple of other of other measurements, but these results are in agreement with that it is the transverse stiffener and the T-stiffener that debonds.

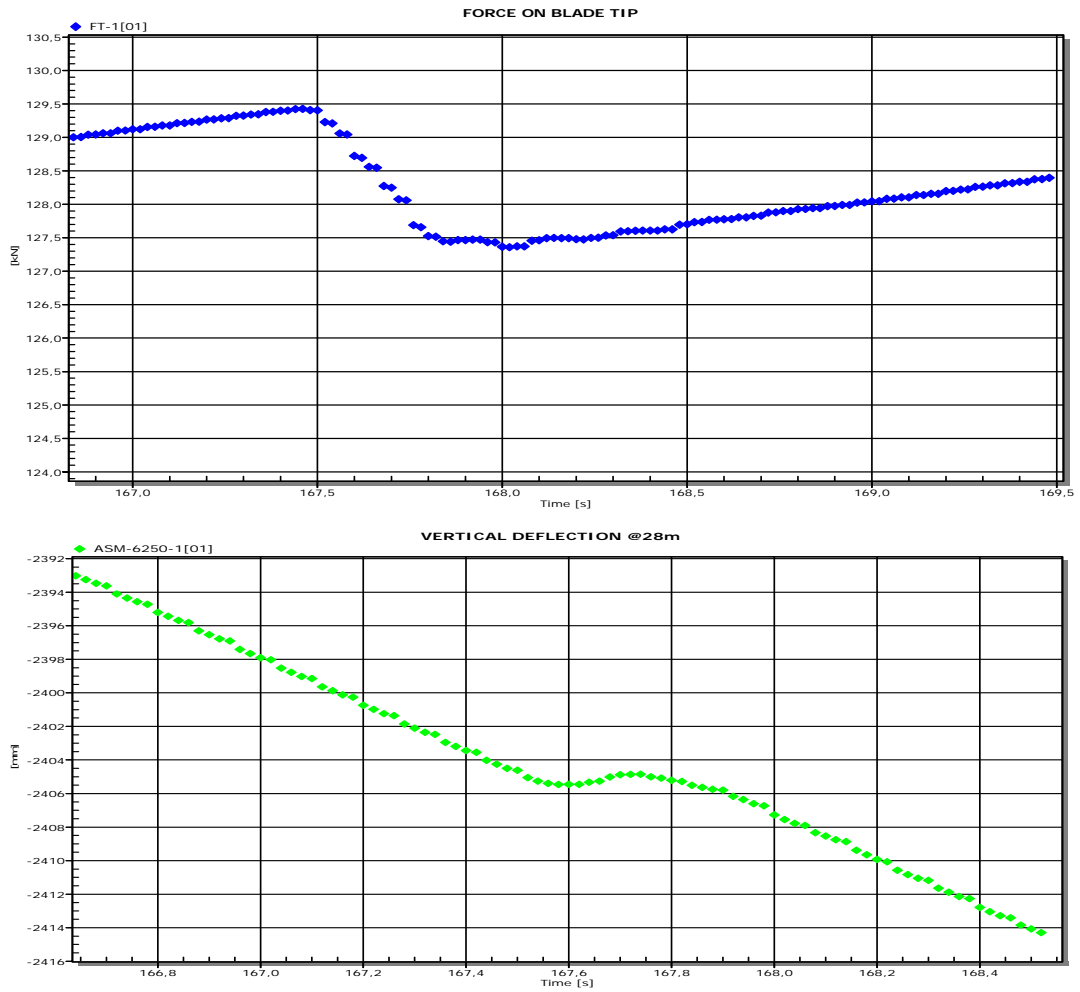


Figure 75 Graphs with the behaviour of Forces and Deflection at 167 sec. The test was performed under constant tip displacement.

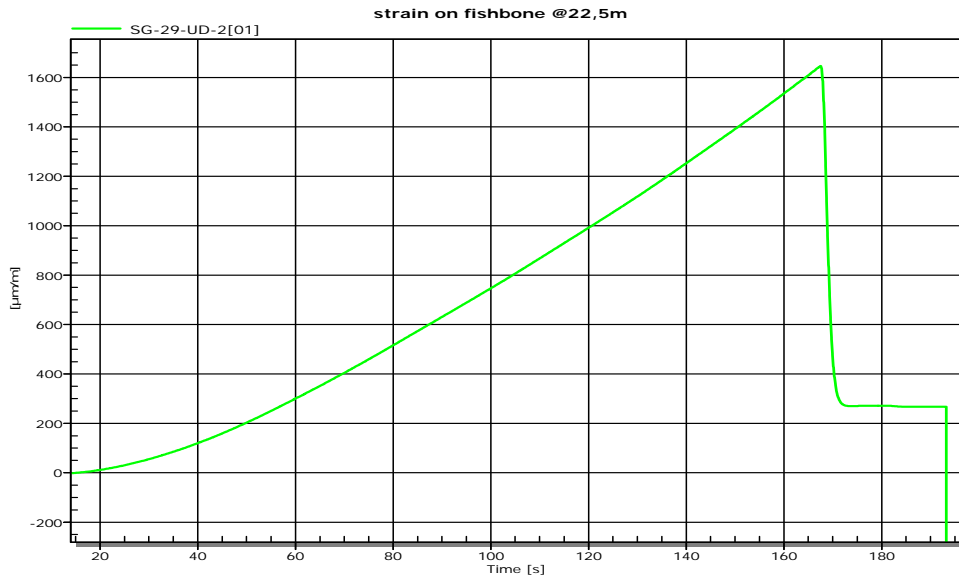


Figure 76 Graph showing the strain on the transverse stiffener during the test. The transverse stiffener at 22.5m debonds at 167.5 sec

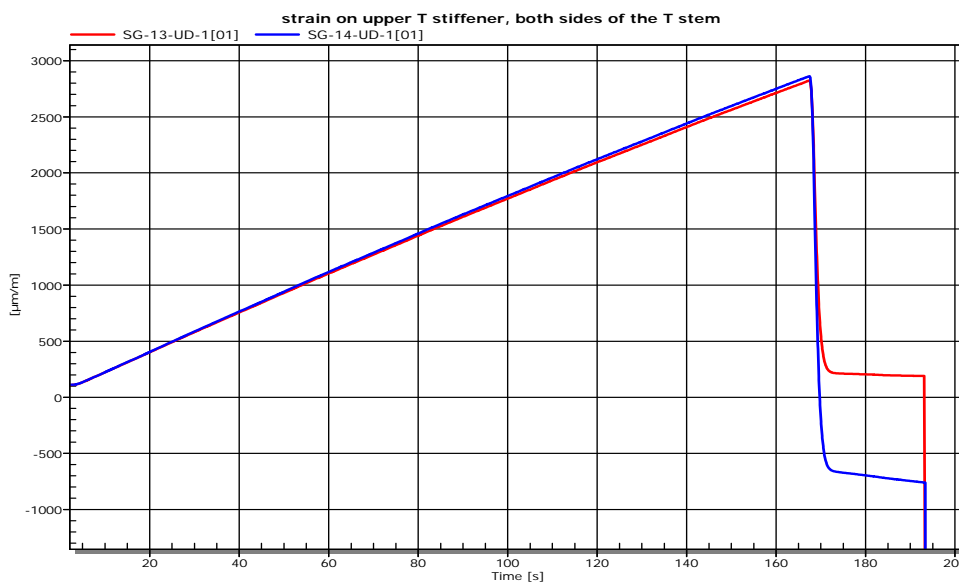


Figure 77 Graph showing the strain on the T-stiffener during the test. The T-stiffener at 22.5m debonds at 167.5 sec

As in the previous test, DMT_2012_05_31_A, it is the upper T-stiffener and transverse stiffener which debonds. The T-stiffener on the lower cap hasn't debonded.

Looking at the result from acoustic emission, see Figure 74, the big hits seems to happens at 20 m. upper at around 167 sec.

181.7 sec:

This jump is seen in the measurements on the web see Figure 72, but it is even more pronounced in the measurements from the Blade Monitoring System, see Figure 78

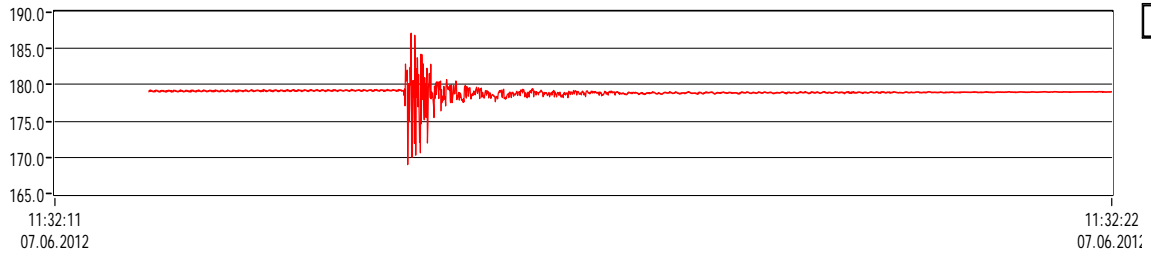


Figure 78 Result from the Blade monitoring measurements (acoustic emission (.

Looking at the acoustic emission over the period between 167.5 and 193.5 sec., there is high activity at 16m upper until around 182 sec and later on there is activity at 20m lower .

193.5 sec:

The girder collapsed at 58% of the expected maximum load.

Looking at the acoustic emission, see Figure 74, at the biggest hits, it appears that there is three places contributing to it at the same time nearly. 16m lower is a little bit ahead of 8m upper and 20 m lower. The latter seems to appear at the same time.

Strain measurements, Figure 79, on the transverse stiffeners, lower cap, at the time very close to the collapse is showing that there is a distribution in the time when they fail.

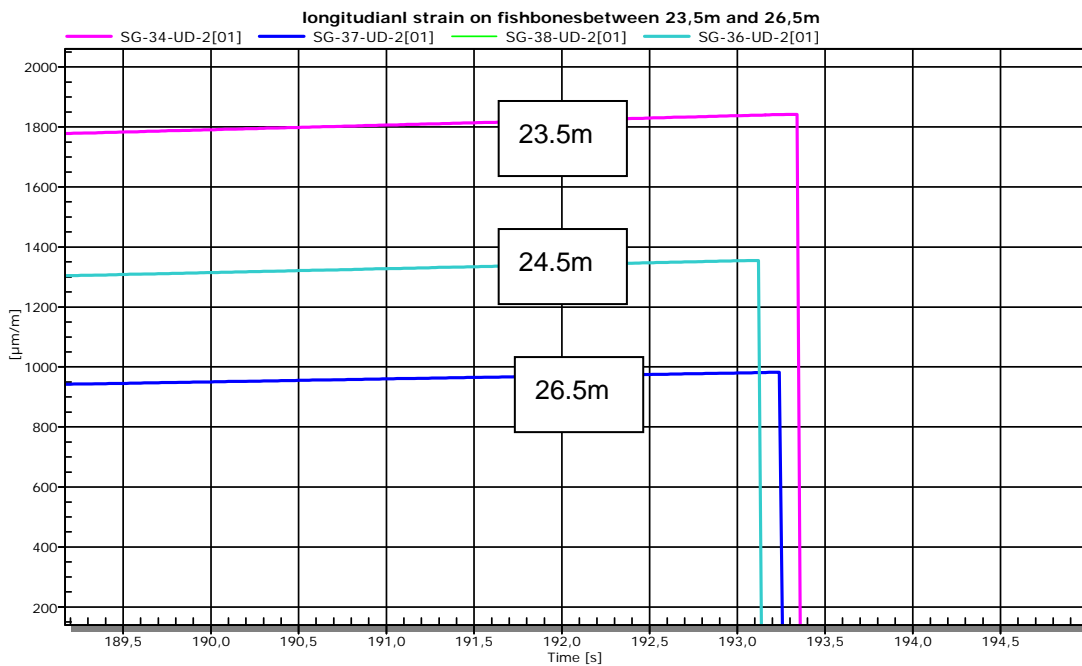


Figure 79 Graphs with strain on the lower transverse stiffener near collapse, showing that there is a distribution in the time when they fail.

h. General observation

The strain on diagonals changes signs between 10 and 16m. This is the same area where the opening in the glued connection are changing from the right side of the box to the left (seen from the root) see Figure 80

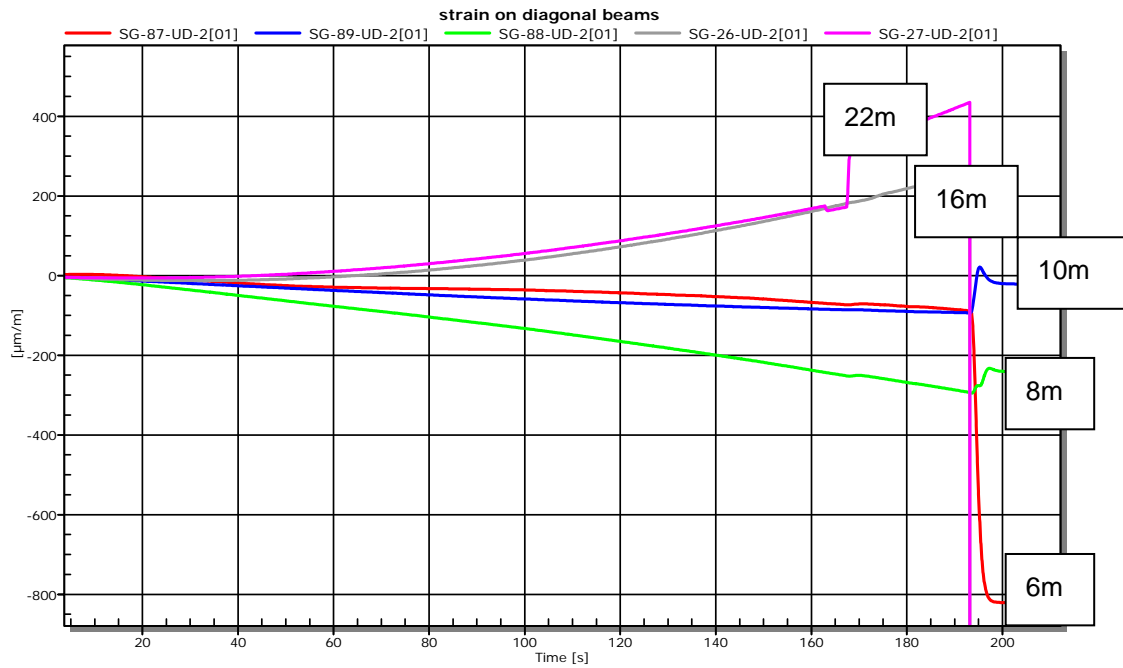


Figure 80 Graps presenting the change in the strains on the diagonals at different distance from the root

i. Observation from the final collapse

The videos showed that the box opened at the tip and the lower adhesive bond between the web and the cap. This opening propagated towards the root.

This is seen in the result from the acoustic emission as well, see

Load11 (20120607) Sensor activity during break

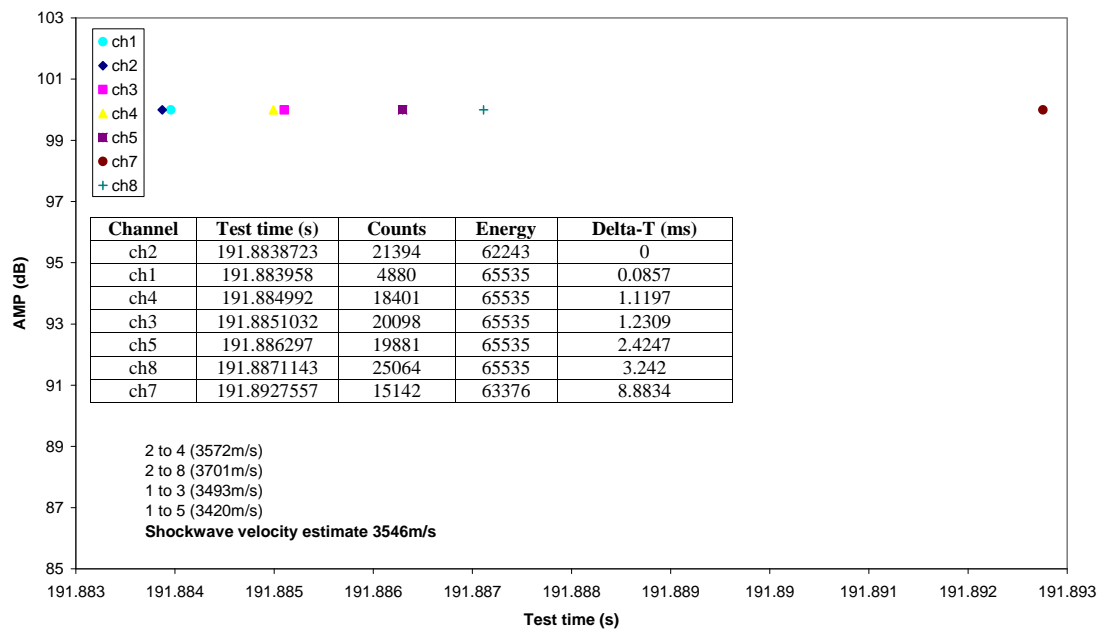


Figure 81. Results from the last seconds showing how the damage propagate. It starts at the tip a proced towards the root.

j. Observation after the ultimate test.

The webs were damaged at several places see Figure 82

The steel support (read steel pipes) of the blade has been hit. Figure 83 shows how the steel pipe has damaged the connection between the cap and the web, and Figure 84 shows how the wooden construction placed between the blade and the pipes was been damaged.



Figure 82 Photos showing damage on the web at around 10m section



Figure 83 Steel pipe supporting the blade. There is a damage in the connection between the web and the cap

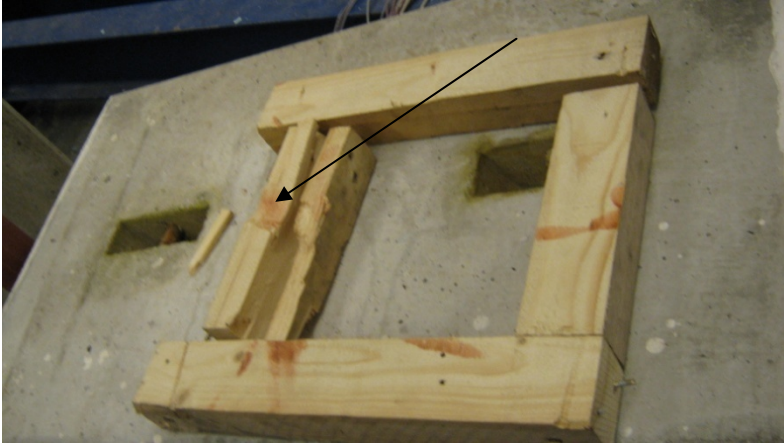


Figure 84 wooden construction to protect the blade

The adhesive joint on both side of the blade was damaged. Near the root, it was damaged towards the upper cap, and near the tip towards the lower cap, see Figure 85 and Figure 86



Figure 85 Damage of the adhesive bond near the root

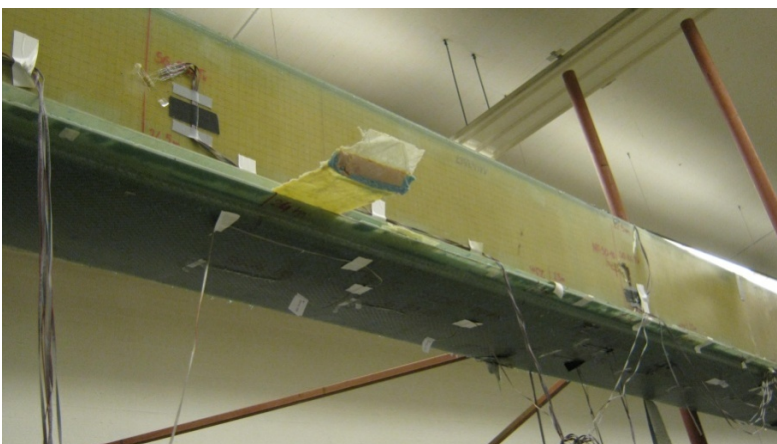


Figure 86 Damage of the adhesive bond near the tip

Looking inside the blade, a most of the reinforcement on the upper cap was damaged, whereas only a few of these were destroyed on the lower cap. Figure 87 .

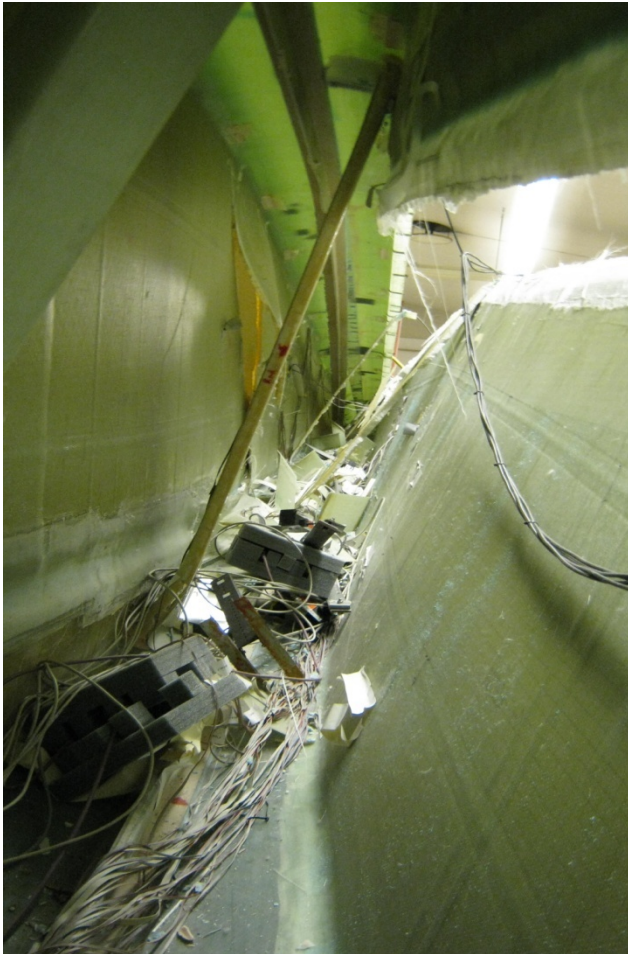


Figure 87 View inside the blade after the final test

7. Summary

The project scope was to design and manufacture a box girder for a 40 m wind turbine blade with significant less weight, using two inventions in combination with advanced numerical analysis. By these methods it was possible to reduce the cap thickness by up to 40%, and thereby reduce the weight.

The inventions, which are structural reinforcements internally in the blade, had to be included in the manufacturing.

During the test the blade was monitored with several systems of measurement equipment and the tests also acted as a platform to show the capabilities of new equipment such as Luna Technologies “Optical Backscatter Reflectometry” and Baumer A/S “Blade Monitoring System”.

Several tests were performed on the boxgirder, and for the final test the boxgirder was loaded to ultimate failure.

Based on all data available, no completely solid conclusion could be drawn on the sequence of events that led to catastrophic failure. However, based on all data available, the following sequence of events is plausible:

1. The adhesive connection between the transverse stiffener (transverse stiffeners and T-profile) and the pressure side cap fails at least at 3 locations around $r=16.5\text{m}$ at a load level of 35%
2. The missing transverse stiffener result in unbalanced tensile forces exerted onto the T-profile by the remaining part of the transverse stiffener.
3. The unbalanced forces lead to debonding of the T-profile from the pressure side cap at least in the region from $r=13\text{m}$ to $r=16\text{m}$.
4. The events described in points 1) to 3) occur again, but this time centered at $r=22\text{m}$ and at a load level of 52%.
5. The partly debonded T-profile leads to an increase of the distortion of the cross-sections and to an increase of the tensile forces in the diagonal reinforcements.
6. As the diagonal reinforcements are glued into the bondline connecting the two halves of the girder, the increased tensile forces in the diagonal reinforcement result in a damage of the bondline.
7. Catastrophic failure during which the upper and lower half of the girder separate completely at a load level of 58%.

The transverse stiffener in the lower part of the girder was undamaged.

References

- [1] Nielsen, M., Jensen, F. M., Nielsen, P. H., Berring, P., Martyniuk, K., Roczek, A., Sieradzan, T., Roudnitski, V., Kucio, P., Bitsche, R., Andreasen, P., Lukassen, T., Andrlová, Z., Branner, K., Bak, C., Kallesøe, B., McGugan M., “*Full Scale Test of SSP 34m blade, edgewise loading LTT. Data Report 1*” Risø-R-1718(EN). (January 2010)

Acknowledgements

The research is conducted within the frame of a project entitled 'Demonstration of new blade design using manufacturing process simulations'. The project is financially supported by the Danish Energy Agency through the Energy Technology Development and Demonstration Programme (EUDP 2009).

DTU Wind Energy is a department of the Technical University of Denmark with a unique integration of research, education, innovation and public/private sector consulting in the field of wind energy. Our activities develop new opportunities and technology for the global and Danish exploitation of wind energy. Research focuses on key technical-scientific fields, which are central for the development, innovation and use of wind energy and provides the basis for advanced education at the education.

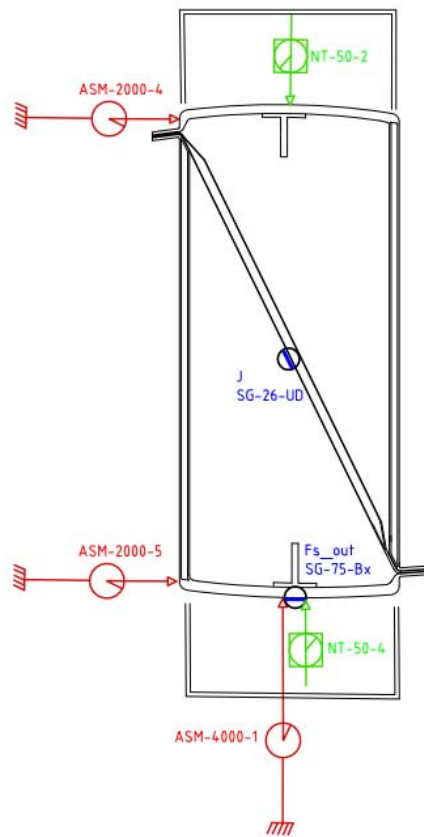
We have more than 230 staff members of which approximately 60 are PhD students. Research is conducted within 9 research programmes organized into three main topics: Wind energy systems, Wind turbine technology and Basics for wind energy.

Technical University of Denmark
DTU Vindenergi
Frederiksborgvej 399
Bygning 118
4000 Roskilde
Telefon 46 77 50 85
info@vindenergi.dtu.dk
www.vindenergi.dtu.dk


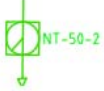

Appendix A Measurement equipment description

The box girder has been instrumented with resistance-based strain gauges, strain pots by ASM and linear position transducers, by Novo Technik.

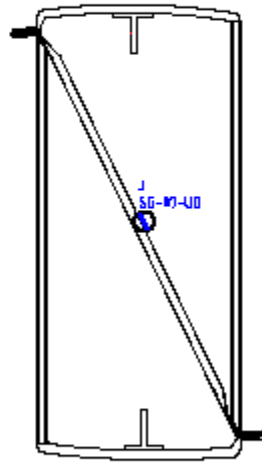
The positions of the instruments are shown in the following pages. A short description is provided in the next drawing, where the 16m section is used as example.



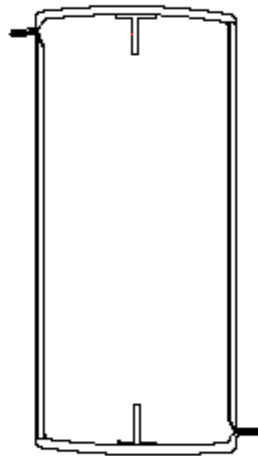
DRAWINGS LEGEND

- 
 this symbol indicates a strain pot (ASM) measuring the distance between the two ends of the arrow
- 
 this symbol indicates a linear transducer (NT) measuring the distance between the two ends of the arrow
- 
 the letter indicates the spot on the section and the small blue line indicates a strain gauge

6 meter section

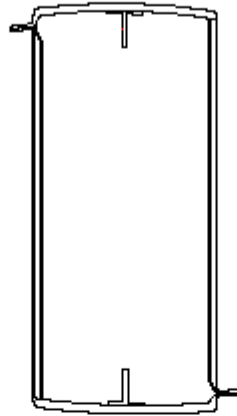


6.5 meter section

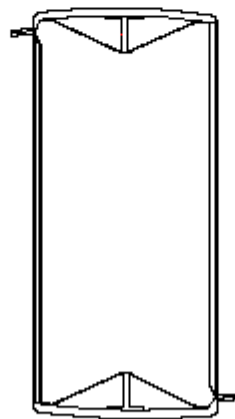


Based on 12 meter section seen from top

7 meter section

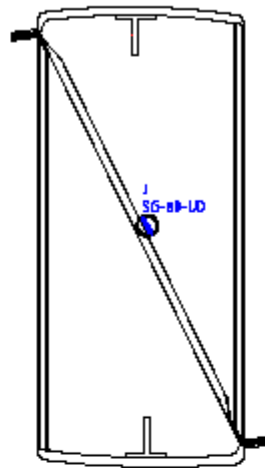


7.5 meter section

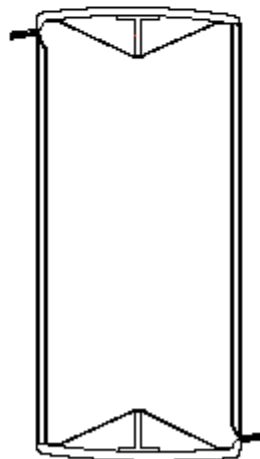


Based on 12 meter section seen from tip

8 meter section

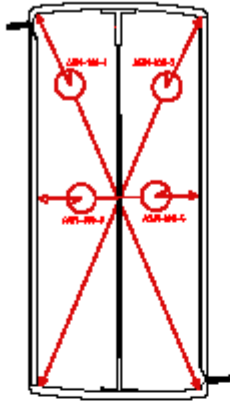


8.5 meter section



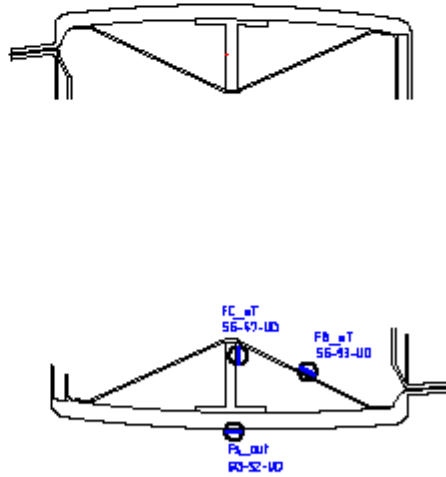
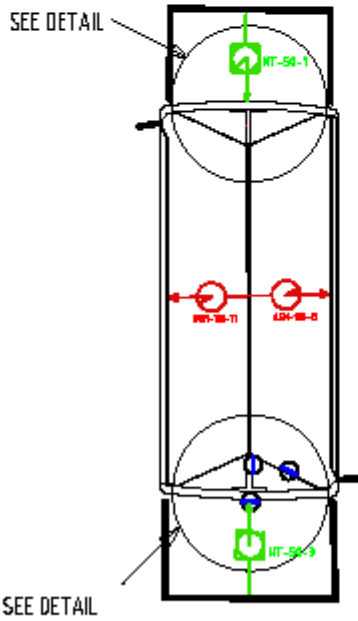
Based on 12 meter section seen from tip

9 meter section



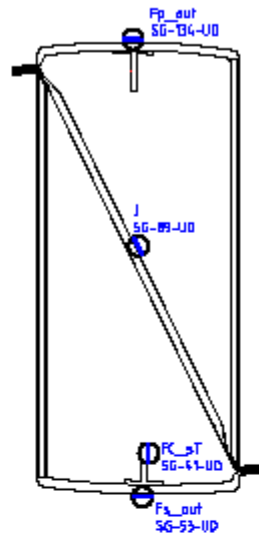
NT-50-1 and NT-50-3 must actually be placed at section 9.6m instead of 9.5m.

9.5 meter section

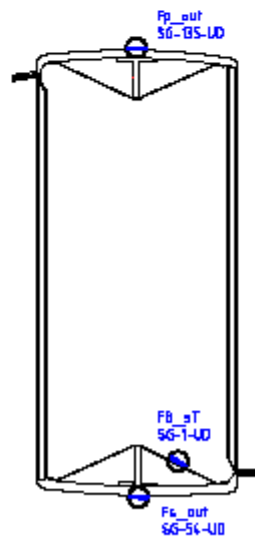


Based on 12 meter section seen from tip

10 meter section

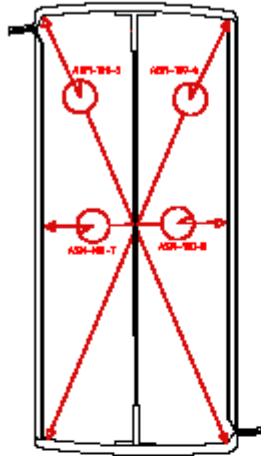


10.5 meter section

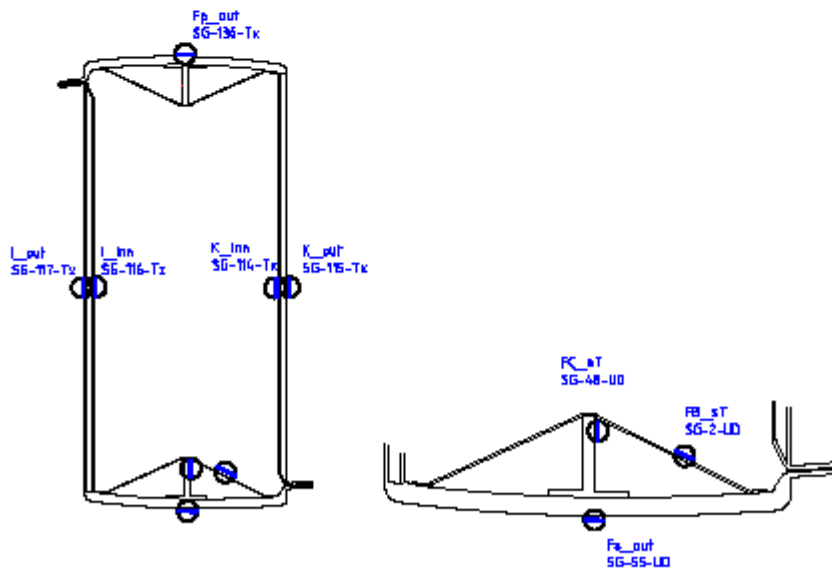


Based on 12 meter section seen from tip

11 meter section

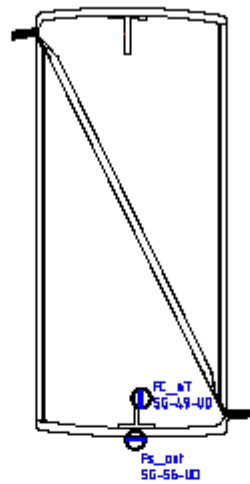


11.5 meter section



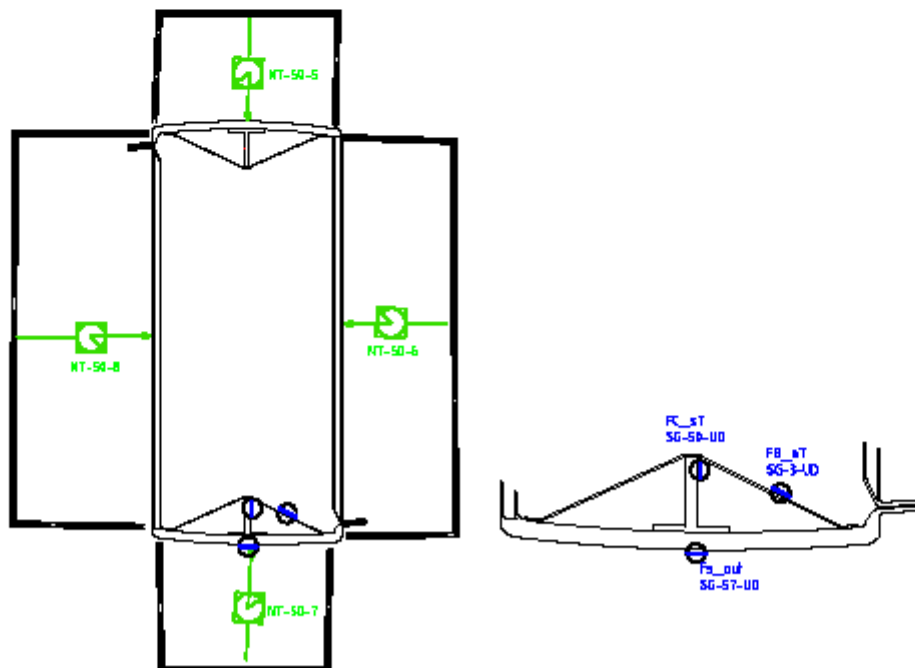
Based on 12 meter section seen from tip

12 meter section



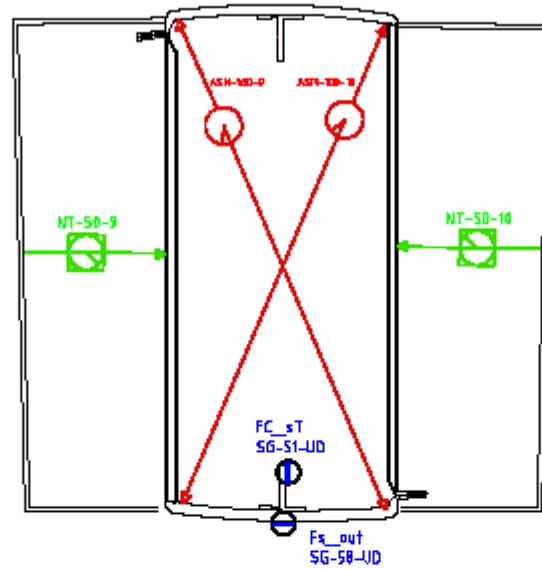
NT-50-5 and NT-50-7 must actually be placed at section 12.6m instead of 12.5m.

12.5 meter section

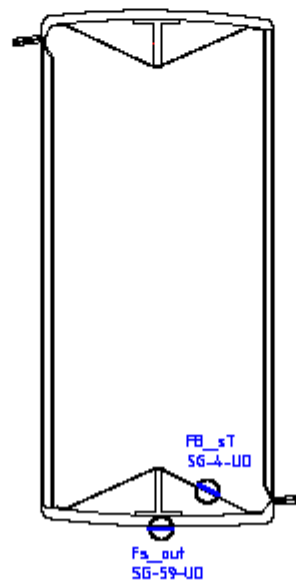


Based on 12 meter section seen from tip

13 meter section

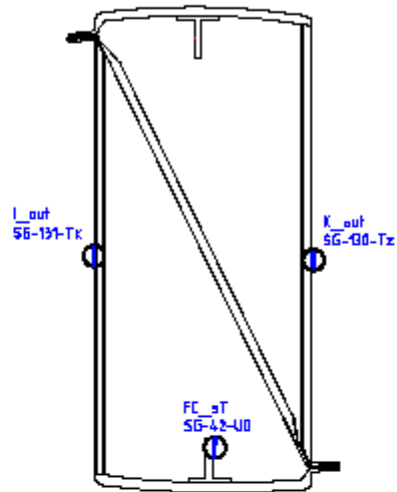


13.5 meter section

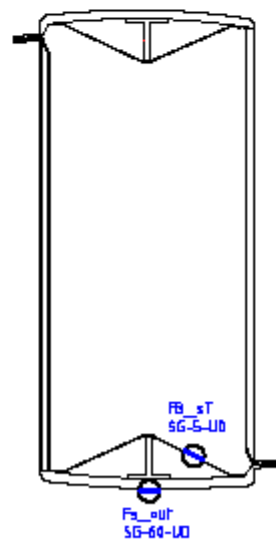


Based on 12 meter section seen from top

14 meter section

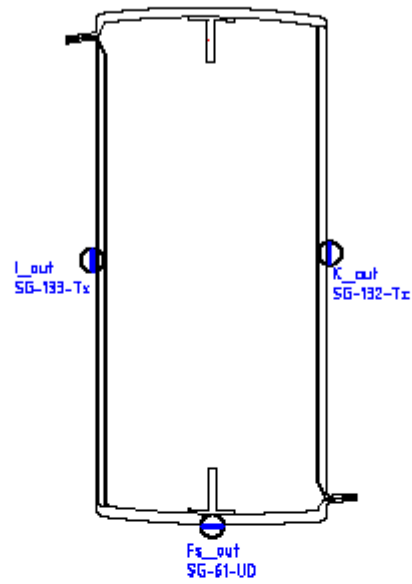


14.5 meter section

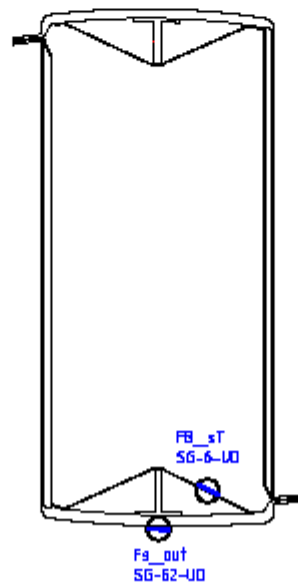


Based on 12 meter section seen from tip

15 meter section

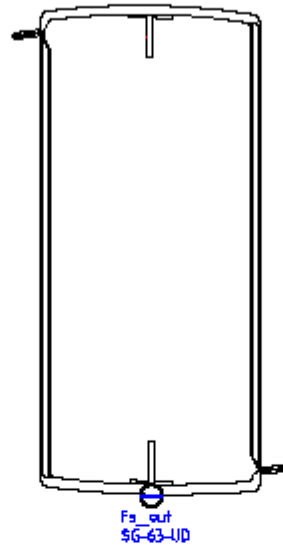


15.5 meter section

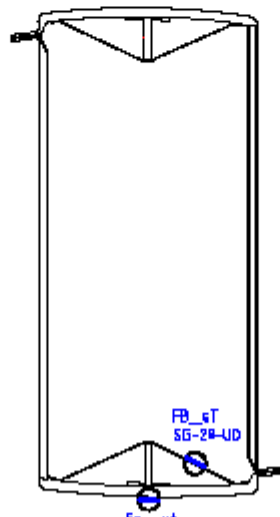


Based on 12 meter section seen from tip

17 meter section

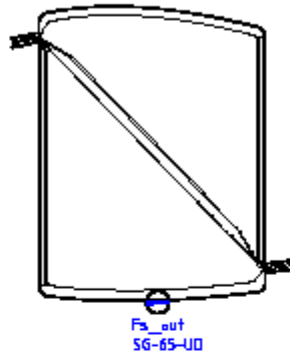


17.5 meter section

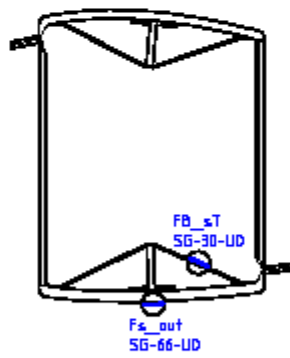


Based on 12 meter section seen from tip

18 meter section

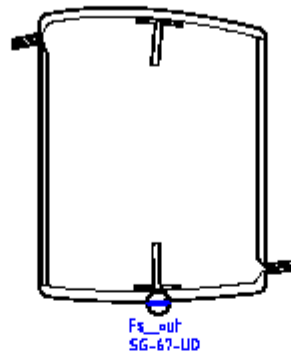


18.5 meter section

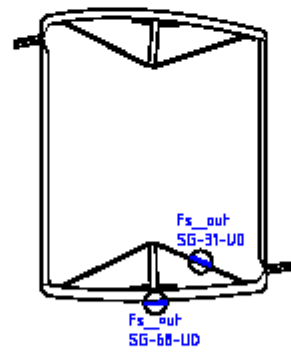


Based on 20 meter section seen from tip

19 meter section

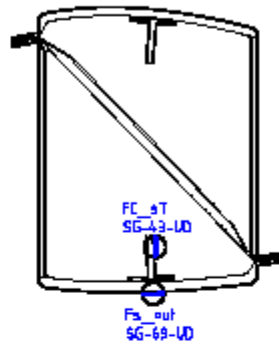


19.5 meter section

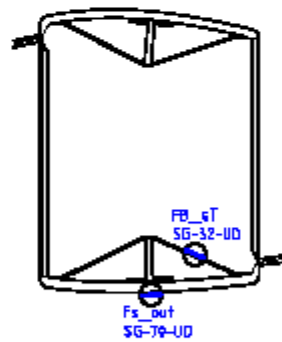


Based on 20 meter section seen from tip

20 meter section

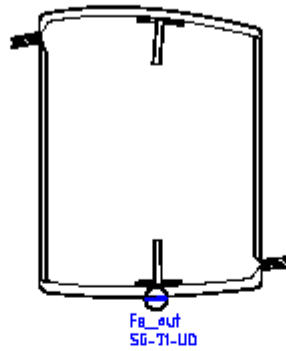


20.5 meter section

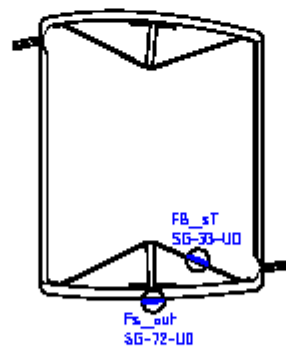


Based on 20 meter section seen from hip

21 meter section

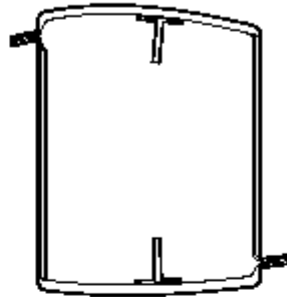


21.5 meter section

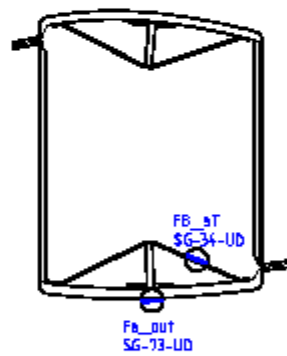


Based on 20 meter section seen from tip

23 meter section

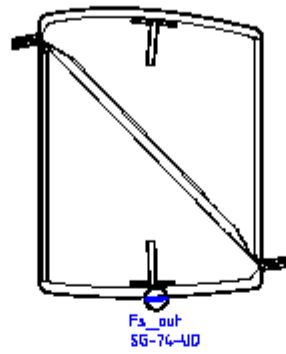


23.5 meter section

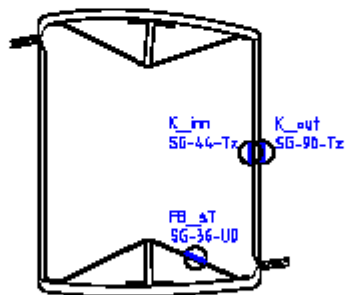


Based on 20 meter section seen from tip

24 meter section

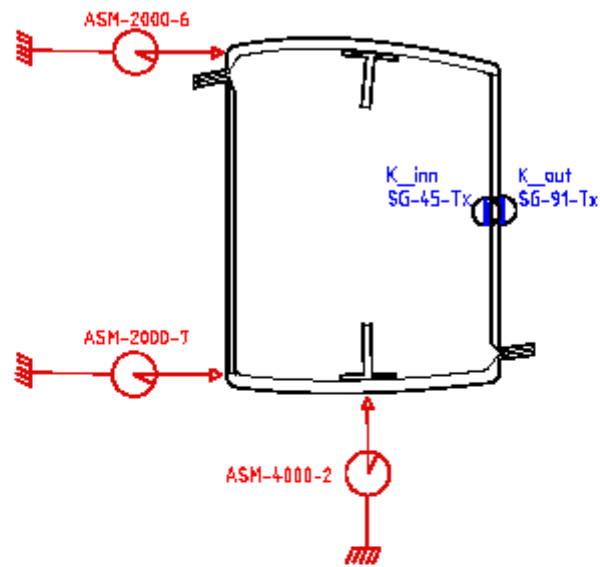


24.5 meter section

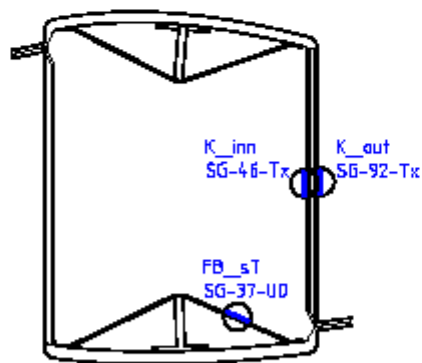


Based on 20 meter section seen from tip

25 meter section

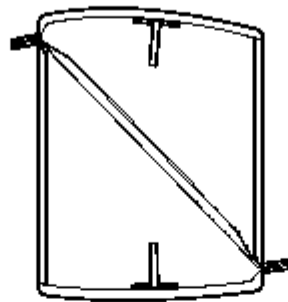


25.5 meter section



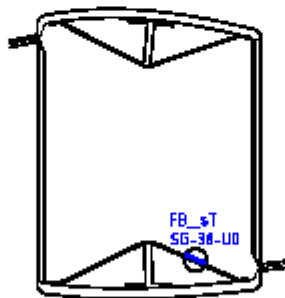
Based on 20 meter section seen from flap

26 meter section



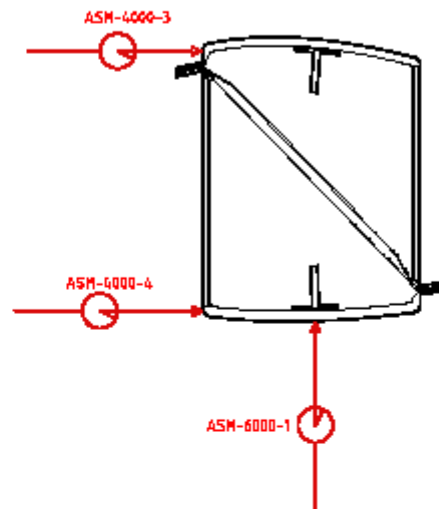
Suction

26.5 meter section



Based on 20 meter section seen from tip

28 meter section



Based on 28 meter section seen from tip

A synthetic overview on the positioning of the strain gauges along the box-girder is provided in the following spreadsheet.

Sections [m]	Langsgående A2 silver			Tverrgående A2 silver			Diagonals			Shear webs			Cab		FAs				
	FC_sT	FC_sL	FC_pT	FC_pL	Fs_out	Fp_out	FB_sT	FB_sL	FB_pT	FB_pL	J	K_inn	K_out	L_inn		L_out	R_inn	R_out	R_limbed
6											SG-87-UD								
7.5																			
8																			
8.5																			
9																			
9.5	SG-47-UD				SG-82-UD														
10	SG-41-UD				SG-53-UD	SG-134-UD													
10.5					SG-54-UD	SG-135-UD													
11																			
11.5	SG-48-UD				SG-55-UD	SG-136-UD													
12	SG-49-UD				SG-56-UD														
12.5	SG-50-UD				SG-57-UD														
13	SG-51-UD				SG-58-UD														
13.5					SG-59-UD														
14	SG-42-UD				SG-60-UD														
14.5					SG-61-UD														
15					SG-62-UD														
15.5																			
16					SG-75-Bx														
16.5	SG-7-UD	SG-8-UD	SG-9-UD	SG-10-UD	SG-15-UD	SG-16-UD	SG-17-UD	SG-18-UD											Main section 1
17					SG-76-Bx	SG-79-Bx													
17.5					SG-63-UD														
18					SG-64-UD														
18.5					SG-65-UD														
19					SG-66-UD														
19.5					SG-67-UD														
20	SG-43-UD				SG-68-UD														
20.5					SG-69-UD														
21					SG-70-UD														
21.5					SG-71-UD														
22					SG-72-UD														
22.5	SG-11-UD	SG-12-UD	SG-13-UD	SG-14-UD	SG-77-Bx														Main section 2
23					SG-19-UD	SG-20-UD	SG-21-UD	SG-29-UD											
23.5					SG-34-UD														
24					SG-73-UD														
24.5					SG-74-UD														
25																			
25.5																			
26																			
26.5																			
27.5																			
28																			
28.5																			

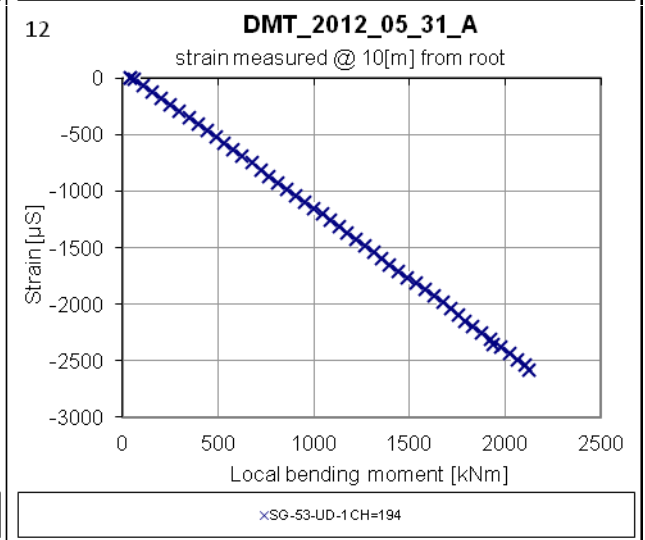
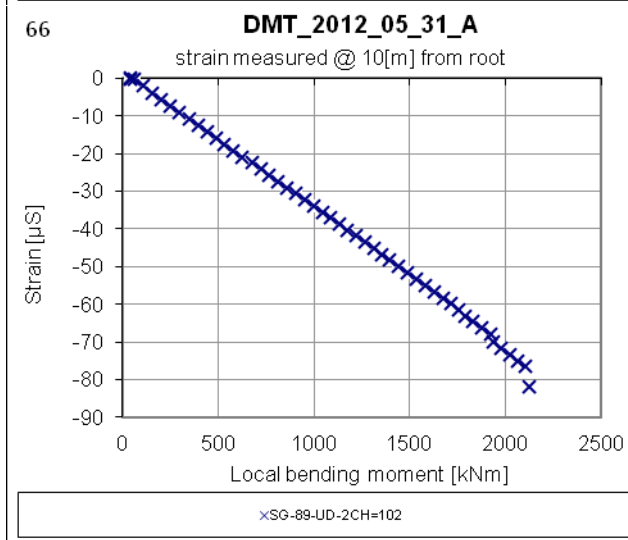
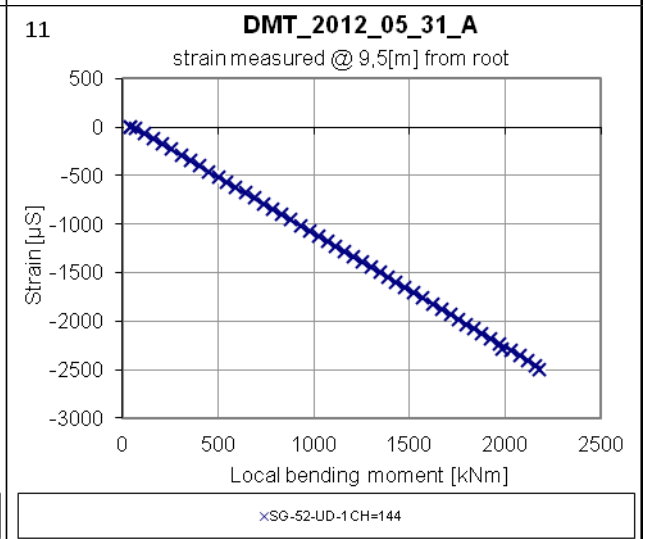
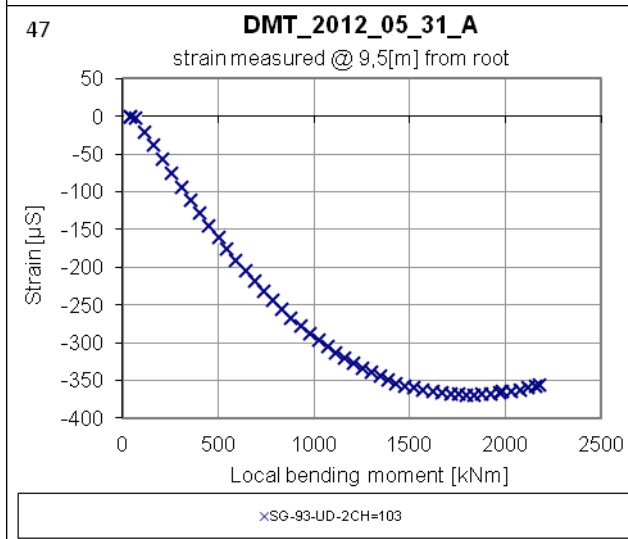
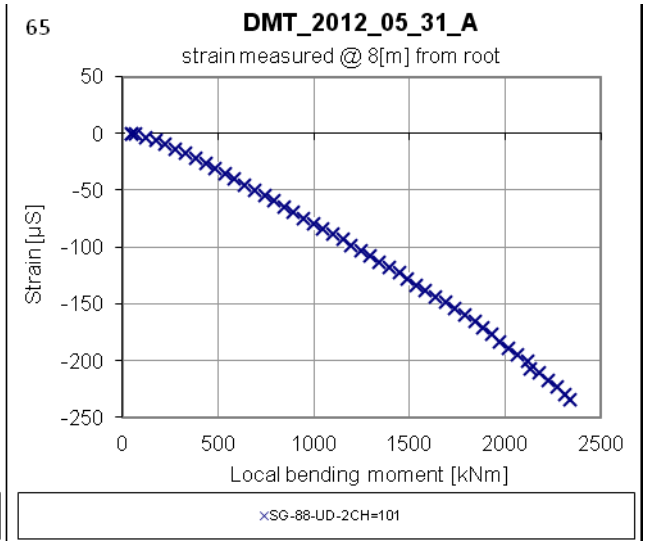
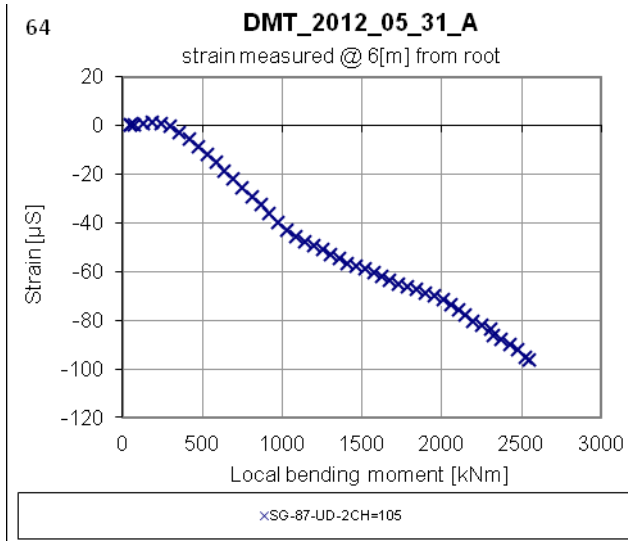
Imbedded Strain gauges SG-9UD to SG-12UD will be put into the blade as close to the connection as possible.

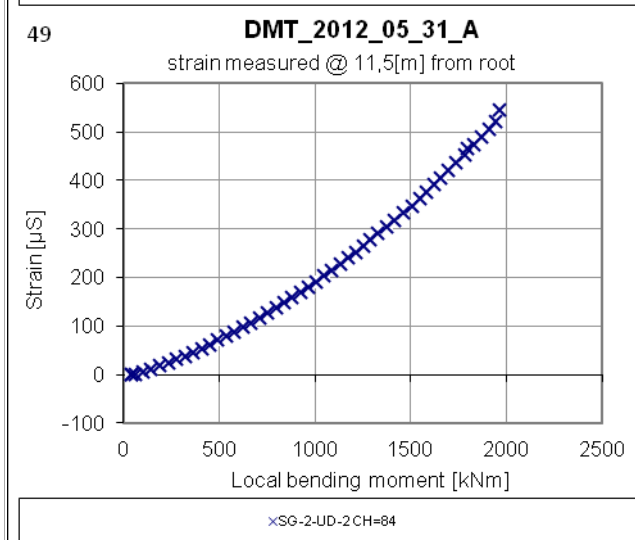
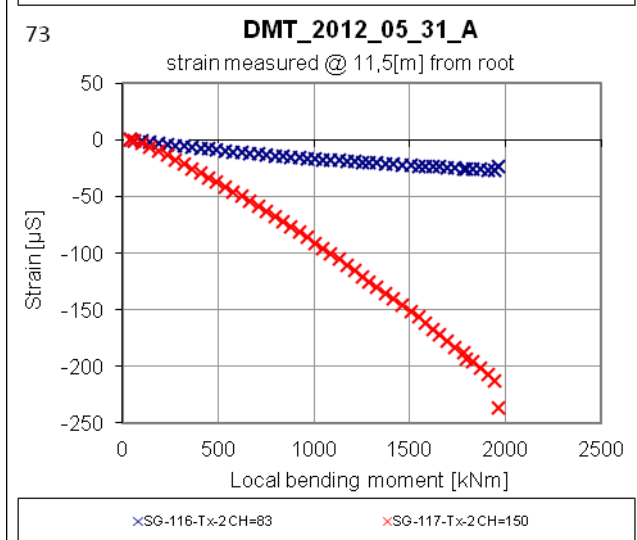
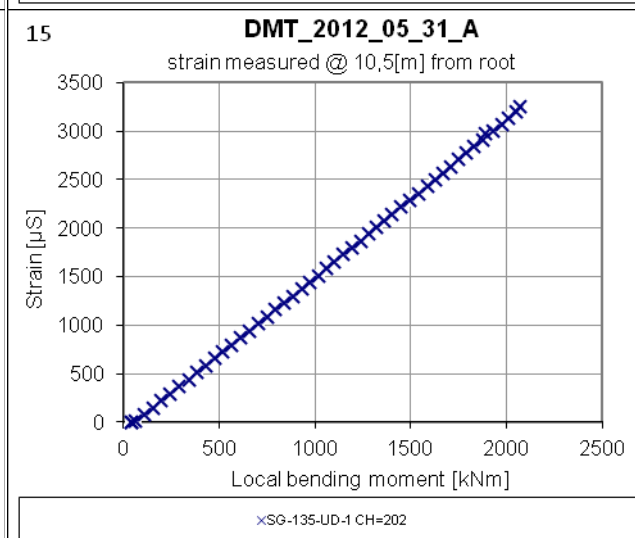
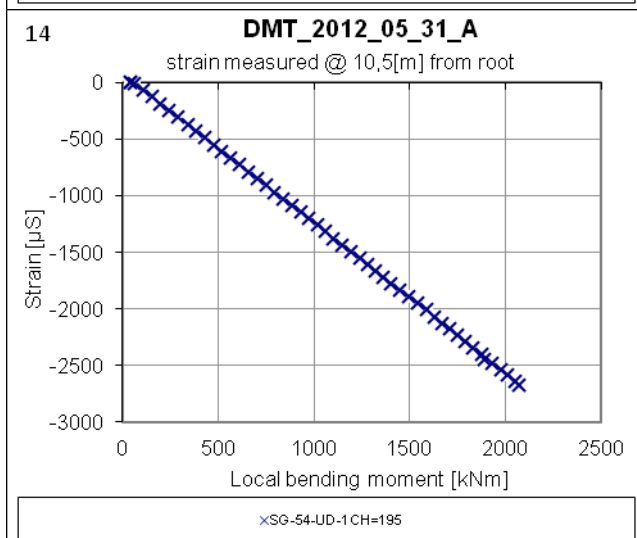
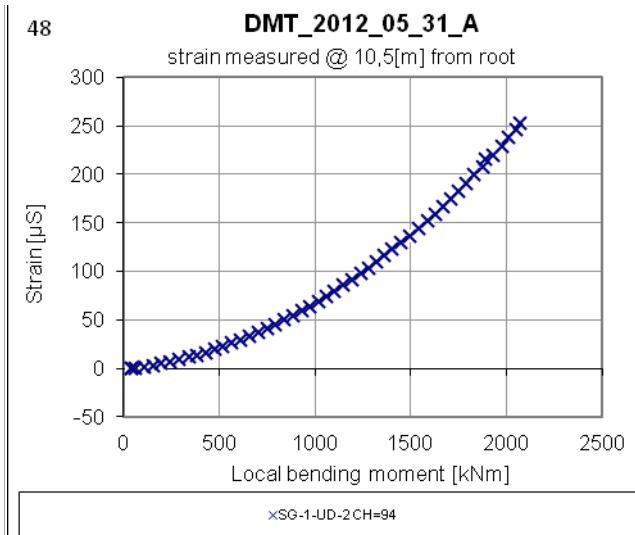
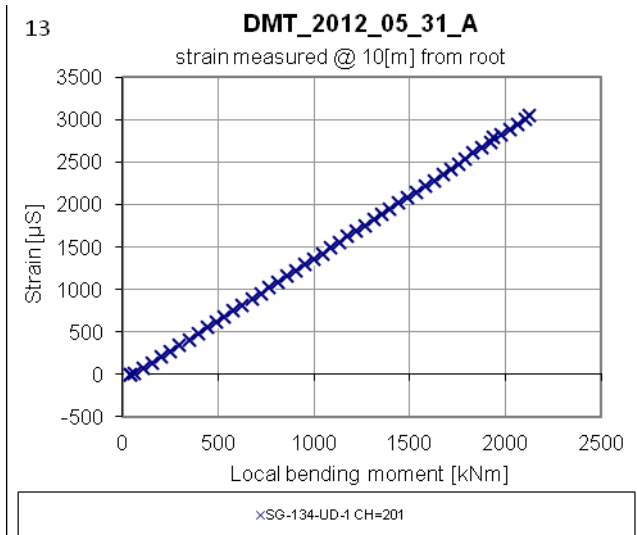
The type of instruments used is listed here:

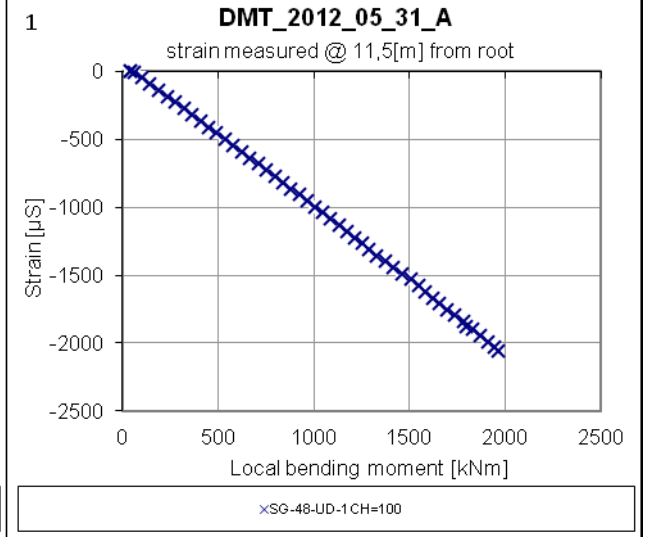
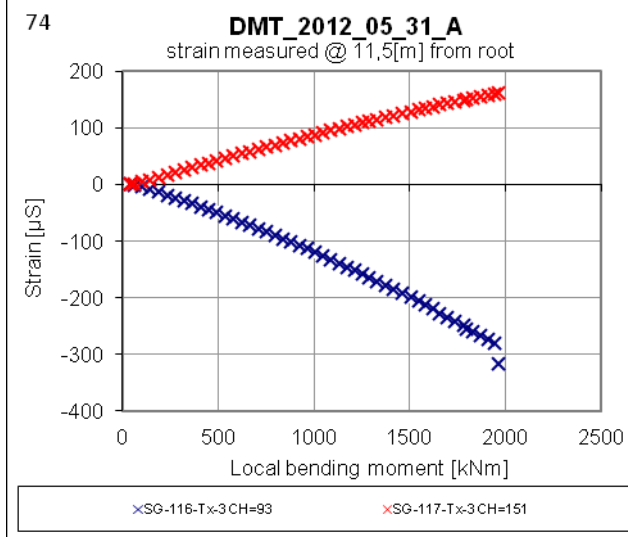
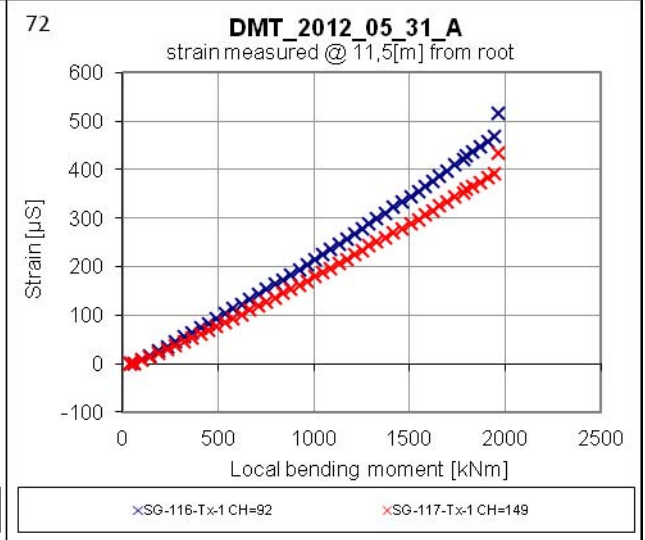
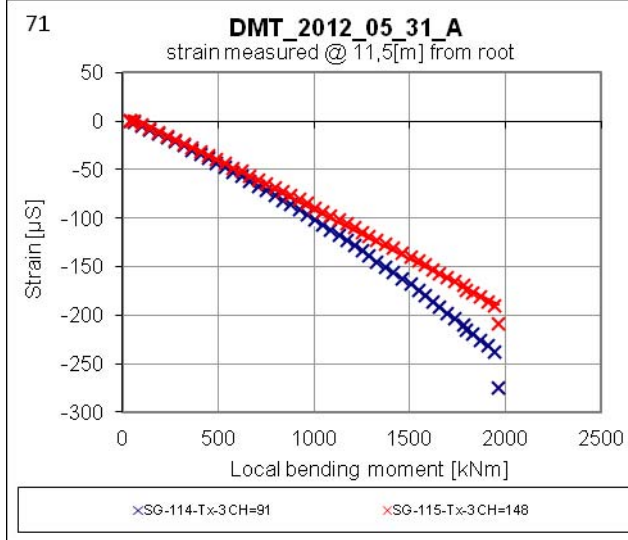
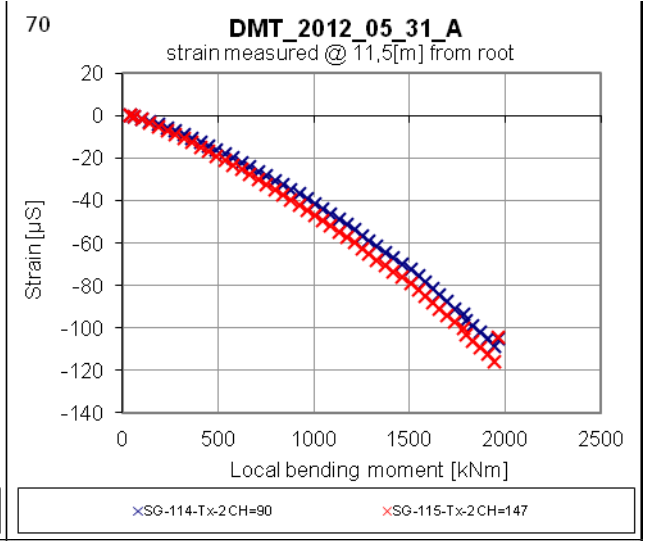
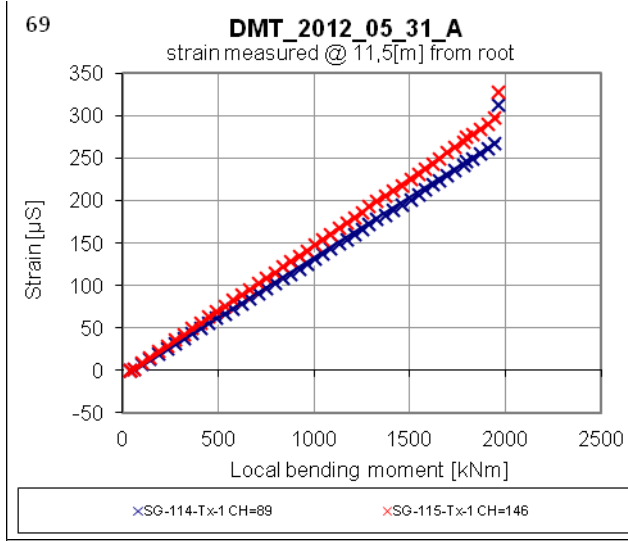
STRING POTS (ASM)	LINEAR TRANSDUCERS (Novo Technik)	STRAIN GAUGES (HBM)	FORCE TRANSDUCERS (Lorenz messtechnik - HBM)
WS17KT-2000-10V-L10	TR 50 mm	UD K-RY81-6/350-4	K-12 200KN
WS17KT-4000-10V-L10	TR 100mm	Bx K-XY31-6/350-4	HBM S-9
WS17KT-6250-10V-L10		Tx K-RY81-6/350-4	

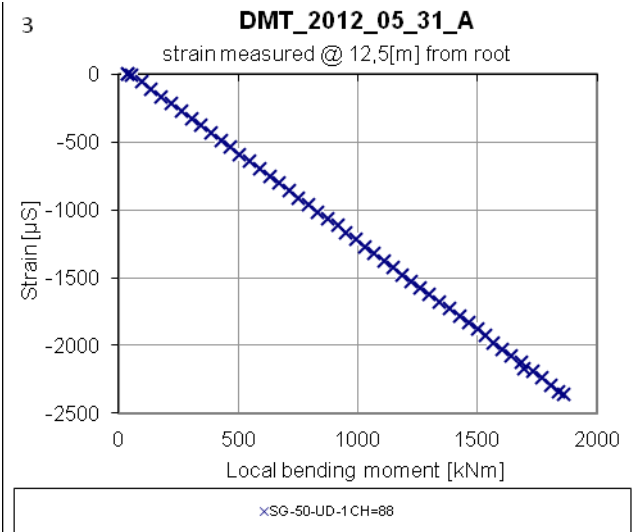
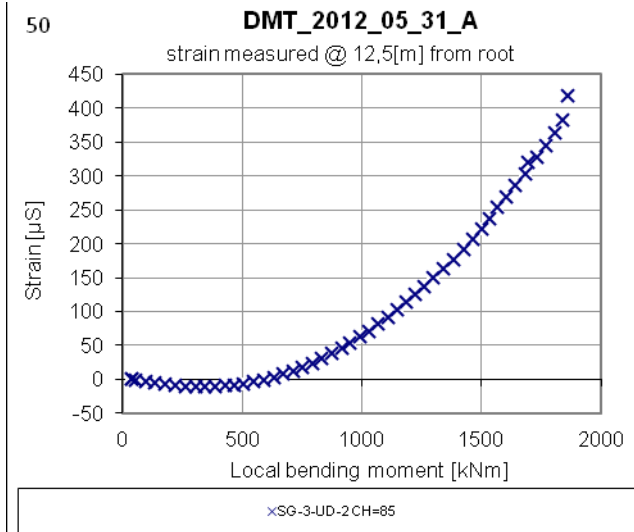
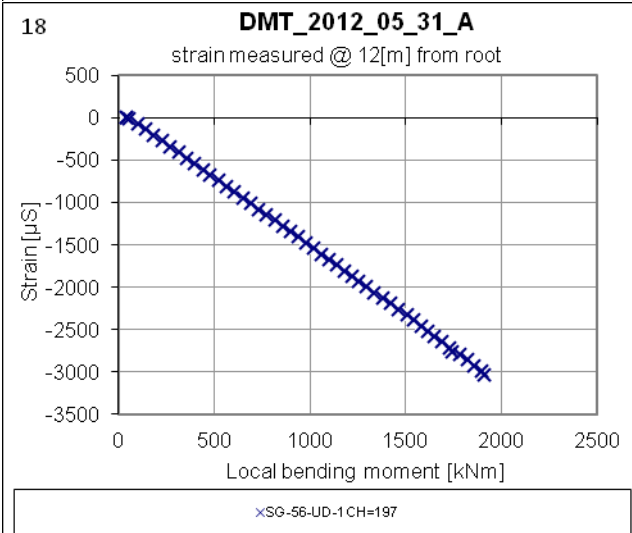
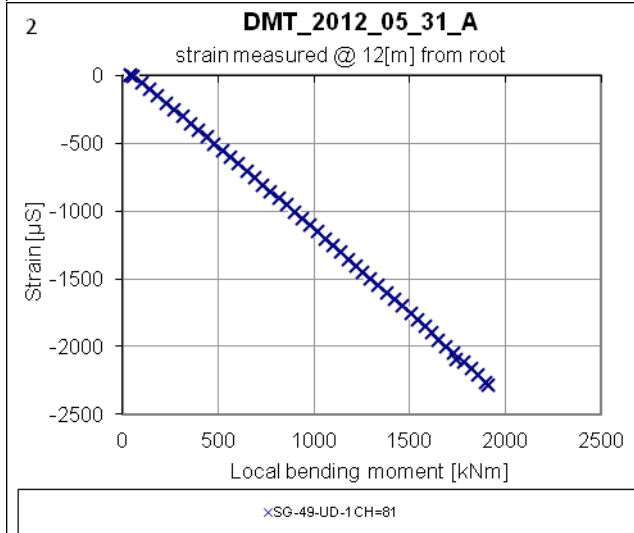
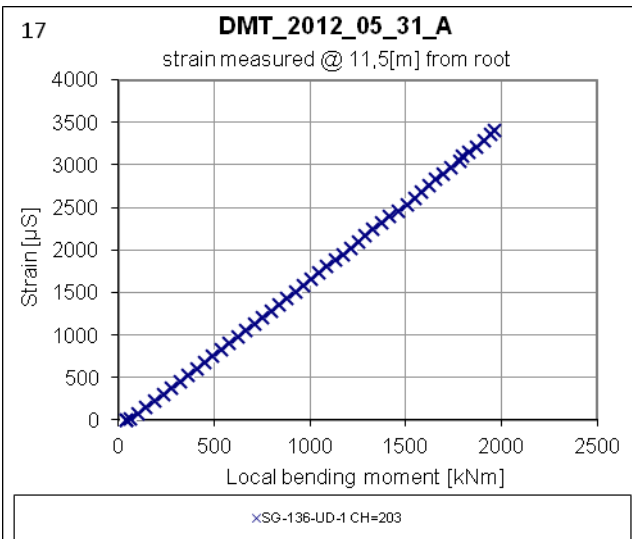
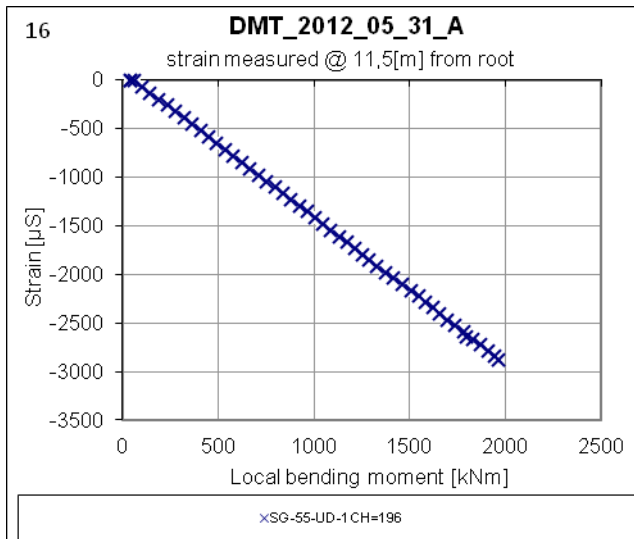
Appendix B Data presented by Graph tool

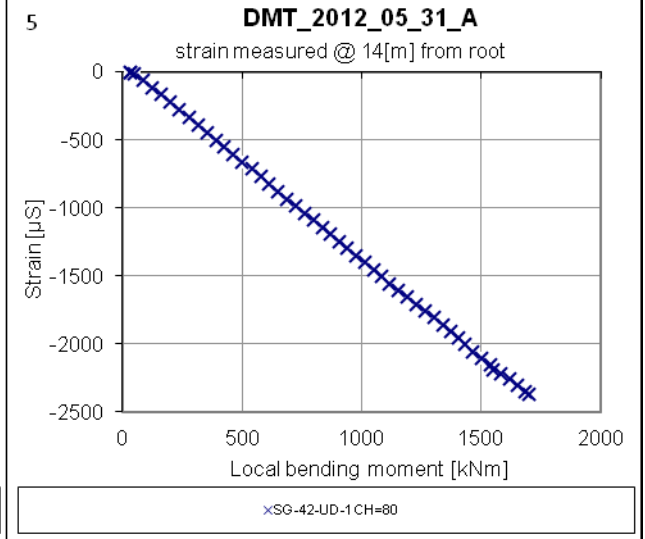
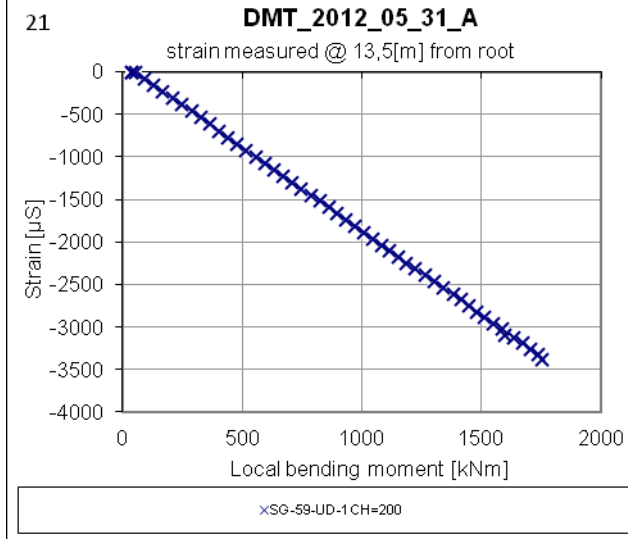
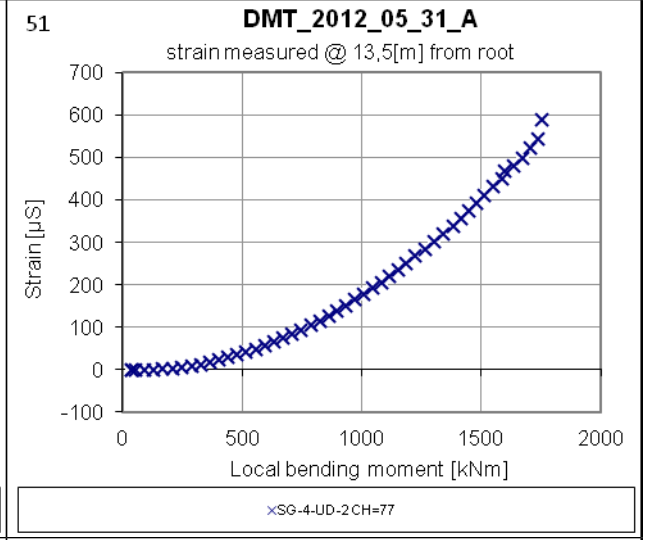
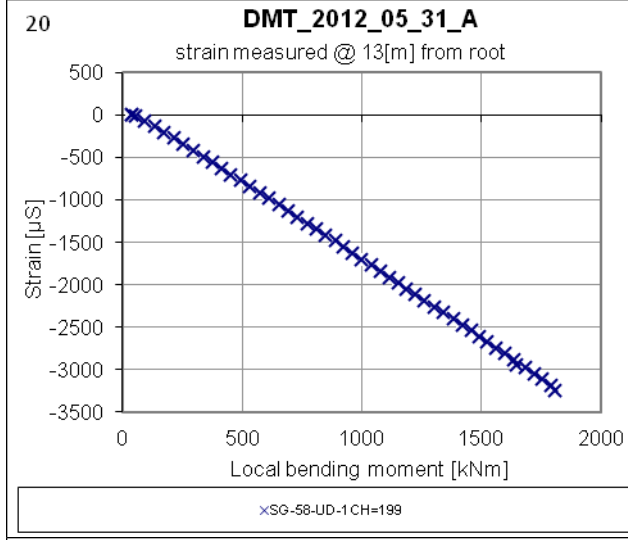
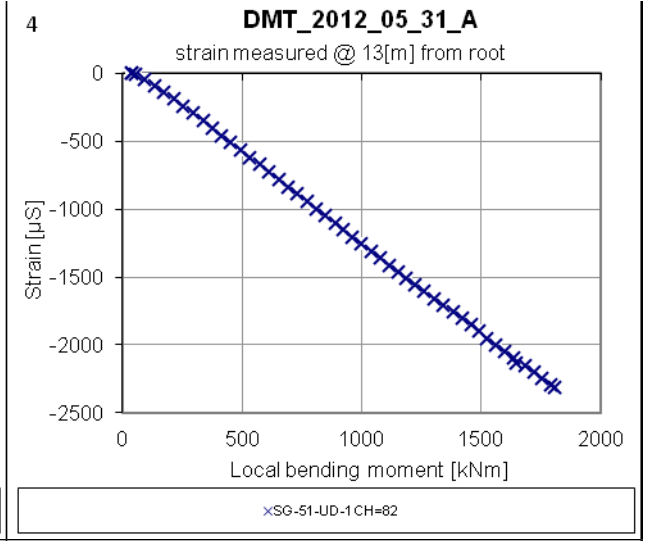
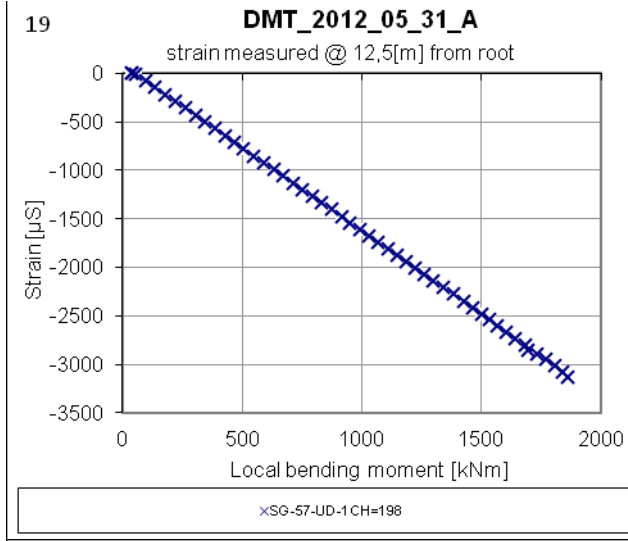
Appendix B1.
Strain gauge measurements presented by Graph tool.
Test DMT_2012_05_31_A

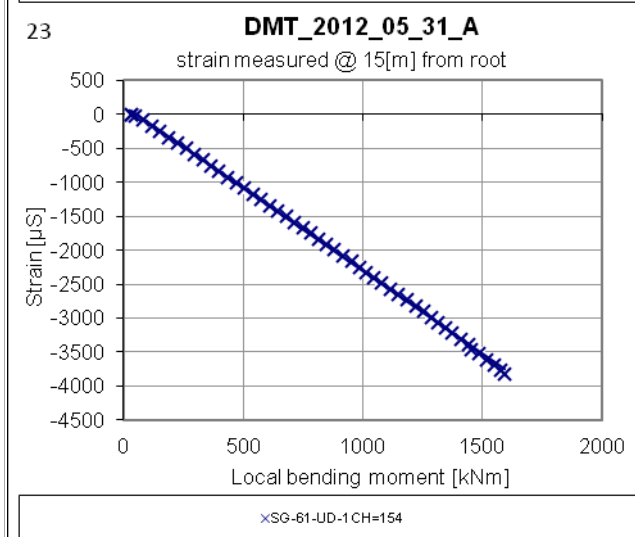
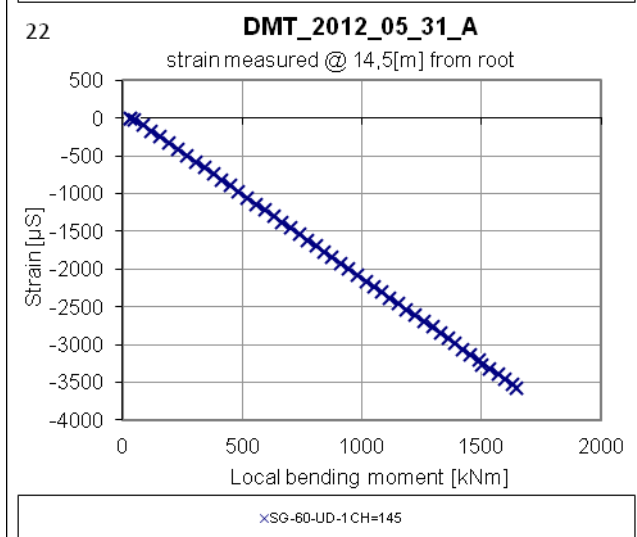
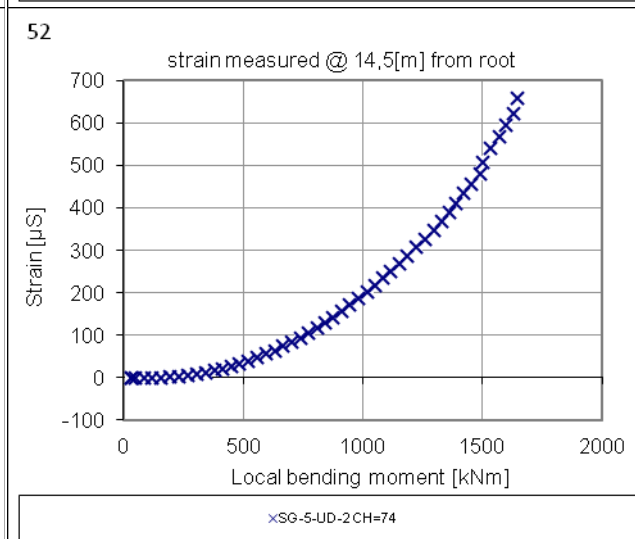
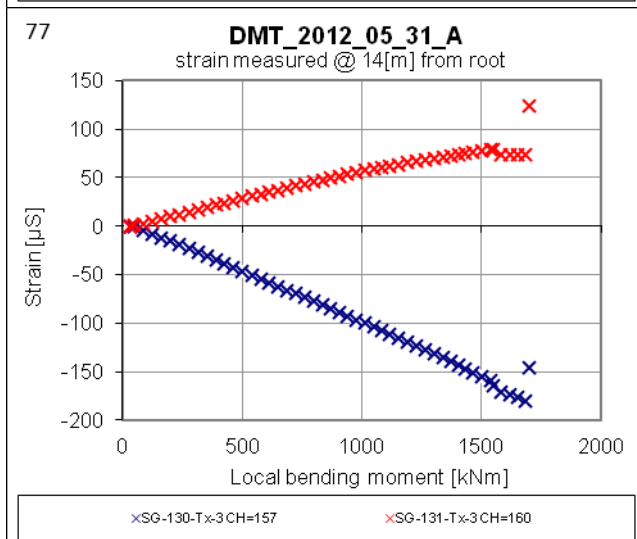
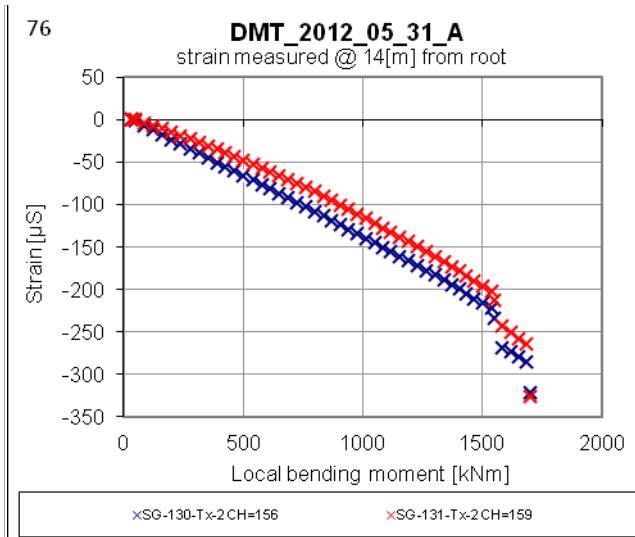
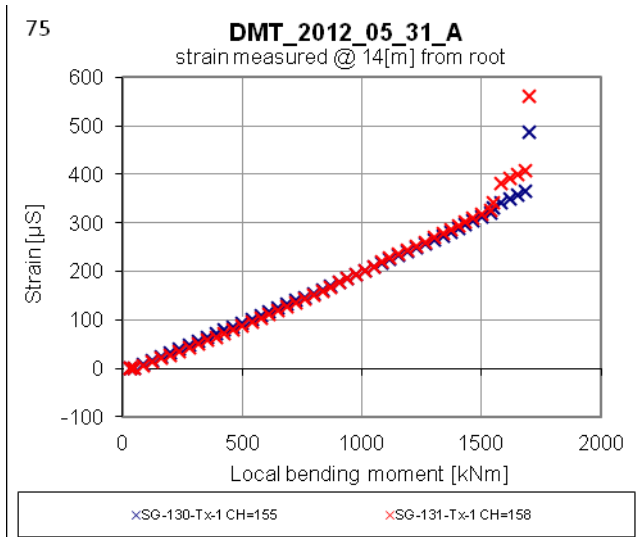


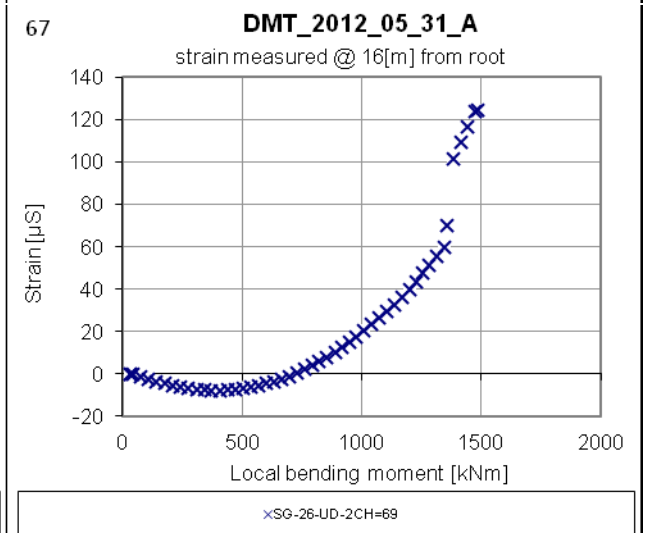
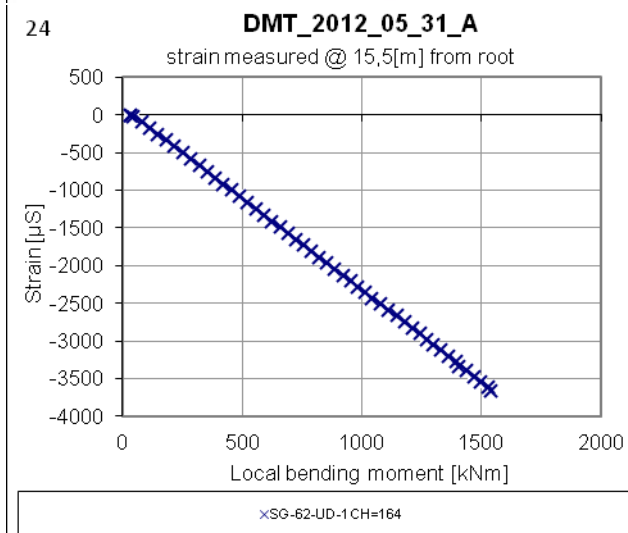
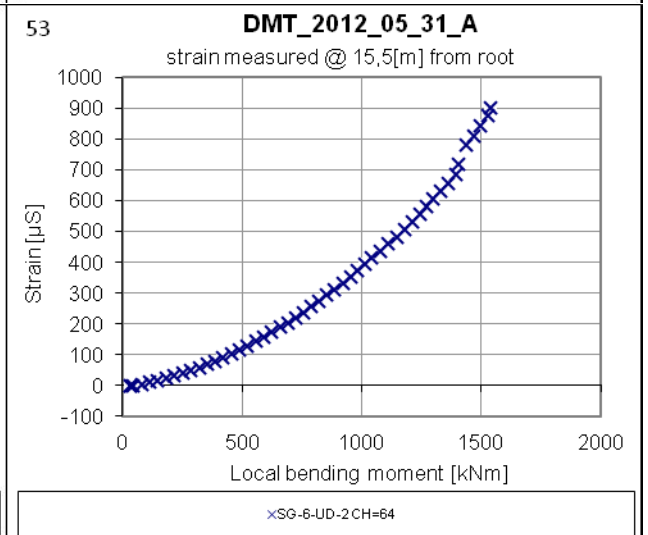
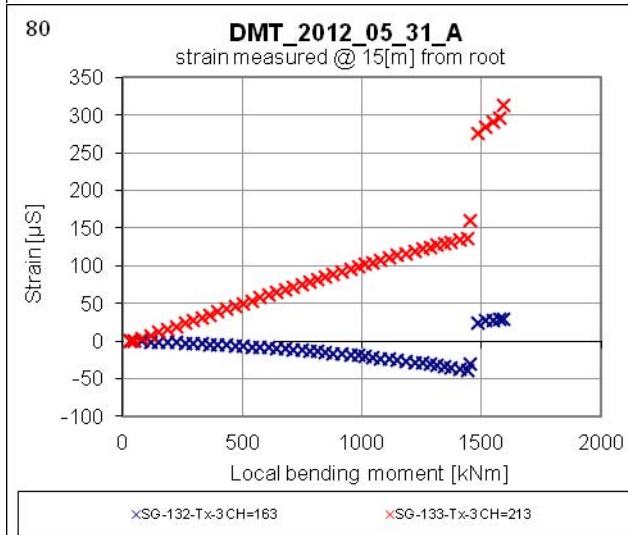
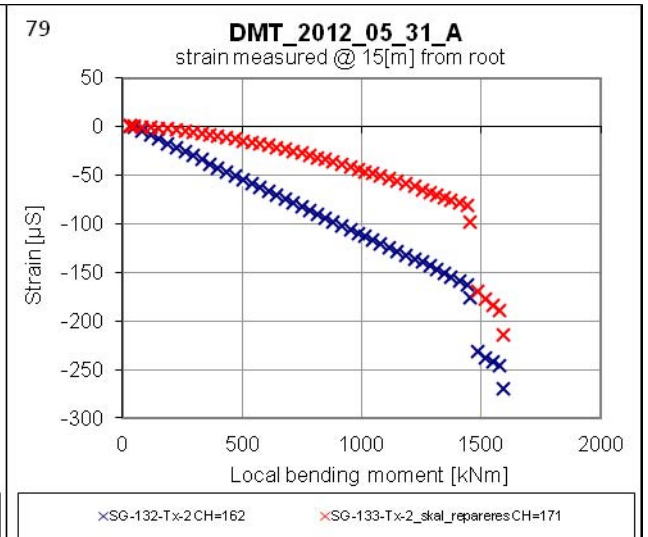
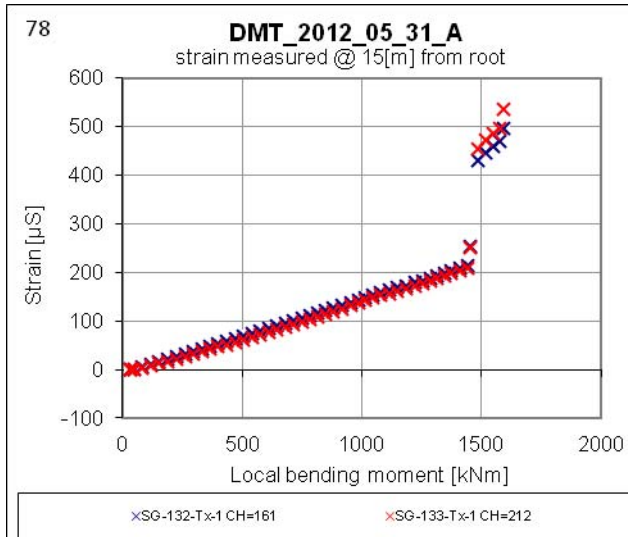


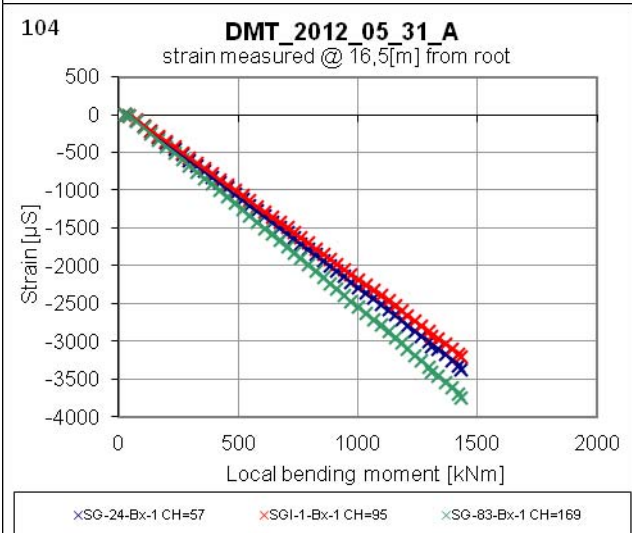
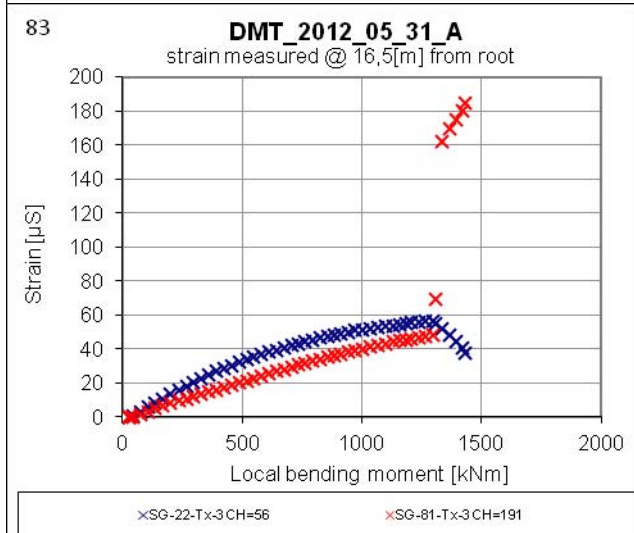
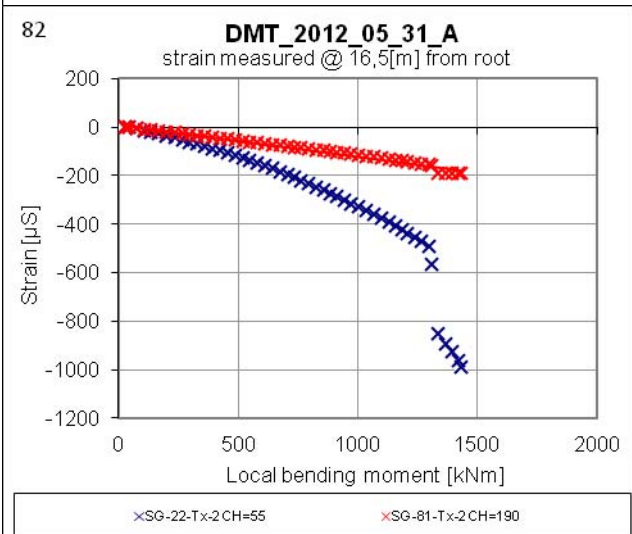
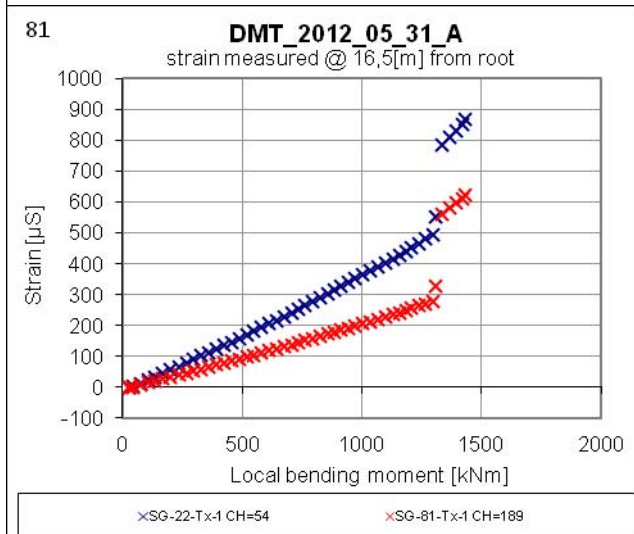
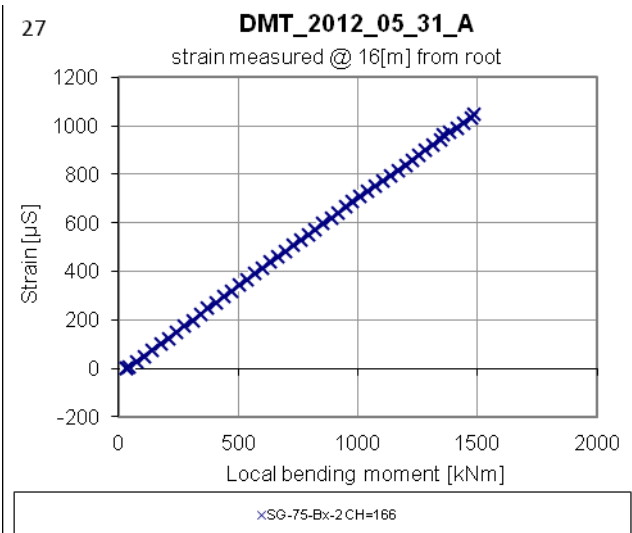
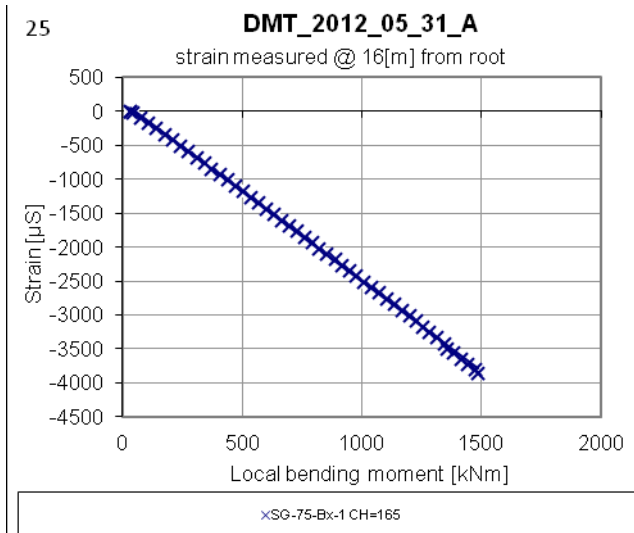


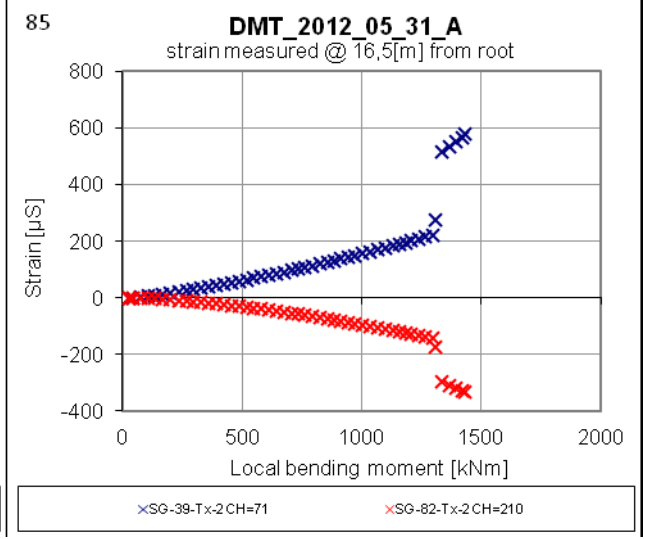
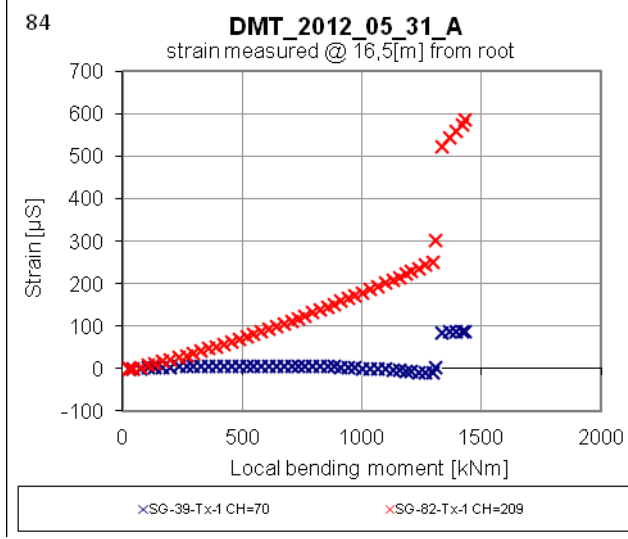
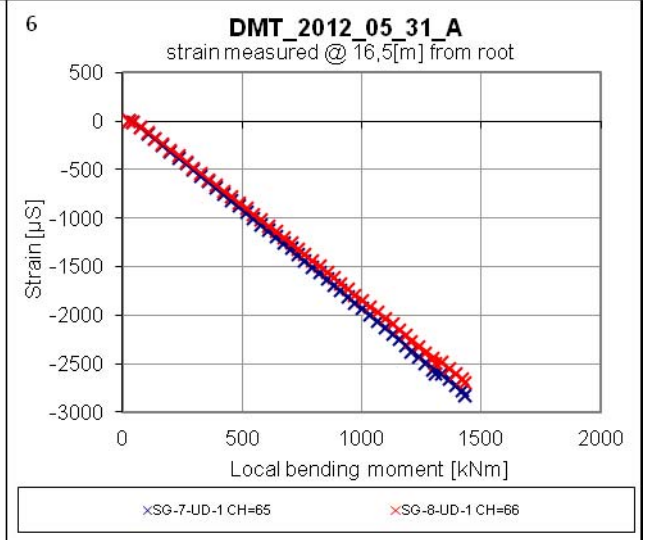
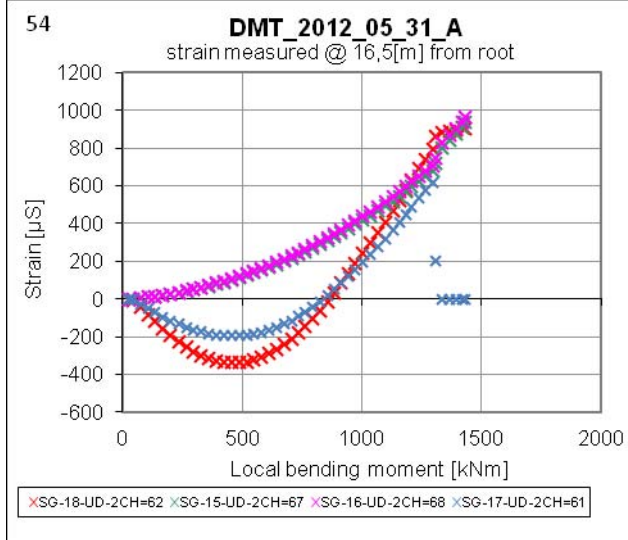
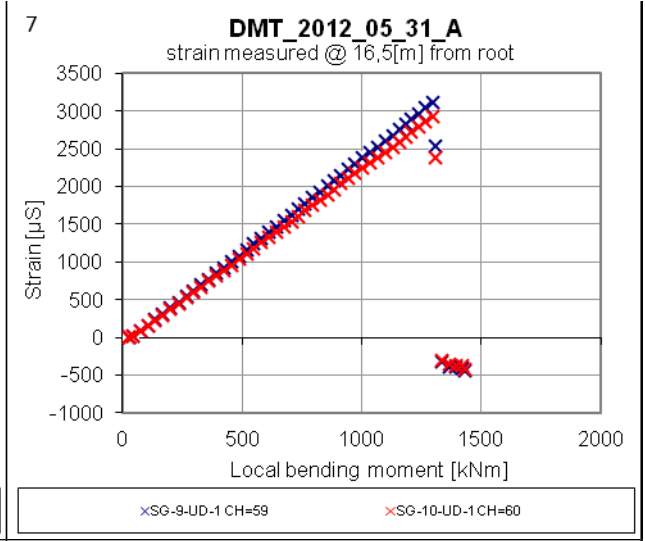
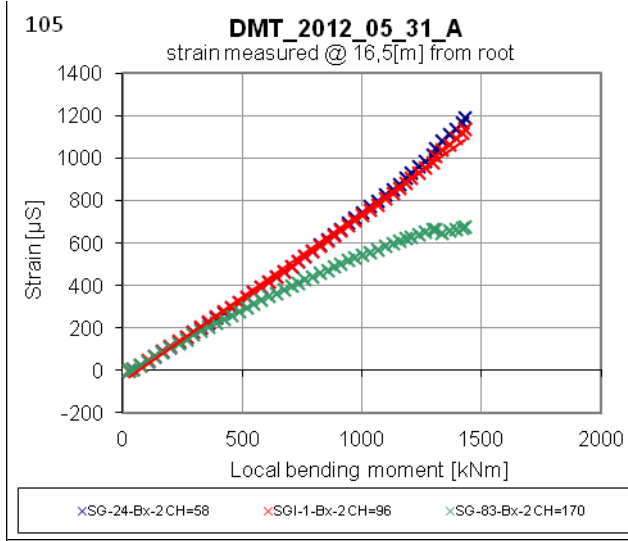


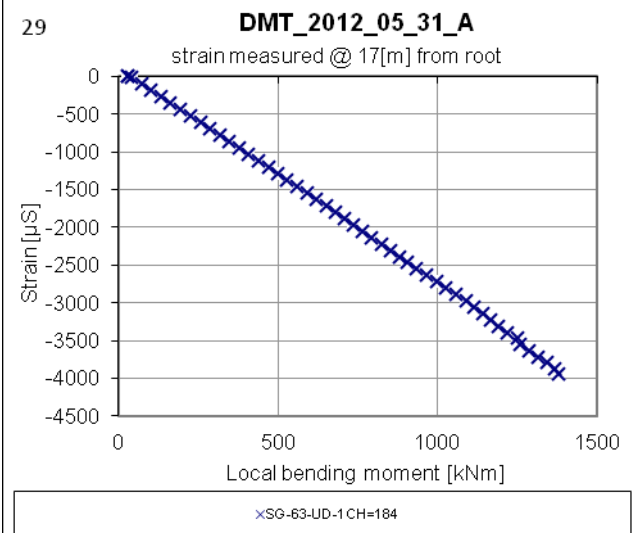
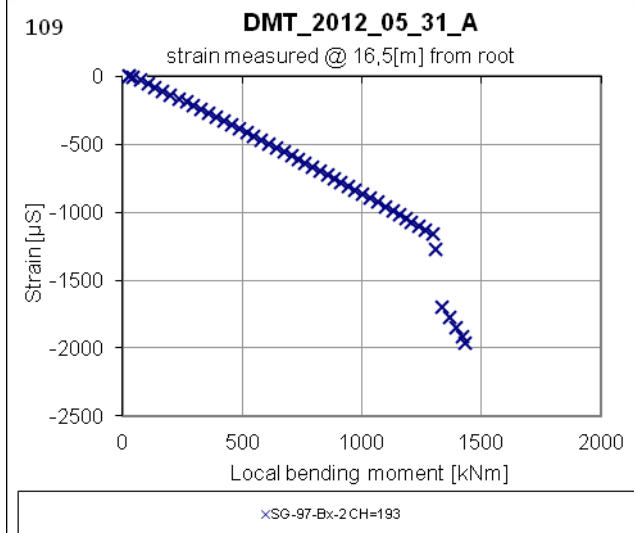
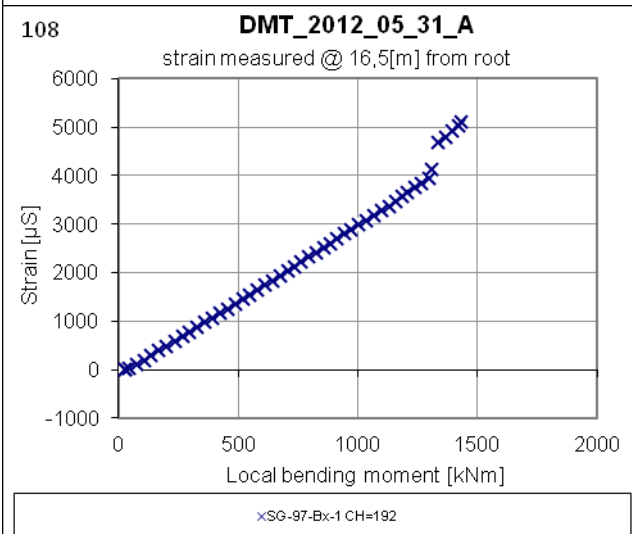
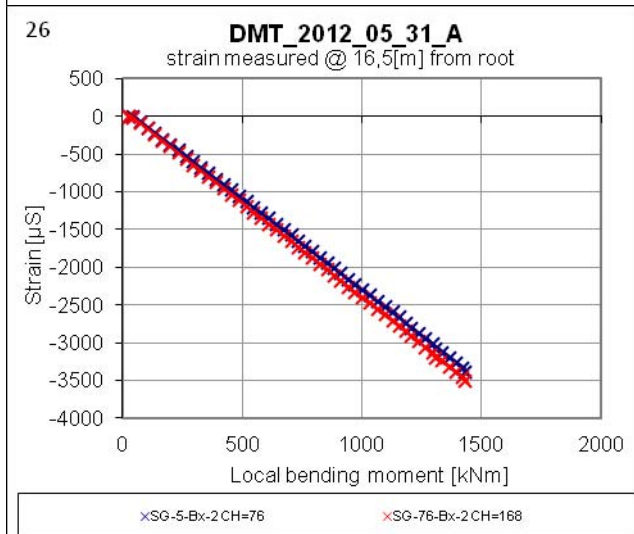
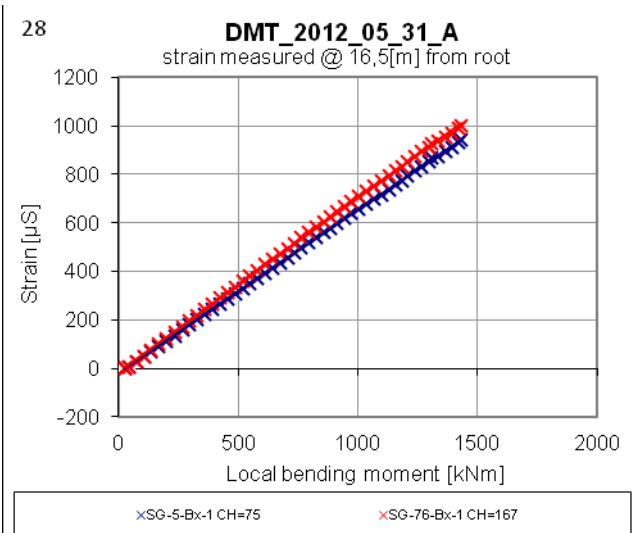
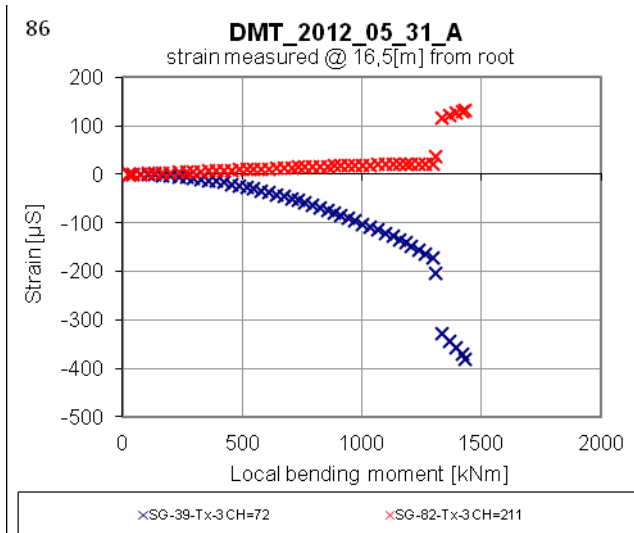


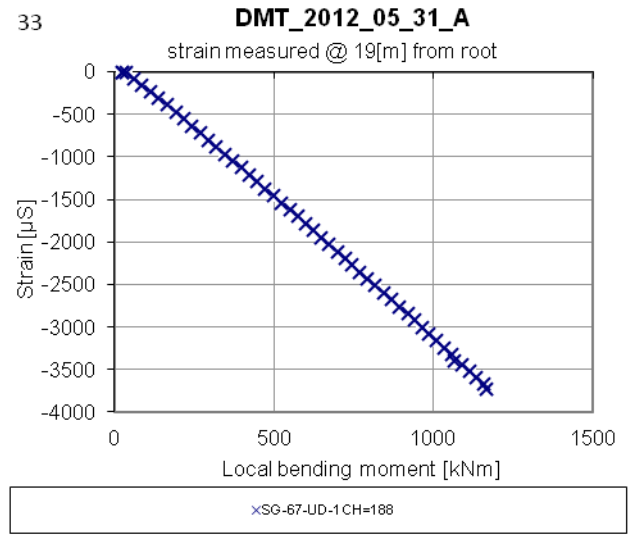
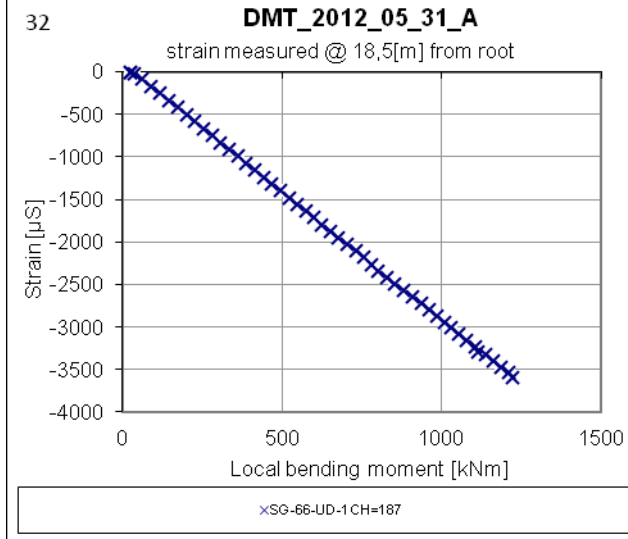
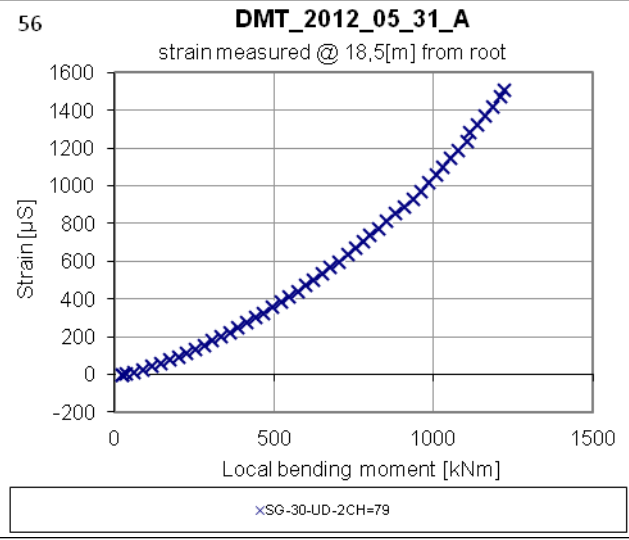
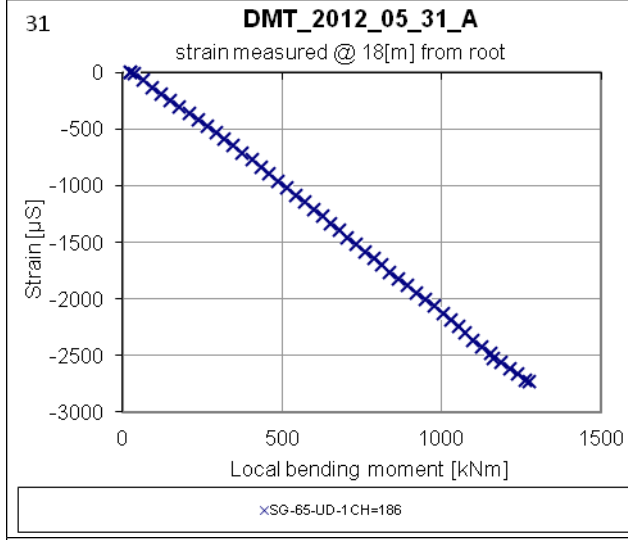
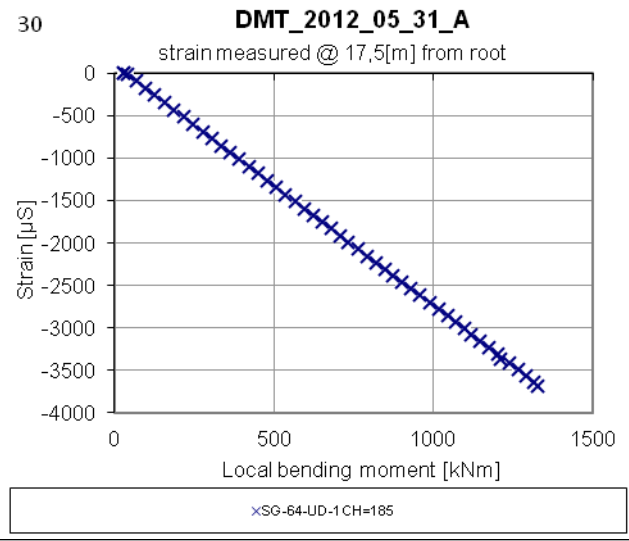
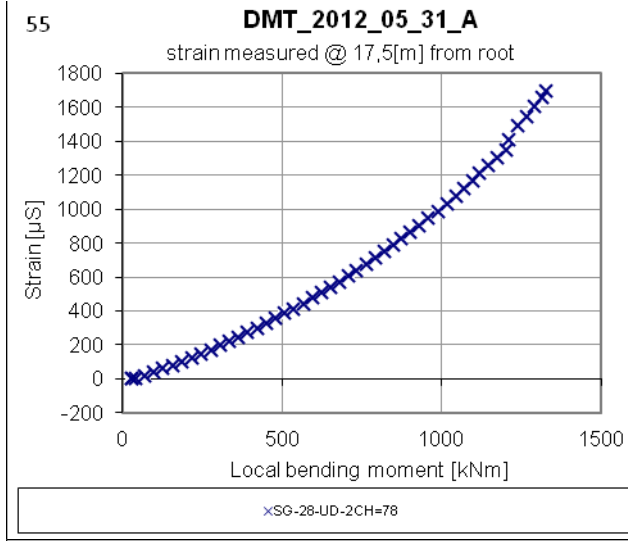


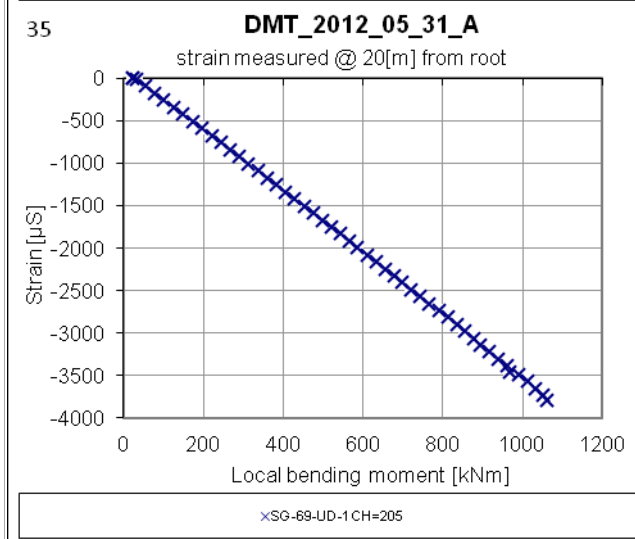
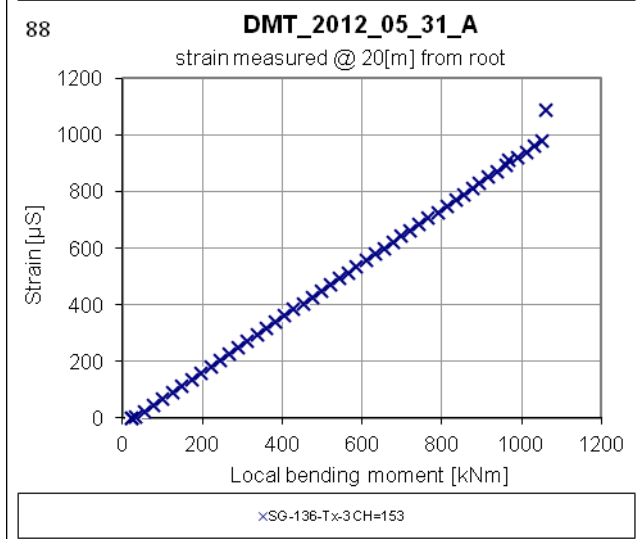
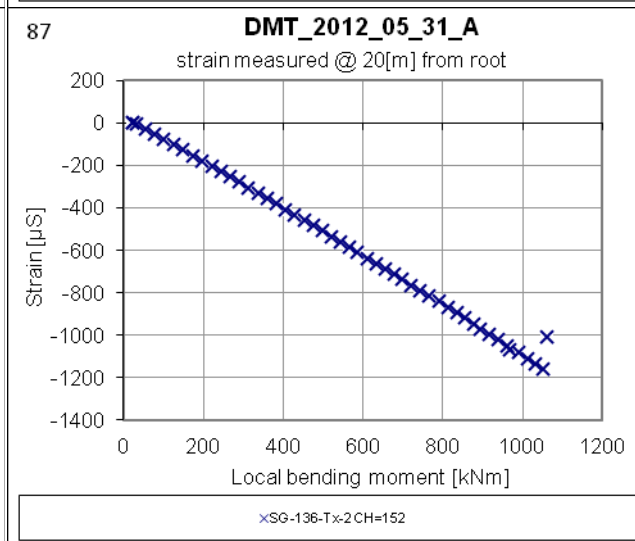
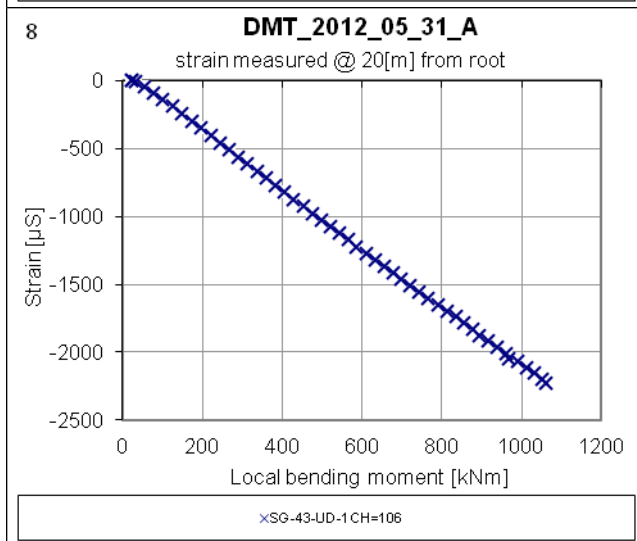
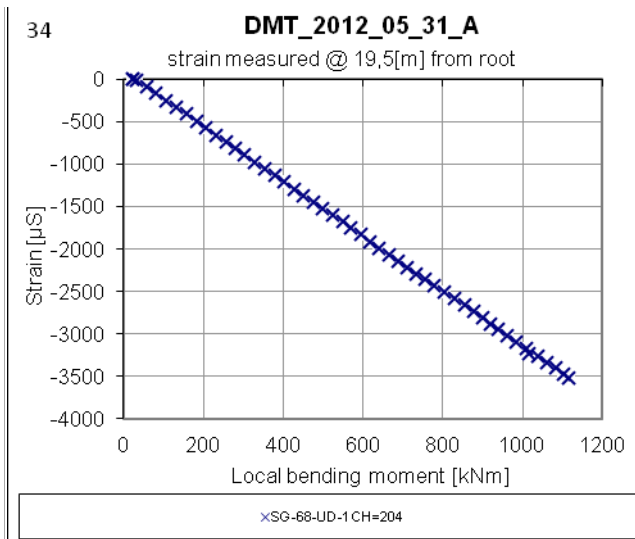
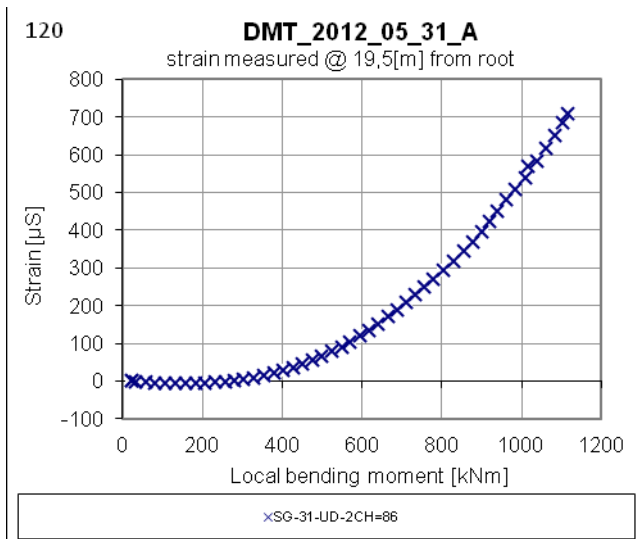


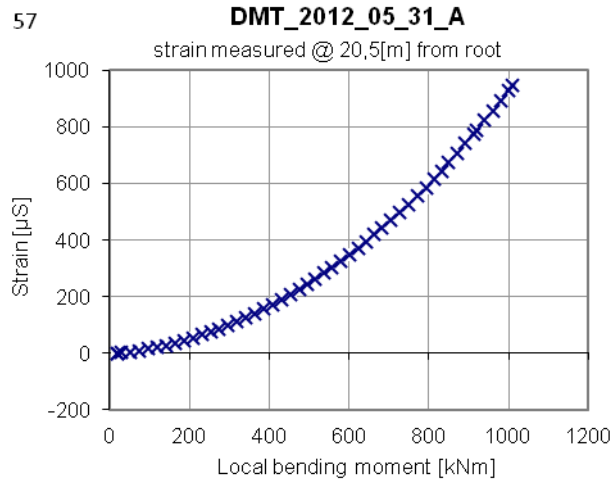




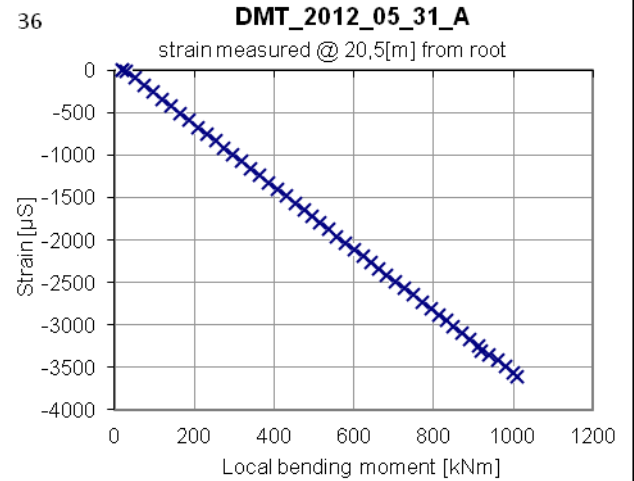




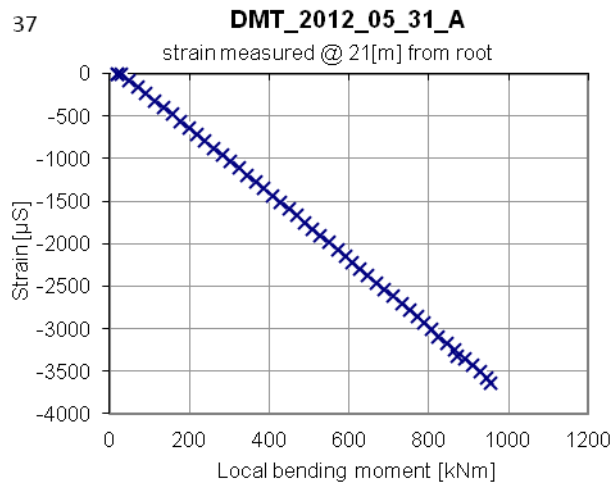




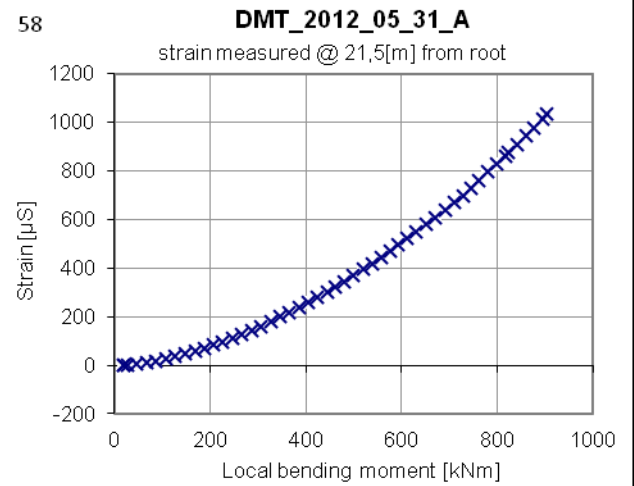
×SG-32-UD-2CH=114



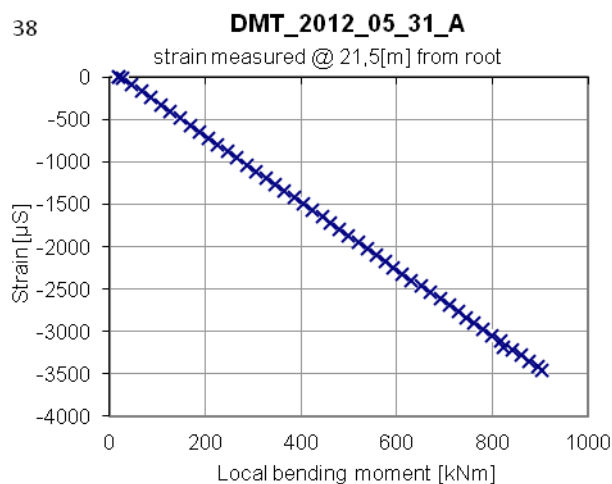
×SG-70-UD-1CH=206



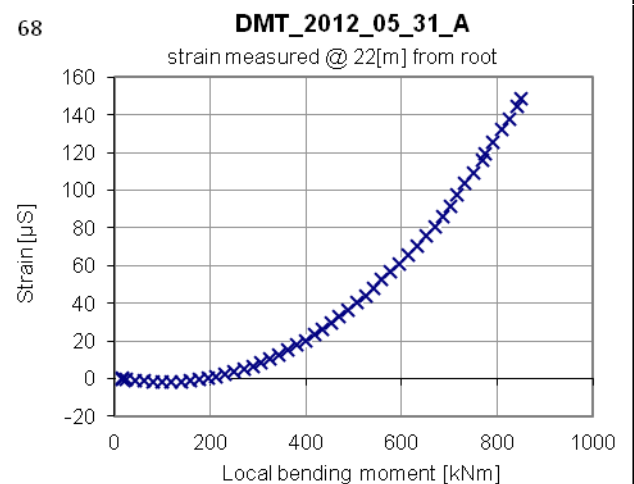
×SG-71-UD-1CH=207



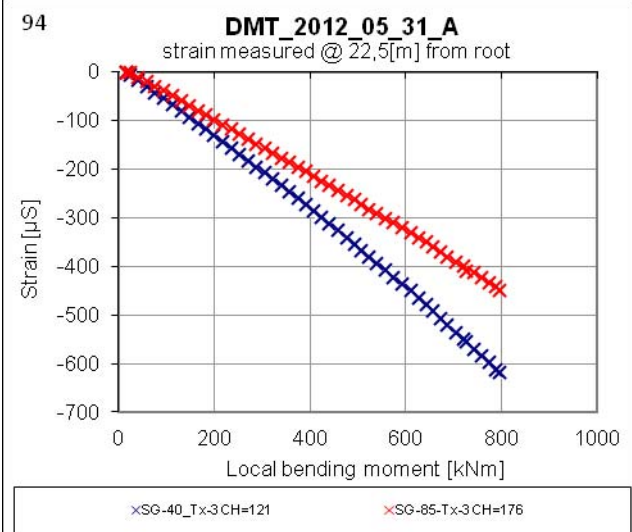
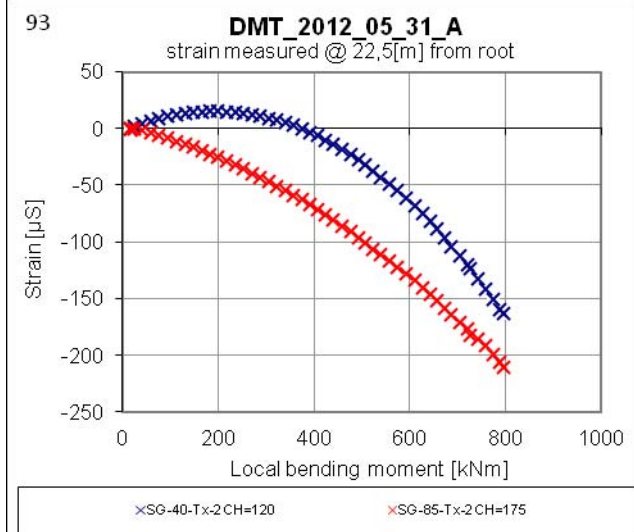
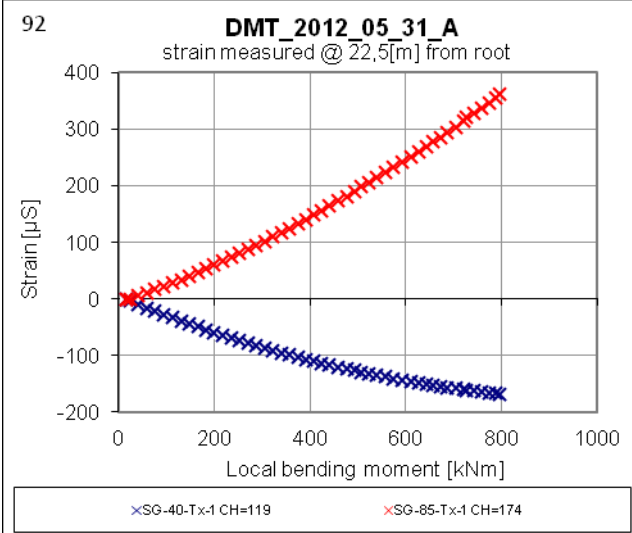
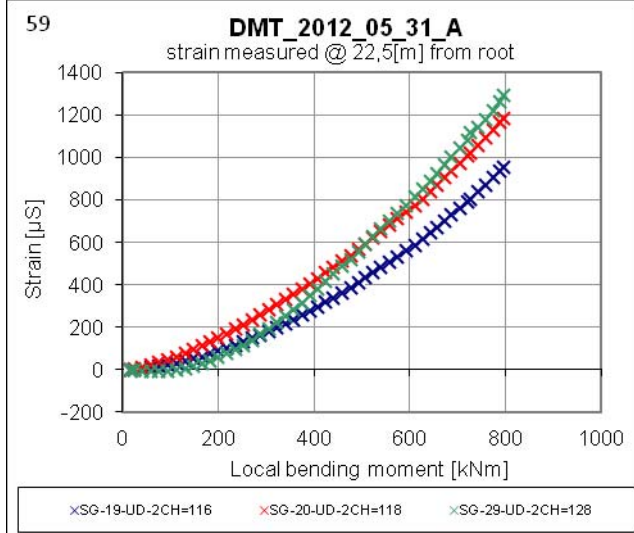
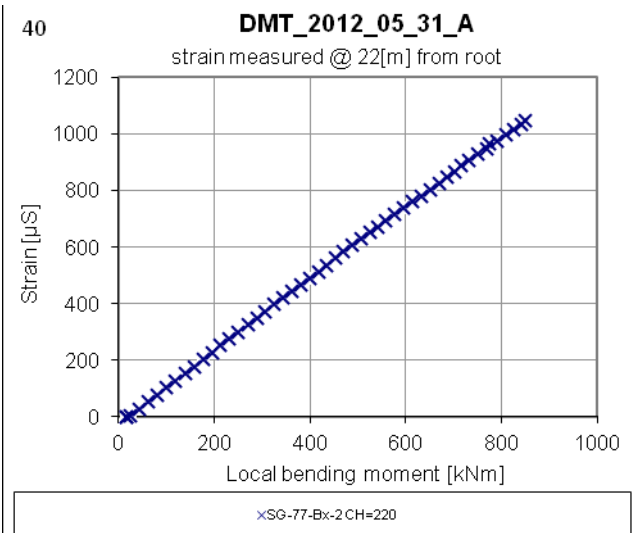
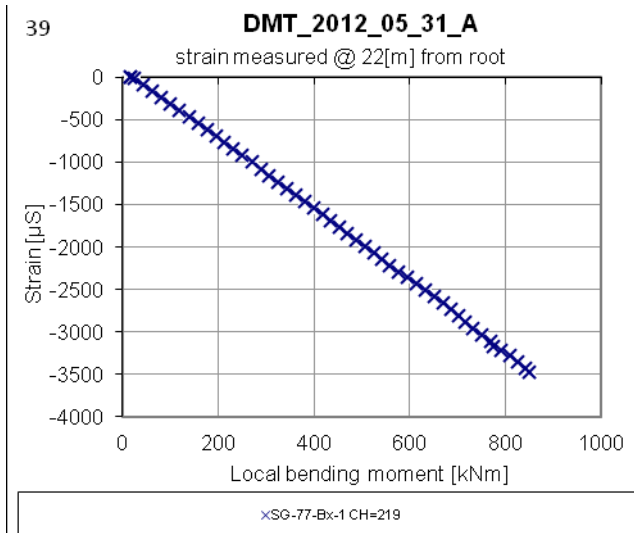
×SG-33-UD-2CH=115

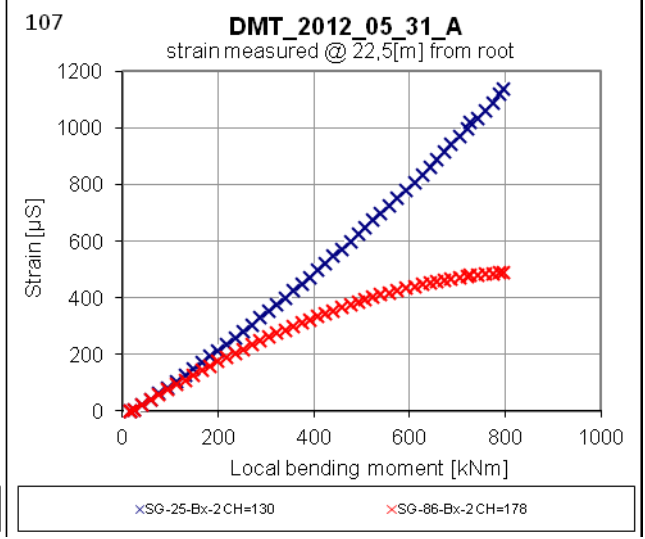
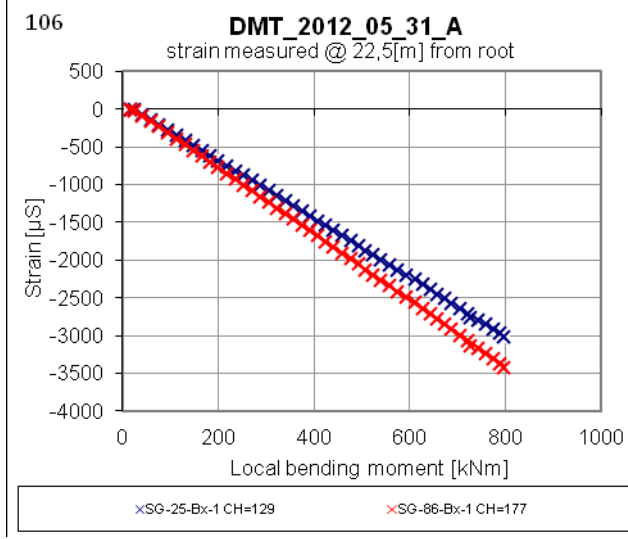
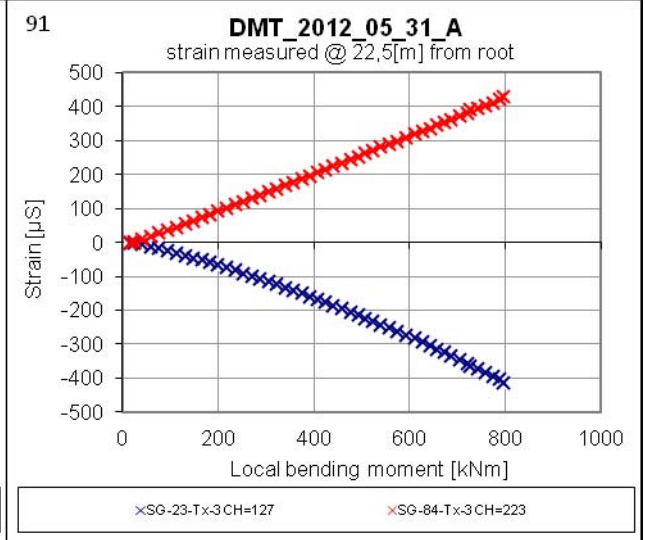
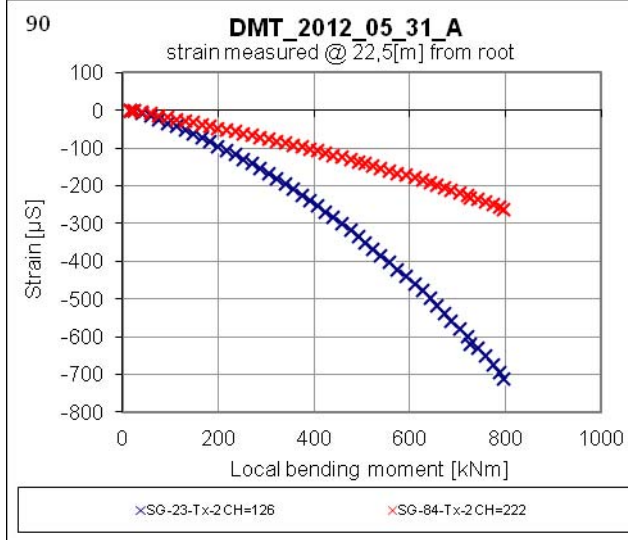
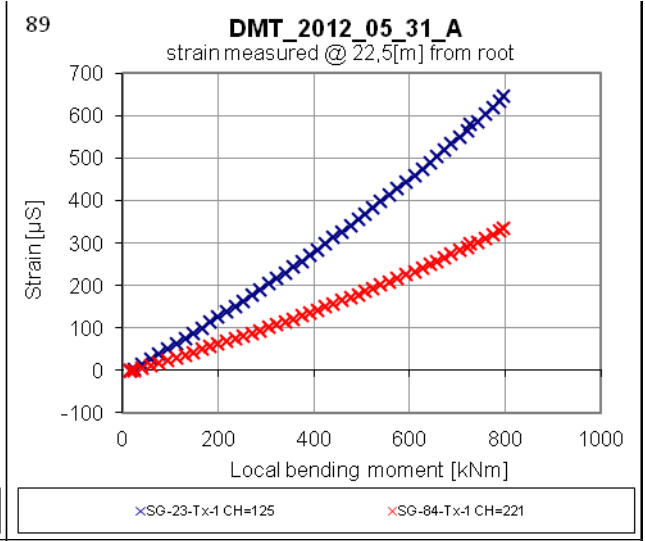
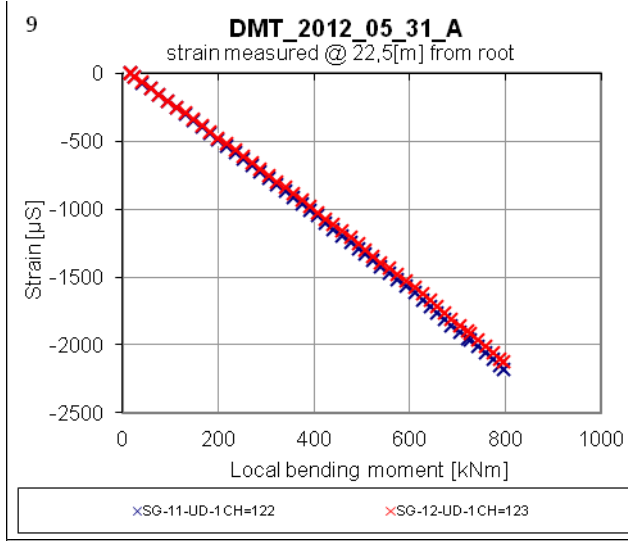


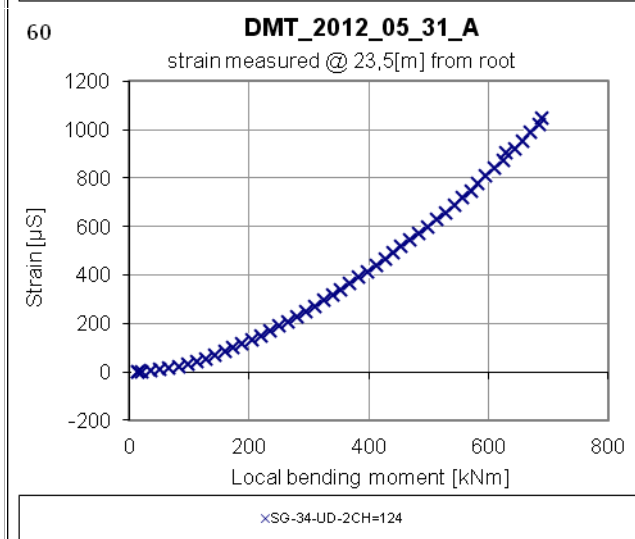
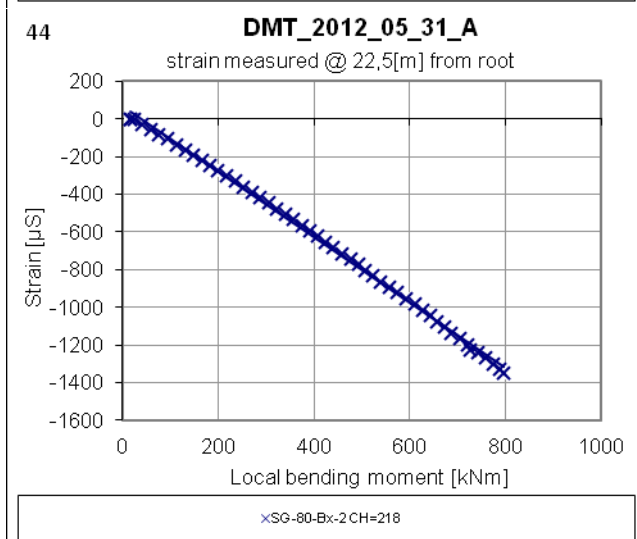
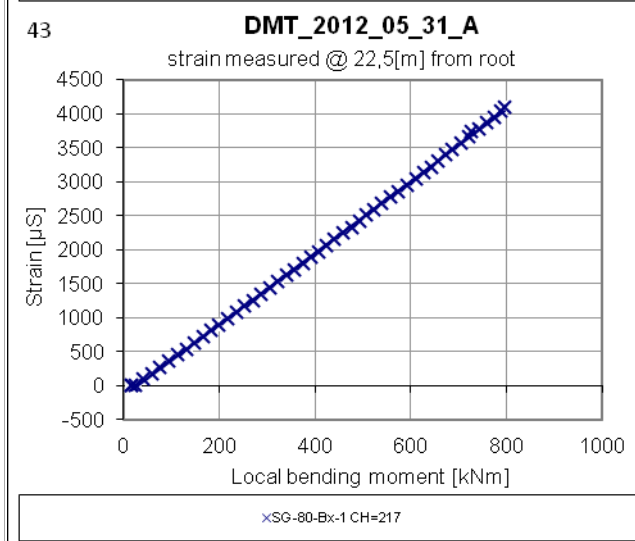
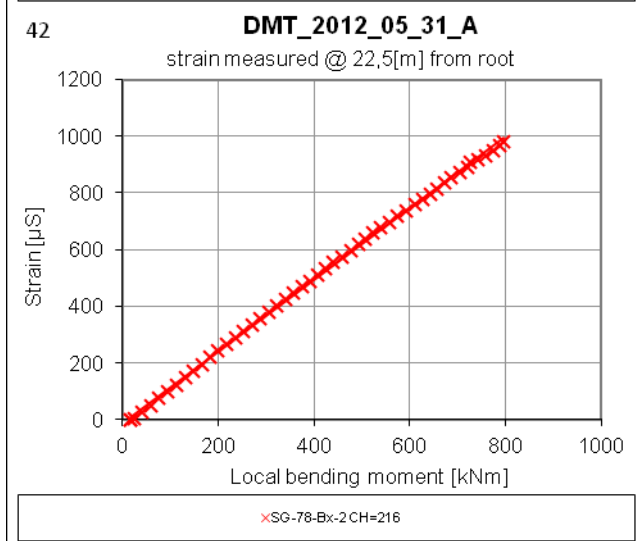
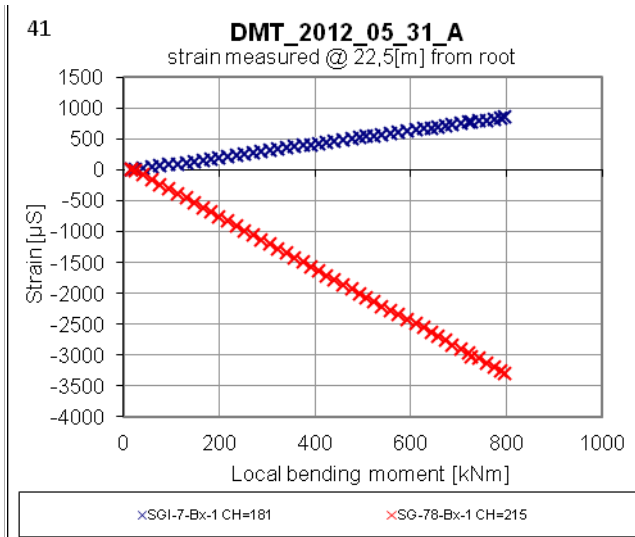
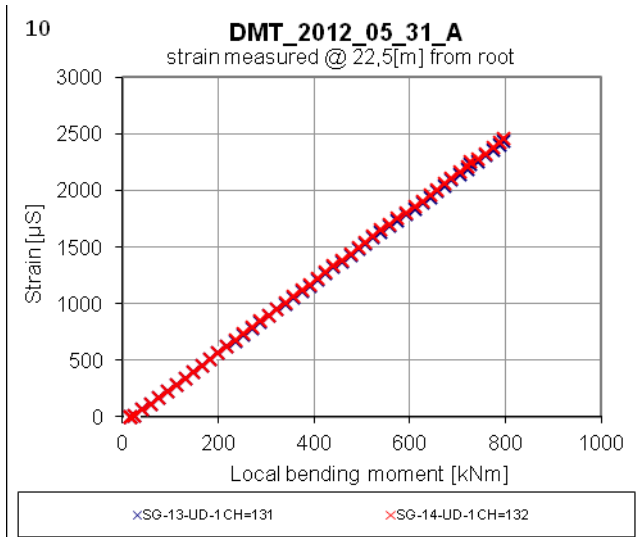
×SG-72-UD-1CH=208

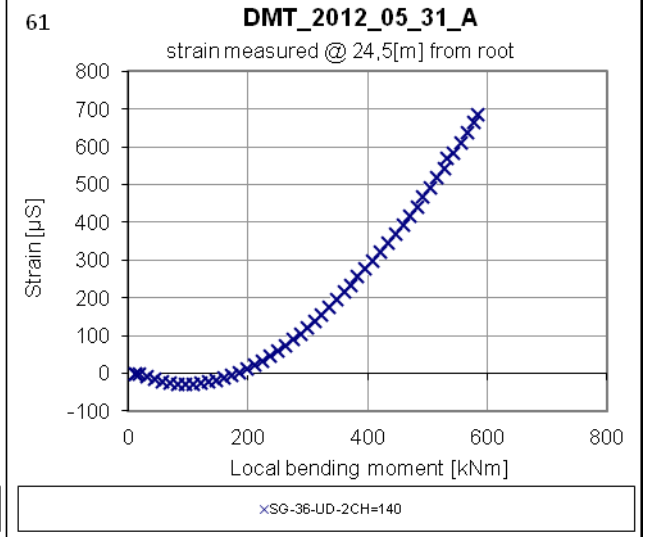
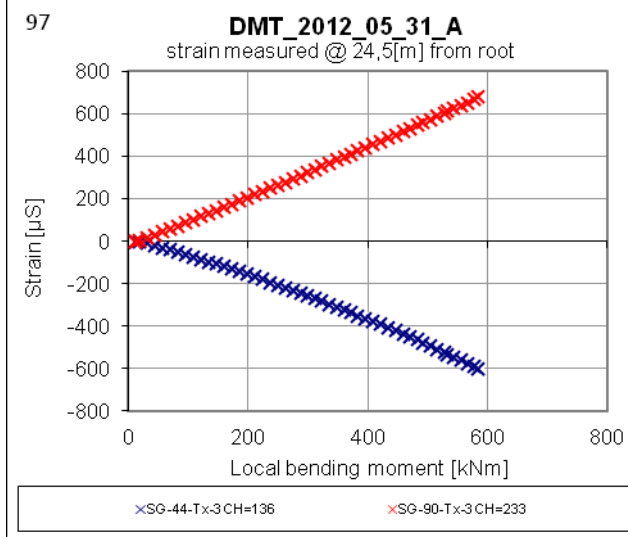
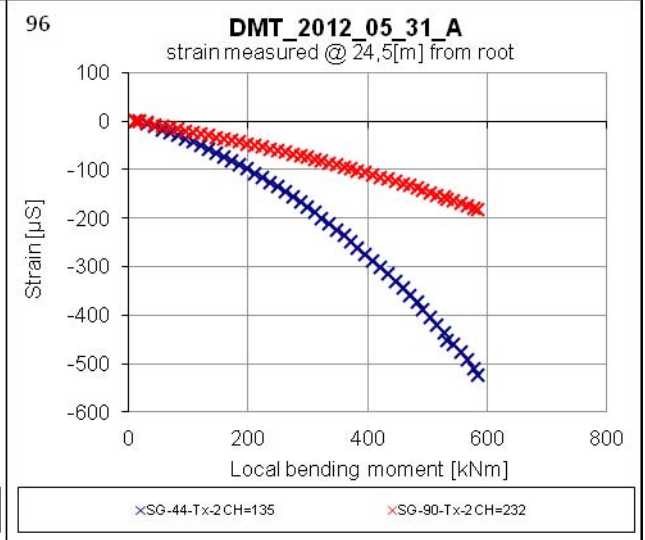
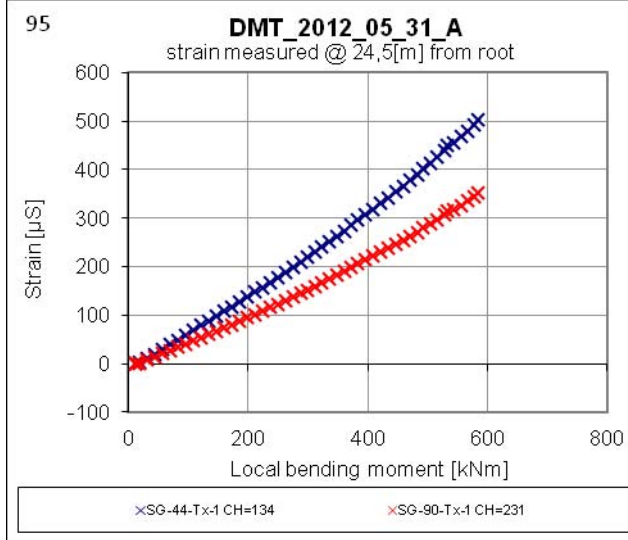
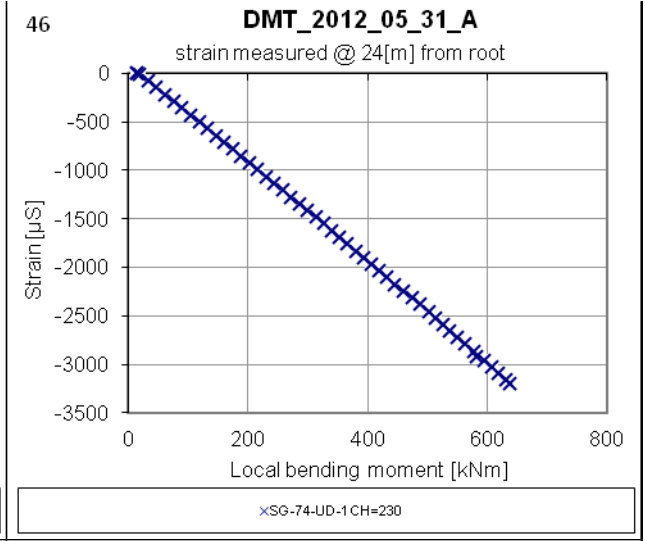
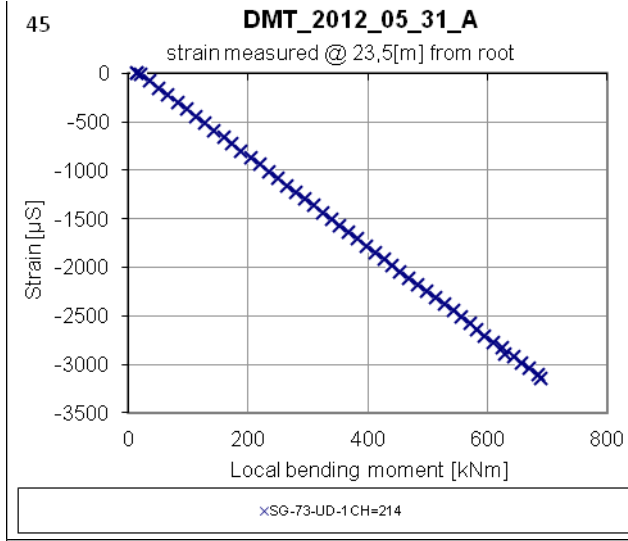


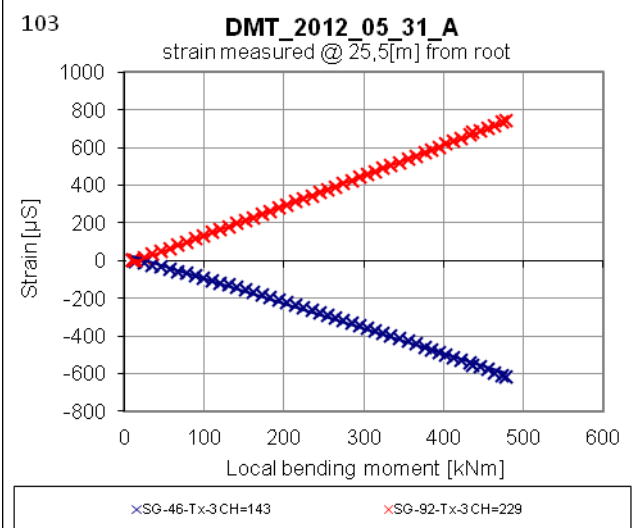
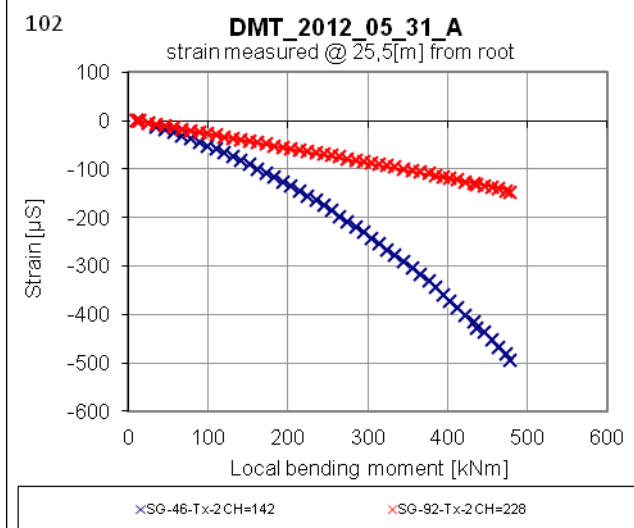
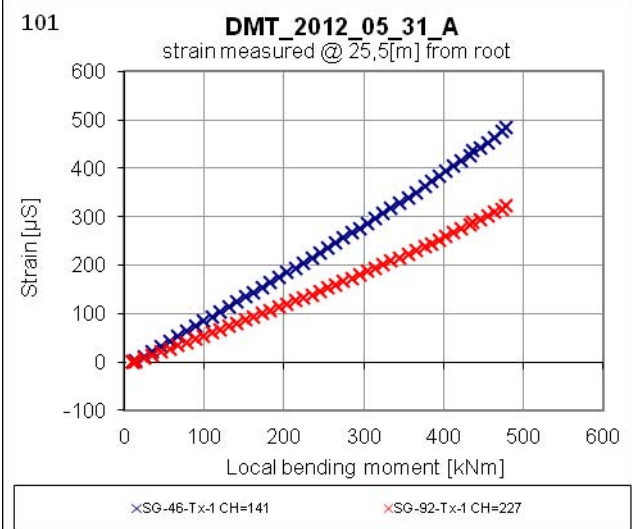
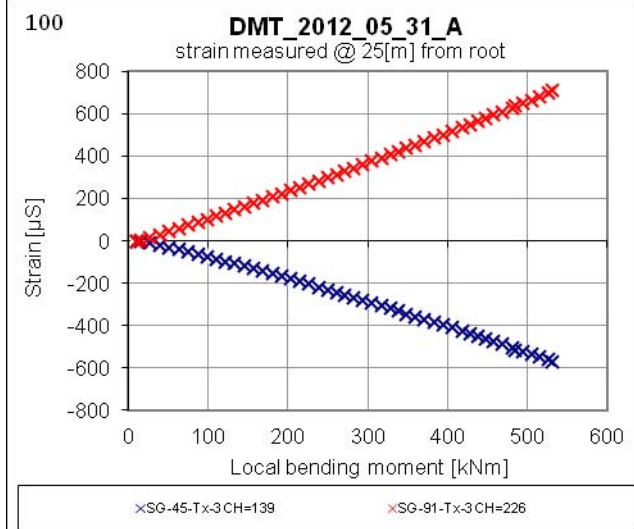
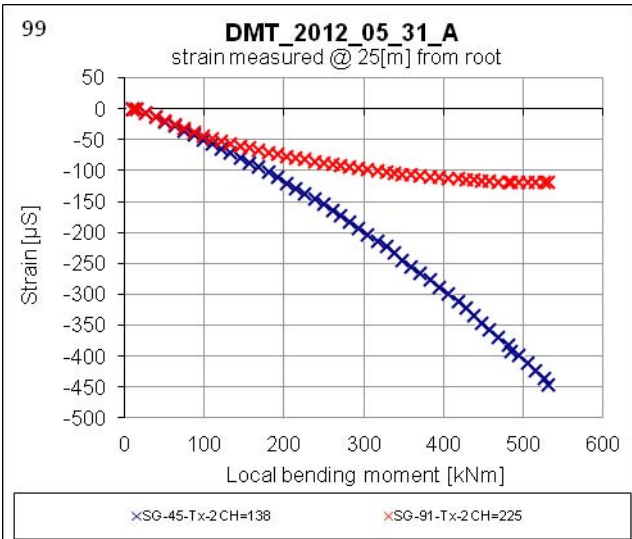
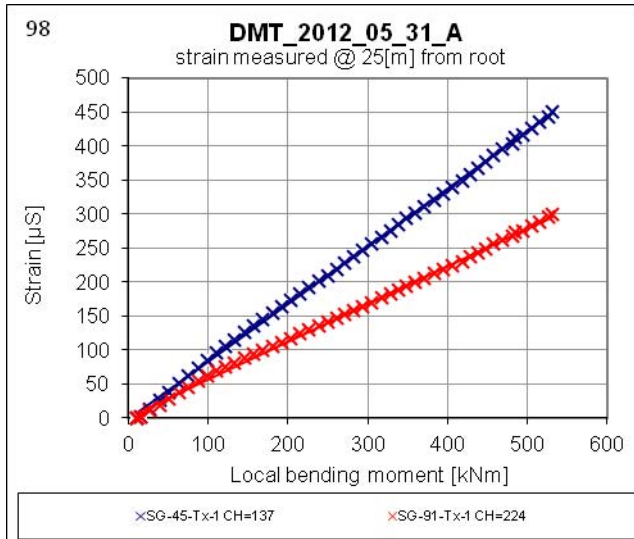
×SG-27-UD-2CH=117







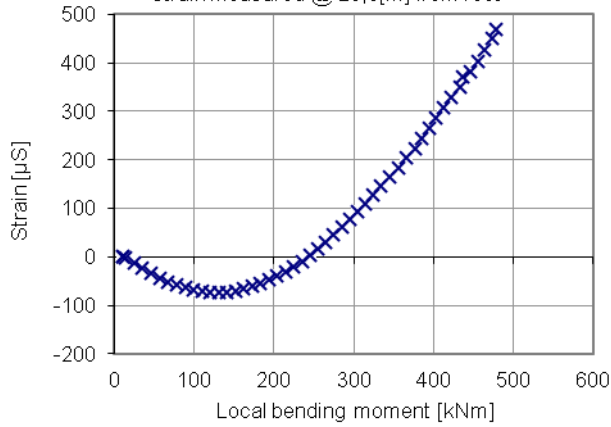




62

DMT_2012_05_31_A

strain measured @ 25,5[m] from root

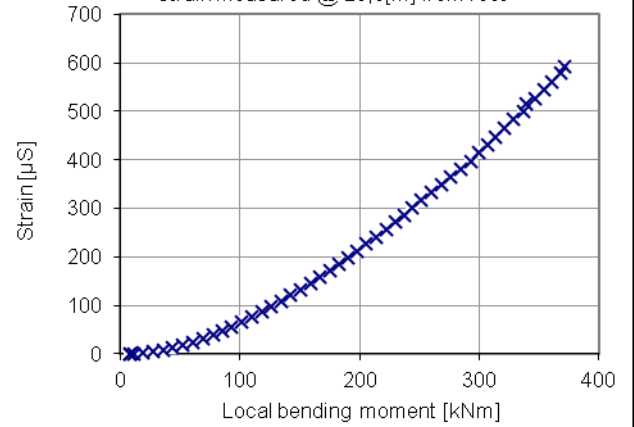


xSG-37-UD-2CH=179

63

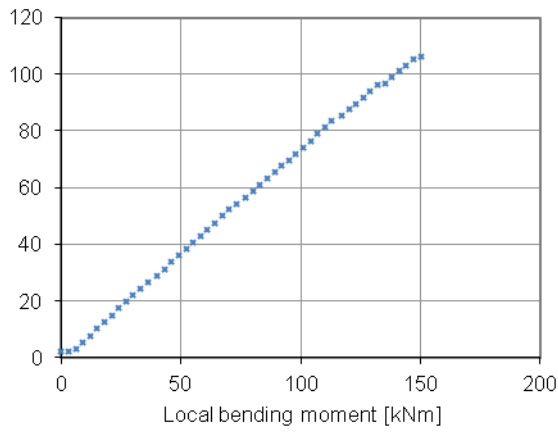
DMT_2012_05_31_A

strain measured @ 26,5[m] from root



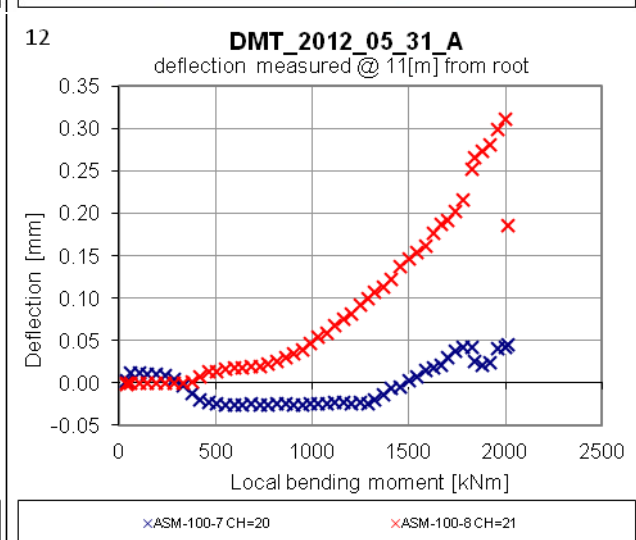
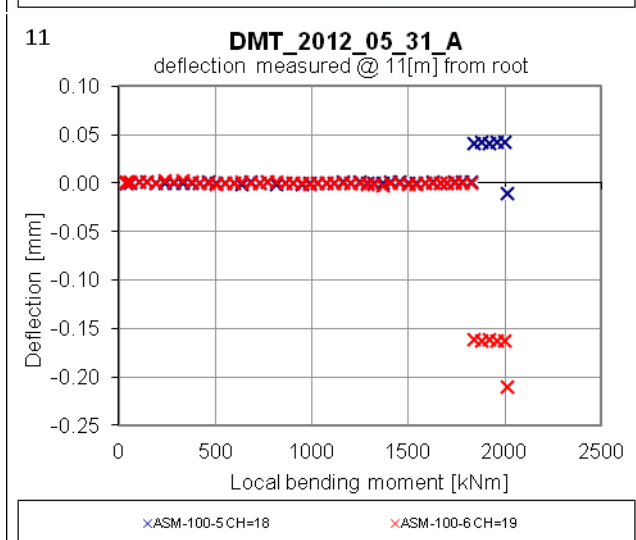
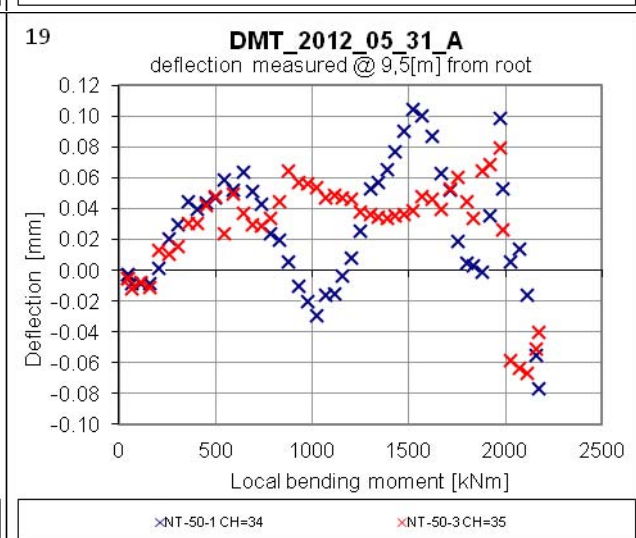
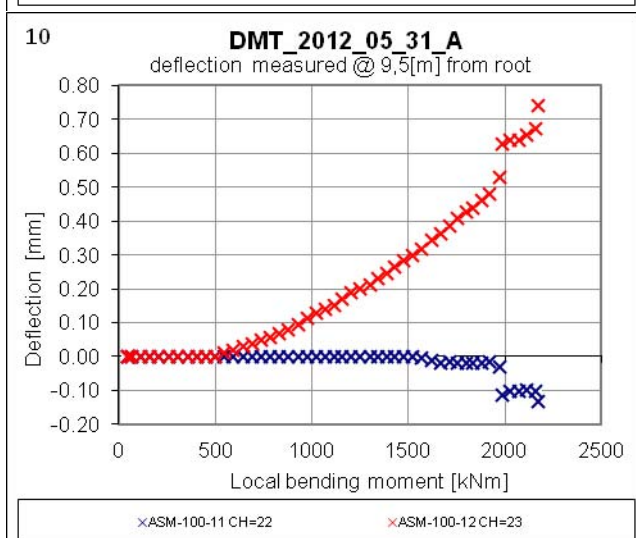
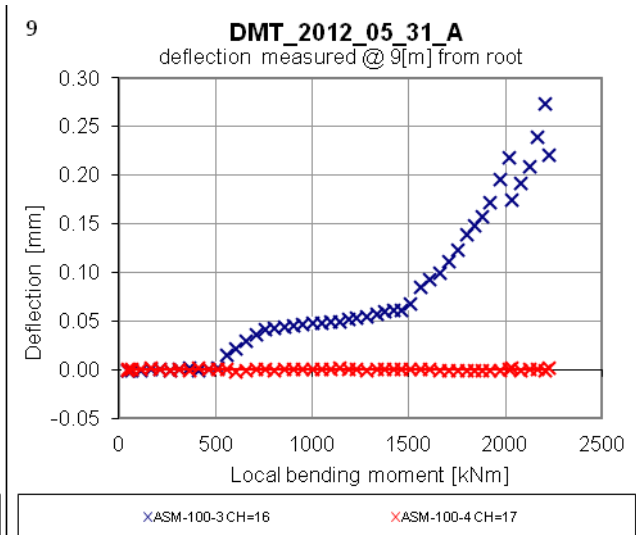
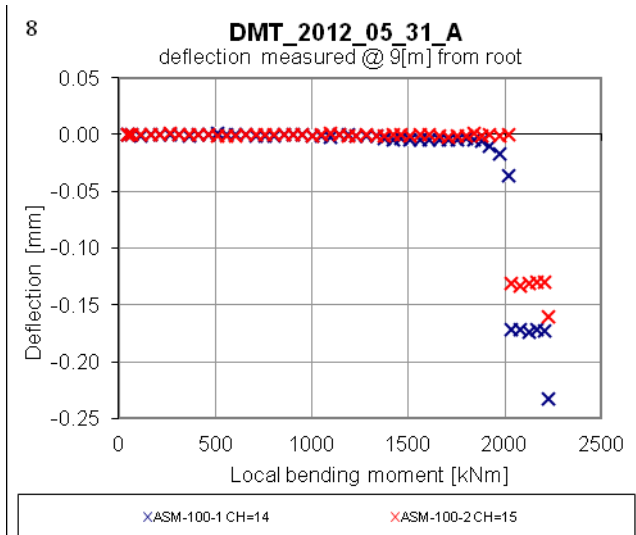
xSG-38-UD-2CH=180

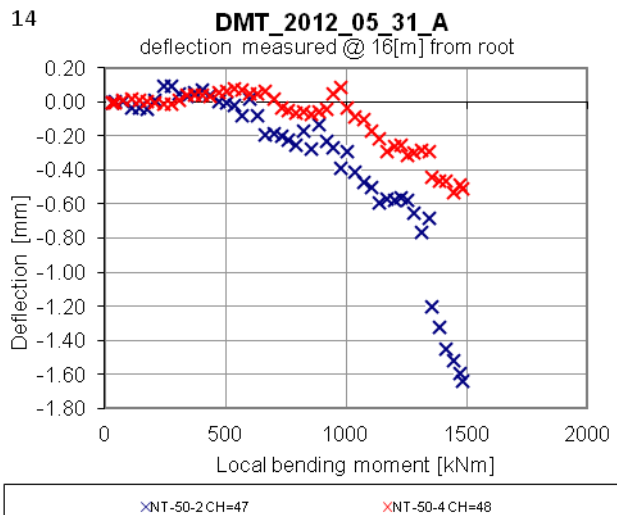
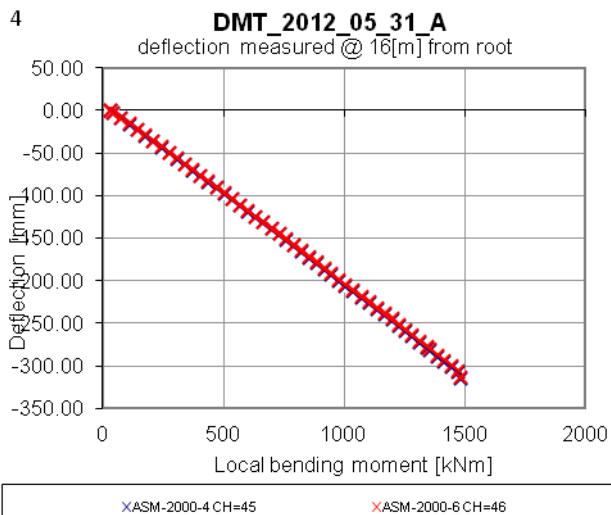
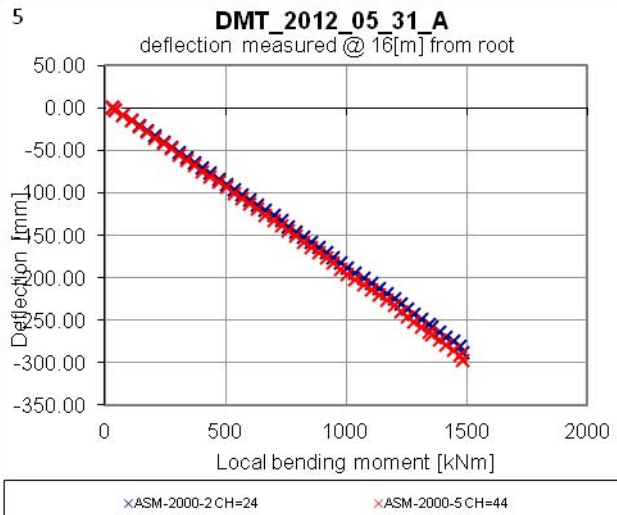
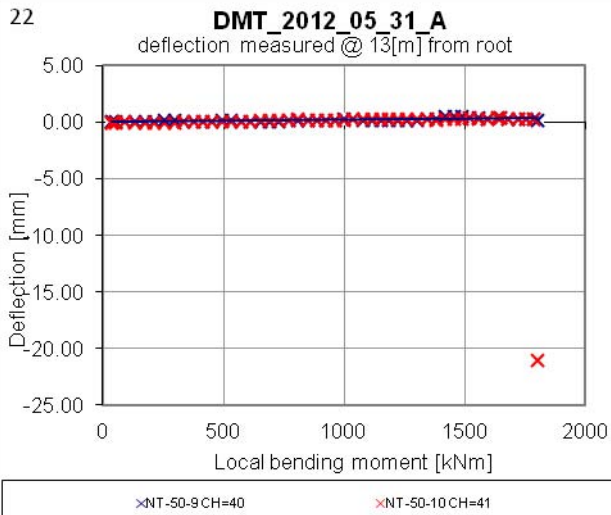
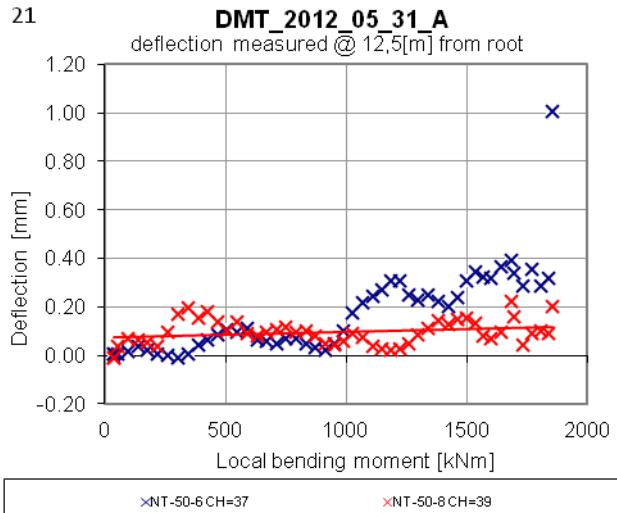
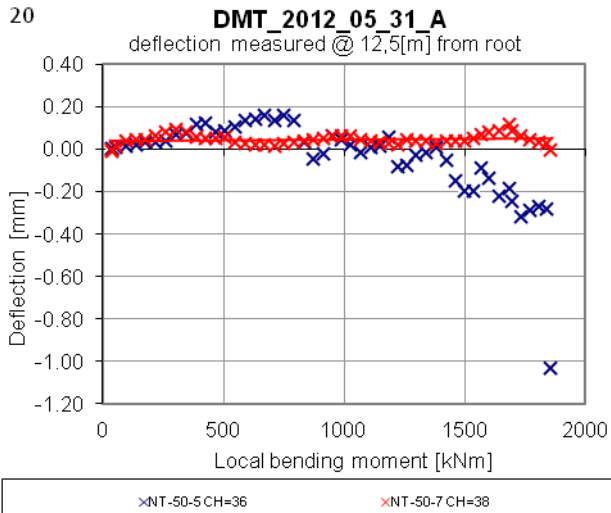
FORCE ON TIP

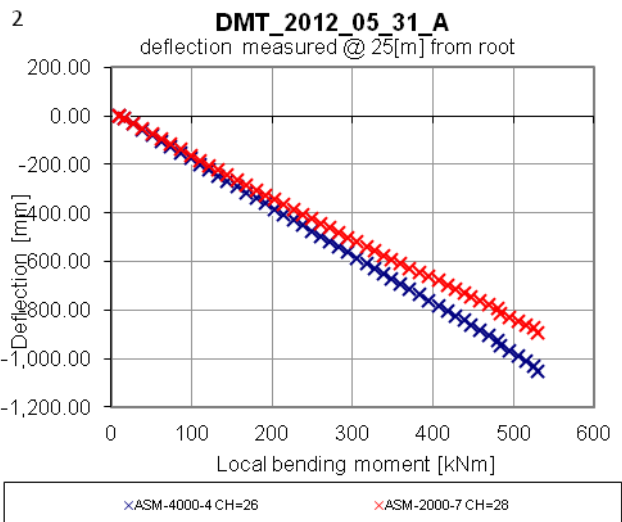
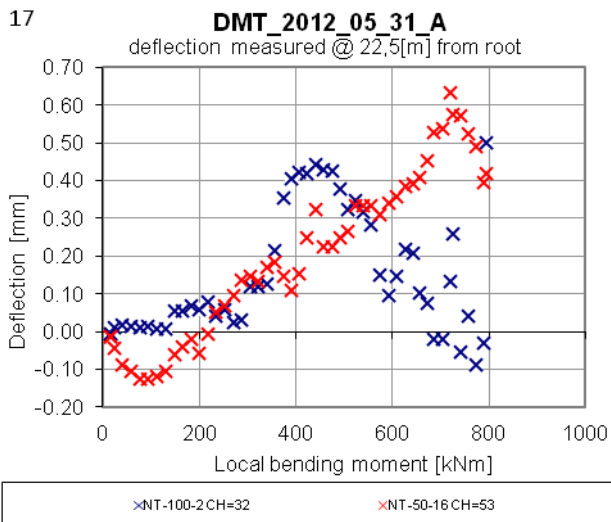
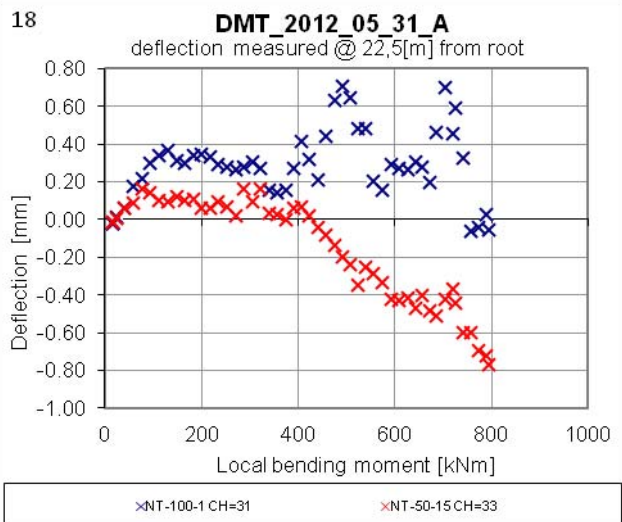
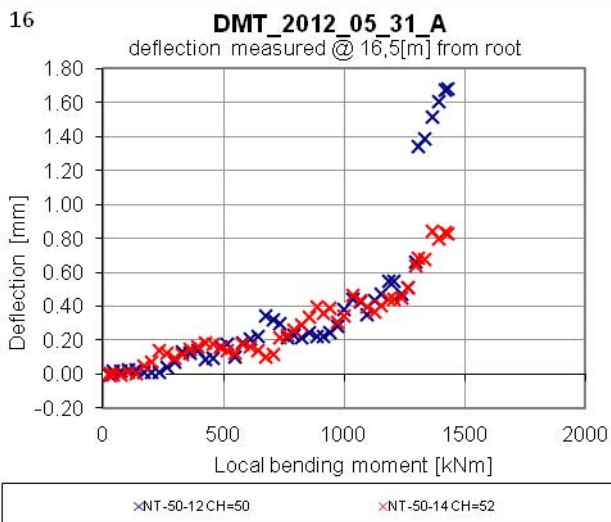
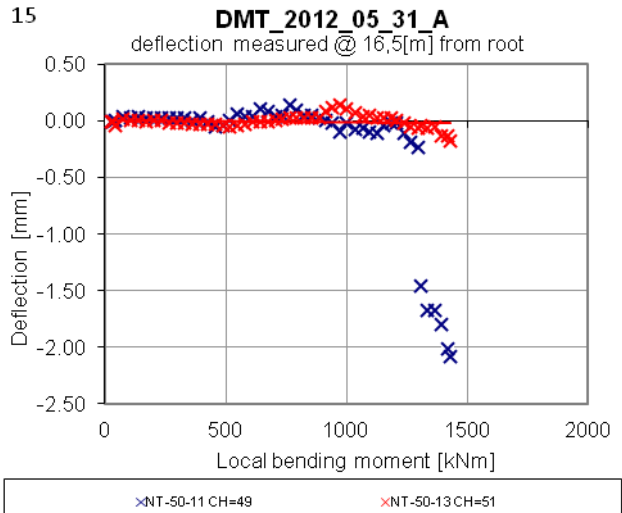
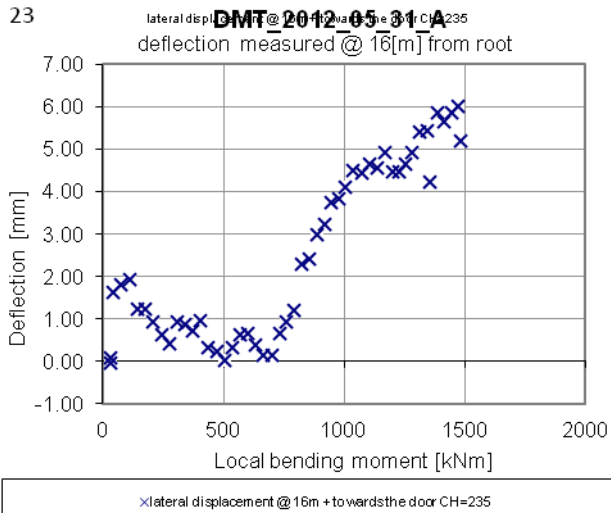


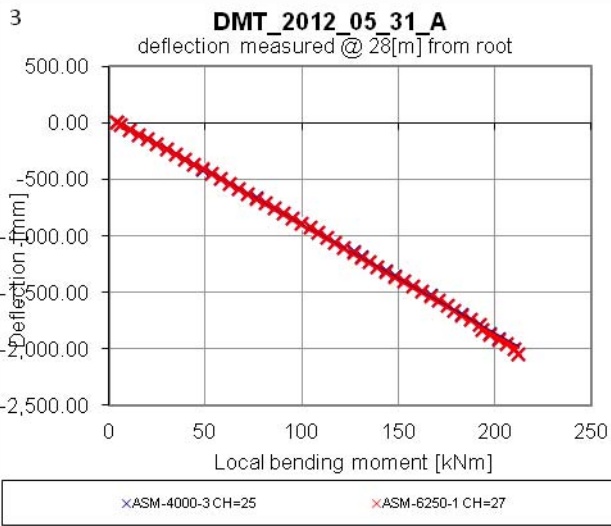
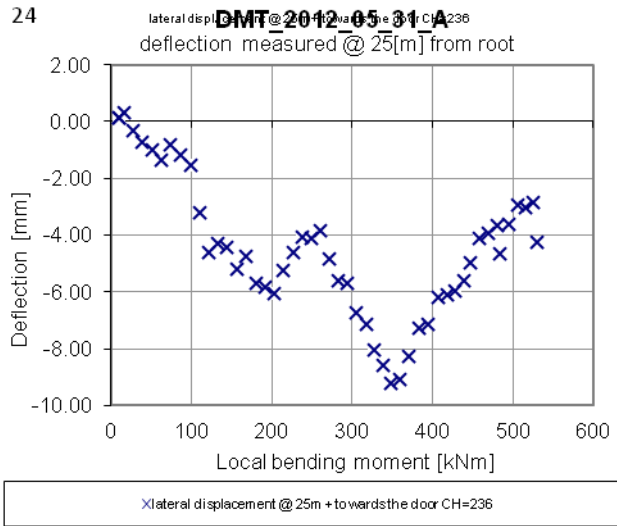
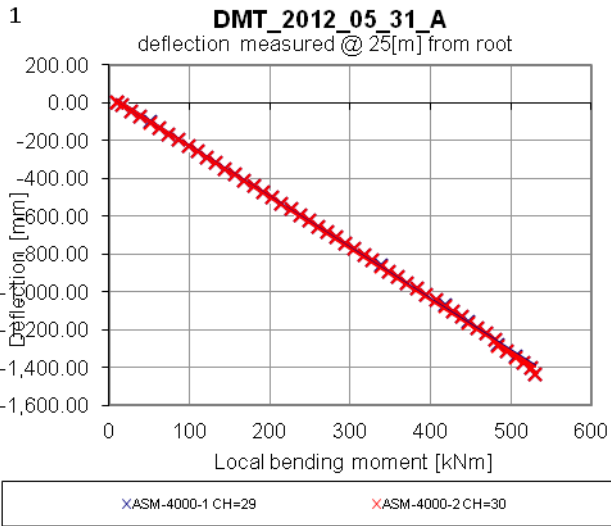
x force on tip [30m]

Appendix B4.
Deflection measurements presented by Graph tool.
Test DMT_2012_05_31









Appendix B3.

Strain gauge measurements presented by Graph tool.

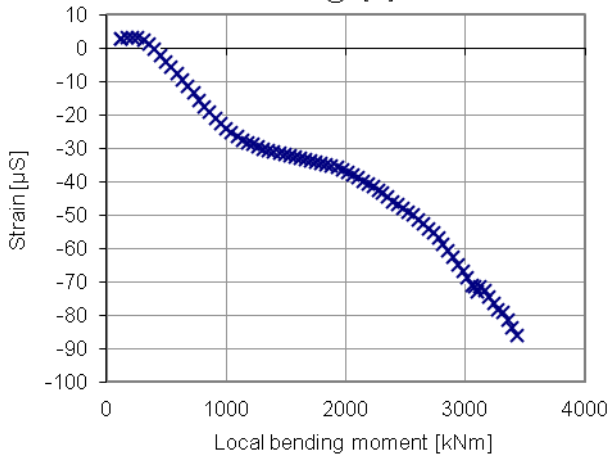
Test DMT_2012_06_07

The last test leading to catastrophic failure

64

DMT_2012_06_07_C

strain measured @ 6[m] from root

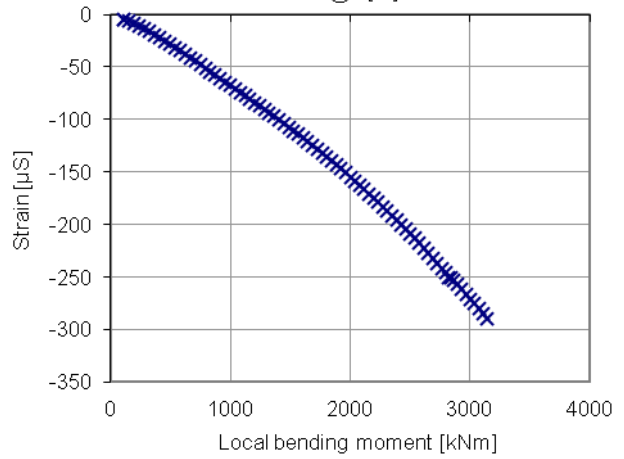


×SG-87-UD-2CH=105

65

DMT_2012_06_07_C

strain measured @ 8[m] from root

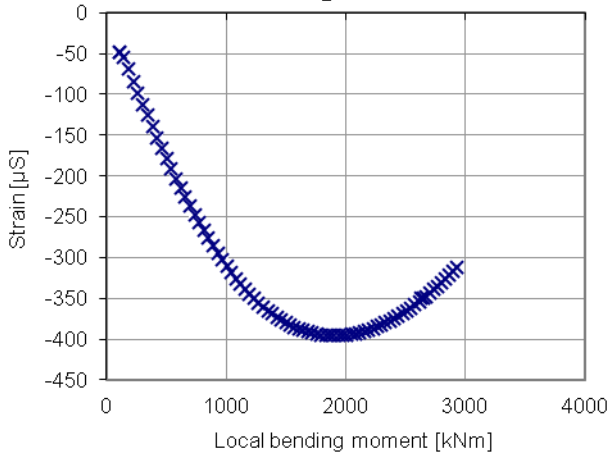


×SG-88-UD-2CH=101

47

DMT_2012_06_07_C

strain measured @ 9,5[m] from root

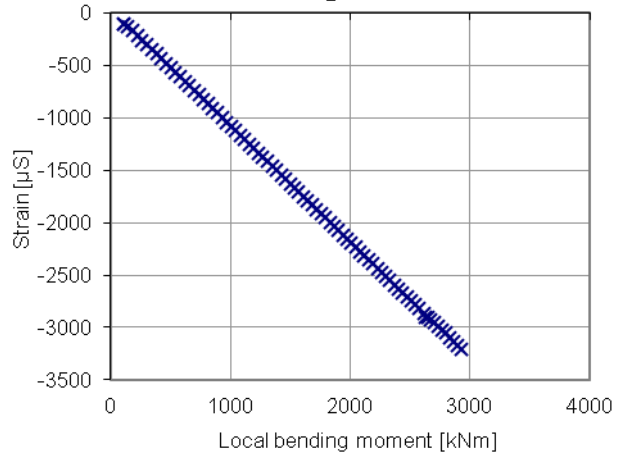


×SG-93-UD-2CH=103

11

DMT_2012_06_07_C

strain measured @ 9,5[m] from root

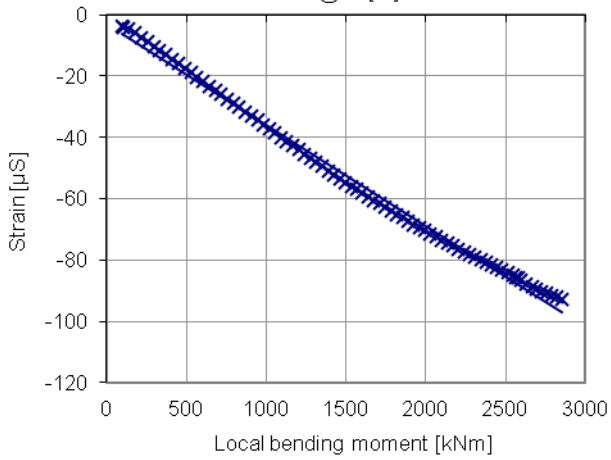


×SG-52-UD-1 CH=144

66

DMT_2012_06_07_C

strain measured @ 10[m] from root

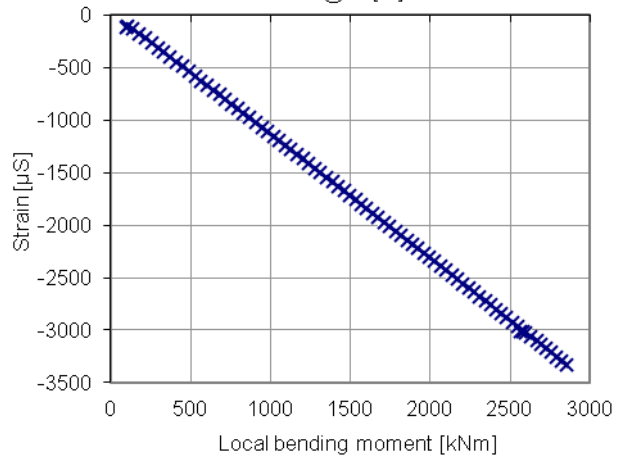


×SG-89-UD-2CH=102

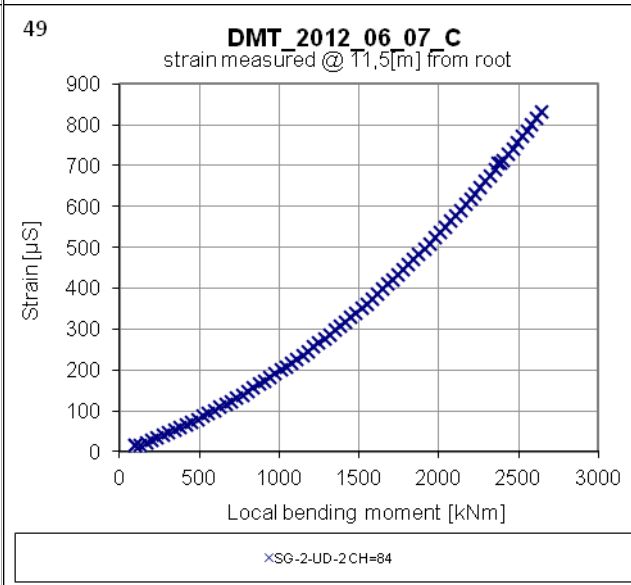
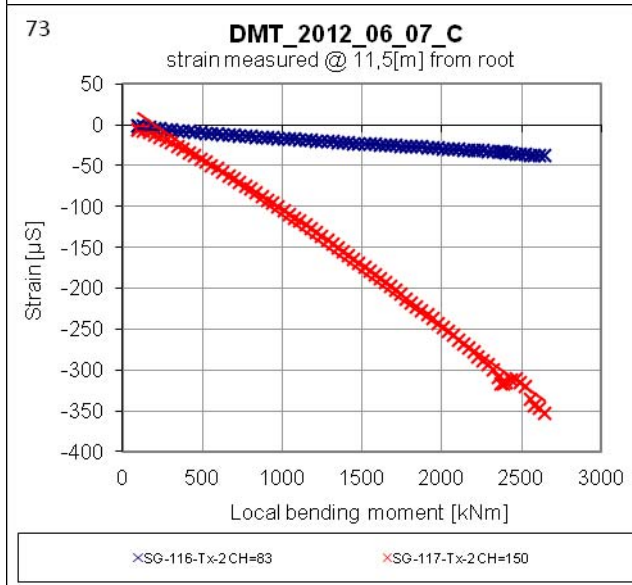
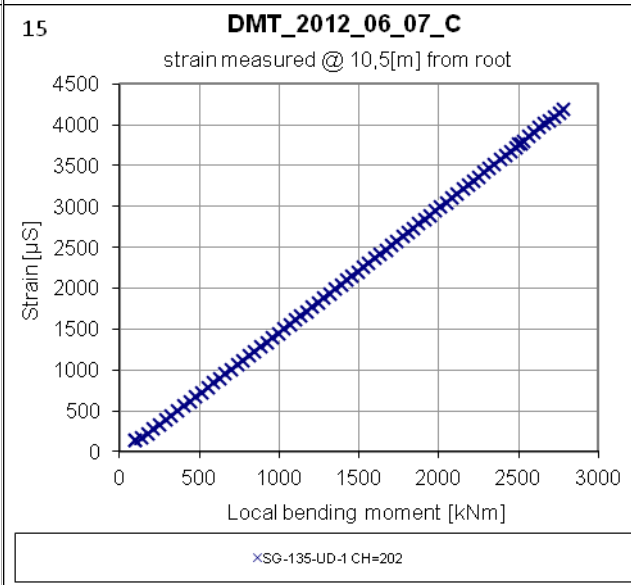
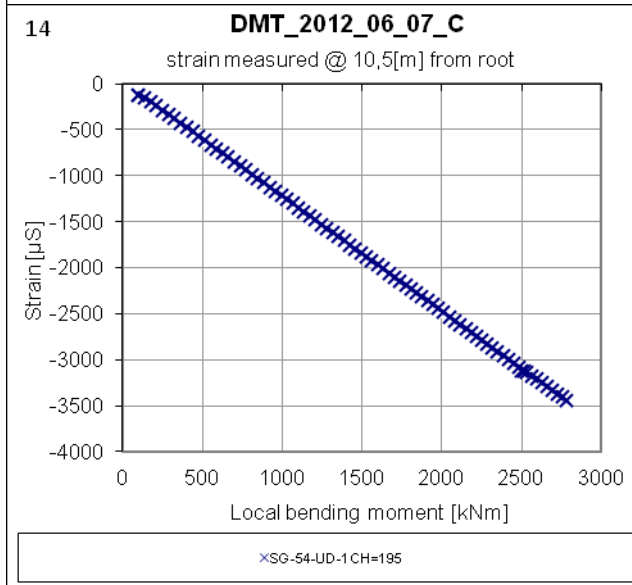
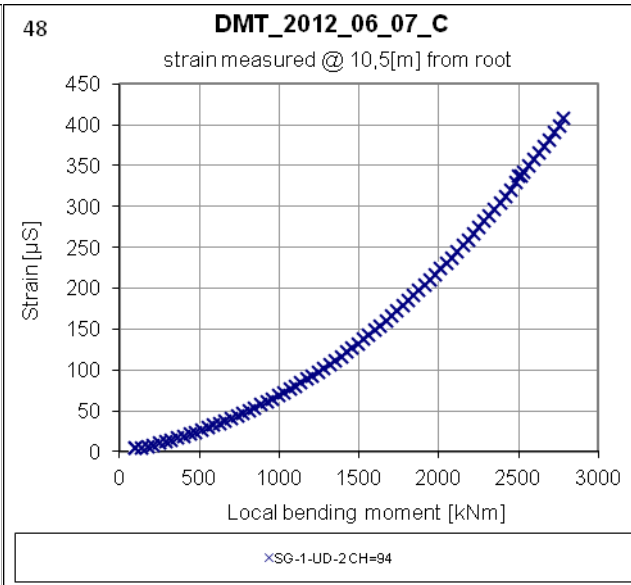
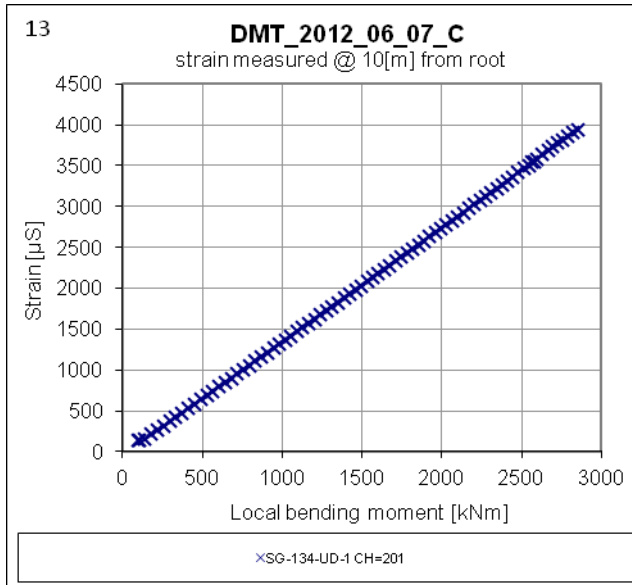
12

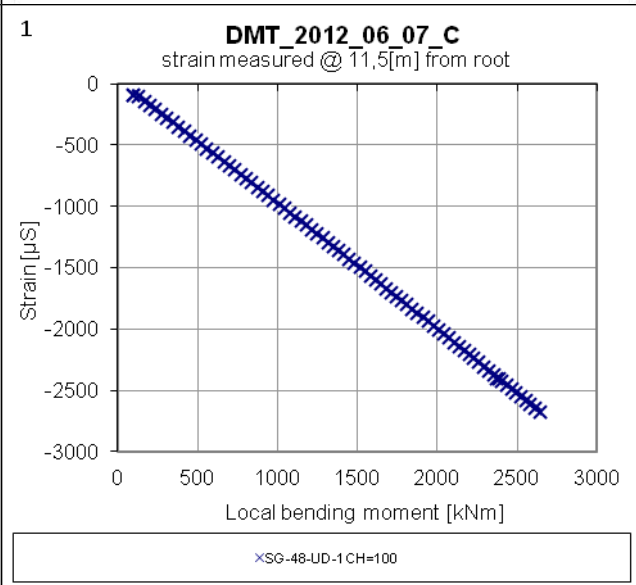
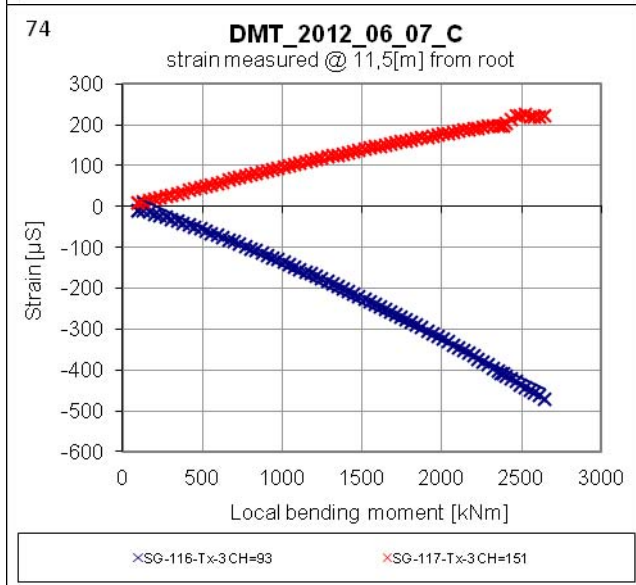
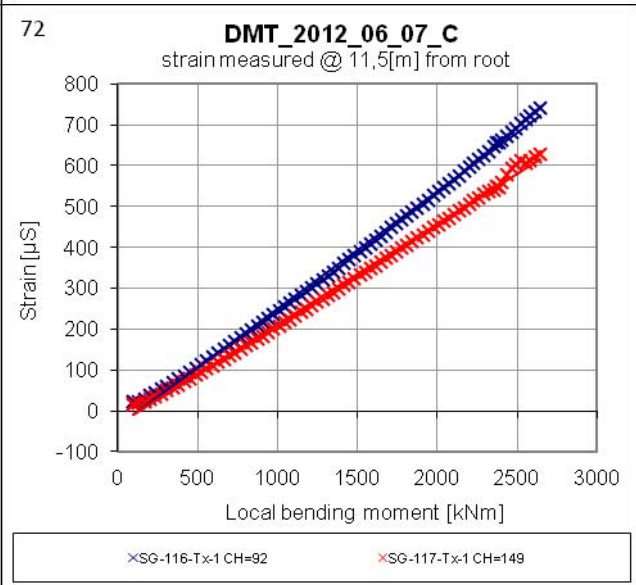
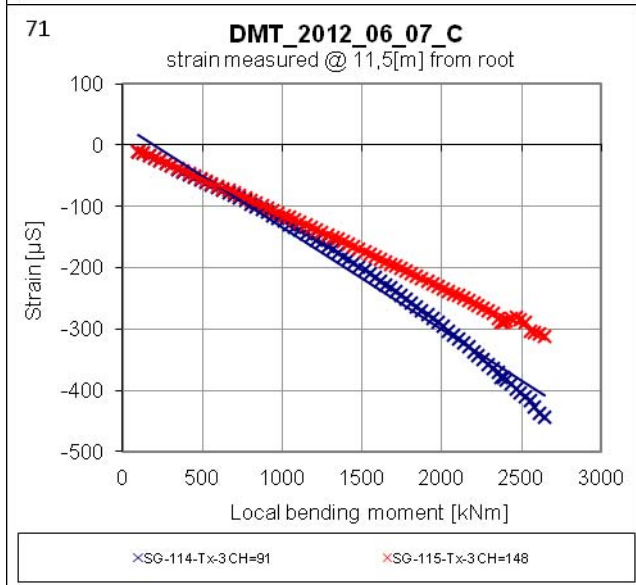
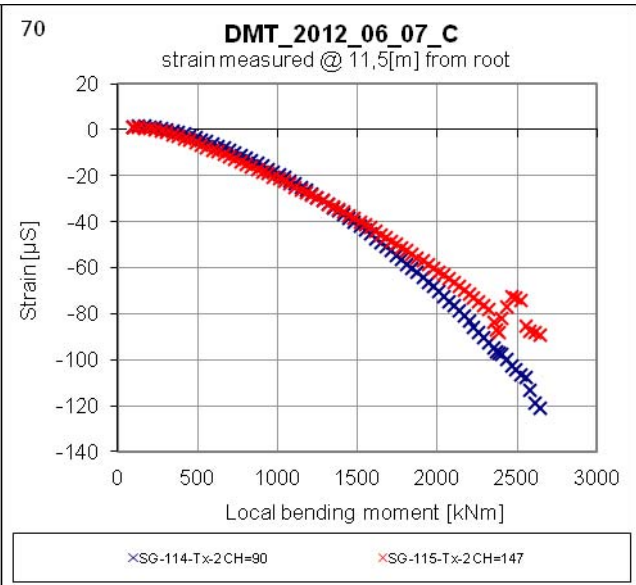
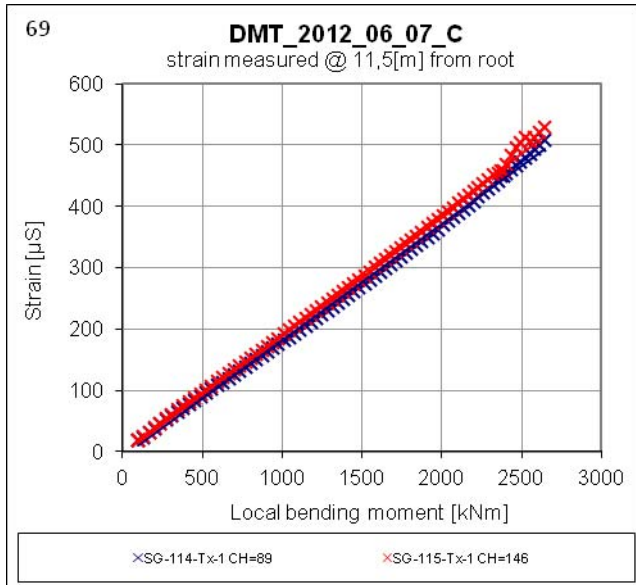
DMT_2012_06_07_C

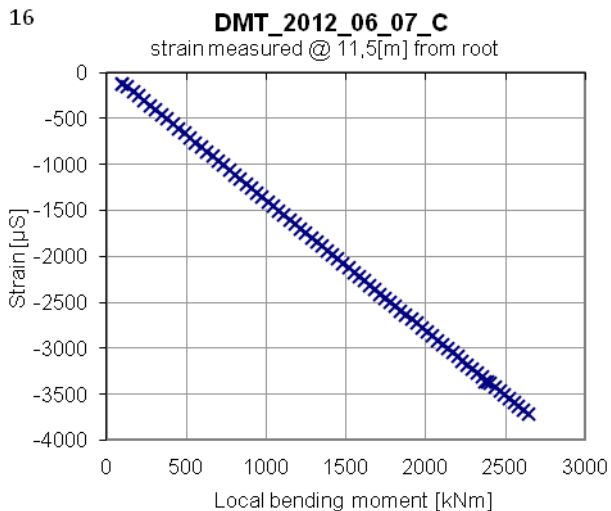
strain measured @ 10[m] from root



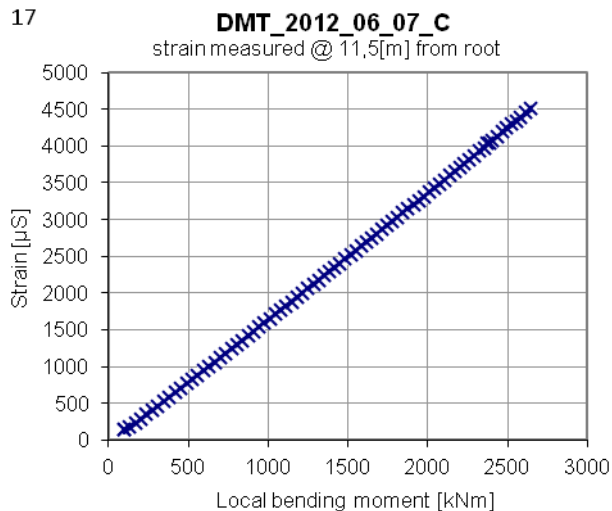
×SG-53-UD-1 CH=194



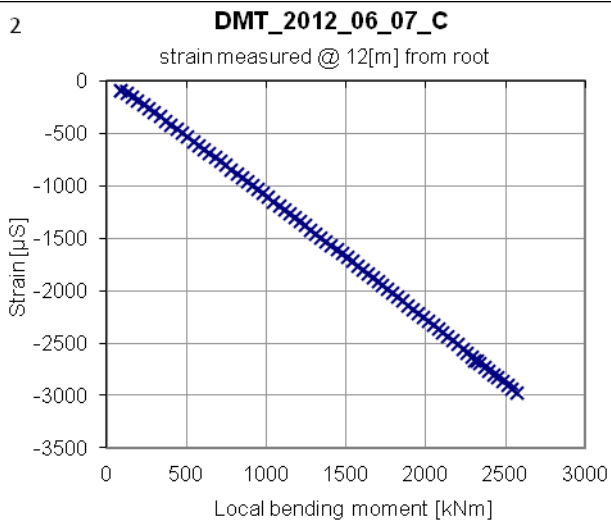




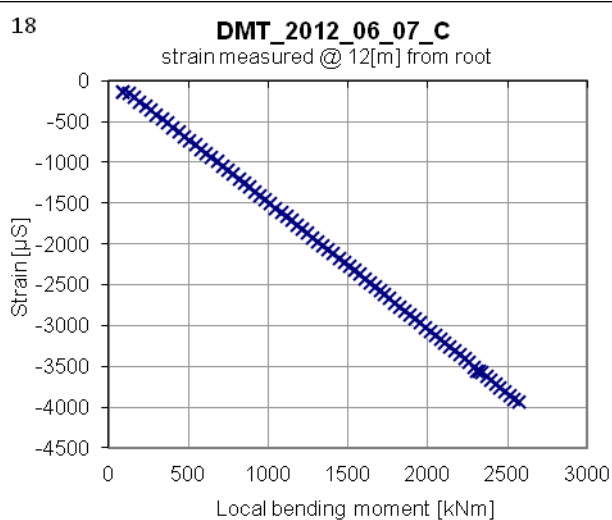
×SG-55-UD-1 CH=196



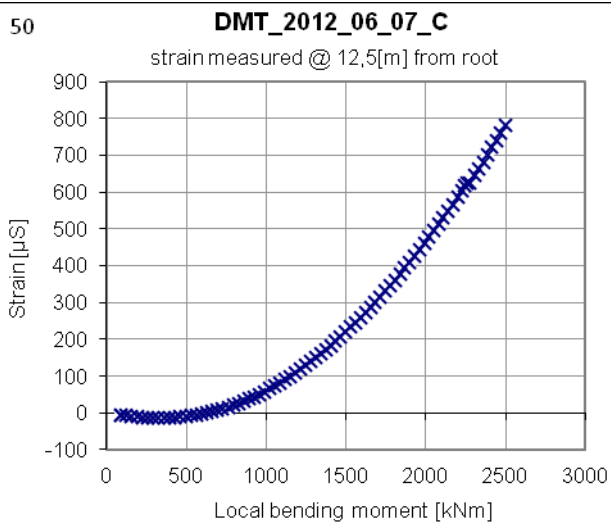
×SG-136-UD-1 CH=203



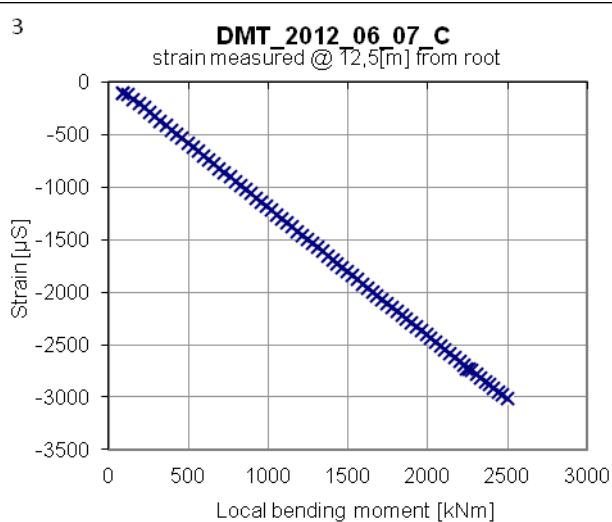
×SG-49-UD-1 CH=81



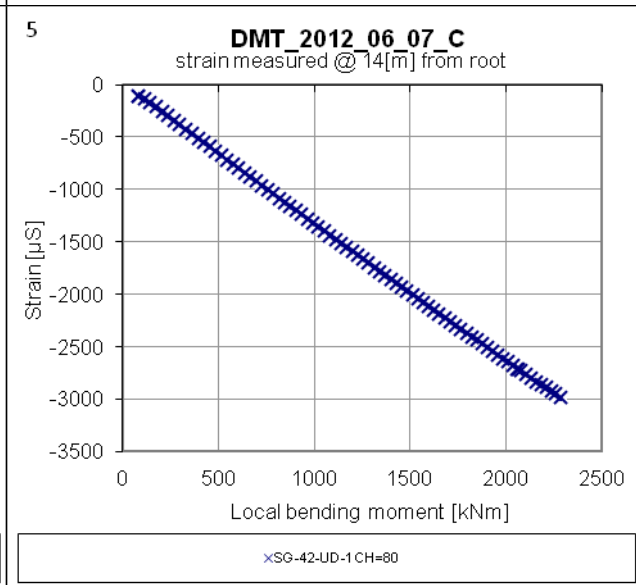
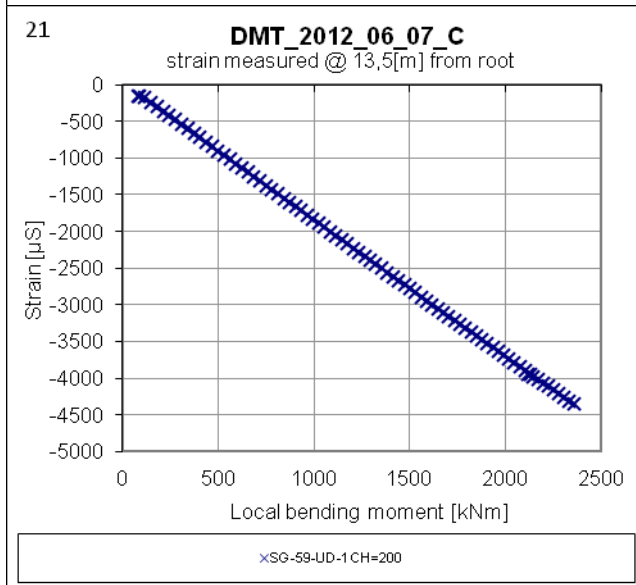
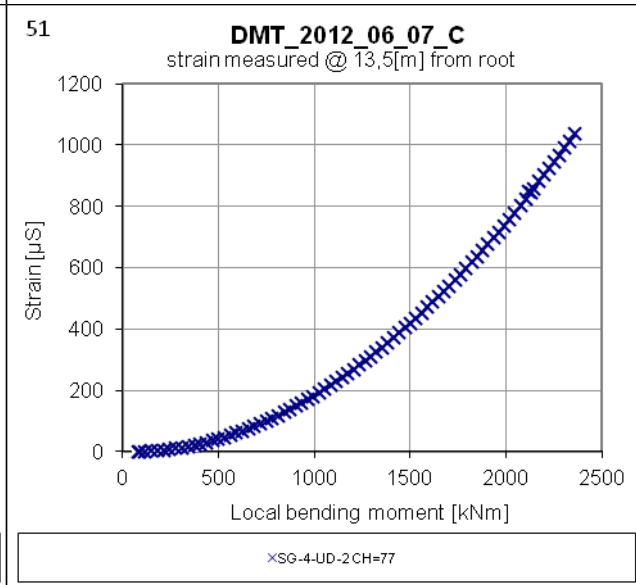
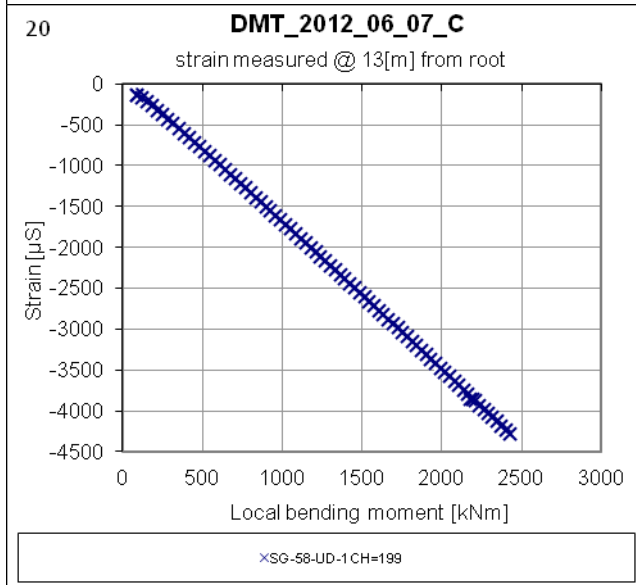
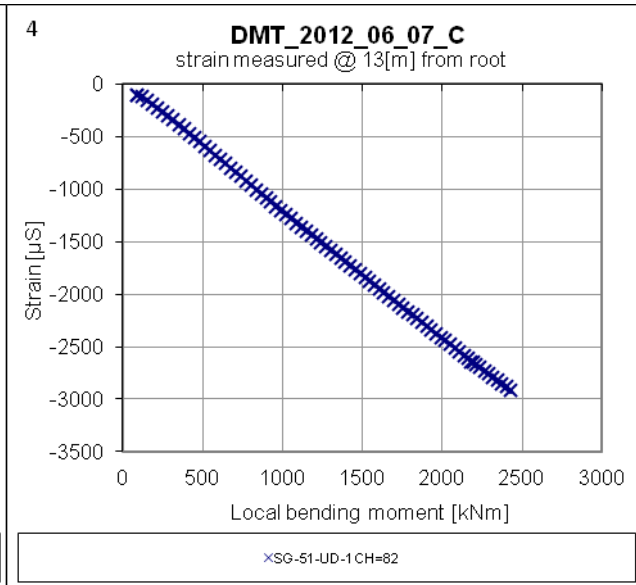
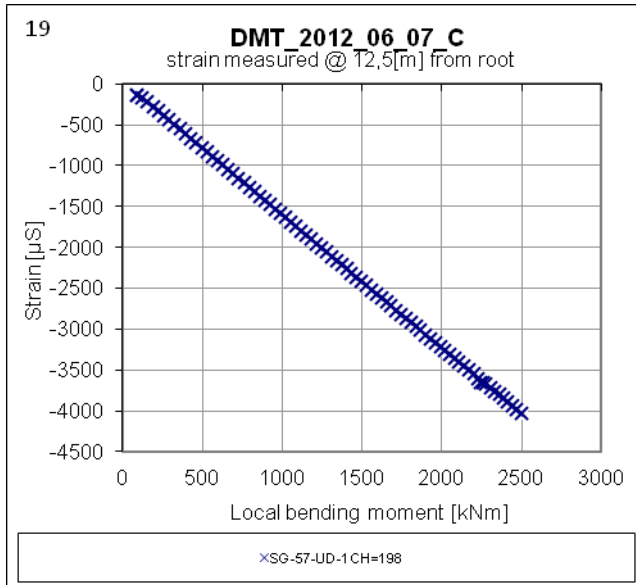
×SG-56-UD-1 CH=197

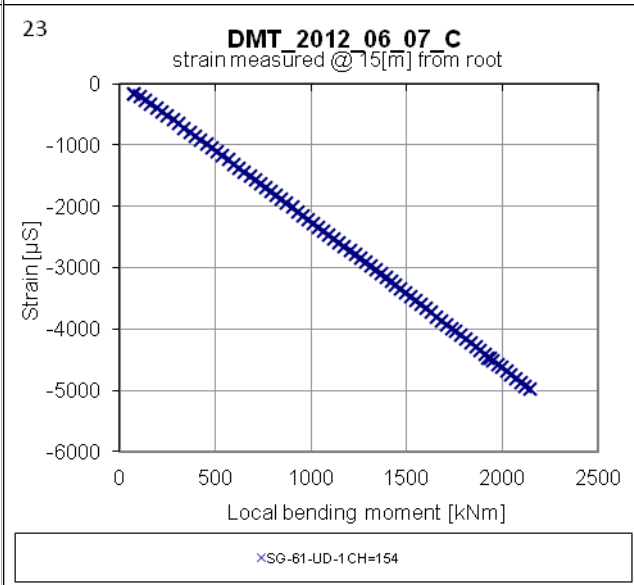
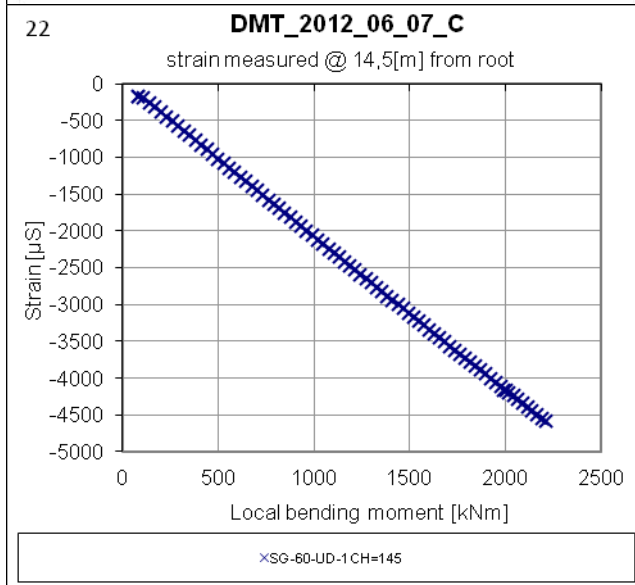
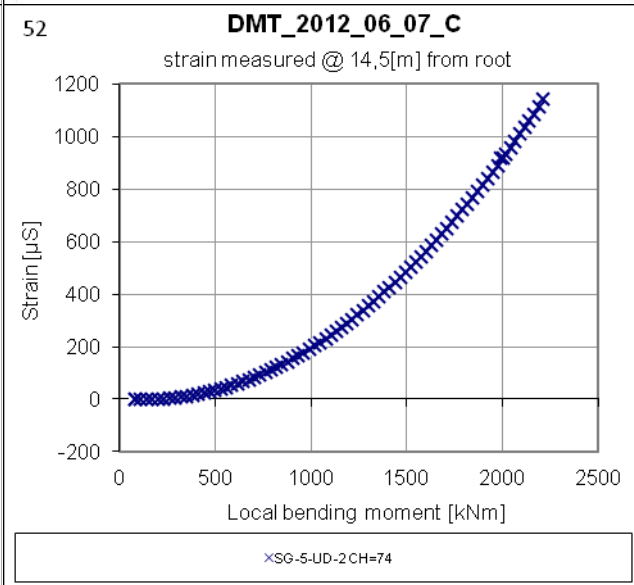
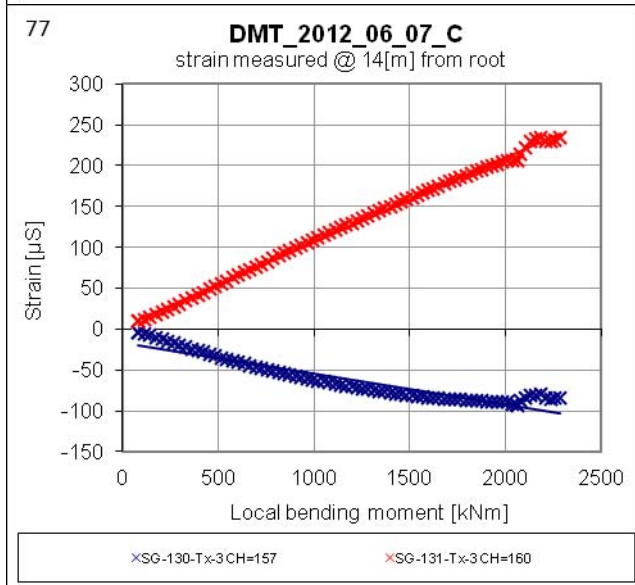
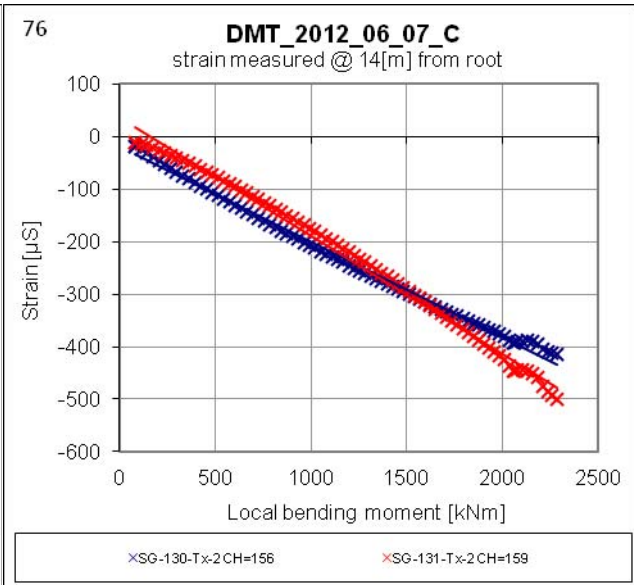
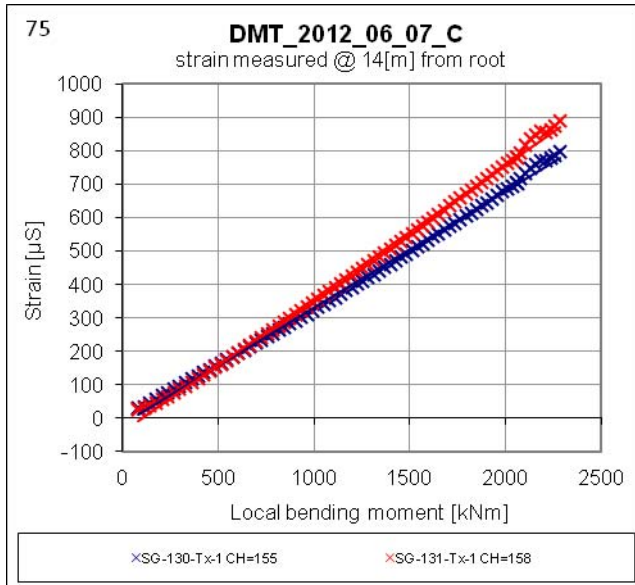


×SG-3-UD-2 CH=85



×SG-50-UD-1 CH=88

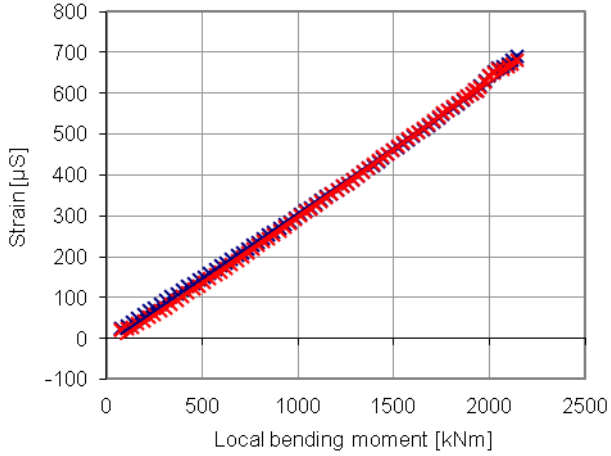




78

DMT_2012_06_07_C

strain measured @ 15[m] from root

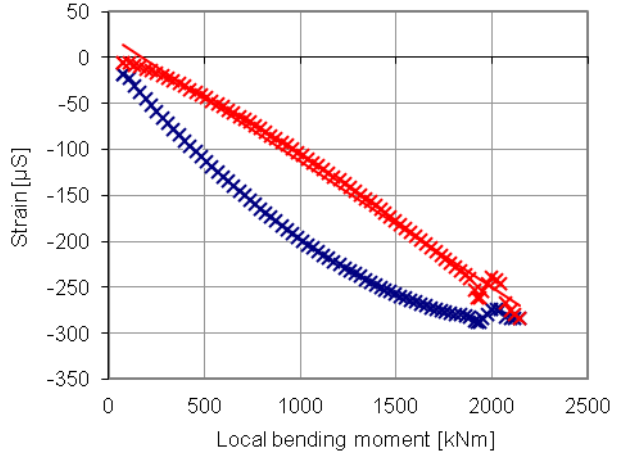


×SG-132-Tx-1 CH=161 ×SG-133-Tx-1 CH=212

79

DMT_2012_06_07_C

strain measured @ 15[m] from root

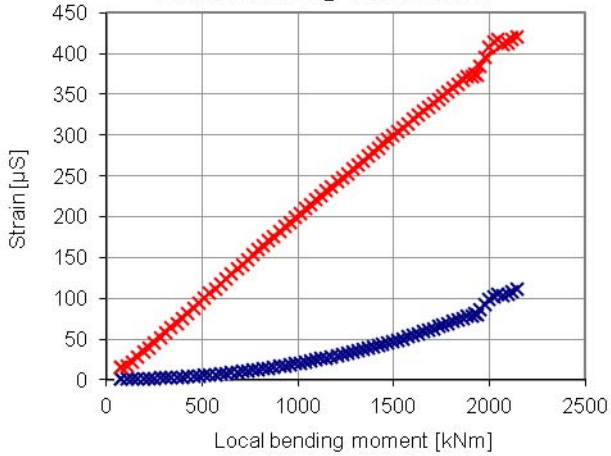


×SG-132-Tx-2 CH=162 ×SG-133-Tx-2_skal_repareres CH=171

80

DMT_2012_06_07_C

strain measured @ 15[m] from root

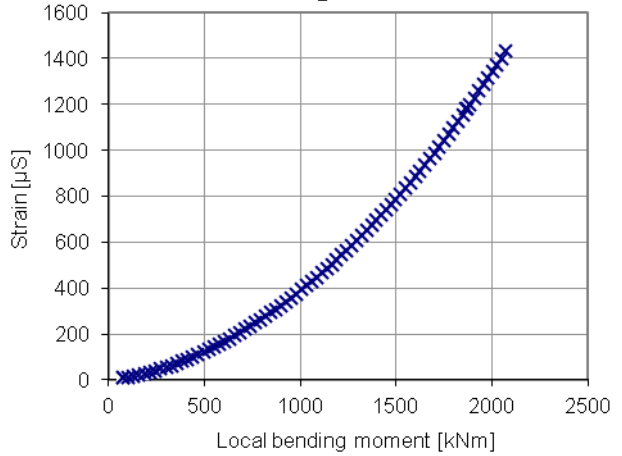


×SG-132-Tx-3 CH=163 ×SG-133-Tx-3 CH=213

53

DMT_2012_06_07_C

strain measured @ 15,5[m] from root

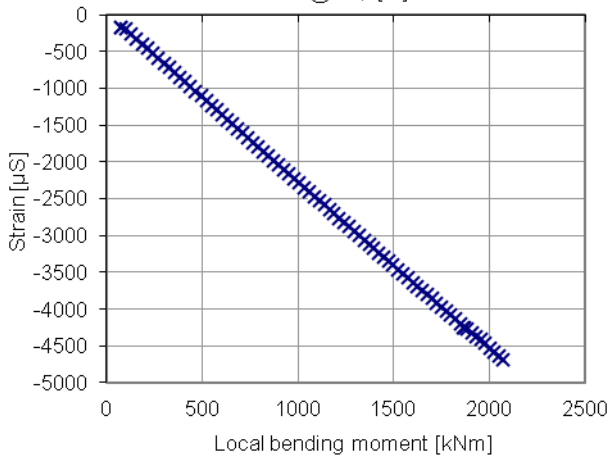


×SG-6-UD-2 CH=64

24

DMT_2012_06_07_C

strain measured @ 15,5[m] from root

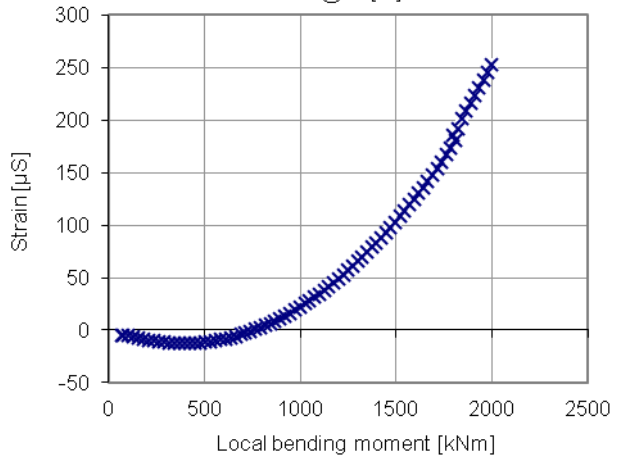


×SG-62-UD-1 CH=164

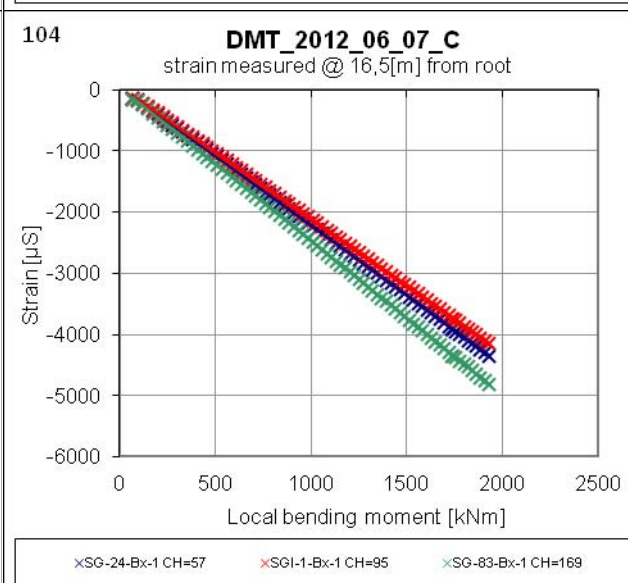
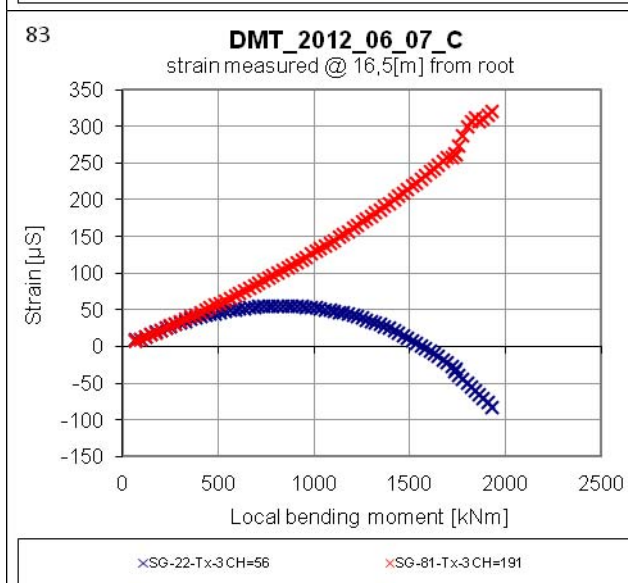
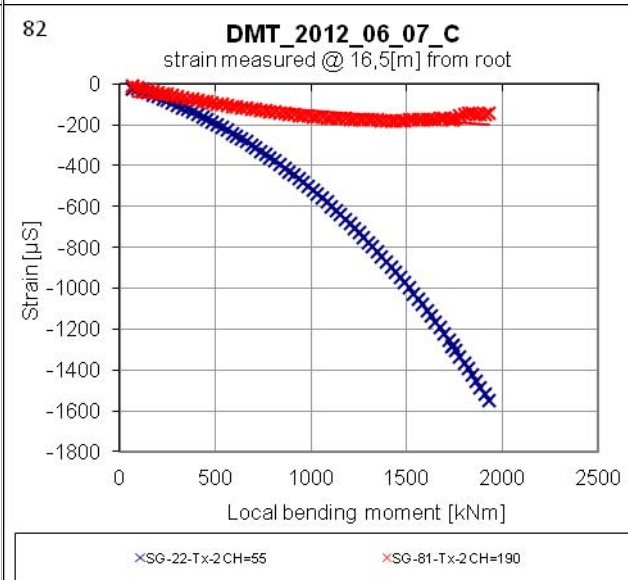
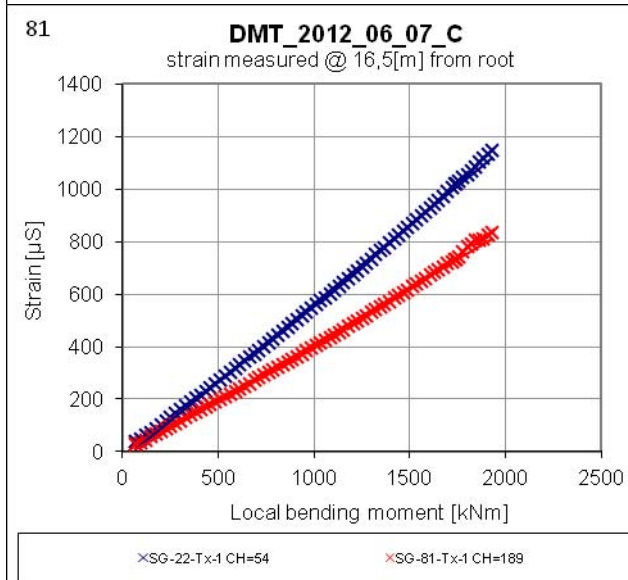
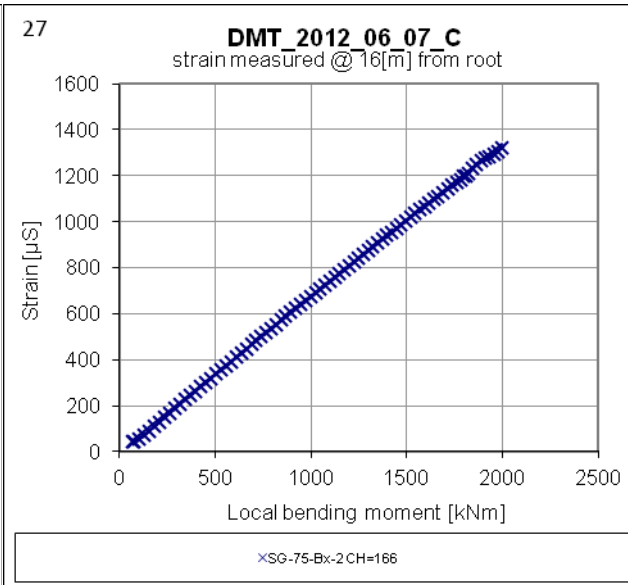
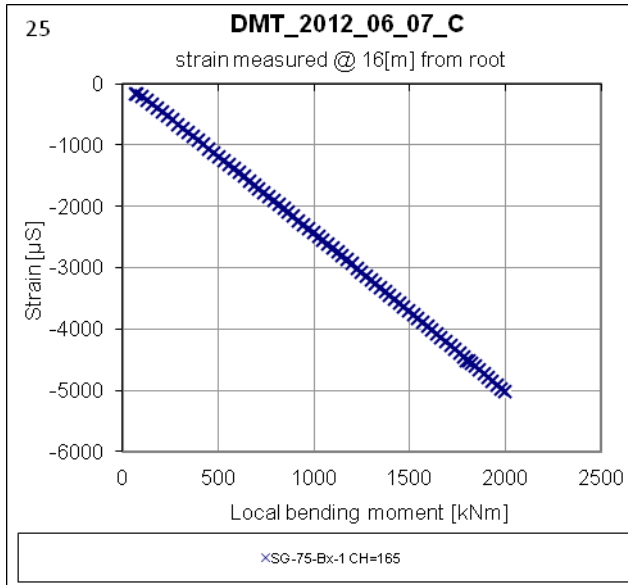
67

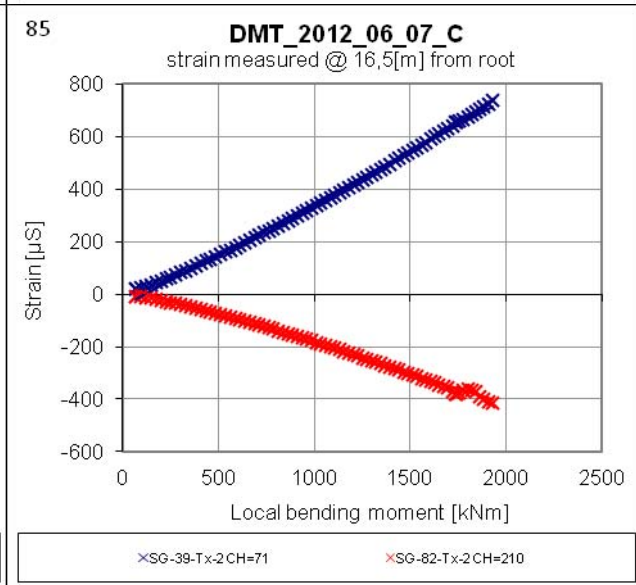
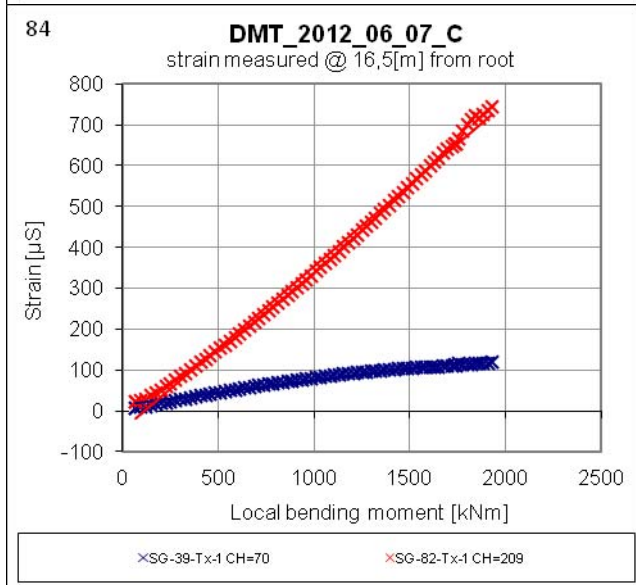
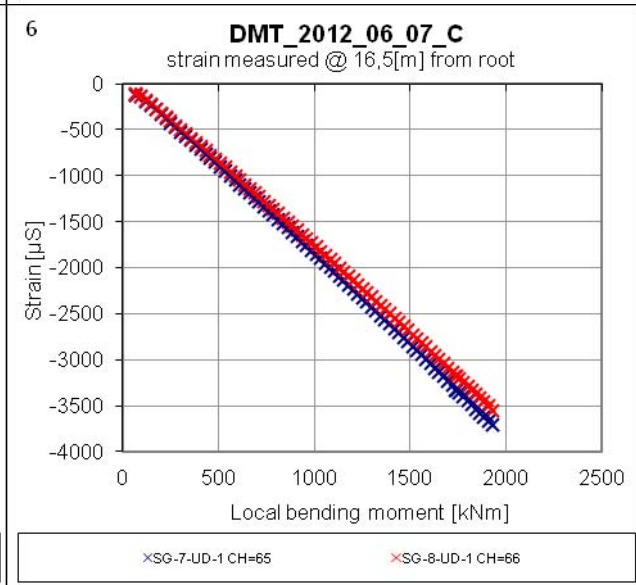
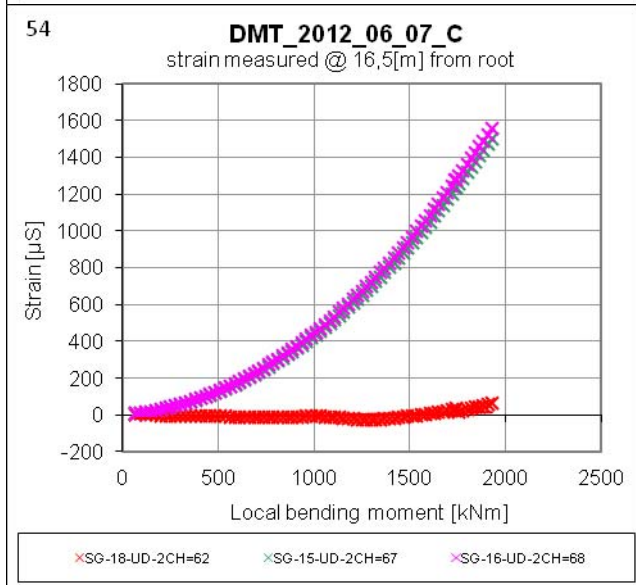
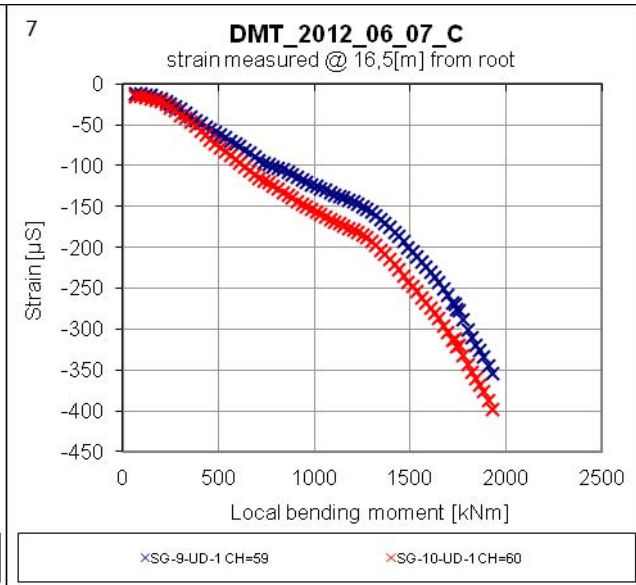
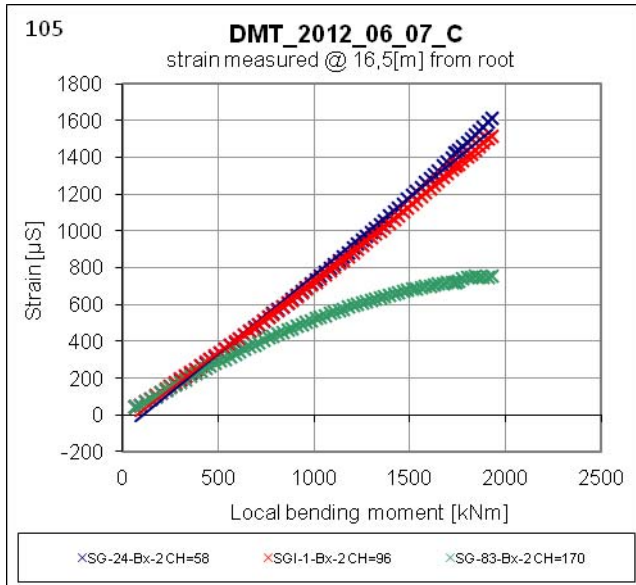
DMT_2012_06_07_C

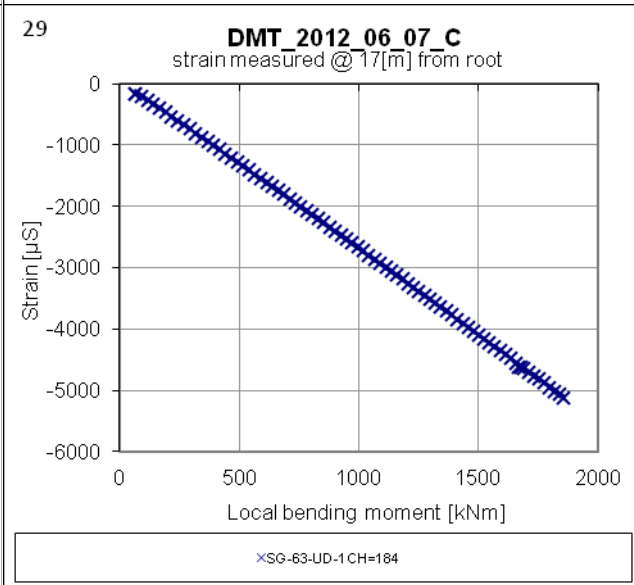
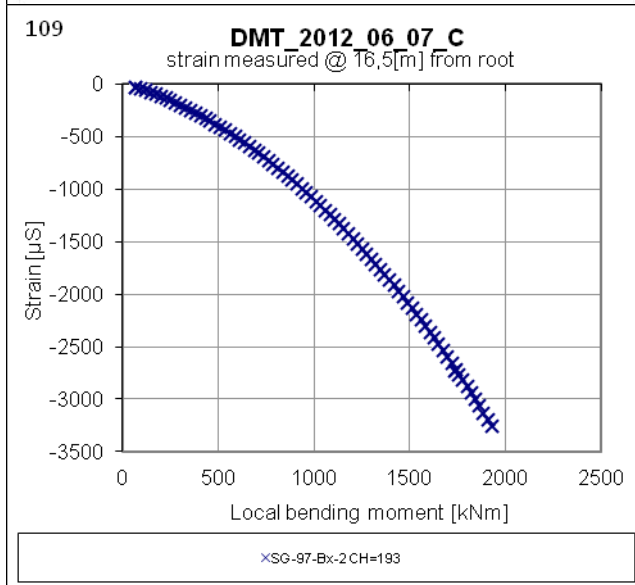
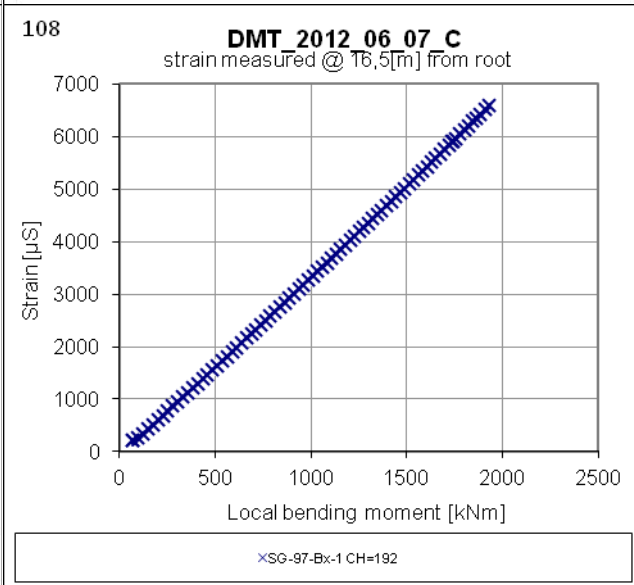
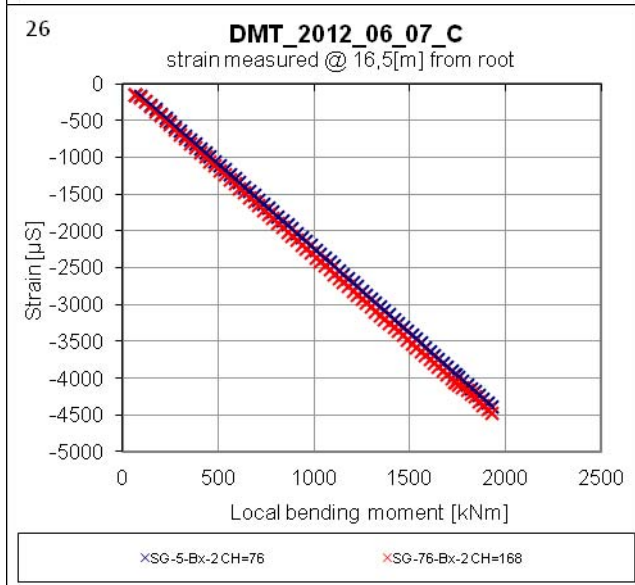
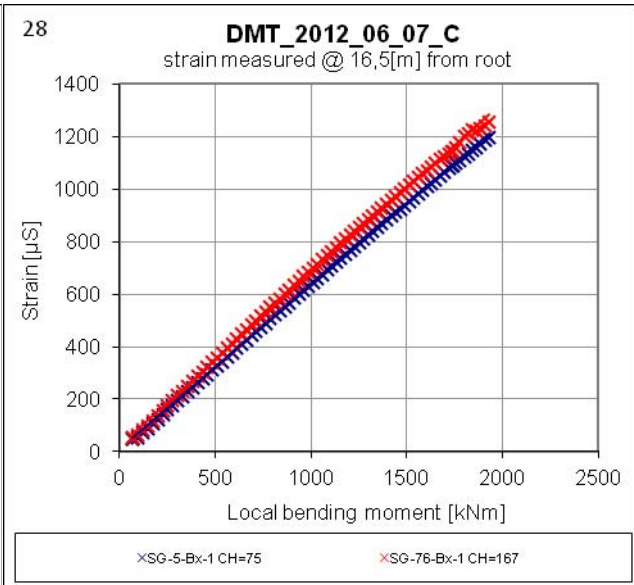
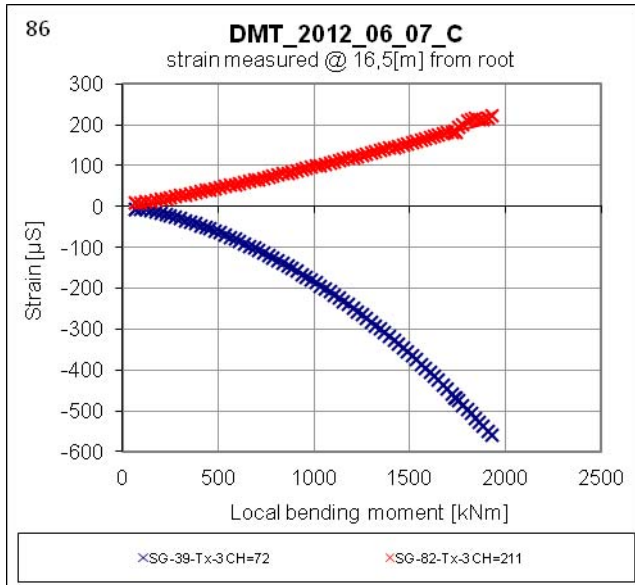
strain measured @ 16[m] from root

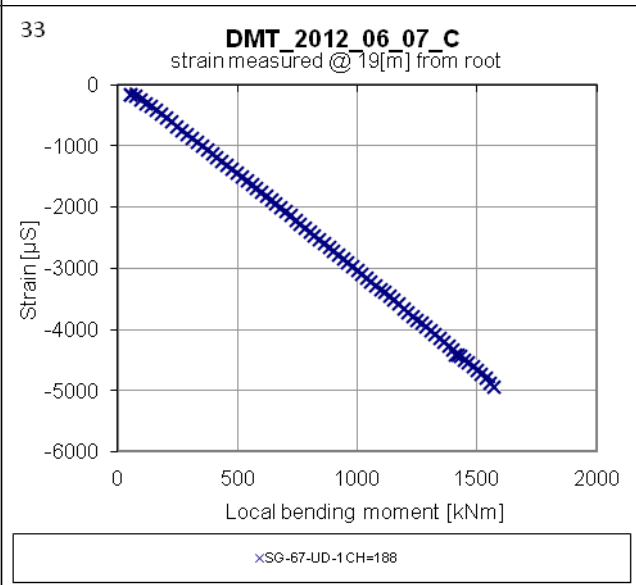
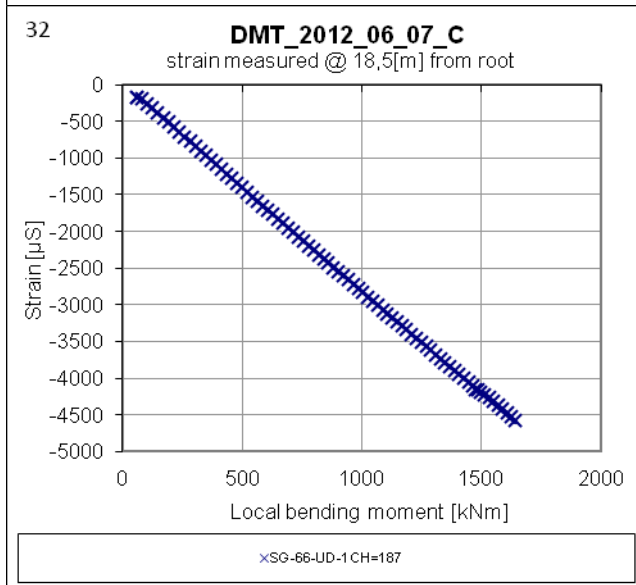
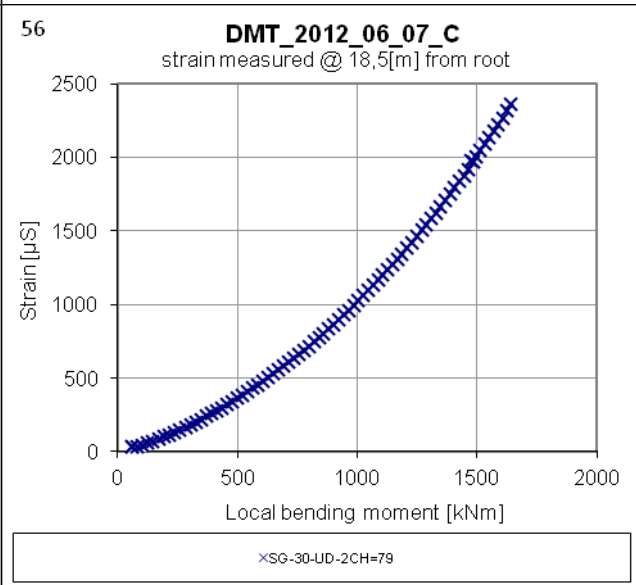
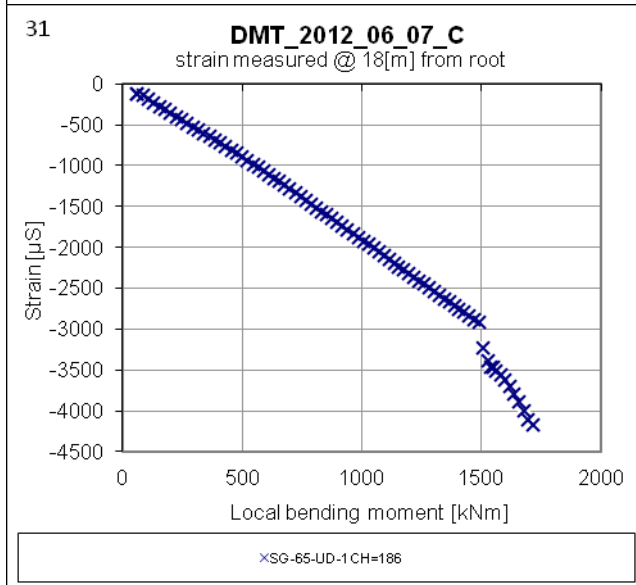
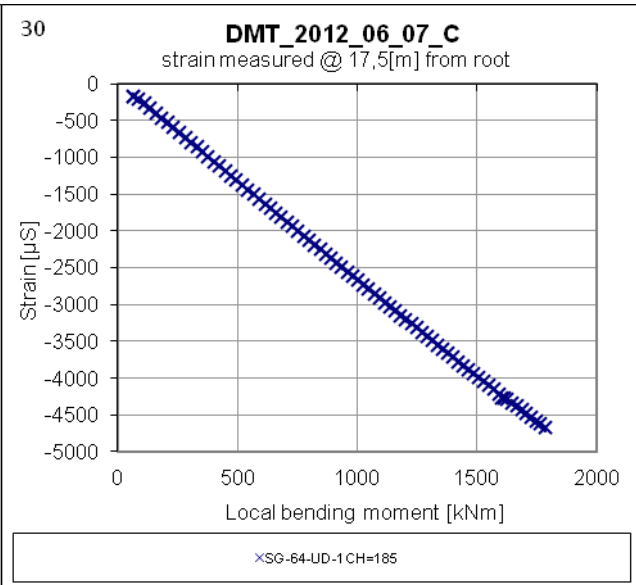
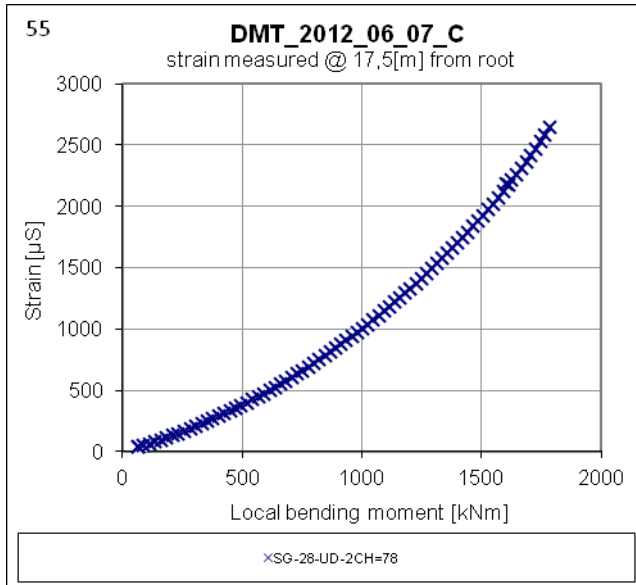


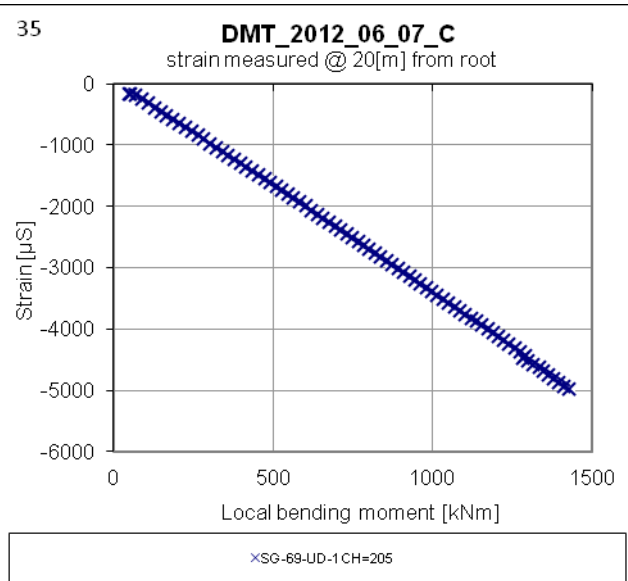
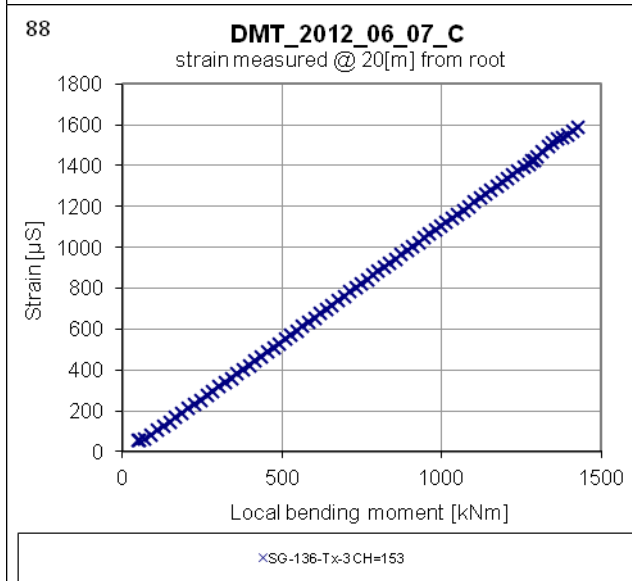
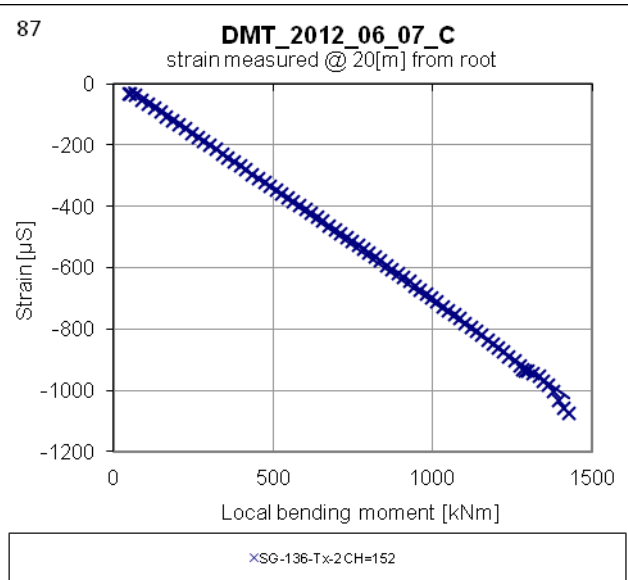
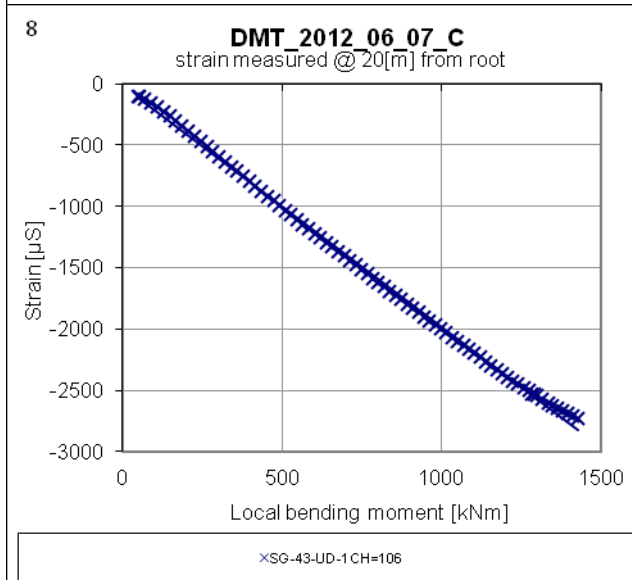
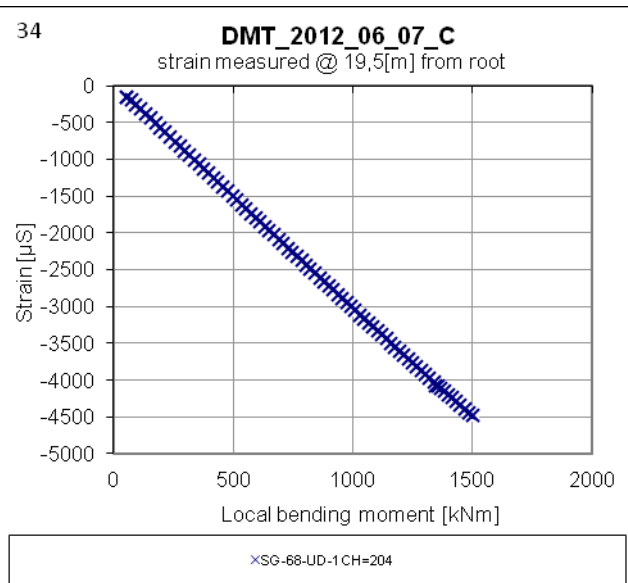
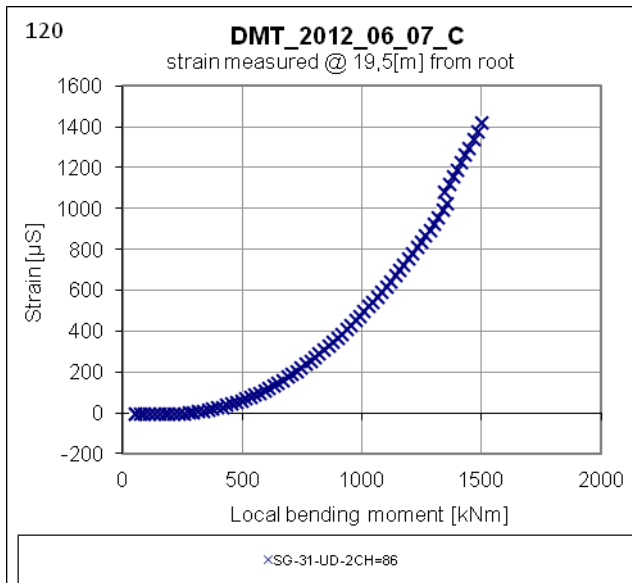
×SG-26-UD-2 CH=69

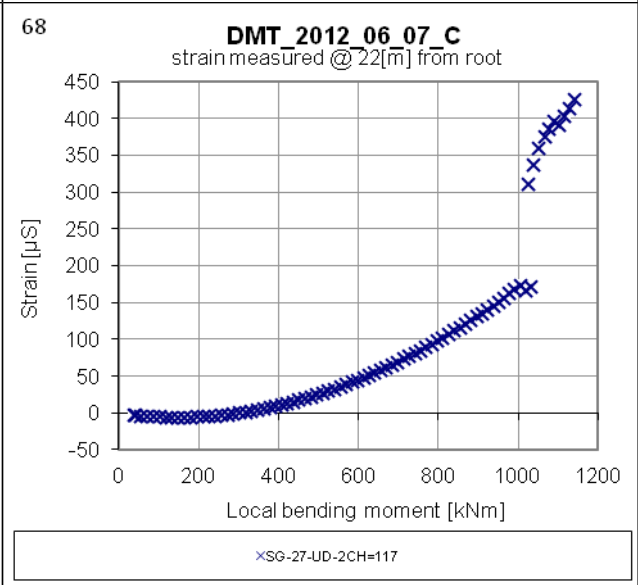
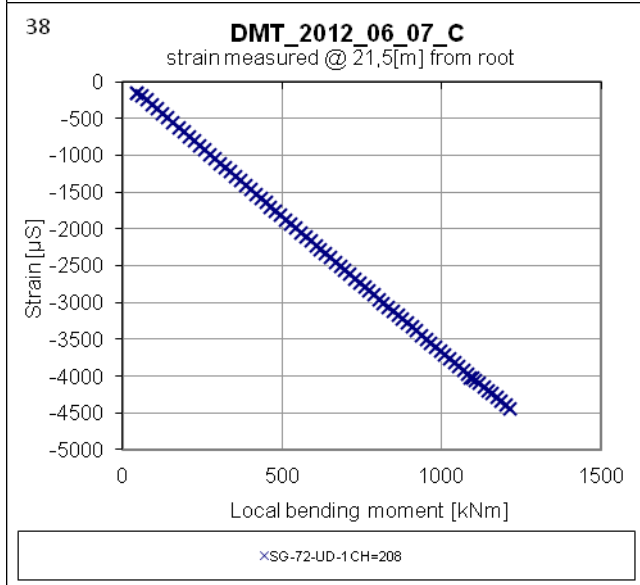
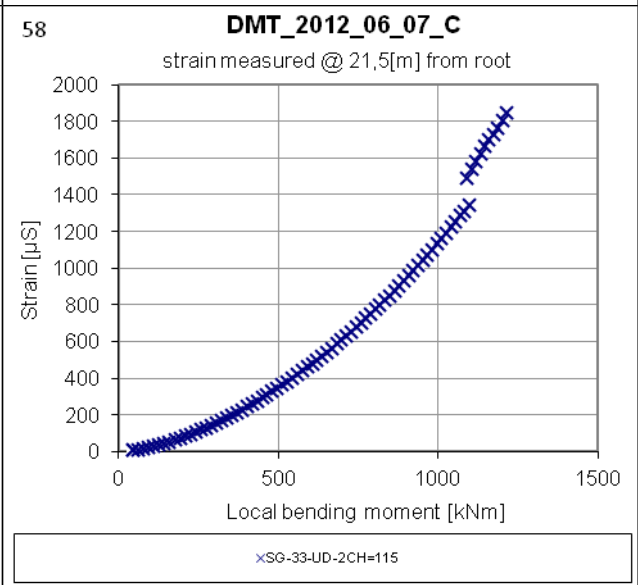
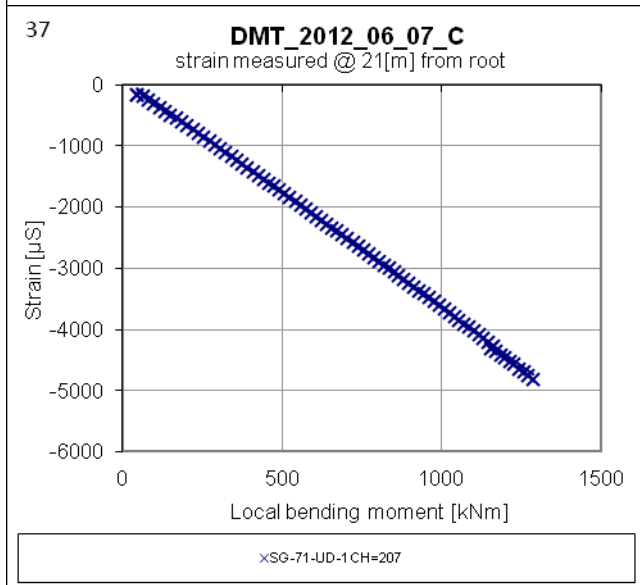
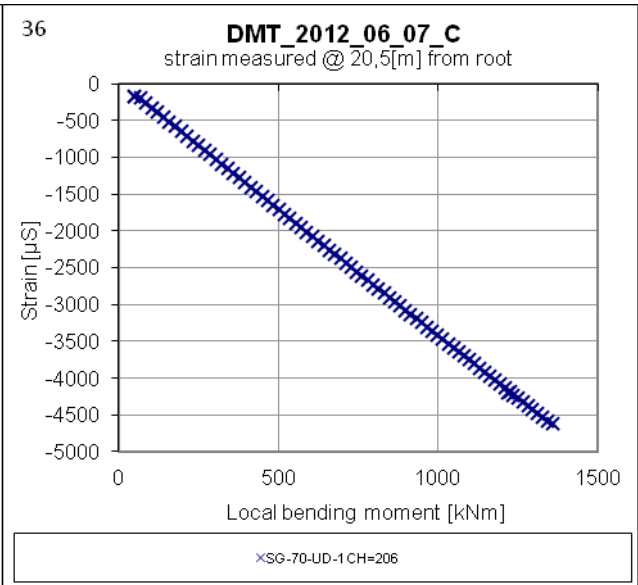
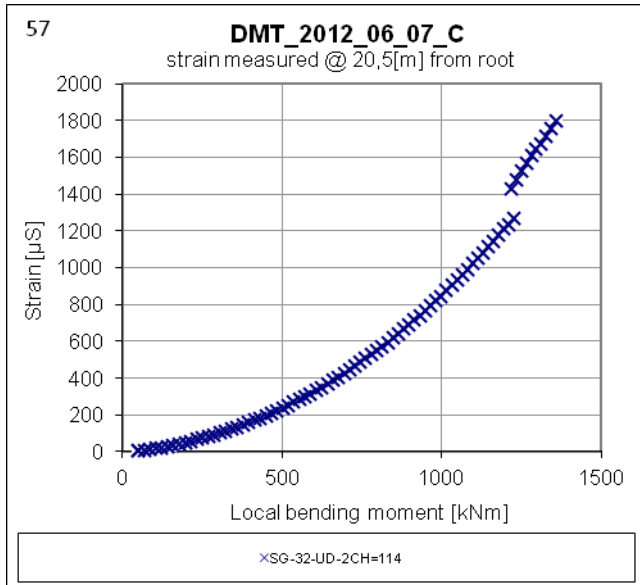


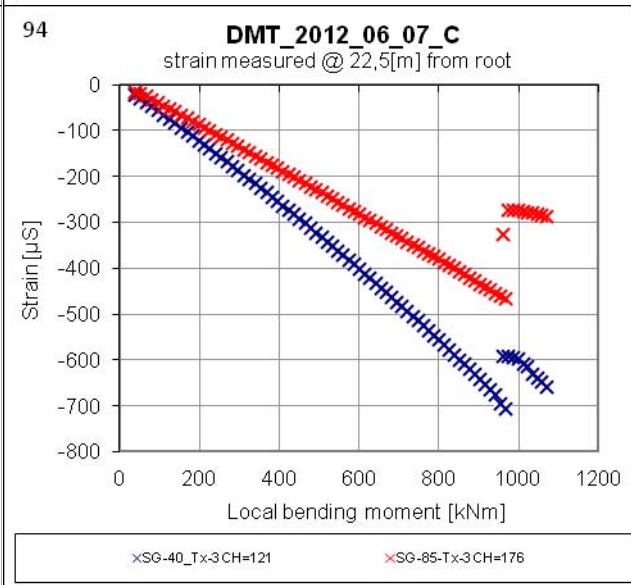
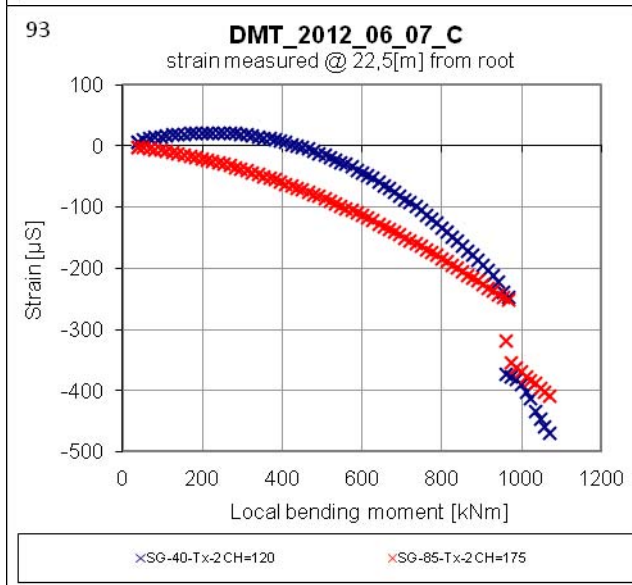
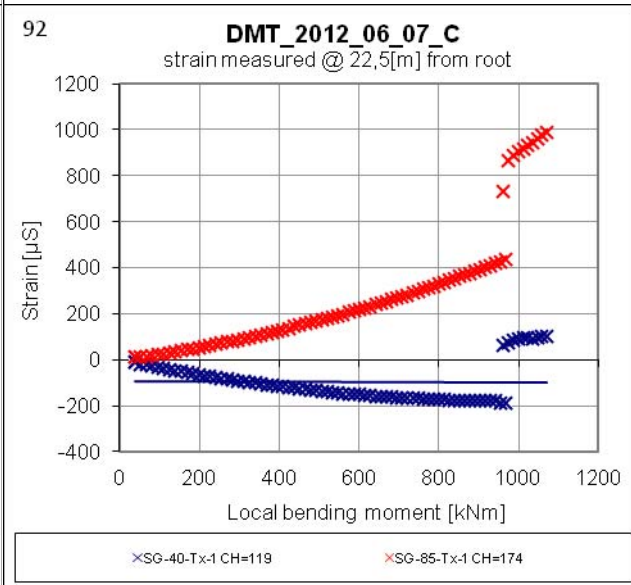
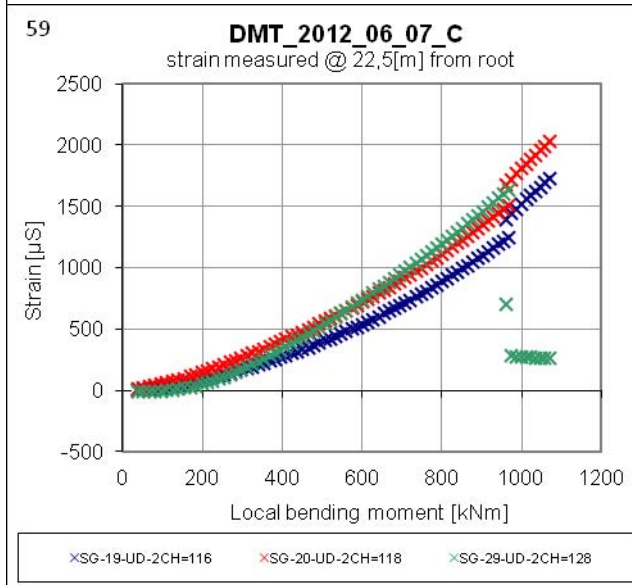
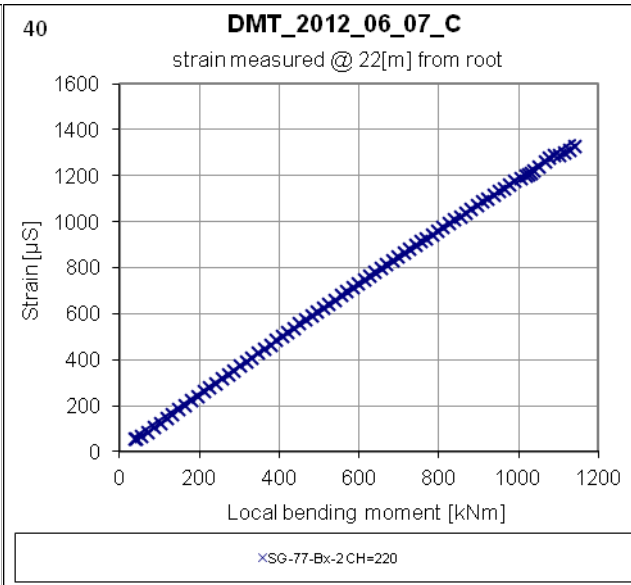
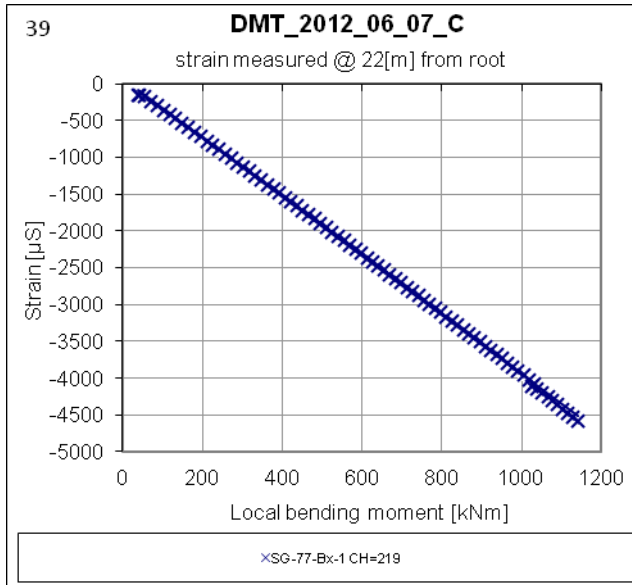


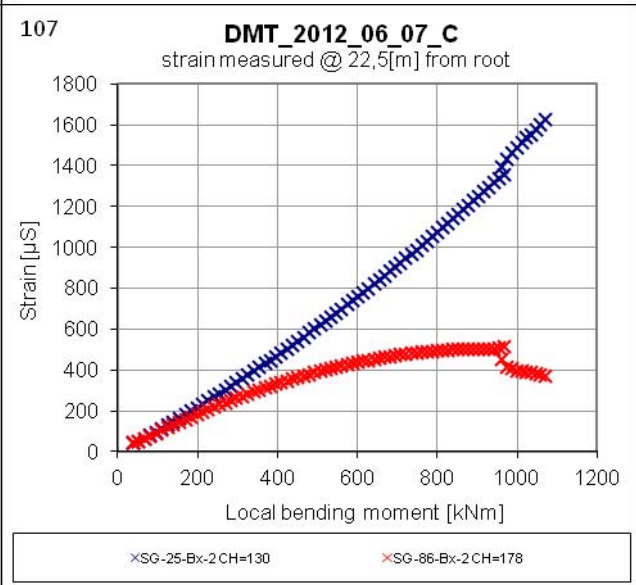
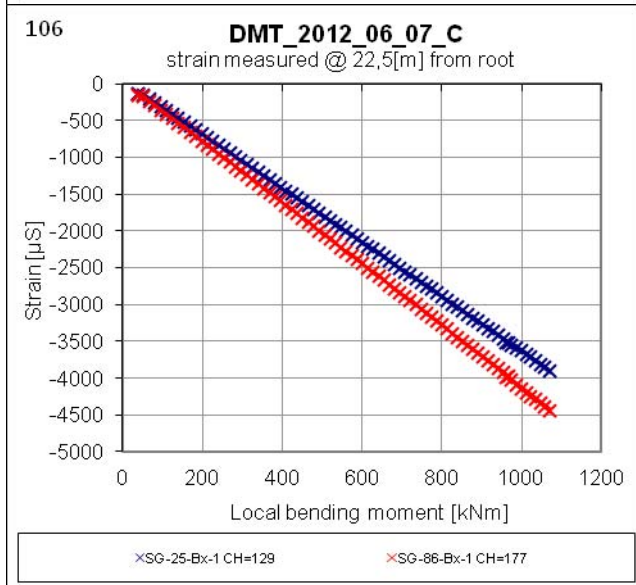
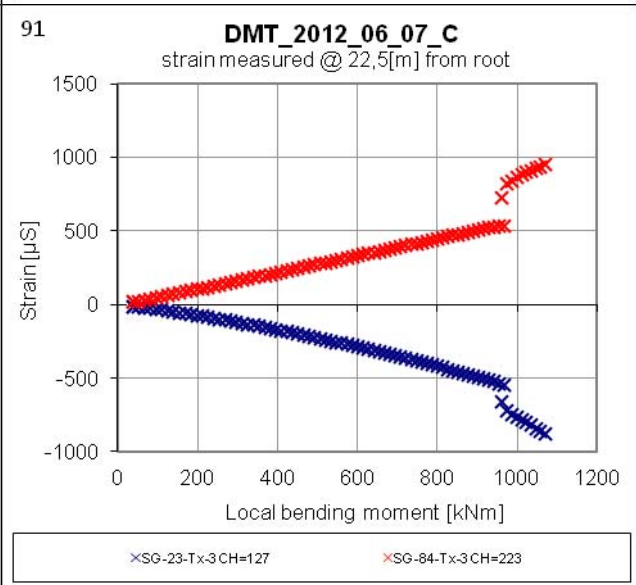
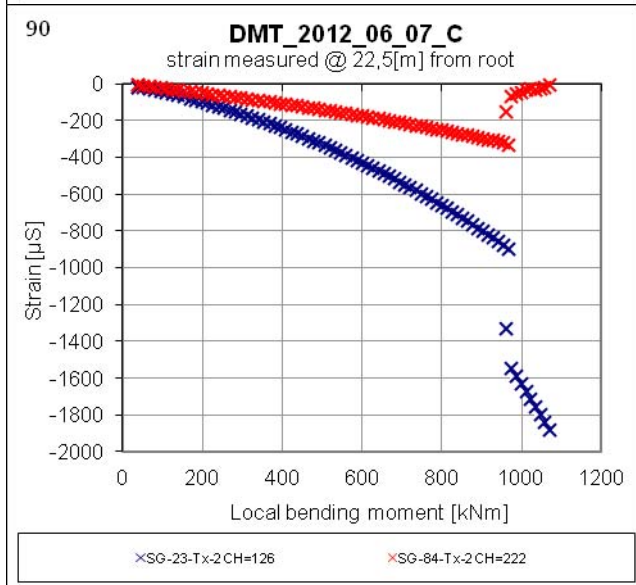
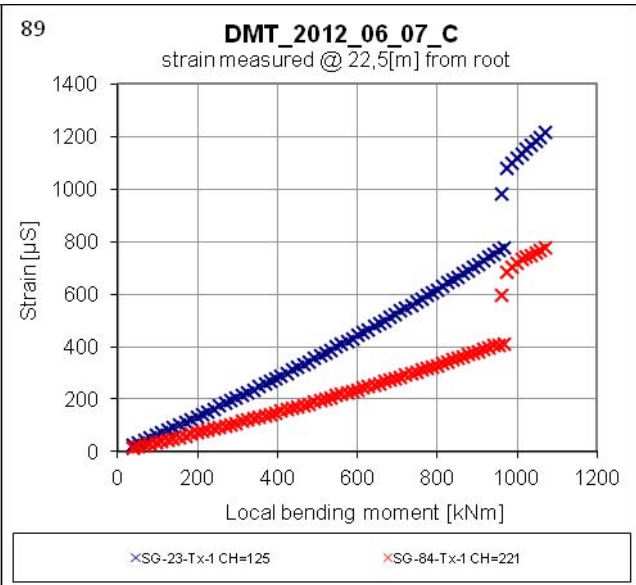
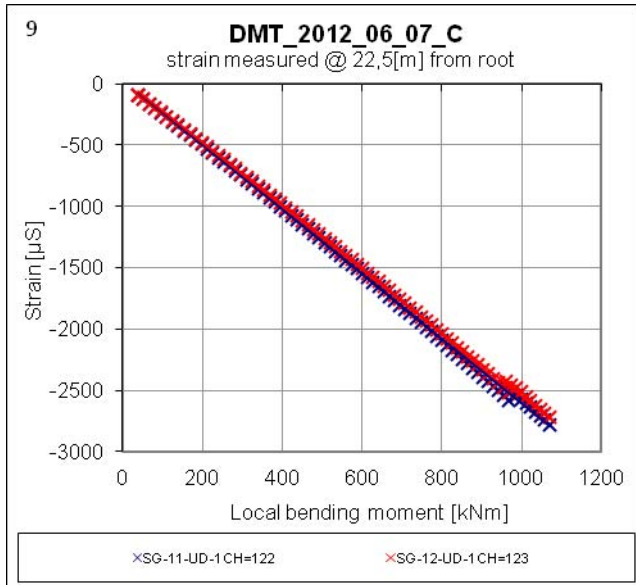


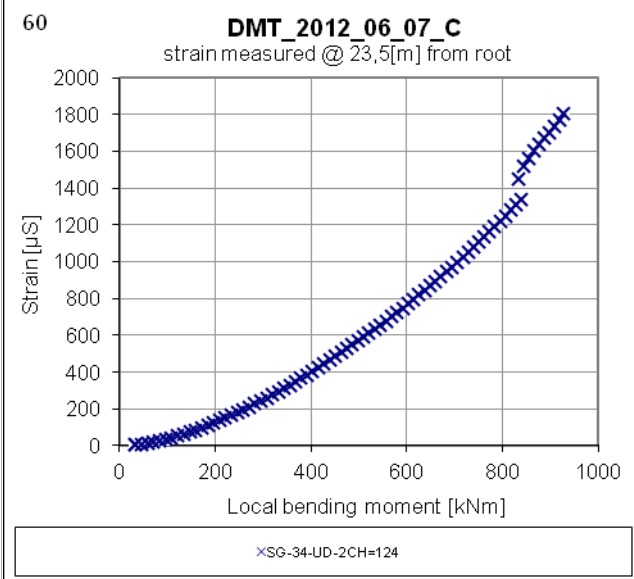
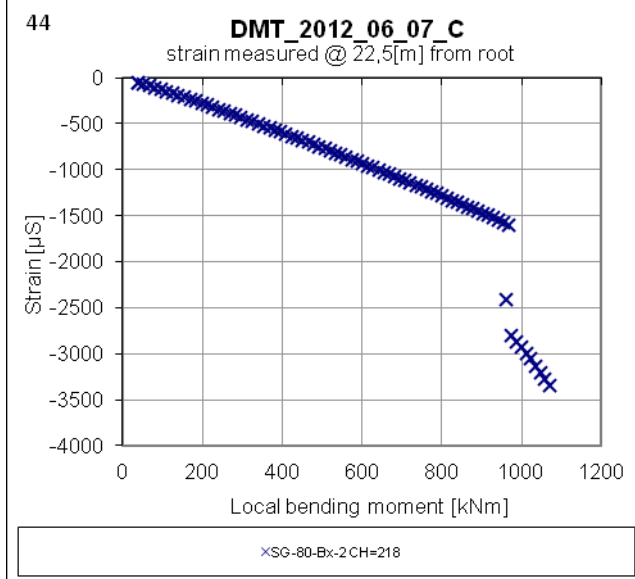
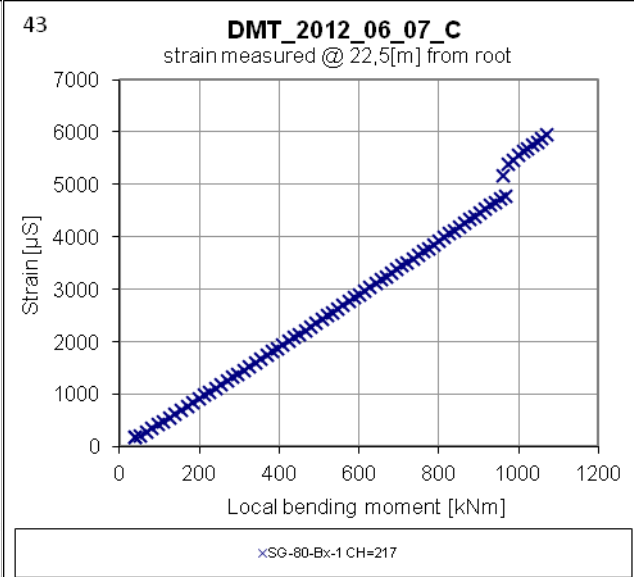
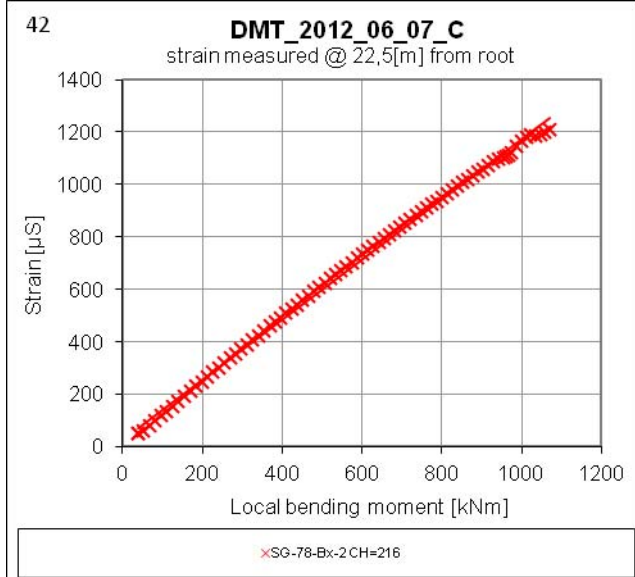
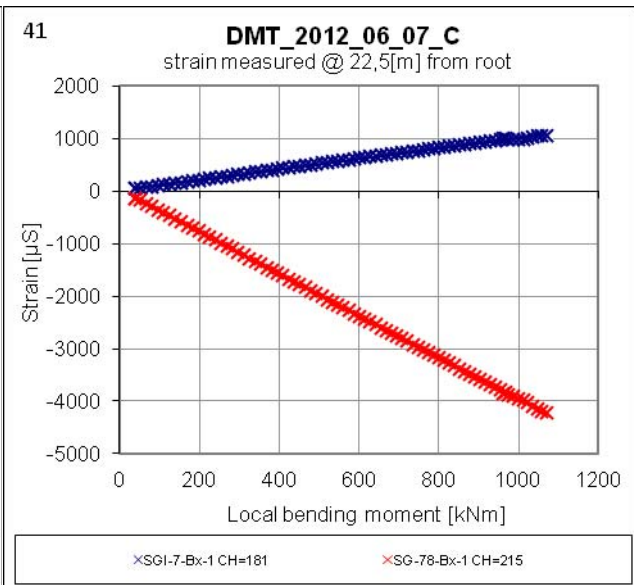
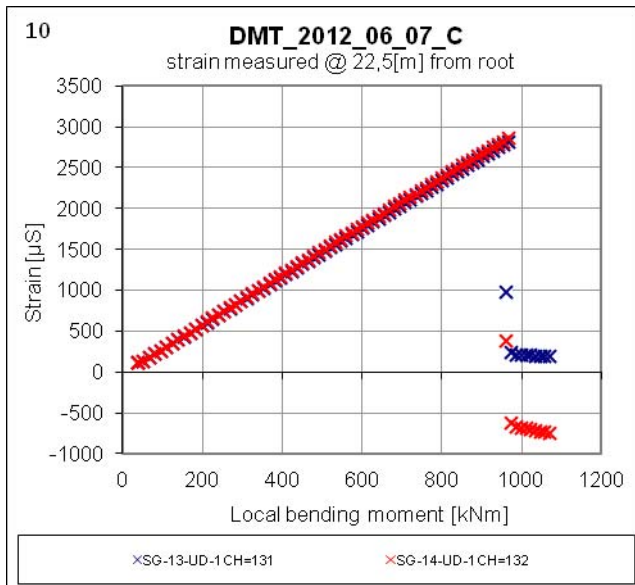


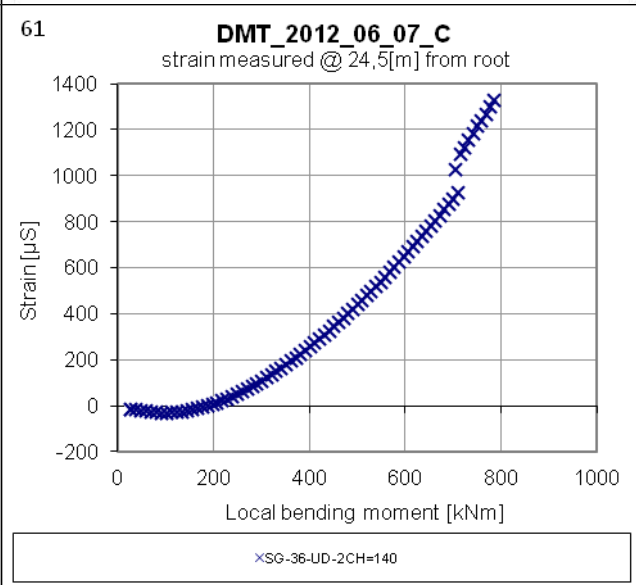
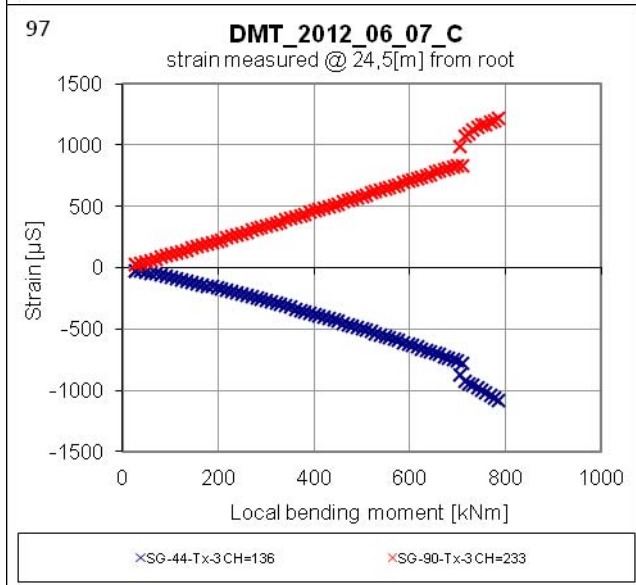
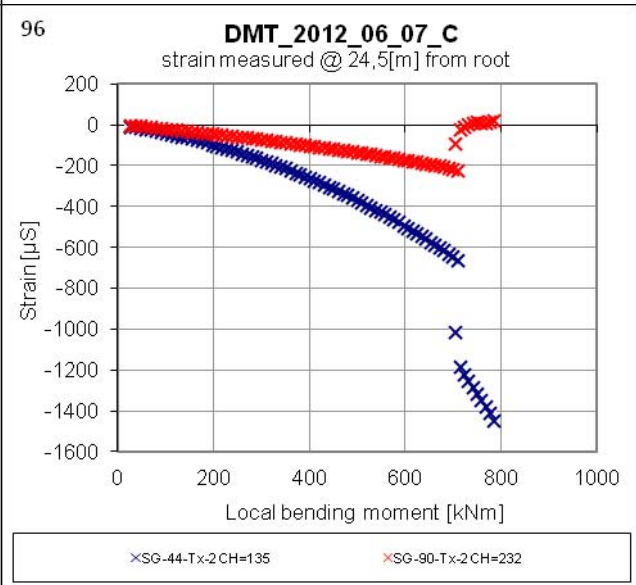
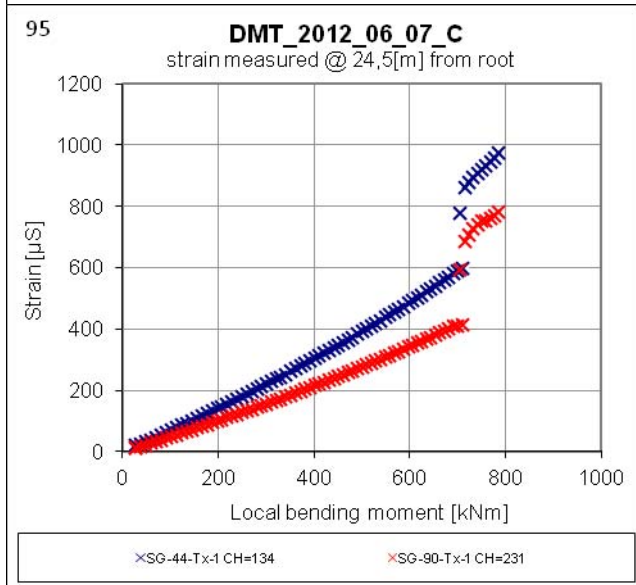
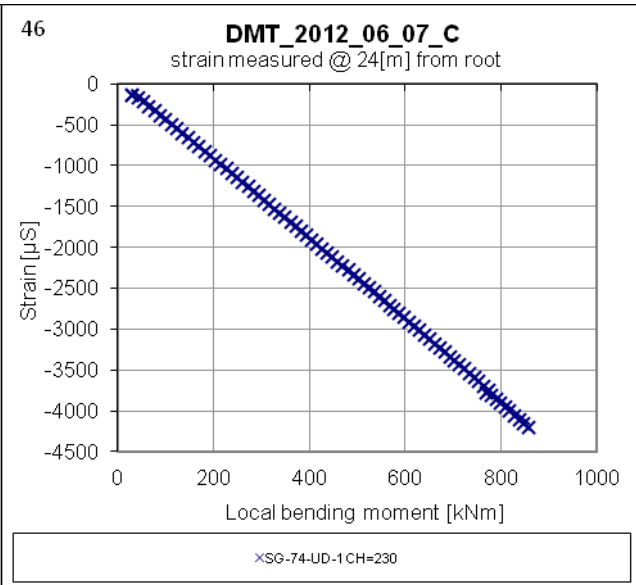
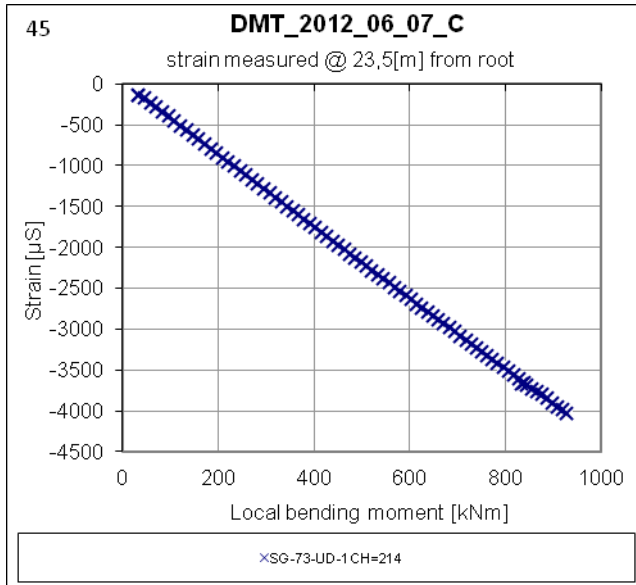


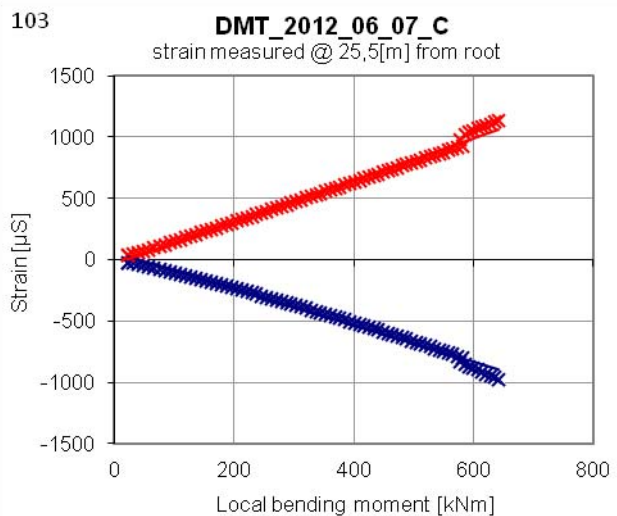
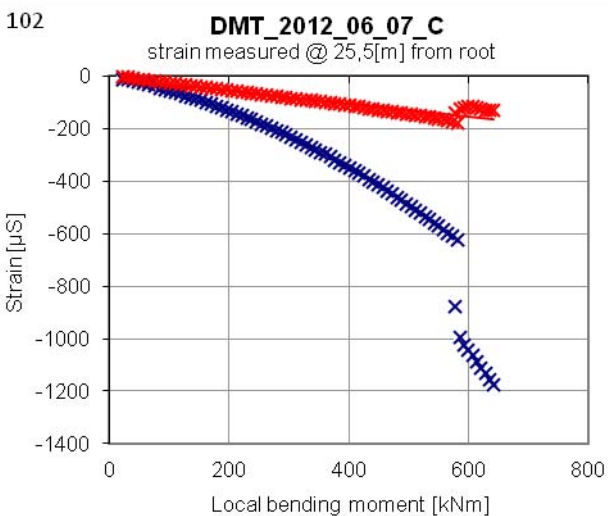
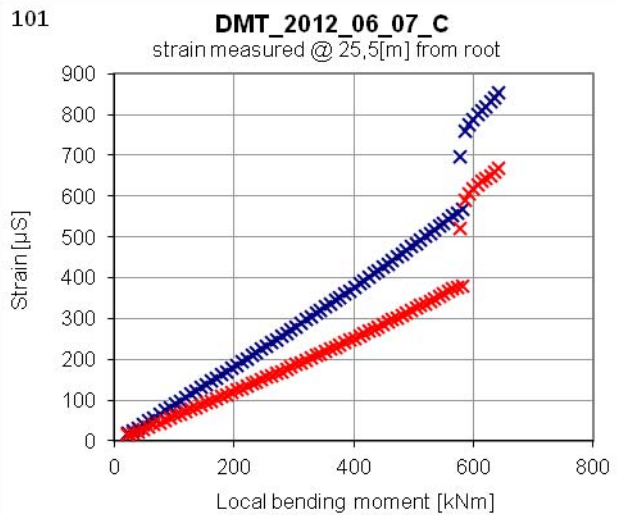
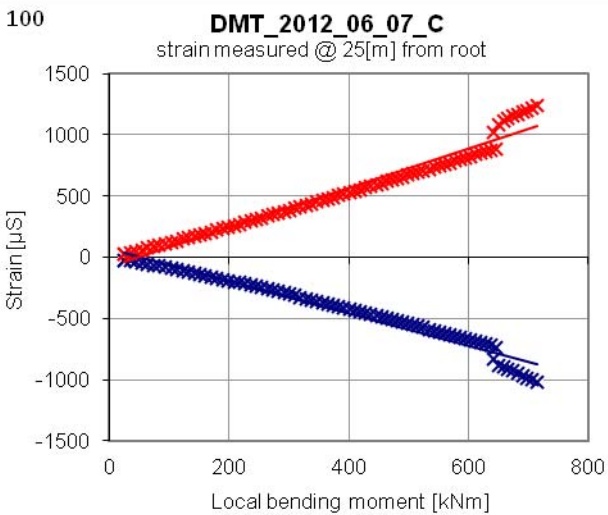
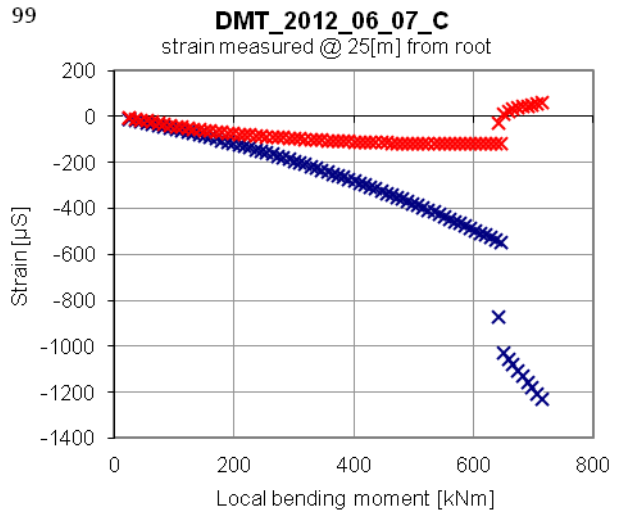
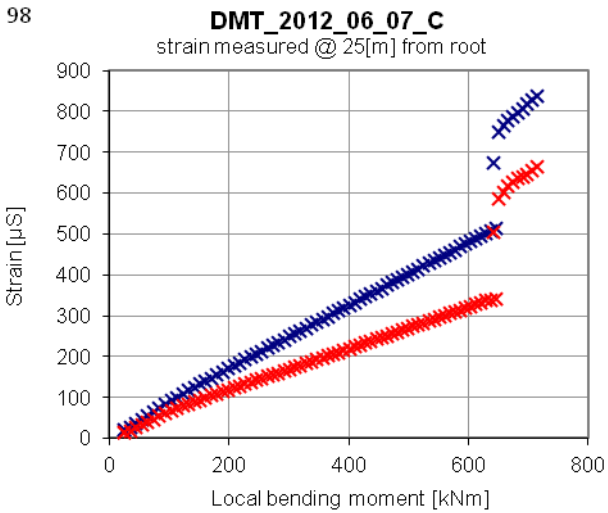


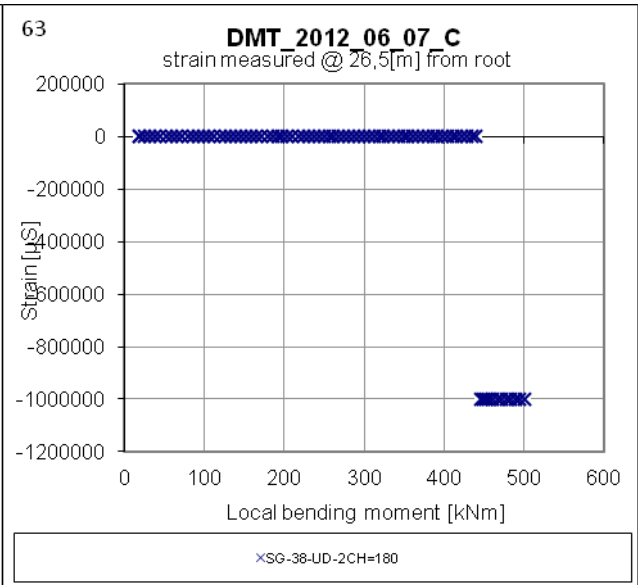
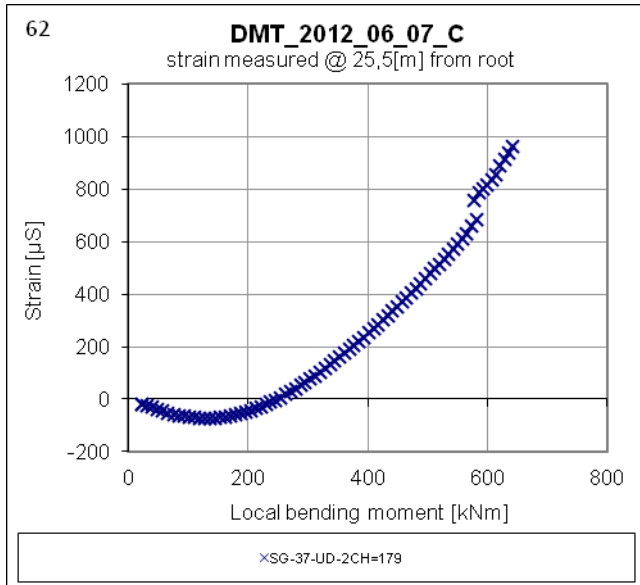




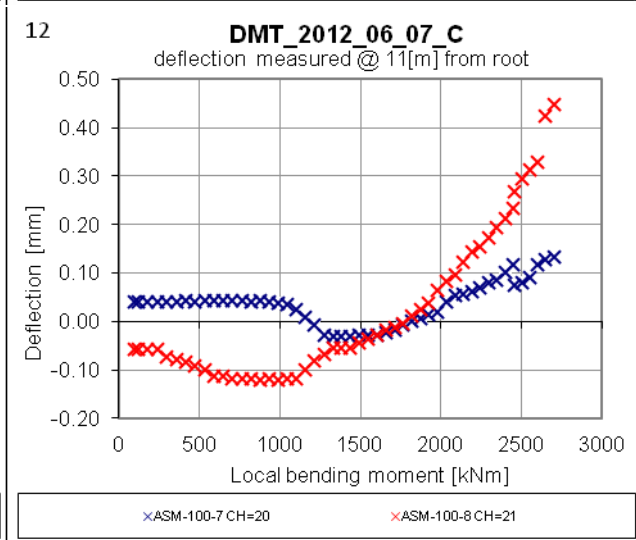
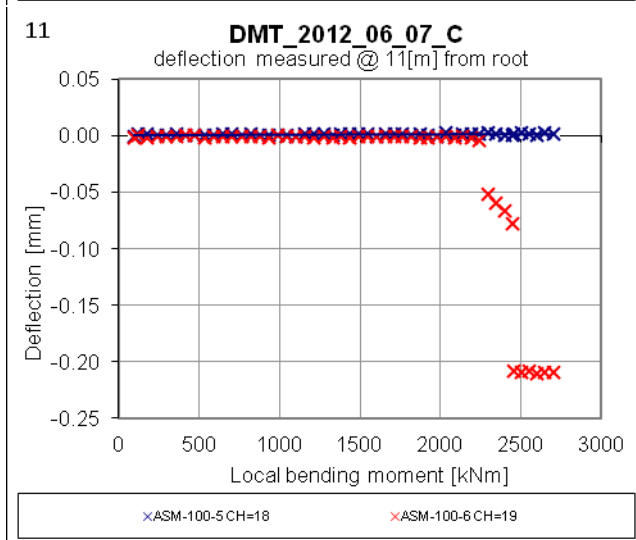
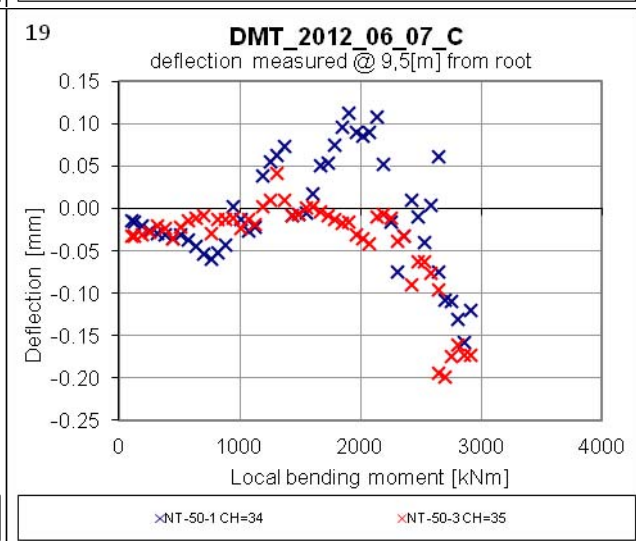
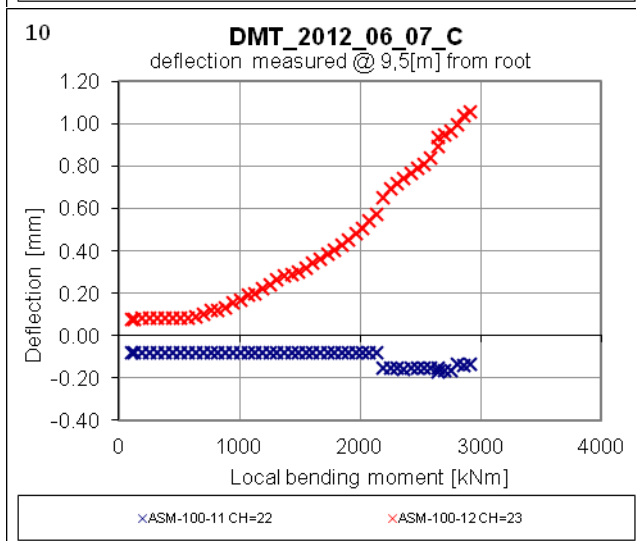
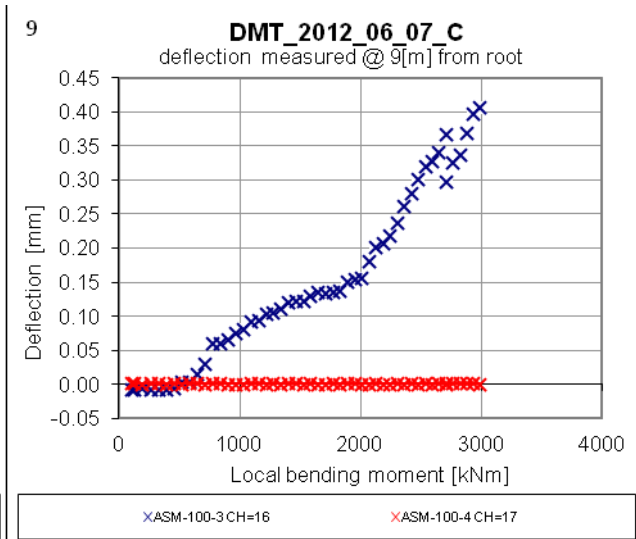
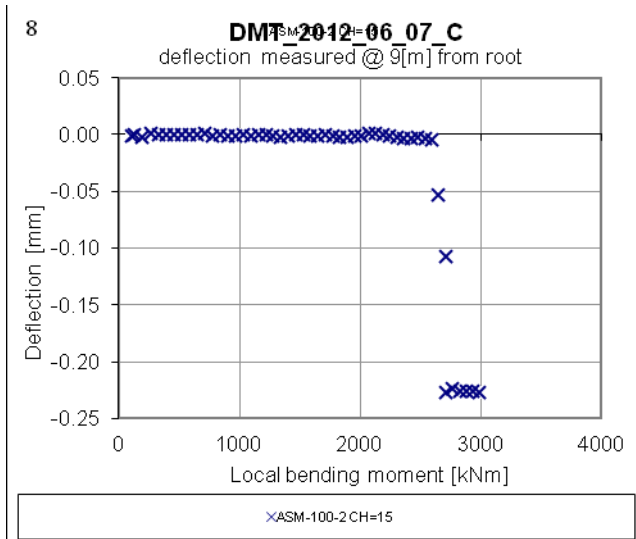


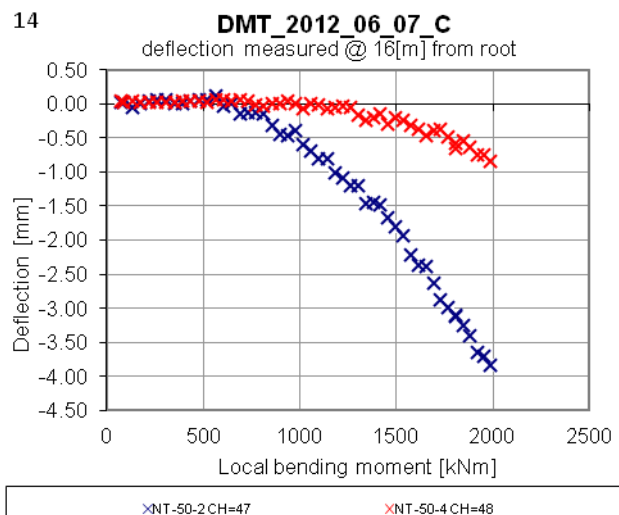
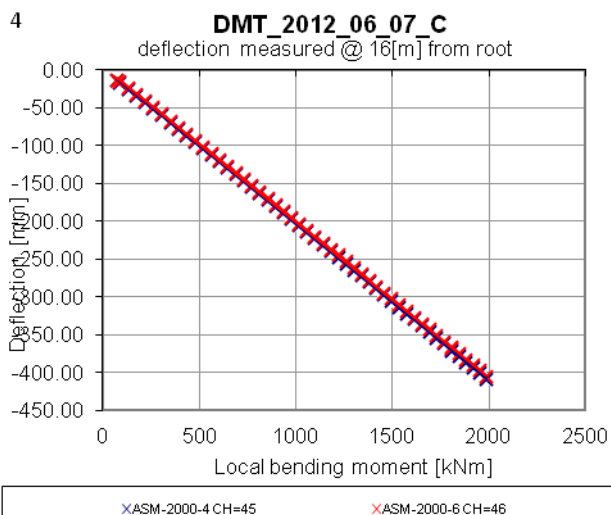
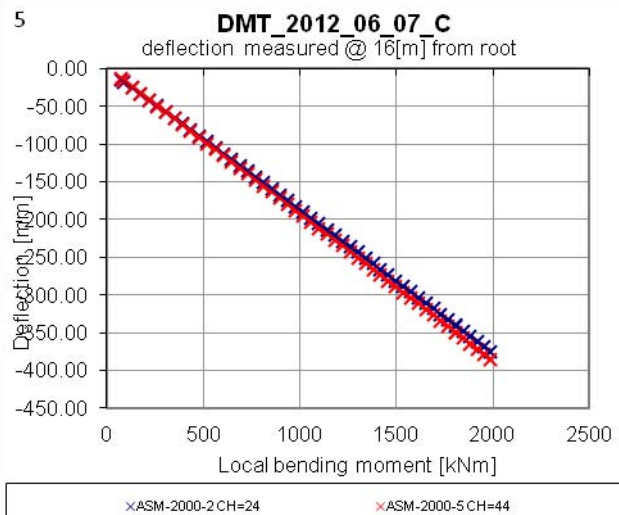
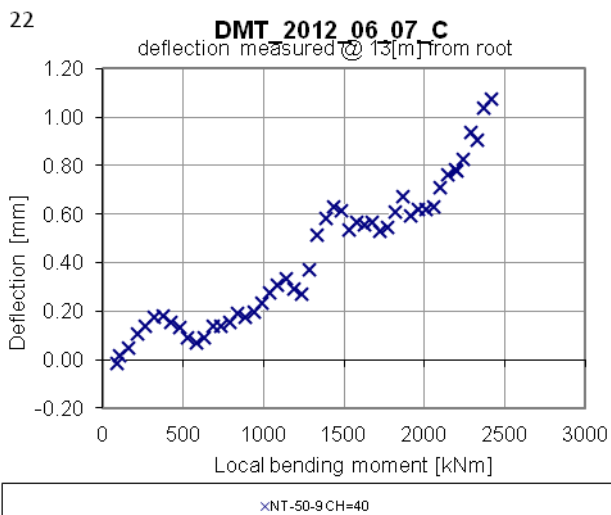
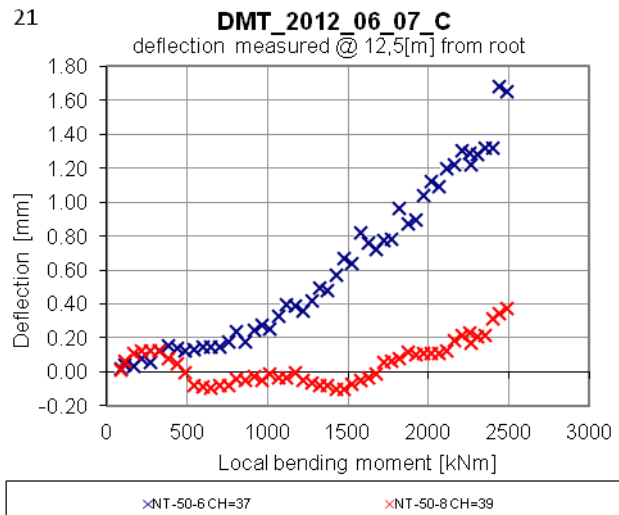
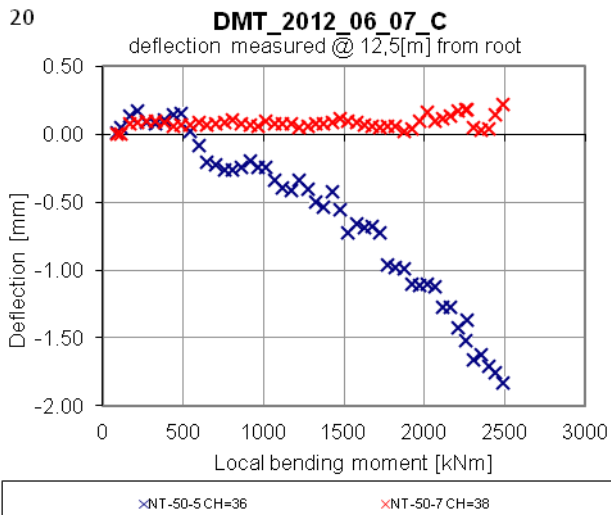


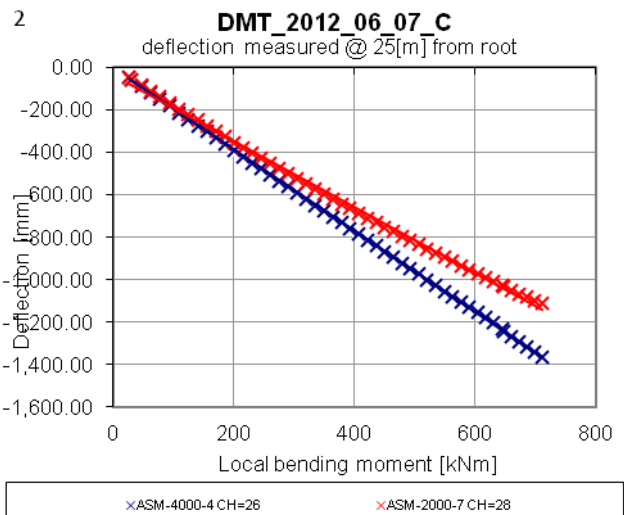
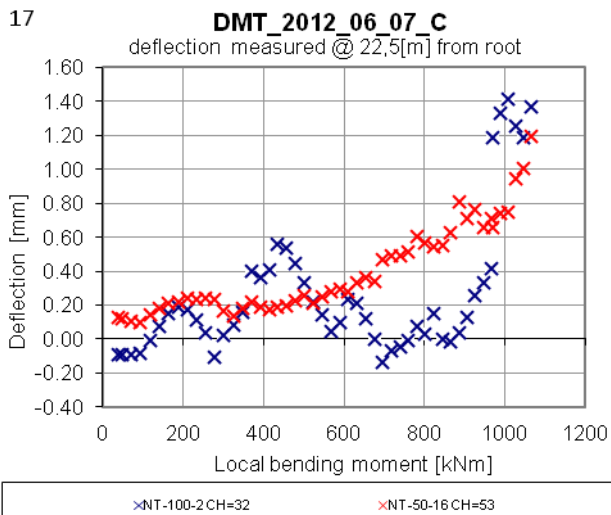
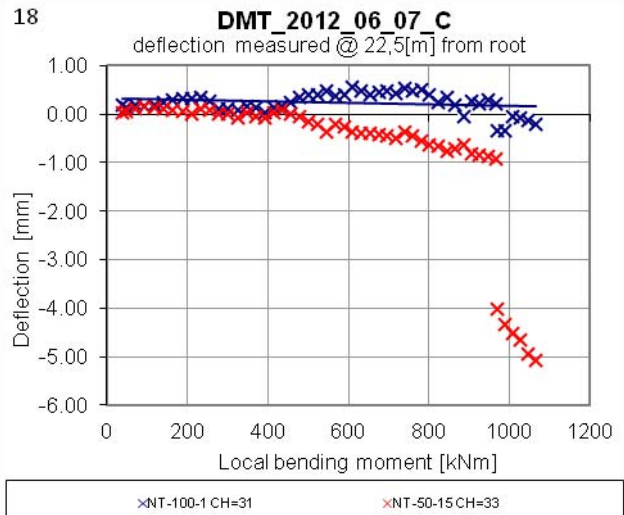
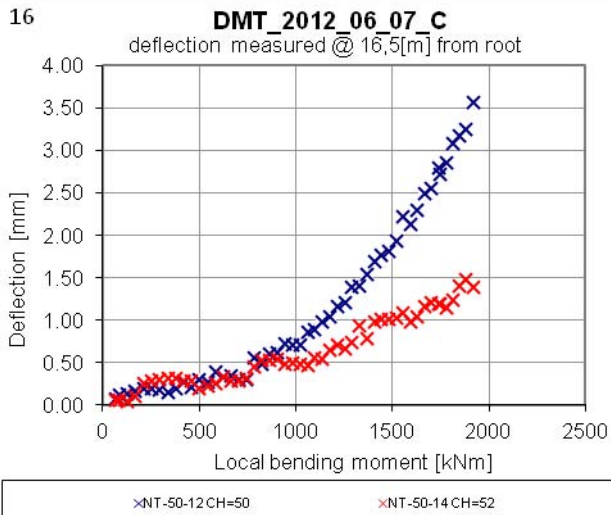
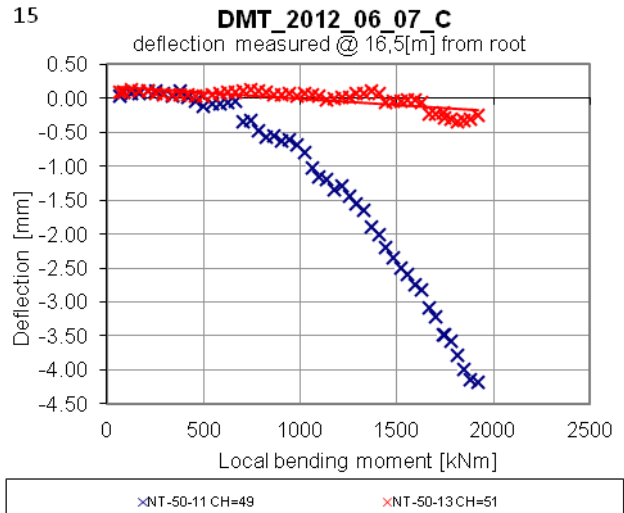
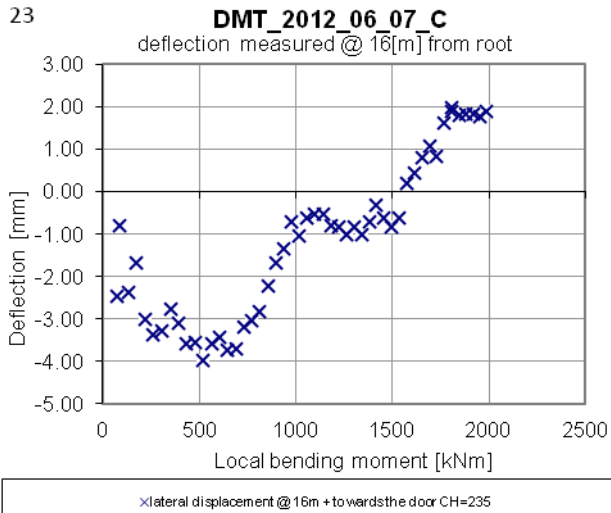


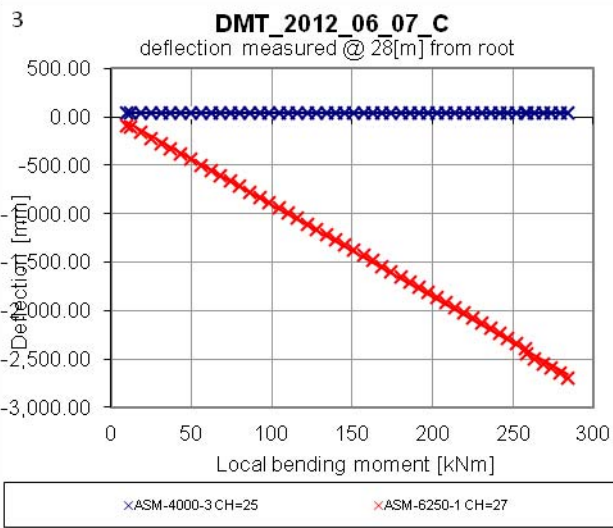
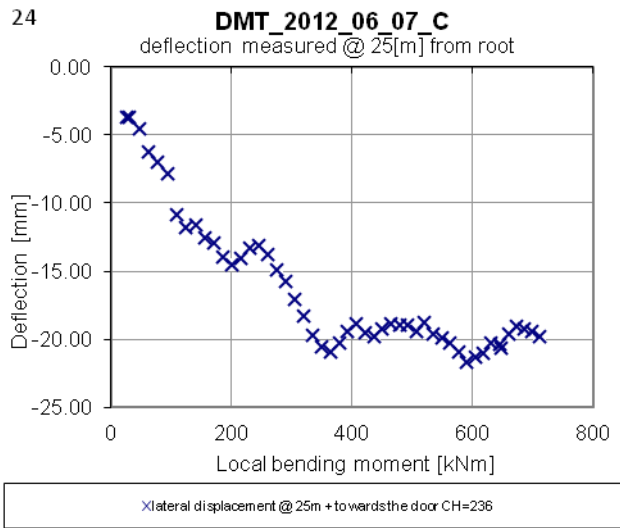
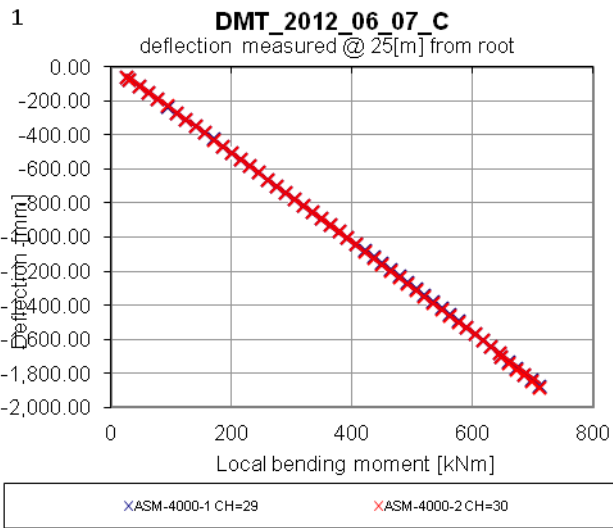


Appendix B4.
Deflection measurements presented by Graph tool.
Test DMT_2012_06_07
The last test leading to catastrophic failure







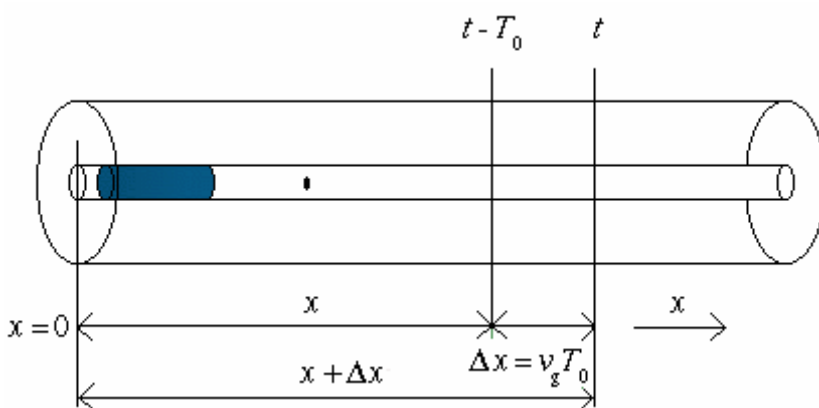


Appendix C Optical Backscatter Reflectometry for static strain measurement in composite structures and components.

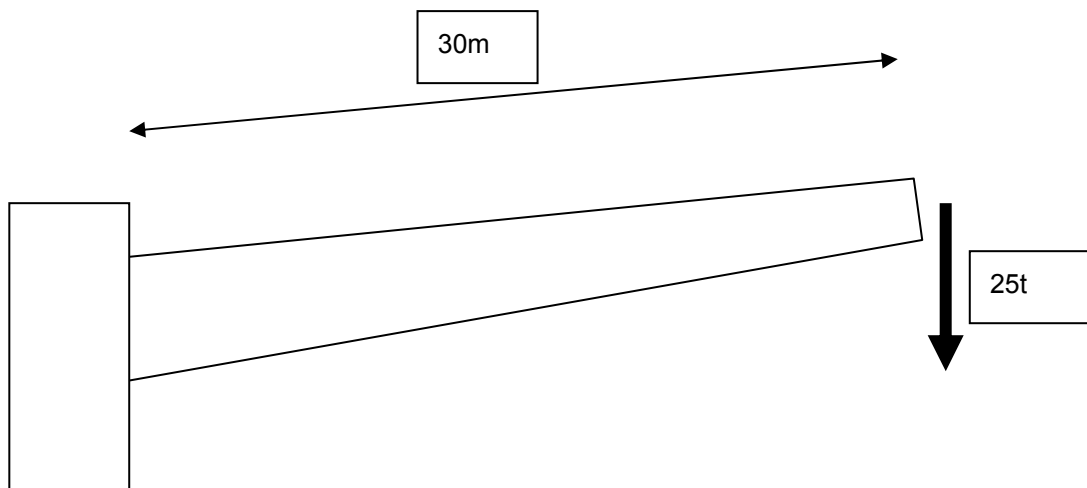
Optical Fiber Distributed Sensing: Background

Laser light projected down the fibre is randomly reflected due to the unique imperfections along the length of the fibre, the “fingerprint” of the fibre. These reflections are affected by the strain applied to the fibre, via the structure on which it is bonded. Strains in the box beam caps along the length of the bonded sections of fibre can therefore be measured with high spatial and strain resolution ($\sim 10\text{mm}$, $\sim 2\mu\epsilon$).

- Continuous strain measurements can be performed on the blade during static tests, providing a valuable source of information regarding any non-linear behaviour.



Test set up



Sketch of the beam in the rig being loaded downwards from the tip

The beam is instrumented with many traditional resistance strain gauges and wire displacement transducers. Several other measurement techniques will be used including Digital Image Correlation, Acoustic Emission, Acousto-ultrasonics, video displacement/twist measurement, internal box shear displacement measurement, and distributed fibre optic measurements.

Passive AE sensors

8 channel DiSP from PAC

4 pairs of sensors on the tension and compression caps at 8m, 12m, 16m and 20m

Active SESS instrumentation

The SESS prototype will be installed as sensor/actuator pairs on the box edges at the 16m chord of the beam. Eight piezoelements with soldered wire connections will be attached with epoxy to the outer surface of the beam by Noliac and Risø. This instrumentation will give some flexibility regarding the four channels to be used in the SESS prototype instrumentation and could allow an eight channel instrumentation using the PAQ16000 system.

The instrumentation

Monday 6th February 2012

Antonio Fernandez-Lopez (UPM) arrives in Denmark with the Luna Technologies Optical Backscatter Reflectometer. It is delivered to the test facility.

Tuesday 7th February 2012

The OBR equipment is started and calibrated after its travel the previous day. The optic connections were aligned and the response from a gold standard fibre optic is checked.

A line along the length of both box beam caps had previously been ground down. This was to allow the fibre optic to be placed in direct contact with a relatively smooth structural laminate material, instead of on the uneven resin rich surface layer.

The fibre is placed along the groove and held in place with small sections of tape. The fibre is then bonded to the surface with a fast curing (10 minutes gel) two part epoxy. Before cure the thixotropic adhesive is smoothed over the fibre to fully encapsulate it with a small spatula. The taped sections are then carefully removed and the bonding process completed here also. This procedure is successfully repeated on the groove along the underside of the box beam.

Two ten meter sections of the fibre optic are bonded on the top and bottom load bearing caps of the box beam, from the 10m to 20m chords. At the ends of the fibre (near the 10m chord) connectors are attached that can link the embedded fibre to the OBR system so a measurement can be taken from either end of the fibre. The middle of the fibre is loose and loops around the box beam from the bonded top and bottom surfaces.

Fibre optic filaments can be cut and bonded using special equipment to “cleave” and “splice” the fibre.

The measurement data is returned for the entire length of the fibre, of interest is the response of the two 10m bonded sections.



Figure 1. The OBR hardware and laptop interface.



Figure 2. Close up on the bonded and smoothed out adhesive over the fibre

The principle

Laser light projected down the fibre is randomly reflected due to the unique imperfections along the length of the fibre, the “fingerprint” of the fibre. These reflections are affected by the strain applied to the fibre, via the structure on which it is bonded. Strains in the box beam caps along the length of the bonded sections of fibre can therefore be measured with ultra-high spatial and strain resolution ($\sim 1\mu\text{m}$, $\sim 1\mu\epsilon$).

Continuous strain measurements can be performed on the blade during static tests, providing a valuable source of information regarding any non-linear behaviour.

REF: “Optical Fiber Distributed Sensing - Physical Principles and Applications”, Alfredo Güemes, Antonio Fernández-López, and Brian Soller, Structural Health Monitoring 2010 vol9 pp:233-245

The measurement

Wednesday 8th February 2012

Relevant strain gauges that had previously been bonded onto the box beam were made ready so that the measurements from the OBR system could be compared with the strain responses from the gauges aligned along the cap axis.

In order to apply a load deformation it was decided to invite people to sit along the length of the beam, which was supported only at tip and root. Preparations were made to ensure that they did not sit on or otherwise damage the delicate fibre...

Static measurements were successfully taken for both loaded and unloaded conditions.

A measurement can be completed in approximately 20 seconds.



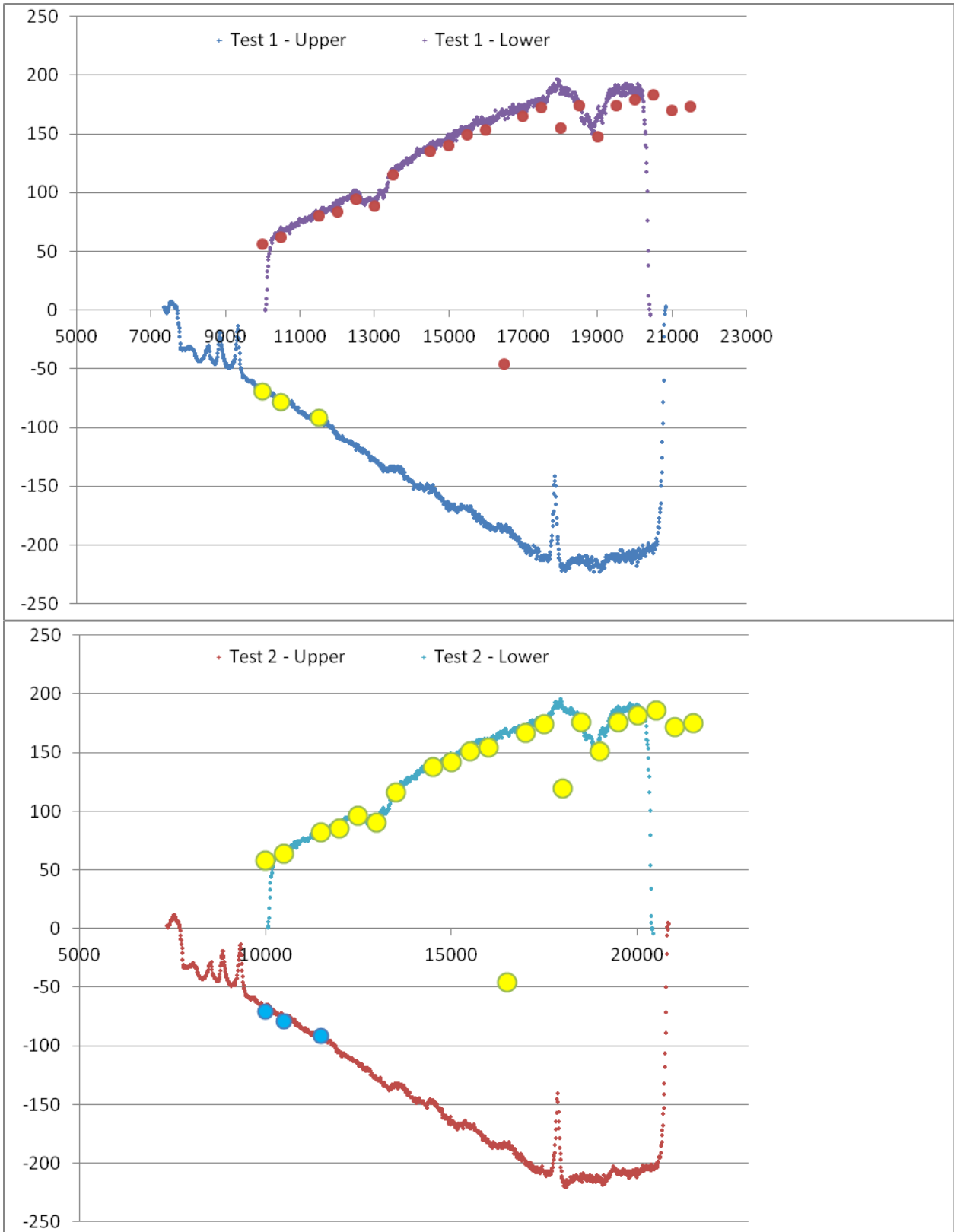
Figure 3. The loading elements are instructed

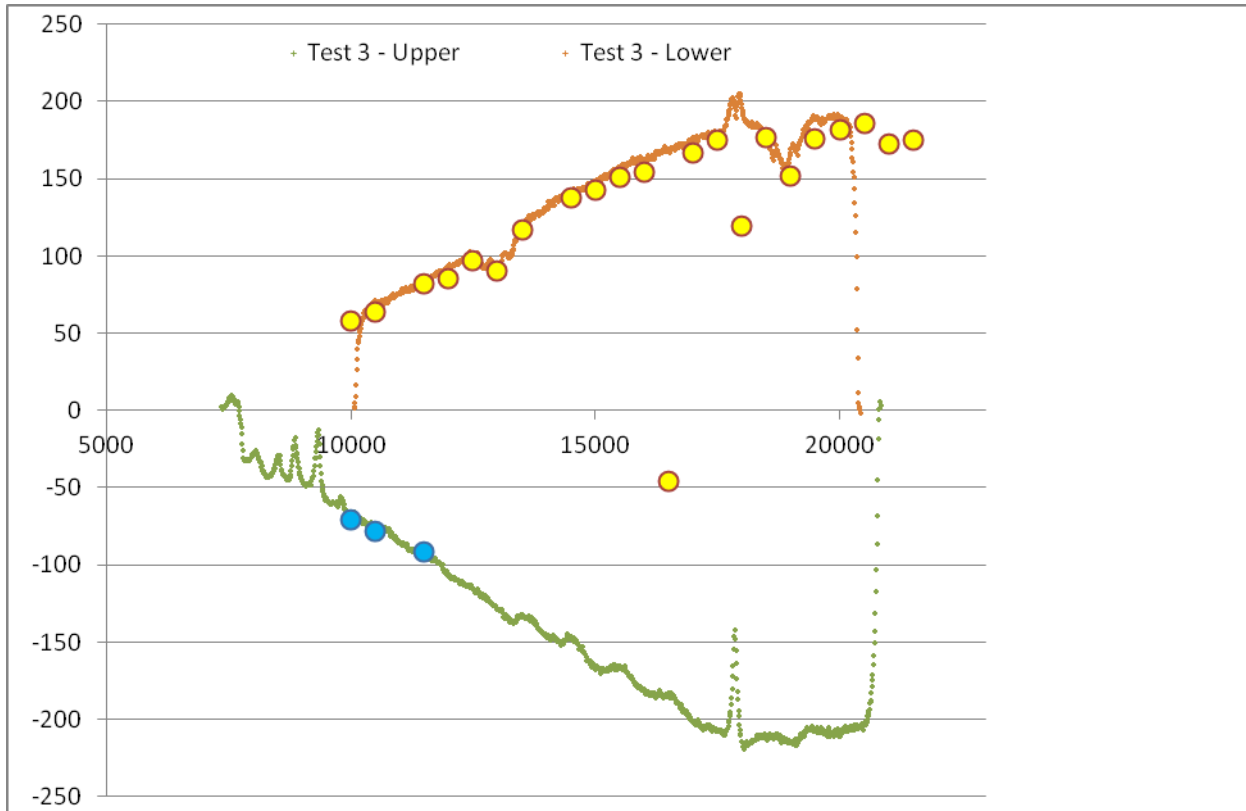


The box beam under static bend loading

Output

Test reading 1





Discussion

Advantages and Disadvantages of the system:

- lots of strain data quickly
- easy instrumentation
- no dynamic measurements
- fragile
- “noise” from loose and vibrating fibre sections

Appendix D Acoustic Emission

Notes from AE monitoring of the DMT Box Beam

12.Jan 2012

The Box Beam was instrumented with AE sensors whilst still lying on the floor of the test hall. This made access easier and safer.



The DMT Box Beam under preparation in the test hall prior to being mounted on the test rig

AE instrumentation details

8 channel PAC DiSP system

R15a sensors

Ch2, 4, 6, and 8

Tensile face

Ch1, 3, 5, and 7

Compression face

Channels 1-4

40m cabling

Channels 5-8

30m cabling

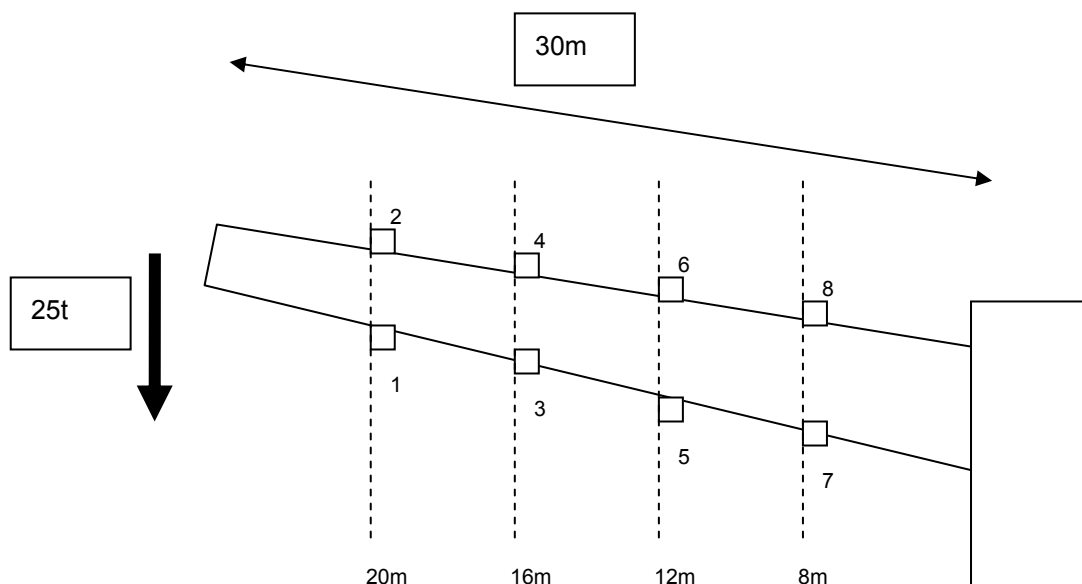
8chzonal.lay file

45dB THS

AMP, NRG, CNT

The sensors were attached with a silicone coupling agent and heavy duty tape used to strap them in place. The cables were fastened against the edge of the beam with strips and brought together in an umbilicus at the root of the beam.

The beam was later raised unto place and all the loading and monitoring preparations completed. At this point the cabling was unrolled from the beam and taken through to the control room where they could be connected to the PAC DiSP system and the AE monitoring was ready to begin.



Schematic showing the position of the 8 AE sensors on the DMT Box Beam

10.May 2012

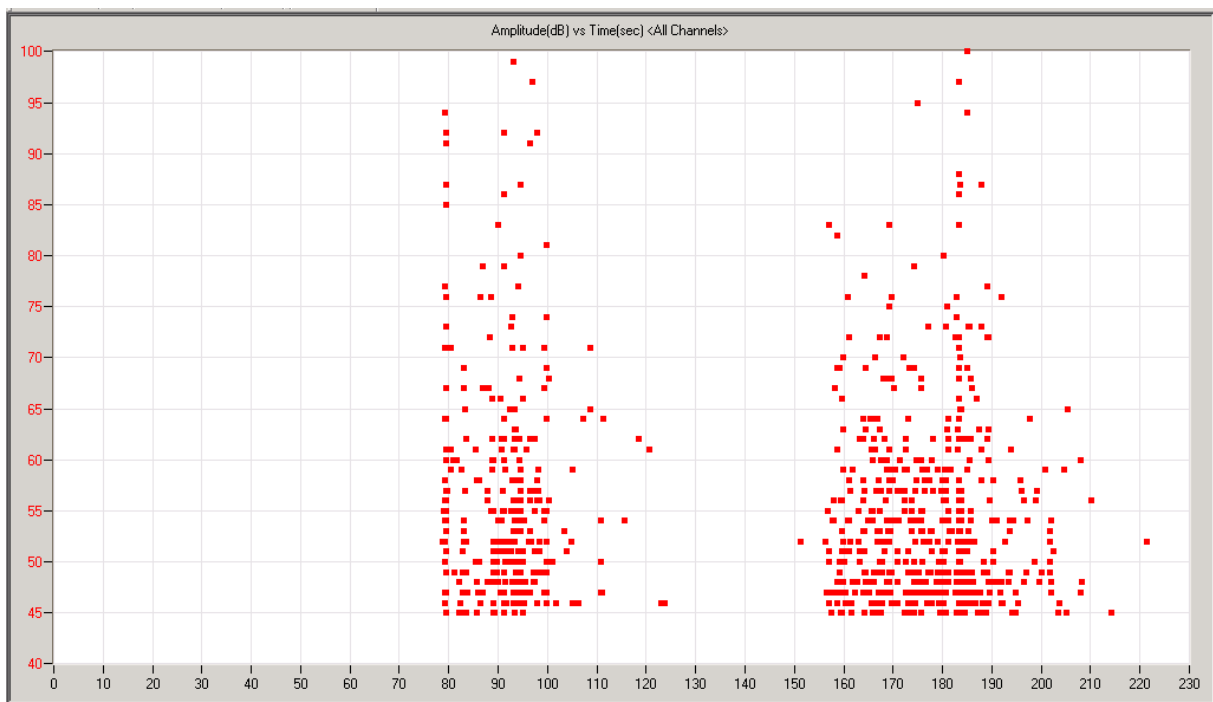
	Start time	Max Load	AE Hits (total)	AE NRG (total)	AE Counts (total)	AE AMP (average)
Test load	10/05 1200	50kN	23	130	301	54.3
DMT_2012_05_10_B	10/05 1209	90kN	893	44651	23764	54.8
DMT_2012_05_10_C	10/05 1240	90kN	24	216	361	54.8

The DMT Box Beam structure shows a significant “Kaiser Effect”, meaning that AE is only prevalent at loads higher than have previously achieved.

- In Test load only very little activity occurs once the load reaches 50kN.
- In DMT_2012_05_10_B there is significant AE once the load is increased above 50kN up to 70kN. After a load hold here where AE activity stabilises there is a second burst of AE as the load is increased again up to 90kN. There is no significant AE during unload.
- In DMT_2012_05_10_C there is no activity during loading to 50kN. Very little during loading to 70kN, and only a little more on loading up to 90kN again.

Analysis of the DMT_2012_05_10_B Acoustic Emission

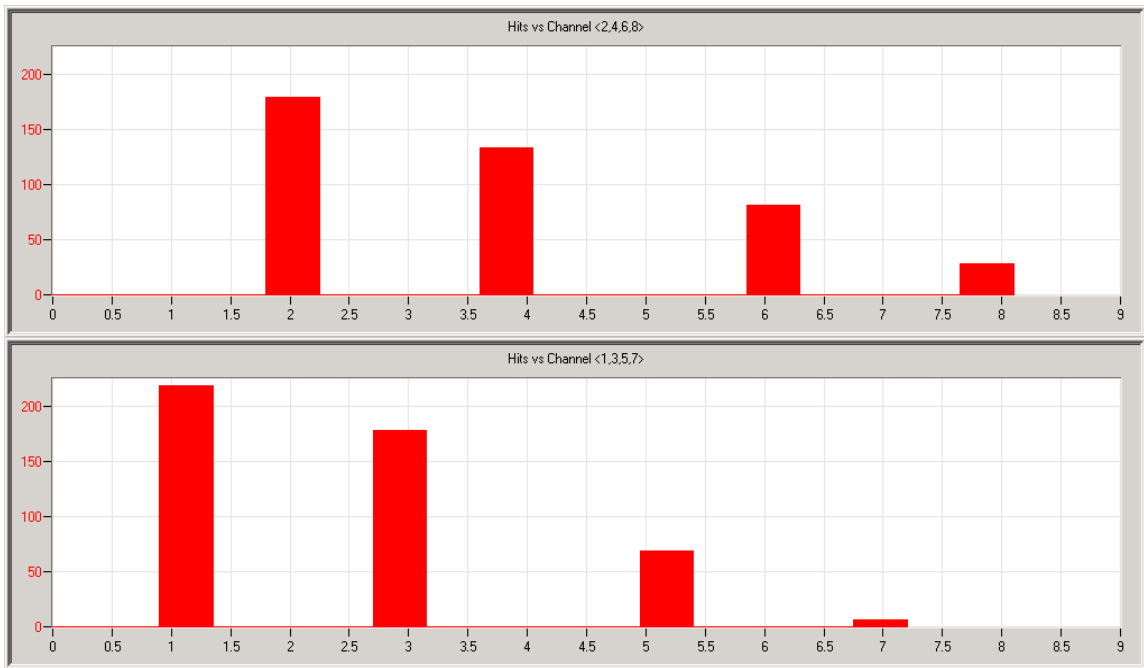
Overview



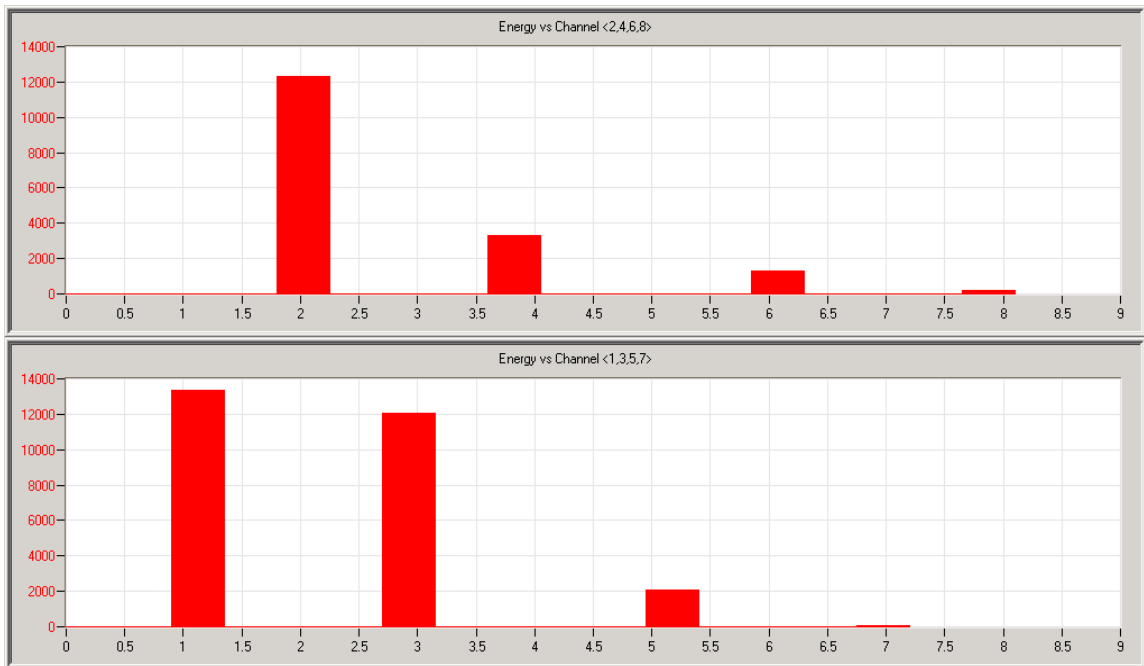
DMT_2012_05_10_B (20120510)
Amplitude vs. time

Shows two bursts of AE, the first from around test time 80-100 seconds where the load is held at 70kN, and the second from around 160-190s where the load is held at 90kN.

	Start time	Max Load	AE Hits (total)	AE NRG (total)	AE Counts (total)	AE AMP (average)
DMT_2012_05_10_B (part1)	kl.1209	70kN	317	15723	8498	56.2
DMT_2012_05_10_B (part2)	kl.1211	90kN	576	28928	15266	54.1
DMT_2012_05_10_B (total)	kl.1209	90kN	893	44651	23764	54.8



DMT_2012_05_10_B (20120510)
 Channel activity (Hits) for Tensile (upper) and Compression (lower) cap faces

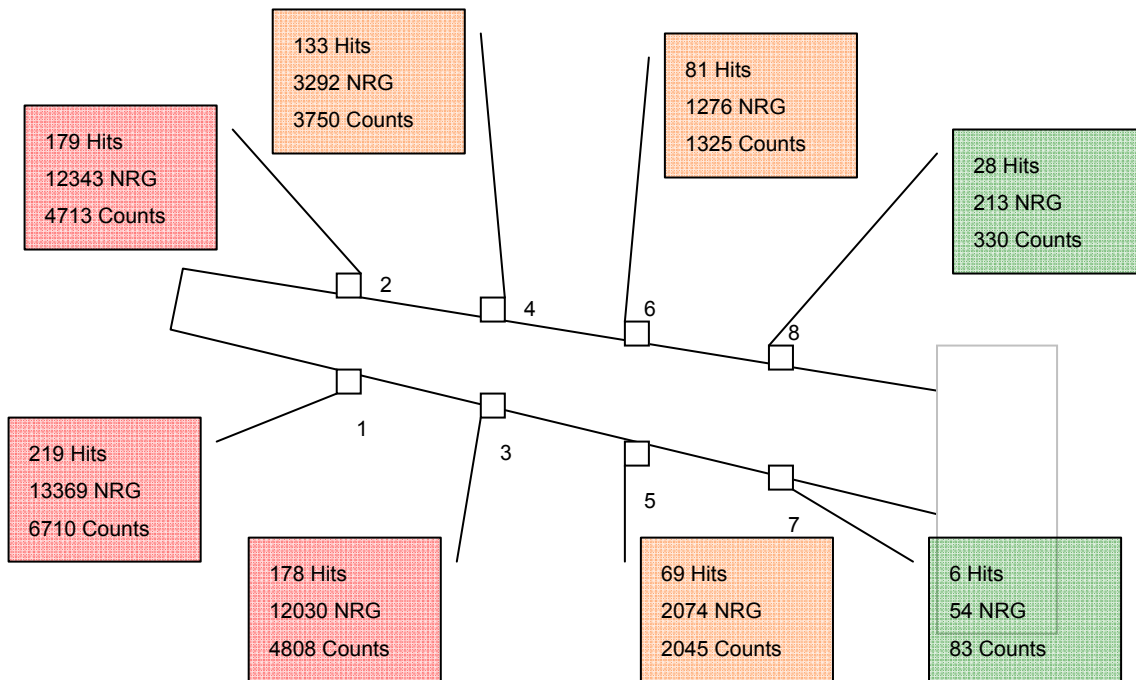


DMT_2012_05_10_B (20120510)
 Channel activity (Energy) for Tensile (upper) and Compression (lower) cap faces

These graphs show that the sensors towards the end of the beam are the most active and generate relatively more energy in their AE than the sensors closer to the root. That is to say the amount of AE follows the relative structural deflection.

Structural Distribution of AE

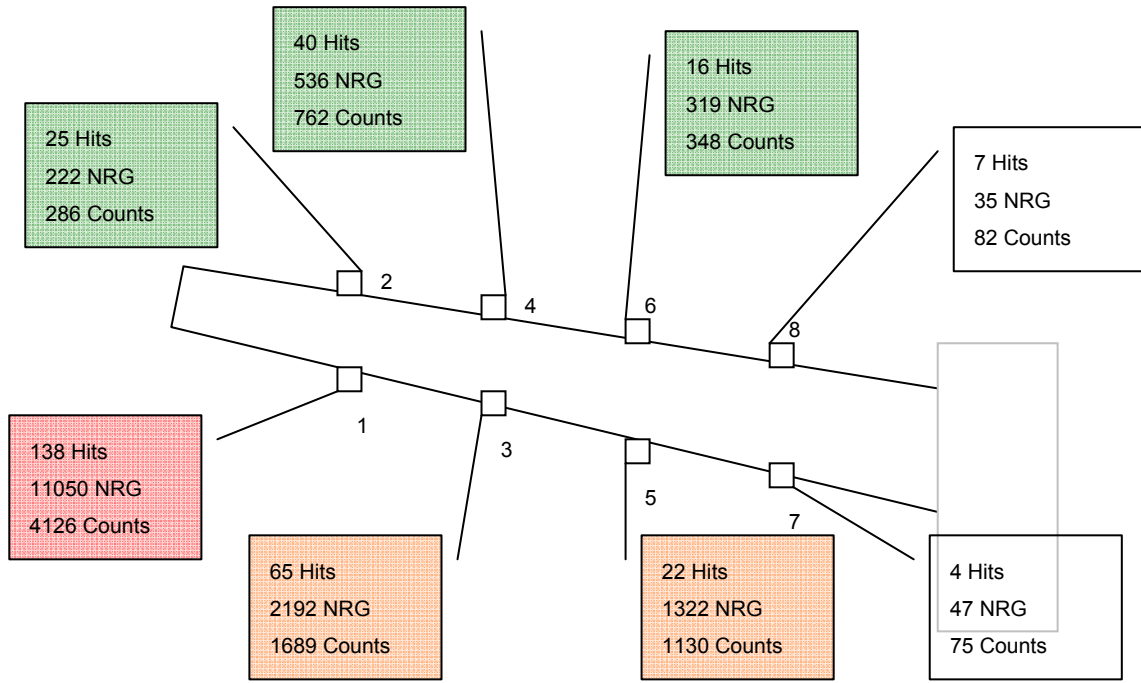
DMT_2012_05_10_B (10120510) - TOTAL



	Hits	Energy	Counts	Av.Amplitude	Energy/Hit	Counts/Hit	Energy/Count
CH1	219	13369	6710	56.5	61.0	30.6	1.99
CH2	179	12343	4713	51.8	69.0	26.3	2.62
CH3	178	12030	4808	55.6	67.6	27.0	2.50
CH4	133	3292	3750	55.8	24.8	28.2	0.88
CH5	69	2074	2045	54.9	30.1	29.6	1.02
CH6	81	1276	1325	54.0	15.8	16.4	0.96
CH7	6	54	83	54.3	9.0	13.8	0.65
CH8	28	213	330	54.2	7.6	11.8	0.64

Structural Distribution of AE

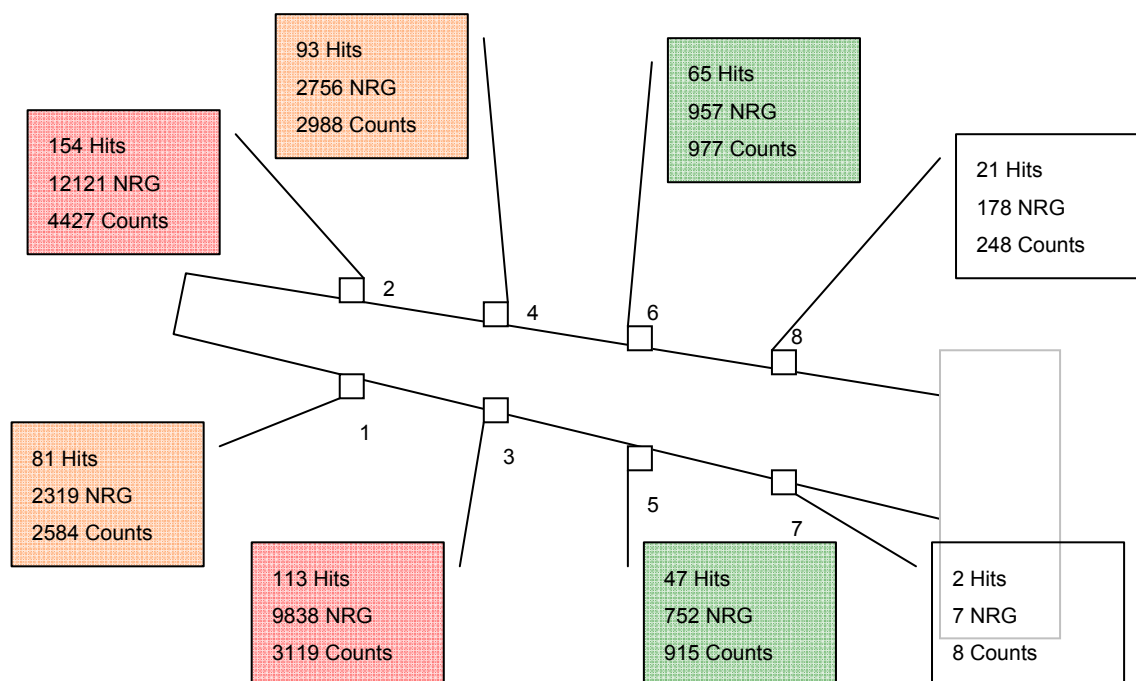
DMT_2012_05_10_B (10120510) - PART 1 (load to 70kN)



	Hits	Energy	Counts	Av. Amplitude	Energy/Hit	Counts/Hit	Energy/Count
CH1	138	11050	4126	57.5	80.1	29.9	2.68
CH2	25	222	286	52.0	8.9	11.4	0.78
CH3	65	2192	1689	55.6	33.7	26.0	1.30
CH4	40	536	762	55.9	13.4	19.0	0.70
CH5	22	1322	1130	56.9	60.1	51.4	1.17
CH6	16	319	348	54.4	19.9	21.8	0.92
CH7	4	47	75	54.5	11.8	18.8	0.63
CH8	7	35	82	57.4	5.0	11.7	0.43

Structural Distribution of AE

DMT_2012_05_10_B (10120510) - PART 2 (load to 90kN)



	Hits	Energy	Counts	Av.Amplitude	Energy/Hit	Counts/Hit	Energy/Count
CH1	81	2319	2584	54.9	28.6	31.9	0.90
CH2	154	12121	4427	51.7	78.7	28.7	2.74
CH3	113	9838	3119	55.6	87.1	27.6	3.15
CH4	93	2756	2988	55.7	29.6	32.1	0.92
CH5	47	752	915	53.9	16.0	19.5	0.82
CH6	65	957	977	54.0	14.7	15.0	0.98
CH7	2	7	8	54.0	3.5	4.0	0.88
CH8	21	178	248	53.1	8.5	11.8	0.72

Analysis of the Structural distribution of the AE

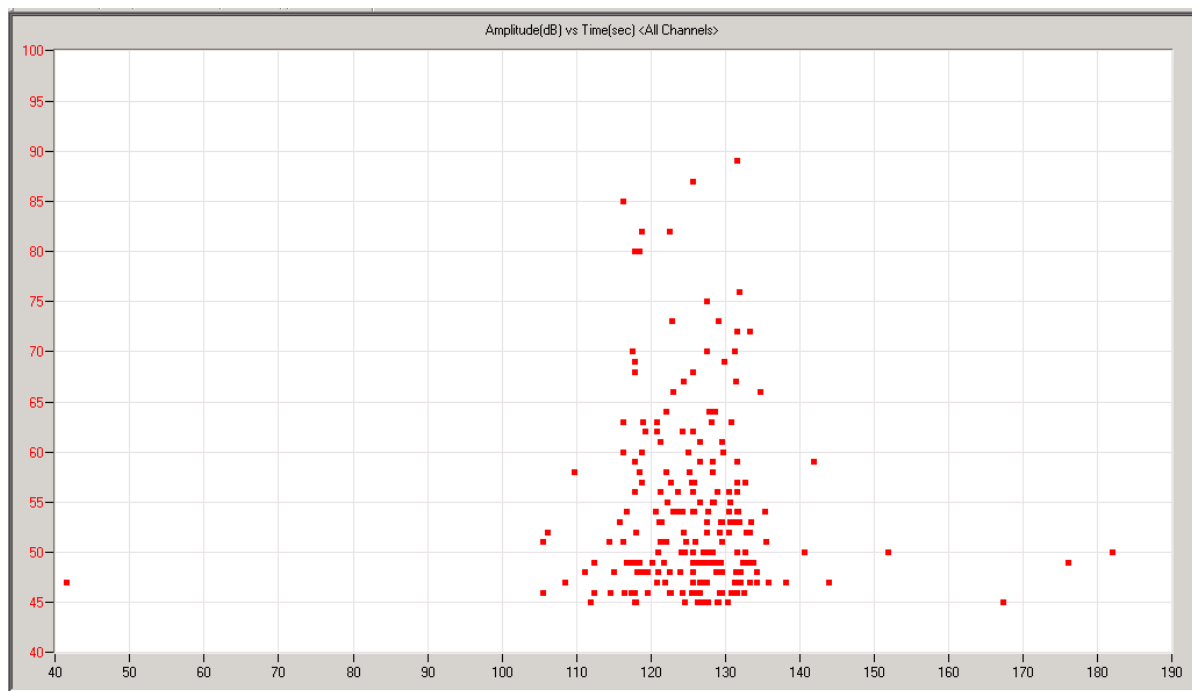
Note that the average Amplitude for all the sensors is between 53.9 and 57.5dB in this loading, except for channel 2 which has a lower value (51.7 to 52.0). This suggests a different source of activity occurring here (20m tension/upper cap) that is not occurring elsewhere. It was noted that the activity on sensor 2 occurred during load application and that a mechanical noise could also be heard during this activity. This was identified as a noise source from the cabling at the load application. The interference of this noise source is most prevalent in PART2 of DMT_2012_05_10_B and accounts for the unusual Structural distribution of AE here.

16 May 2012

	Start time	Max Load	AE Hits (total)	AE NRG (total)	AE Counts (total)	AE AMP (average)
Test load	10/05 1200	50kN	23	130	301	54.3
DMT_2012_05_10_B	10/05 1209	90kN	893	44651	23764	54.8
DMT_2012_05_10_C	10/05 1240	90kN	24	216	361	54.8
DMT_2012_05_16_A	16/05 1250	90kN	227	3201	3488	53.8

In DMT_2012_05_16_A the DMT box beam is simply loaded to the previous maximum level (90kN) with AE activity only occurring once this level is reached. At this point the AE begins strongly and the load is then released; very little AE then takes place. This indicates a Kaiser effect (Felicity effect) and a stable structure with no significant damages.

Analysis of DMT_2012_05_16_A Acoustic Emission



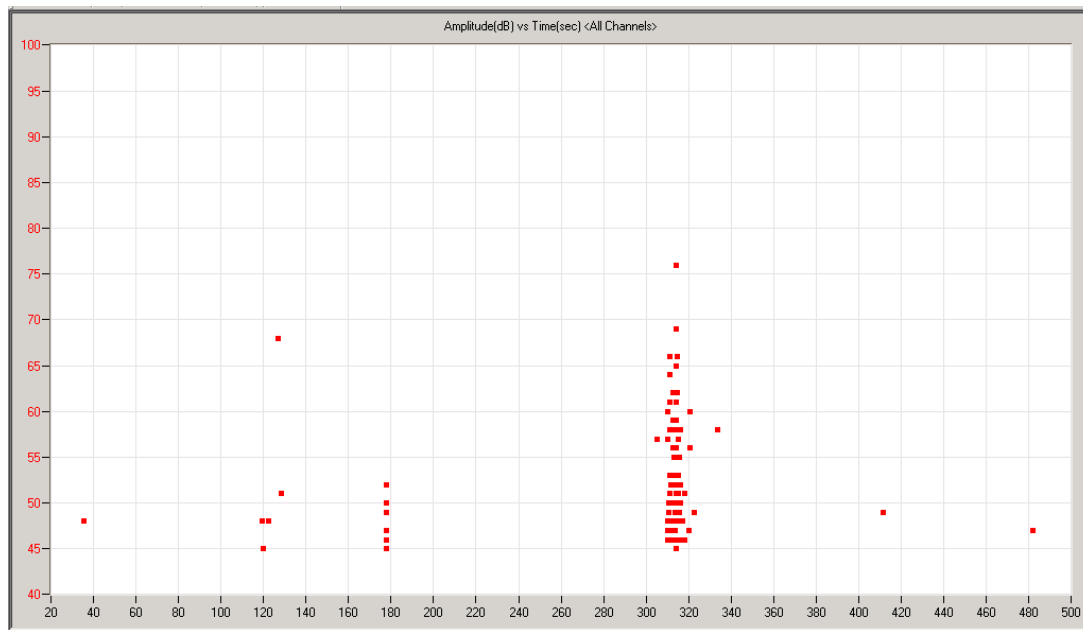
DMT_2012_05_16_A (20120516)
Amplitude vs. test time

24 May 2012

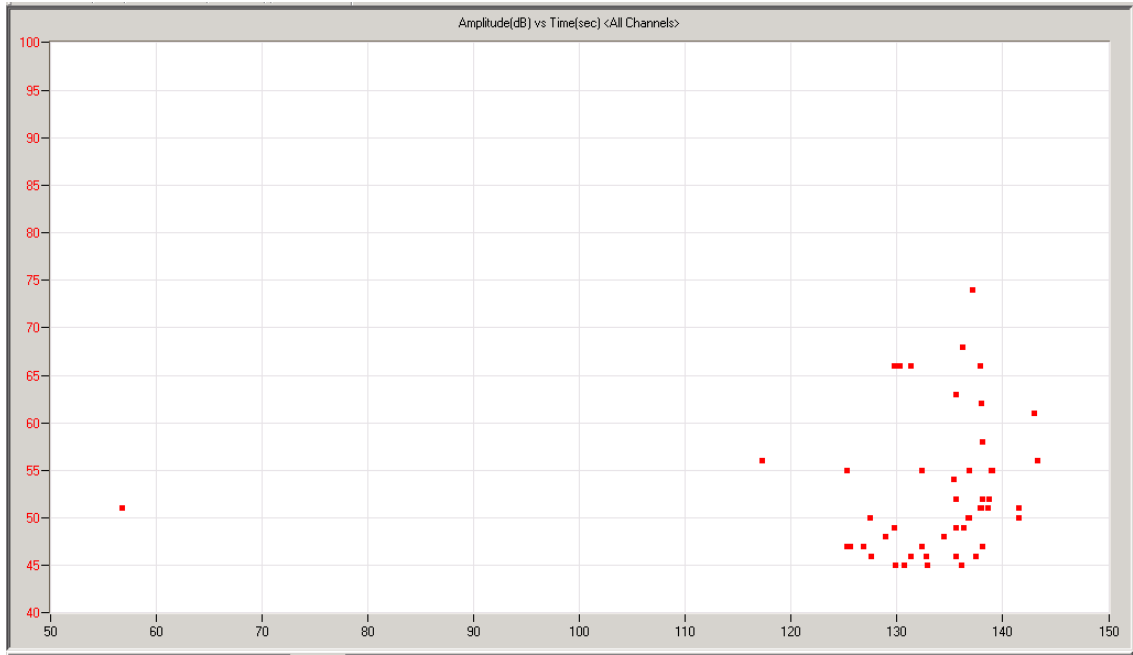
	Start time	Max Load	AE Hits (total)	AE NRG (total)	AE Counts (total)	AE AMP (average)
Test load	10/05 1200	50kN	23	130	301	54.3
DMT_2012_05_10_B	10/05 1209	90kN	893	44651	23764	54.8
DMT_2012_05_10_C	10/05 1240	90kN	24	216	361	54.8
DMT_2012_05_16_A	16/05 1250	90kN	227	3201	3488	53.8
DMT_2012_05_24_A	24/05 1018	90kN	96	608	1370	52.6
DMT_2012_05_24_B	24/05 1038	106kN	50	295	581	52.7

In DMT_2012_05_24_A (which was webcast live) the DMT box beam is once again loaded up to 90kN, with AE only occurring in a limited fashion at the highest load levels. In DMT_2012_05_24_B the load is peaked at 106kN, the highest so far, but again with only limited AE activity. This is most likely due to the number of times the structure has been loaded up to 90kN and held at this load with occasional peak loads above this value.

Analysis of DMT_2012_05_24_A + B Acoustic Emission



DMT_2012_05_24_A (20120524)
Amplitude vs. test time



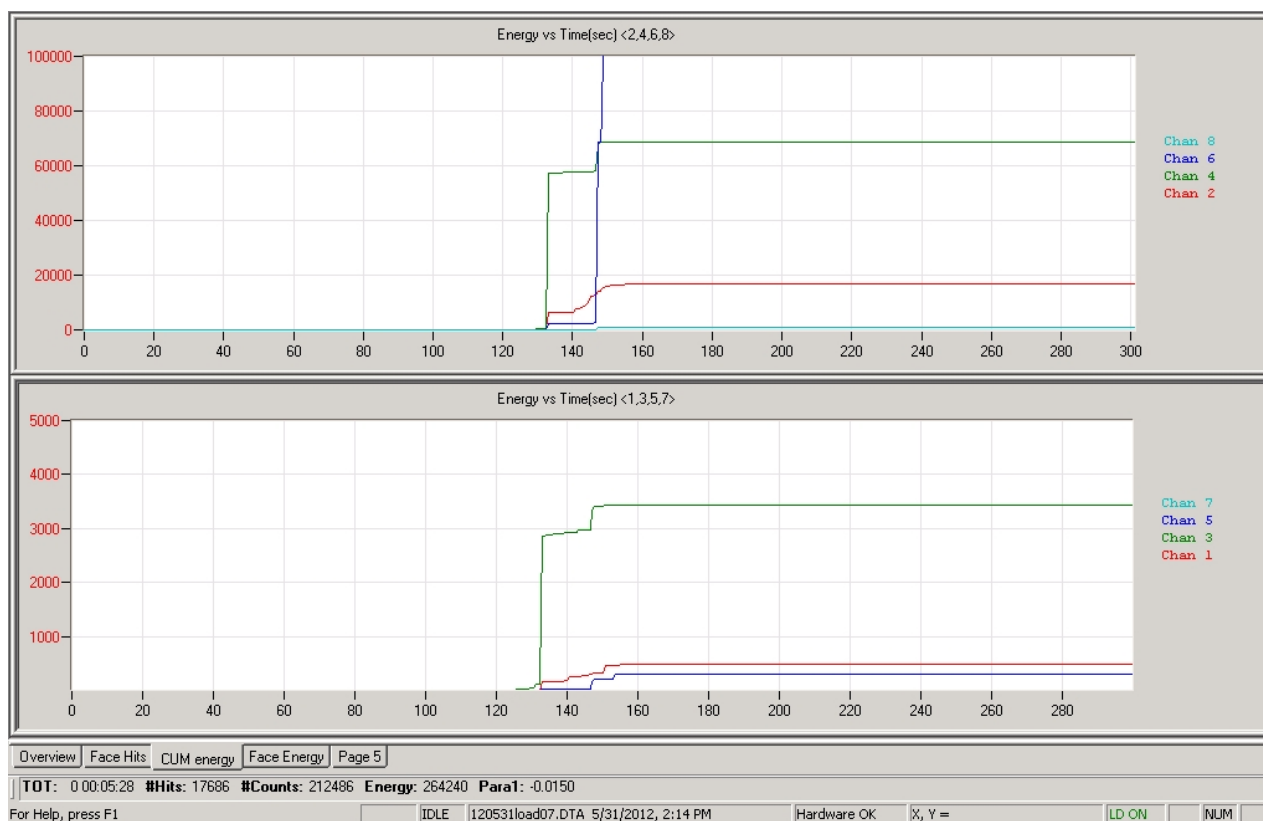
DMT_2012_05_24_B (20120524)
Amplitude vs. test time

31 May 2012

	Start time	Max Load	AE Hits (total)	AE NRG (total)	AE Counts (total)	AE AMP (average)
Test load	10/05 1200	50kN	23	130	301	54.3
DMT_2012_05_10_B	10/05 1209	90kN	893	44651	23764	54.8
DMT_2012_05_10_C	10/05 1240	90kN	24	216	361	54.8
DMT_2012_05_16_A	16/05 1250	90kN	227	3201	3488	53.8
DMT_2012_05_24_A	25/05 1018	90kN	96	608	1370	52.6
DMT_2012_05_24_B	25/05 1038	106kN	50	295	581	52.7
DMT_2012_05_31_A	31/05 1414	100kN	17686	264240	212486	51.0
DMT_2012_05_31_B	31/05 1427	110kN	22852	270137	392821	52.6

Both these loadings were also webcast, and video recorders were also used (including one from the Light and Strong Materials group). The reason for this is that the load level is now such that structural collapse is a possibility.

During DMT_2012_05_31_A (at test time 133s, kl.1416) there was a sudden burst of high energy activity on channels 3 and 4 (16m - tension and compression caps), and at a lower intensity on channels 1 and 2 (20m - tension and compression caps). This was followed by an even higher energy burst at test time 147s (kl.1417) on channel 6. See the cumulative energy traces for all sensors in load07 below.

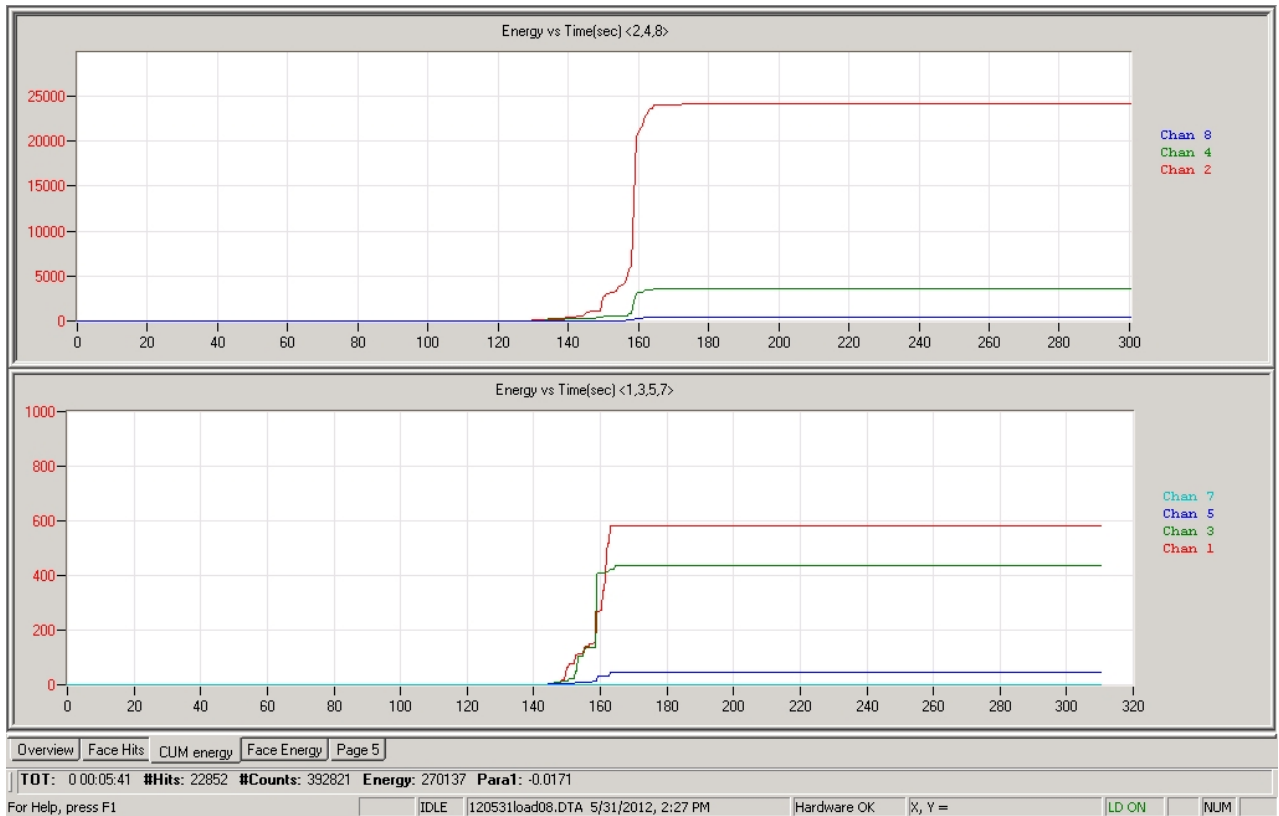


DMT_2012_05_31_A (20120531)

Energy traces for tensile (ch2,4,6,8) and compression (ch1,3,5,7) face caps

These bursts of acoustic emission were initially assumed to have been caused by measurement frames adhesively bonded to the box beam breaking loose under the developing bending load. However it emerged that damage to the internal stiffeners close to these sensors also took place, closer analysis with other measurement tools will be conducted for this double event...

In the case of channel 6, a sharp impact on the sensor resulted in intermittent activity that continued for the rest of the test; and in fact also in test 08 which followed immediately afterwards. This “ringing” of the sensor after an extreme impact is not unusual with resonant sensors.



*DMT_2012_05_31_B (20120531)
Energy traces for tensile (ch2,4,6,8) and compression (ch1,3,5,7) face caps*

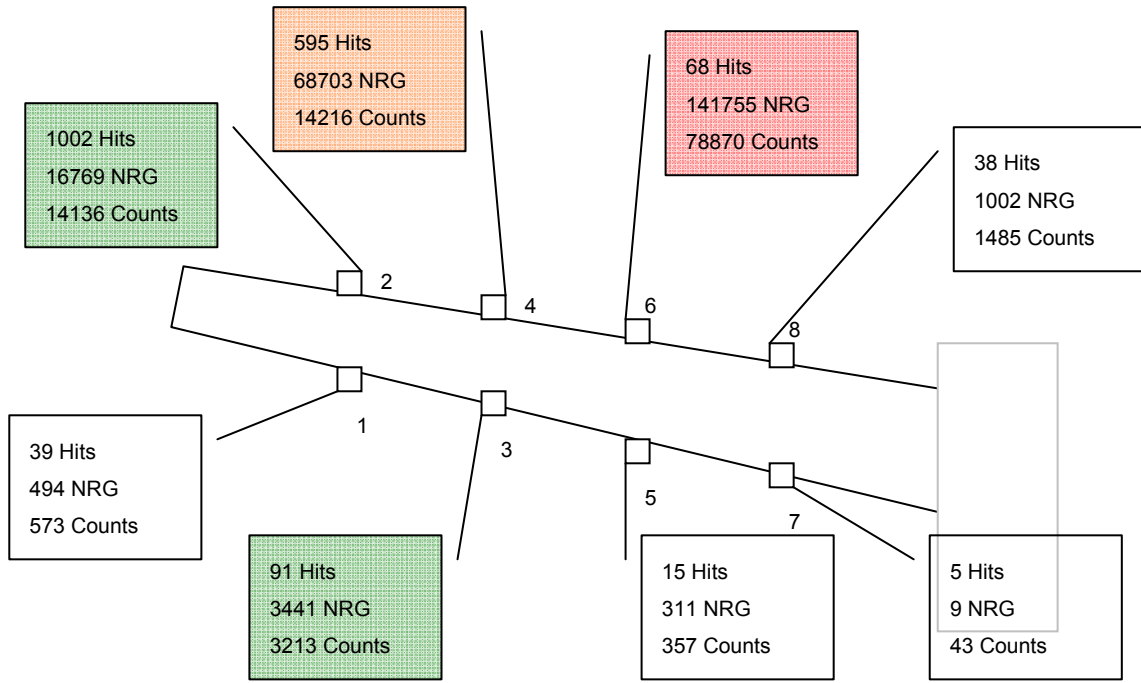
During DMT_2012_05_31_B the “ringing” activity on channel 6 continued, while the other sensors responded correctly to the loading, this time to a maximum of 110kN. Once the load was higher than 100kN the activity in the structure began (Kaiser Effect), mostly on channel 2 (20m - tension cap), but also on significant on channel 4 (16m tension cap). During unloading there was no activity from the structure.

Removing the AE from defective channel 6 (all data after 151s test time on load07) gives the following (more accurate) overview of DMT_2012_05_31_A + B.

	Start time	Max Load	AE Hits (total)	AE NRG (total)	AE Counts (total)	AE AMP (average)
Test load	10/05 1200	50kN	23	130	301	54.3
DMT_2012_05_10_B	10/05 1209	90kN	893	44651	23764	54.8
DMT_2012_05_10_C	10/05 1240	90kN	24	216	361	54.8
DMT_2012_05_16_A	16/05 1250	90kN	227	3201	3488	53.8
DMT_2012_05_24_A	25/05 1018	90kN	96	608	1370	52.6
DMT_2012_05_24_B	25/05 1038	106kN	50	295	581	52.7
DMT_2012_05_31_A	31/05 1414	100kN	1853	232484	112893	51.7
DMT_2012_05_31_B	31/05 1427	110kN	1837	29170	33445	51.4

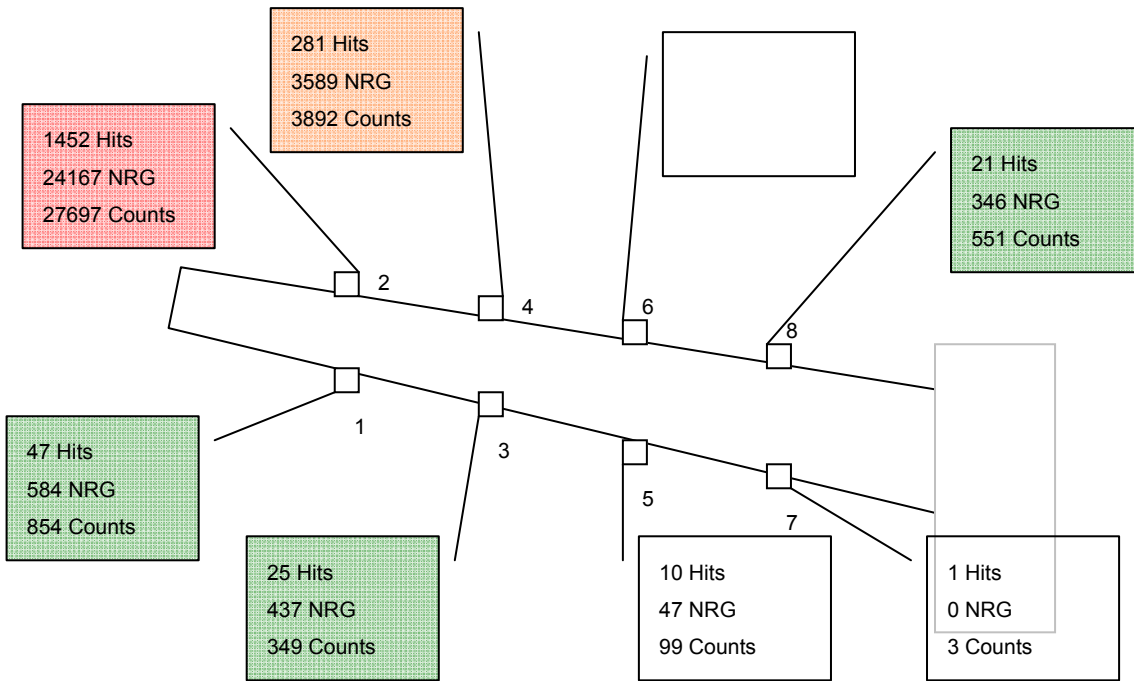
Structural Distribution of AE

DMT_2012_05_31_A (20120531)



	Hits	Energy	Counts	Av. Amplitude	Energy/Hit	Counts/Hit	Energy/Count
CH1	39	494	573	51.7	12.7	14.7	0.86
CH2	1002	16769	14136	51.1	16.7	14.1	1.19
CH3	91	3441	3213	55.0	37.8	35.3	1.07
CH4	595	68703	14216	50.8	115.5	23.9	4.83
CH5	15	311	357	52.4	20.7	23.8	0.87
CH6*	68	141755	78870	62.7	2084.6	1159.9	1.80
CH7	5	9	43	48.8	1.8	8.6	0.21
CH8	38	1002	1485	53.0	26.4	39.1	0.67

CH6* - data to test time 151s only...



	Hits	Energy	Counts	Av.Amplitude	Energy/Hit	Counts/Hit	Energy/Count
CH1	47	584	854	53.8	12.4	18.2	0.68
CH2	1452	24167	27697	51.2	16.6	19.1	0.87
CH3	25	437	349	52.9	17.4	13.9	1.25
CH4	281	3589	3892	51.7	12.8	13.9	0.92
CH5	10	47	99	53.8	4.7	9.9	0.47
CH6							
CH7	1	0	3	49.0	-	3	-
CH8	21	346	551	54.8	16.5	26.2	0.63

07 June 2012

	Start time	Max Load	AE Hits (total)	AE NRG (total)	AE Counts (total)	AE AMP (average)
Test load	10/05 1200	50kN	23	130	301	54.3
DMT_2012_05_10_B	10/05 1209	90kN	893	44651	23764	54.8
DMT_2012_05_10_C	10/05 1240	90kN	24	216	361	54.8
DMT_2012_05_16_A	16/05 1250	90kN	227	3201	3488	53.8
DMT_2012_05_24_A	25/05 1018	90kN	96	608	1370	52.6
DMT_2012_05_24_B	25/05 1038	106kN	50	295	581	52.7
DMT_2012_05_31_A	31/05 1414	100kN	17686	264240	212486	51.0
DMT_2012_05_31_B	31/05 1427	110kN	22852	270137	392821	52.6
DMT_2012_06_07_A	07/06 1118	75kN	18	24	80	50.8
DMT_2012_06_07_B	07/06 1123	50kN	4	1	10	47.8
DMT_2012_06_07_C	07/06 1133	140kN	2771	661299	242097	52.6

Again for these loadings a live webcast was available and video recorders (including a HD camera from Light and Strong Materials) were used to document the test.

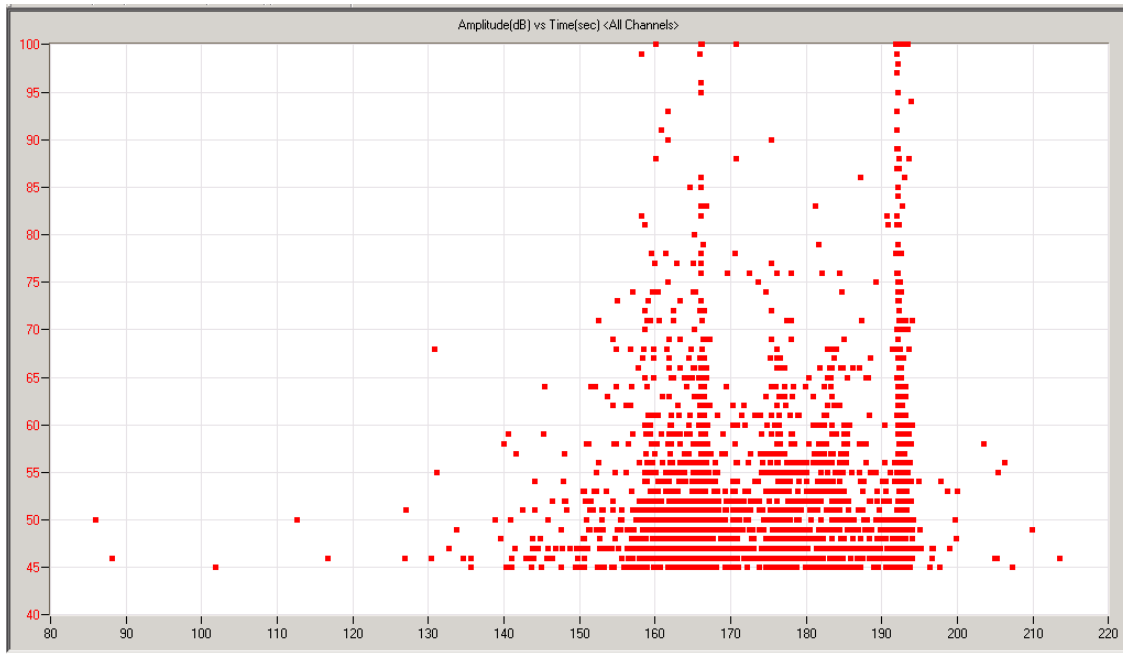
Sensor 6 was not activated for these tests as it had been damaged in DMT_2012_05_31_A during the partial failure of the structure and the loss of the measurement frames at 12m on the tension face.

DMT_2012_06_07_A + B were simply test loadings to confirm good data acquisition and load application. These tests also allowed optical deflection data from the Baumer system to be obtained at test load levels.

In DMT_2012_06_07_C the deflection was increased until structural failure. This occurred at the tip, possibly from an initial failure at the load application point.

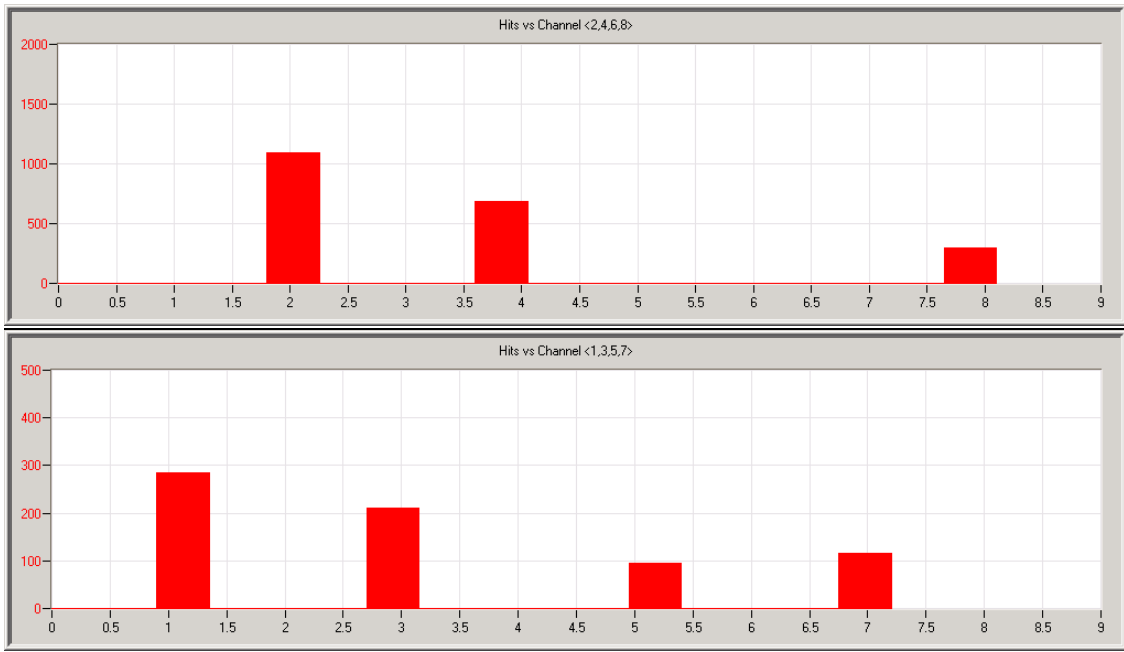
- The AE data shows activity beginning on sensors 1 and 2 (and 4 to some extent) once the previous maximum has been reached at about 155-160 seconds test time
- Load was continually increased and a significant burst of energy occurred at test time 166s (approx.) which resulted in internal failure of stiffening elements and a drop in the applied load level; this activity was detected by all sensors but originated in channels 1 and 2 (20m both tension/compression)
- Load application continued and AE activity began to increase again (sensors 2, 3, and 4) but at test time 192s (approx.) the structure failed resulting in a huge event detected by all sensors but originating at sensors 1 and 2 (20m both tension/compression)

Overview

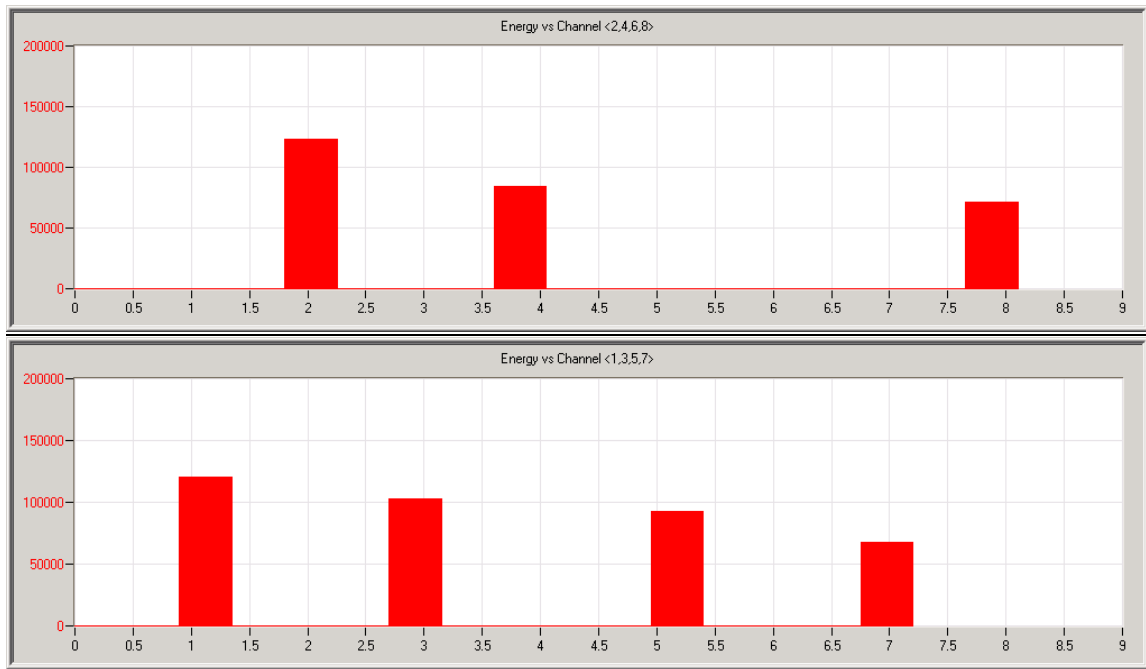


*DMT_2012_06_07_C (20120607)
Amplitude vs. test time*

Note the build up in AE activity to the initial failure event (at 166s) followed by the build up of AE again as the load relaxation due to initial failure is taken up and the structure fails at 192s.

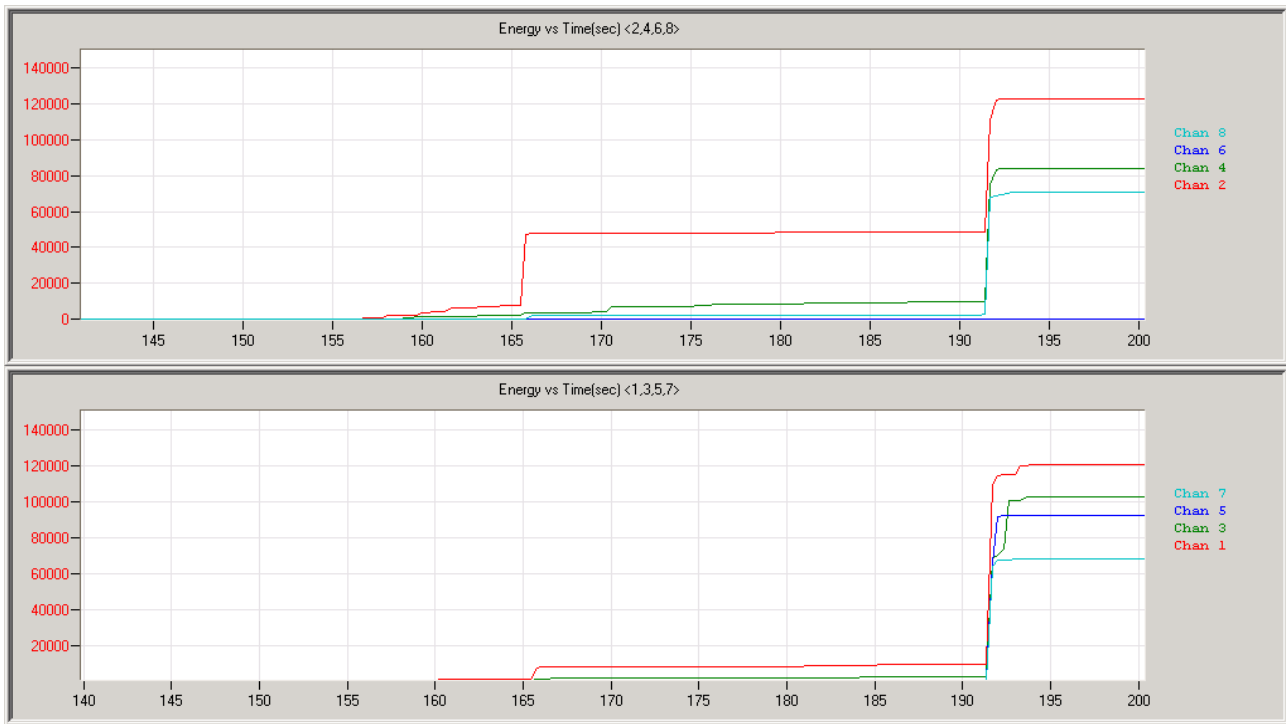


DMT_2012_06_07_C (20120607)
Channel activity (Hits) for Tensile (upper) and Compression (lower) cap faces



DMT_2012_06_07_C (20120607)
Channel activity (Energy) for Tensile (upper) and Compression (lower) cap faces

These graphs show the distribution of activity (Hits and Energy) along the tension and compression caps. As in previous tests the extent of local deflection in the structure determines how much AE is detected; the further along the beam towards the tip, the greater the amount and intensity of the AE activity.

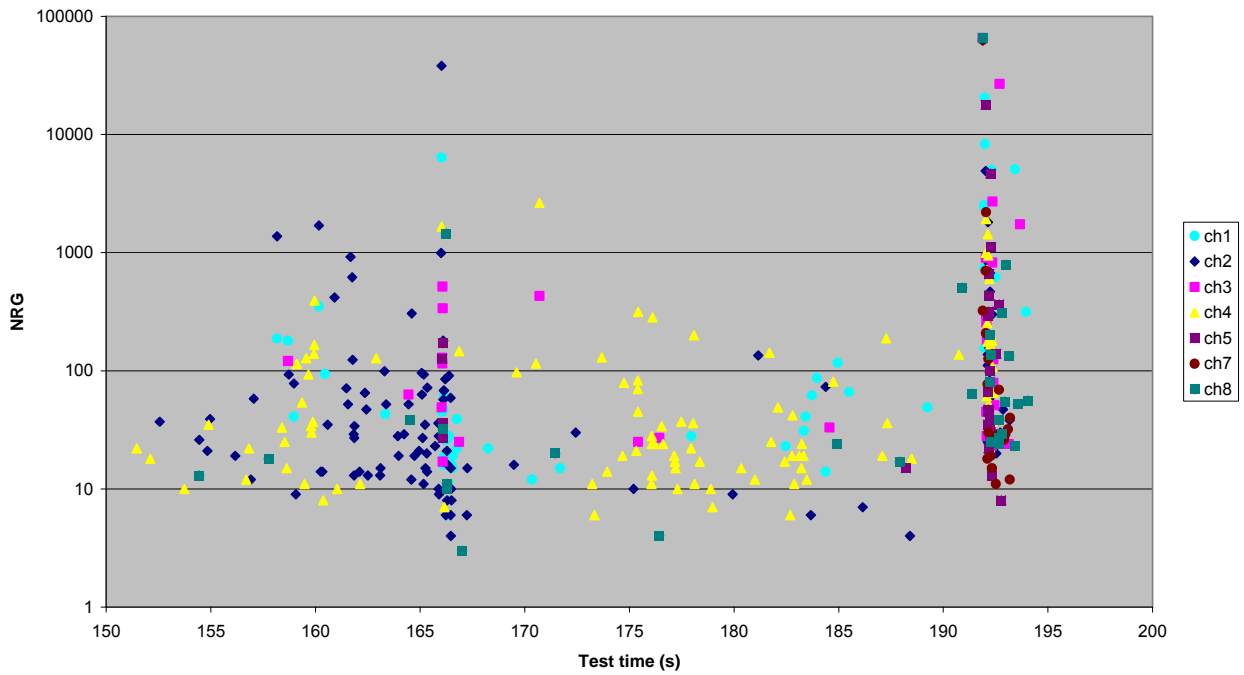


DMT_2012_06_07_C (20120607)

AE energy trace for the tension (2,4,6,8) and compression (1,3,5,7) face sensors

These traces show the initial AE activity burst at 166s (on ch2 and 1) followed by the failure at 192s (on all channels, but initially on ch2 and 1 again).

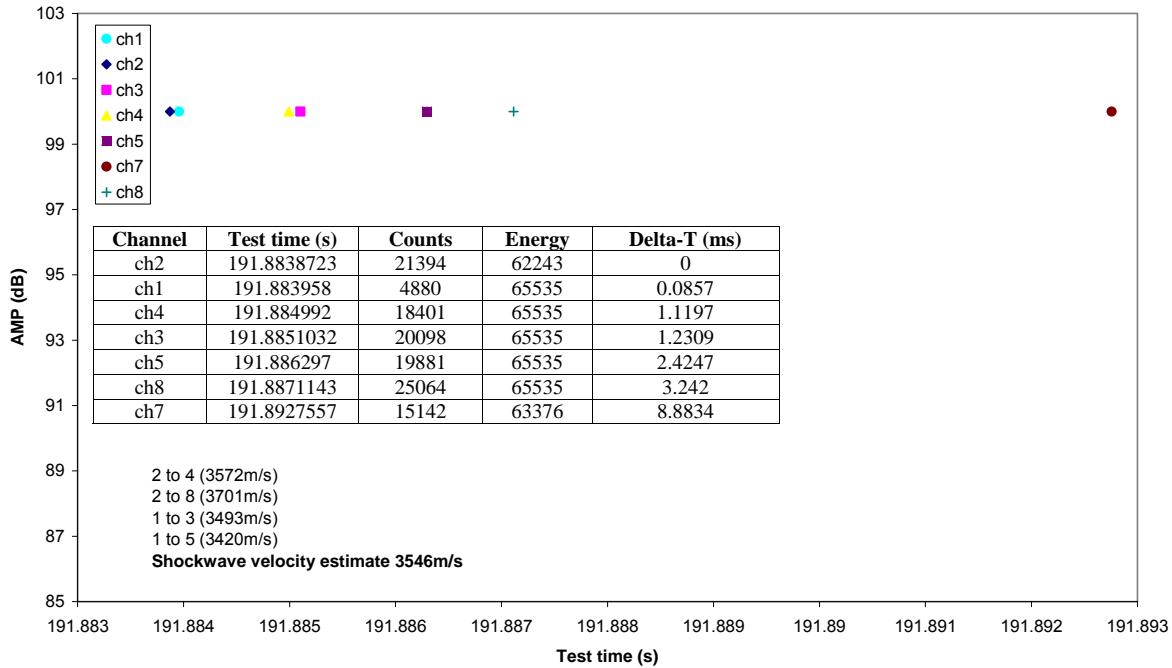
Load11 (20120607) Sensor activity during break



DMT_2012_06_07_C (20120607) Sensor activity (Energy) at failure by sensor

Note that the y-axis is logarithmic to highlight the activity before initial failure and between initial and ultimate failure. In both cases activity at sensor 4 (tension face 16m) is prevalent suggesting the presence of damage here (possibly a developing interface failure from the damage that initially occurred during DMT_2012_05_31_A + B).

Load11 (20120607) Sensor activity during break



DMT_2012_06_07_C (20120607)

Sensor response at high AMPLitude during the moment of ultimate failure

This “close-up” of the failure event shows the 100dB events that occur on each of the seven working sensors at the moment of failure. The initial event is at test time 191.8838723s on channel 2. The events occurring subsequent to this allow an estimate of the shockwave velocity in the structure. Note that there are large errors associated with this calculation due to both the macroscale placement of the sensors at roughly 20m, 16, 12m, and 8m chord lengths, and the slight variations in the “event time” calculated by the AE system for a travelling, dispersive stress wave.

These calculations give a value between 3420 and 3701 m/s, with an average of 3546m/s. This is slightly higher than might be estimated for a glass UD composite, but it is in the correct range.

This plot also confirms the video (and strain gauge?) evidence of a failure occurring at the tip (loading application) and propagating down the length of the beam.

SSSSSSSS

mmmuuun	CH	COUN	ENER	AMP
158.1648	2	102	1372	99
160.1666	2	108	1696	100
165.9961	2	81	992	99
166.0219	2	5940	38144	100
166.0219	1	1532	6380	96
166.0756	3	70	338	95
166.2334	8	332	1453	100
170.7024	4	326	2633	100
191.8839	2	21394	62243	100
191.884	1	4880	65535	100
191.885	4	18401	65535	100
191.8851	3	20098	65535	100
191.8863	5	19881	65535	100
191.8871	8	25064	65535	100
191.8928	7	15142	63376	100
191.9416	1	10	2472	100
191.9514	1	11	738	99
191.958	1	80	2525	97
191.9784	1	76	20509	100
191.9969	1	19	8320	100
192.0836	4	1152	714	95
192.1351	2	1799	1811	98
192.2994	1	21	5017	100
192.4878	1	2	621	100
192.6922	3	1524	26807	100
193.4236	1	19	5082	100

Data read-out for the final test (*DMT_2012_06_07_C*)

Filtered to remove all hits under 95dB

Note:-

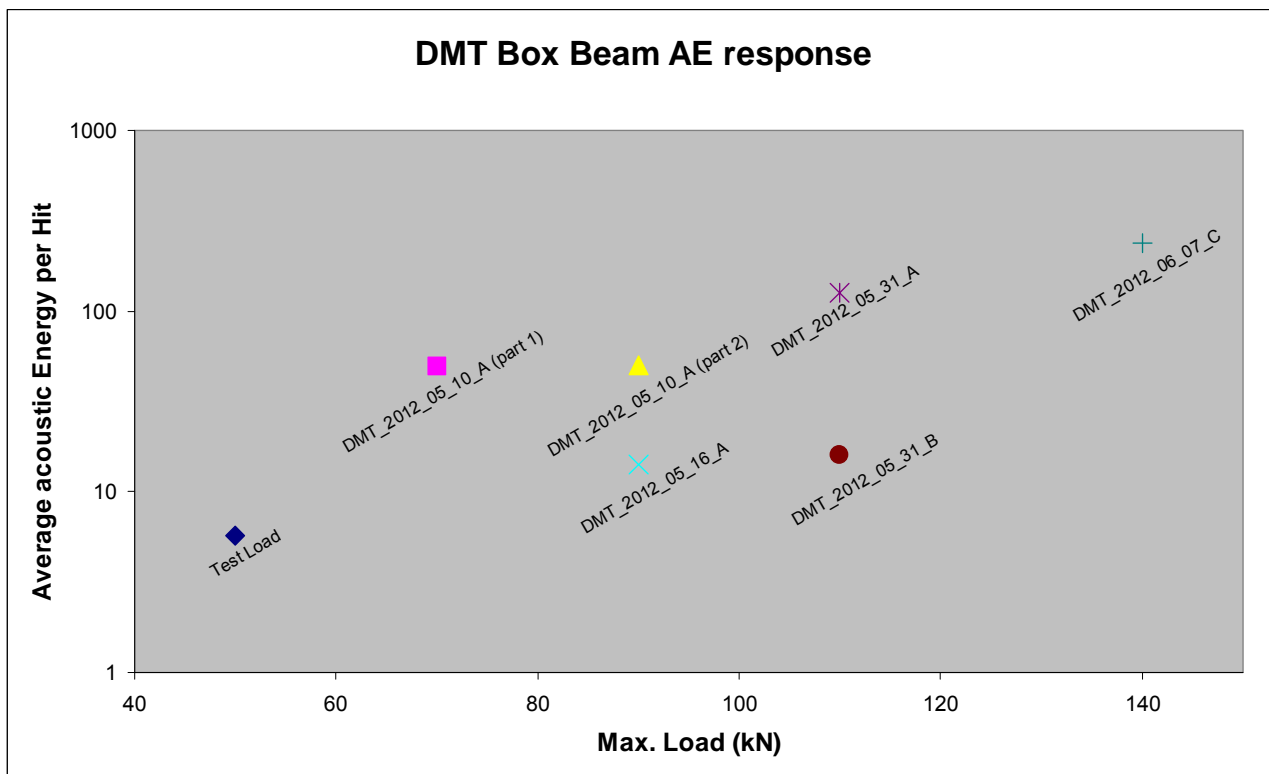
Initial event at 166s on sensor 2 (TEN 20m)

Intermediate event at 170s on sensor 4 (TEN 16m)

Failure event at 192s on all sensors (starting at s2, TEN 20m)

	Start time	Max Load (kN)	NRG/Hit
Test Load	10/05 1200	50	5.7
DMT_2012_05_10_A (part 1)	10/05 1209	70	49.6
DMT_2012_05_10_A (part 2)	10/05 1211	90	50.2
DMT_2012_05_16_A	16/05 1250	90	14.1
DMT_2012_05_31_A	31/05 1414	110	125.5
DMT_2012_05_31_B	31/05 1427	110	15.9
DMT_2012_06_07_C	07/06 1133	140	238.6

This graph shows the relative structural AE response for each test against the maximum applied load. It illustrates the increase in the amount of AE relative to the applied load (note the logarithmic y-axis) and also the Kaiser principle where the second loading to a previously achieved load level gives much less AE, only when the previous load level is exceeded does the AE begin at high intensity again...



Appendix E Baumer Blade Monitor System Description

The system is an optical based device to **measure displacements**. It consists of:

- one **camera** mounted on the test rig
- two **reflectors pairs** mounted on the box girder respectively at 10m and 16m from the root

The following image illustrates the system setup.

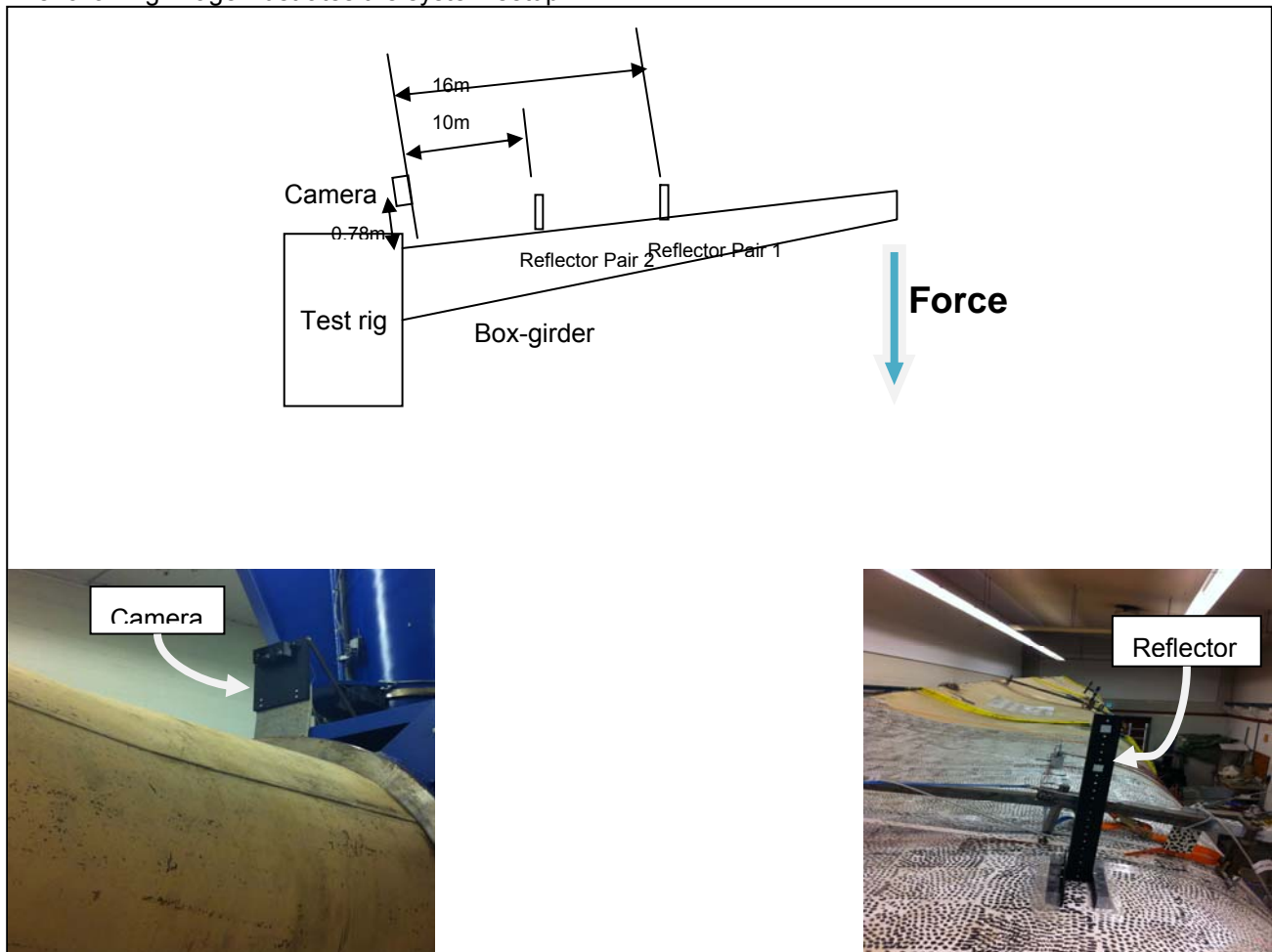


Fig. 1 Baumer Blade Monitor: system overview.

1.1 Functioning Principle

The Baumer Blade Monitor uses an active illumination camera approach. At the measurement distances retro-reflectors are attached to the box-girder. The active illumination of the camera causes a strong reflection towards the receiver optics of the camera. The reflectors are reproduced as spots on the CMOS or CCD sensor. The positions of these spots are proportional to the angle of the retro-reflectors and the optical axis of the camera. The principle is shown in Fig. 2. This figure also indicates the algorithms used to deduce deflection and torsion. The optical principal allows for the very high accuracy for small and large positional changes of the reflectors. The angular resolution exceeds 0,0002deg, which allows detecting displacements in the order of 50 μ m at the reflectors distance.

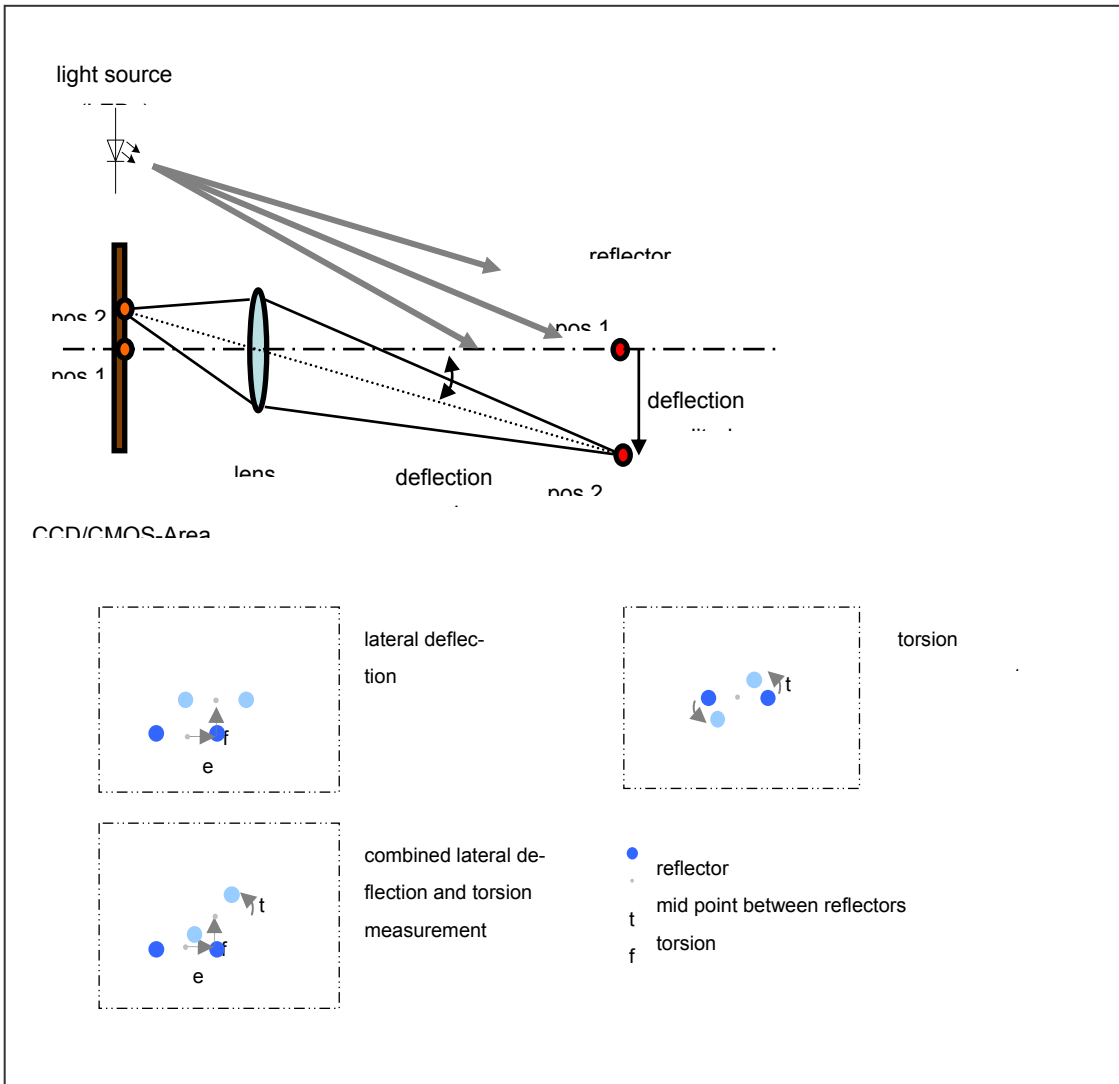


Fig. 2 Baumer Blade Monitor: Measurement principle.

Data Visualization DTU DMT data

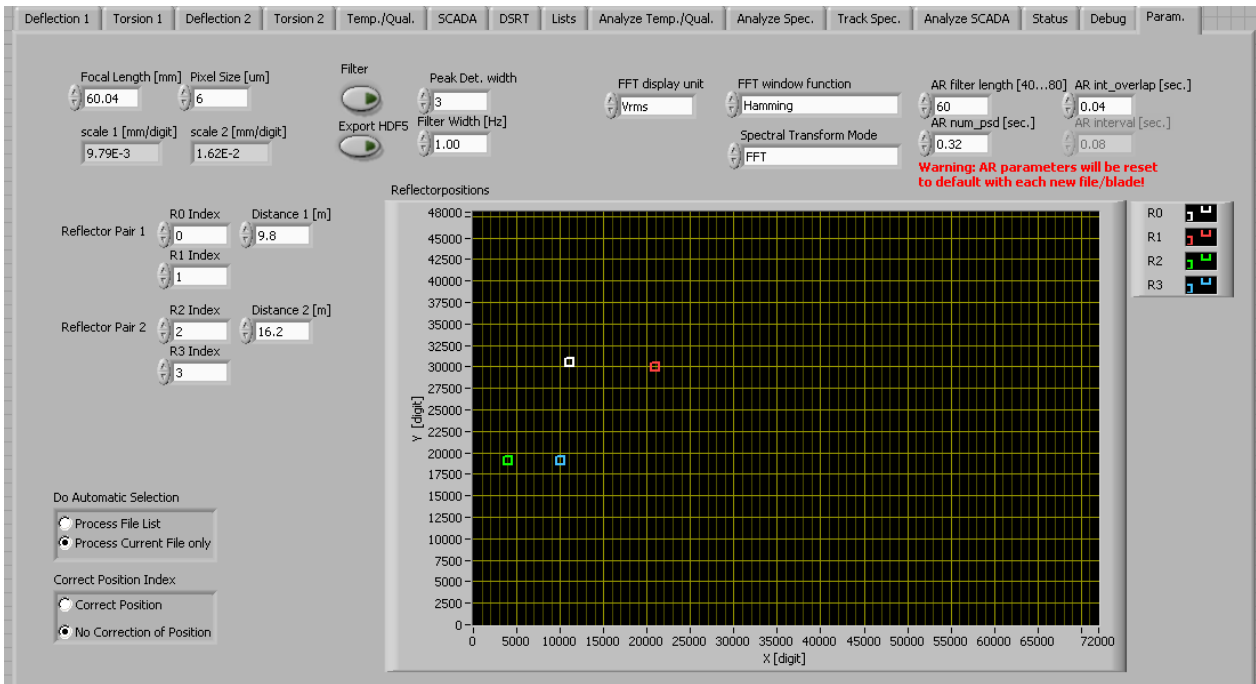
M Weigel

Date: 14.8.2012

Tool Version: Blademonitor Data Analysis.vi, rev. 662

Configuration (Param. Tab)

The correctness of the result depends on values of Focal Length, Pixel Size, Distance 1, Distance 2:



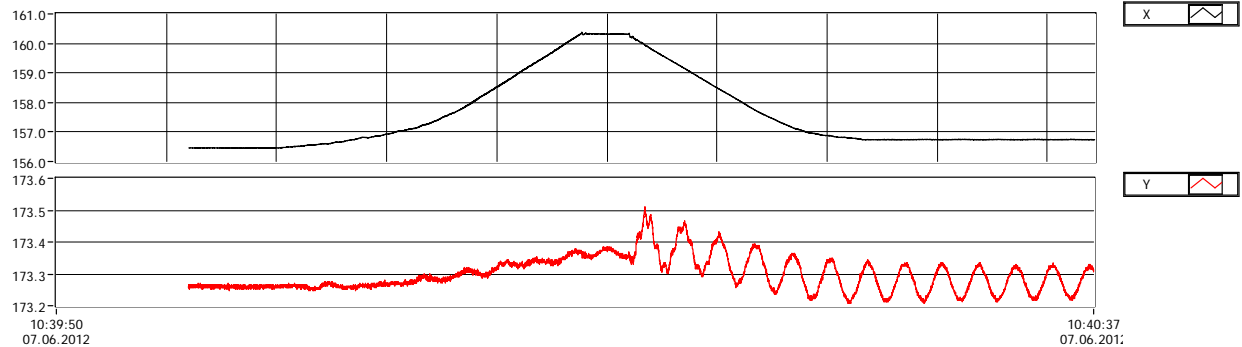
File Index CBF6192C

Position in File 9677

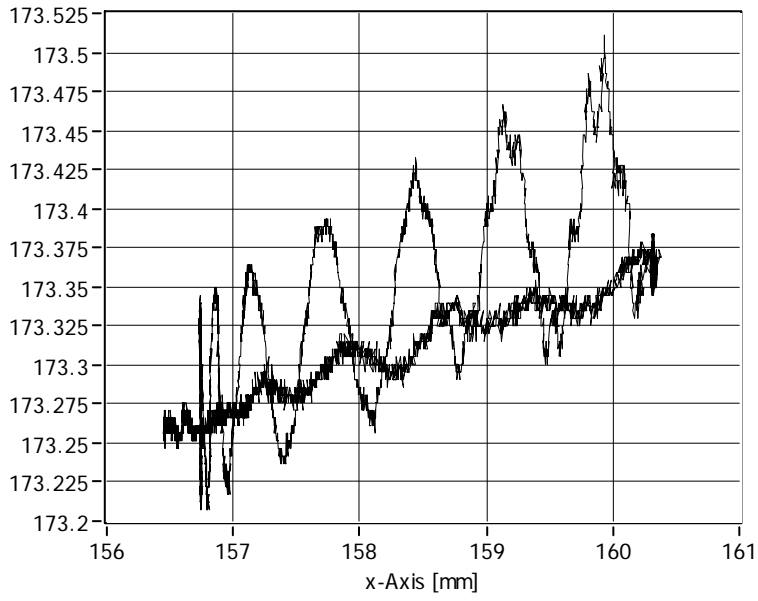
Sample Exponent: 13 (8192 analysis samples)

Deflection 1

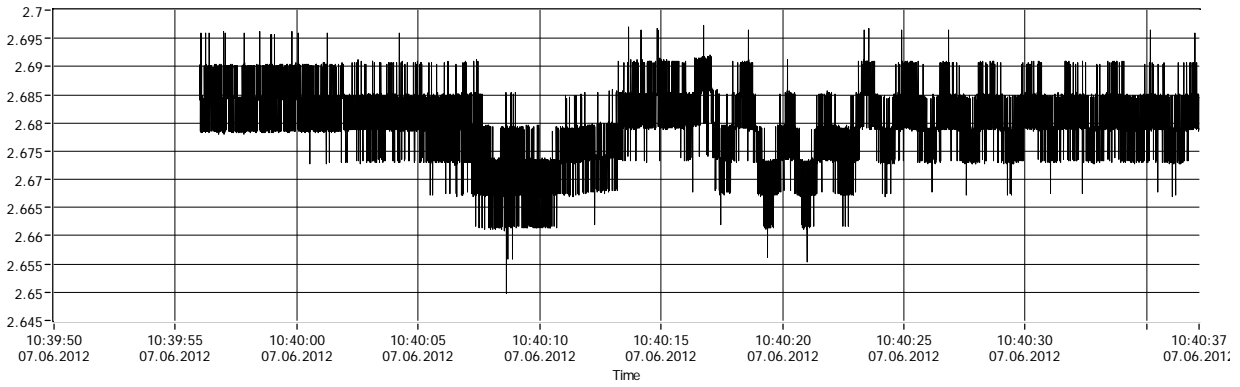
Deflection 1



XY Deflection 1

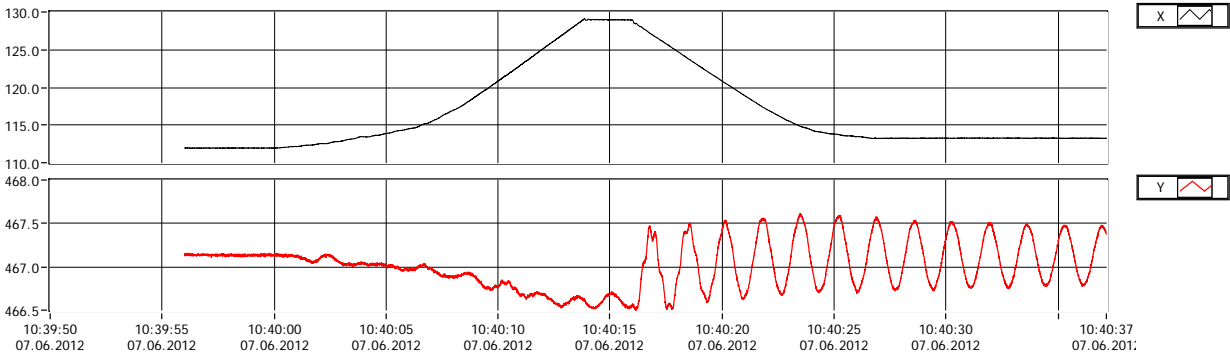


Torsion 1

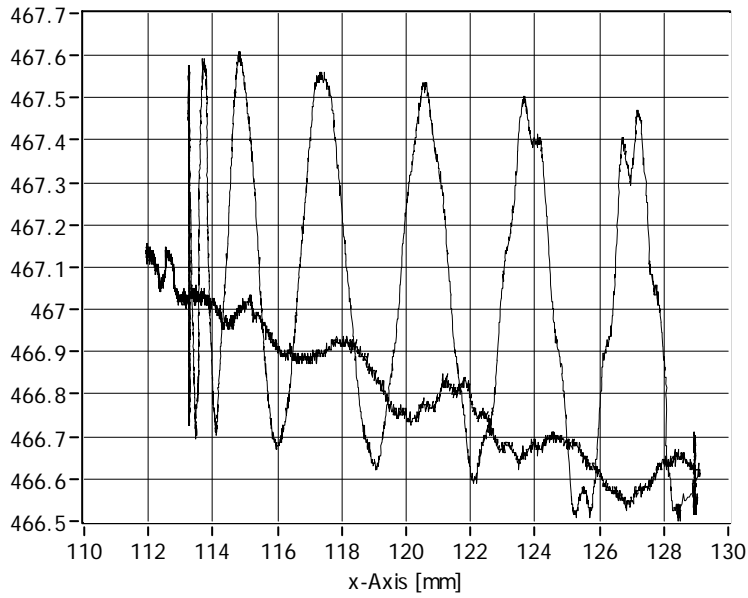


Deflection 2

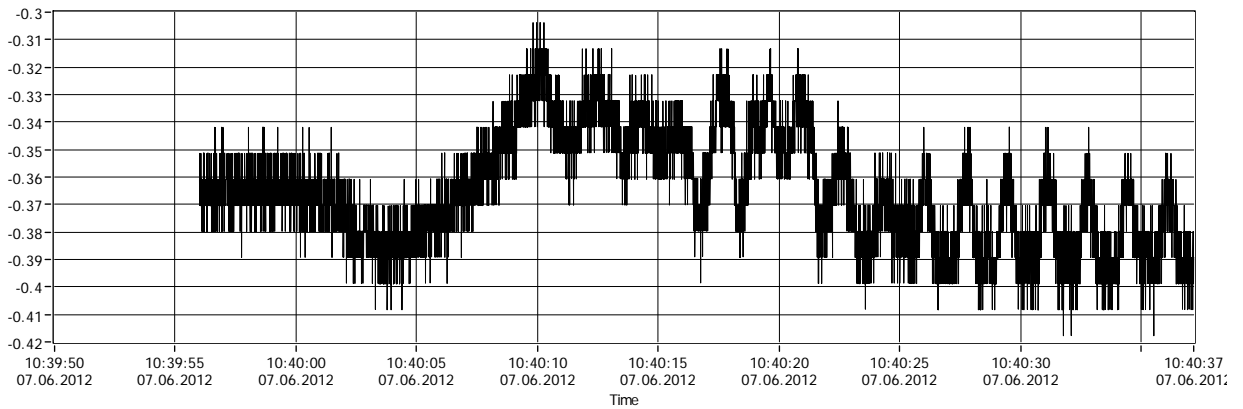
Deflection 2



XY Deflection 2



Torsion 2



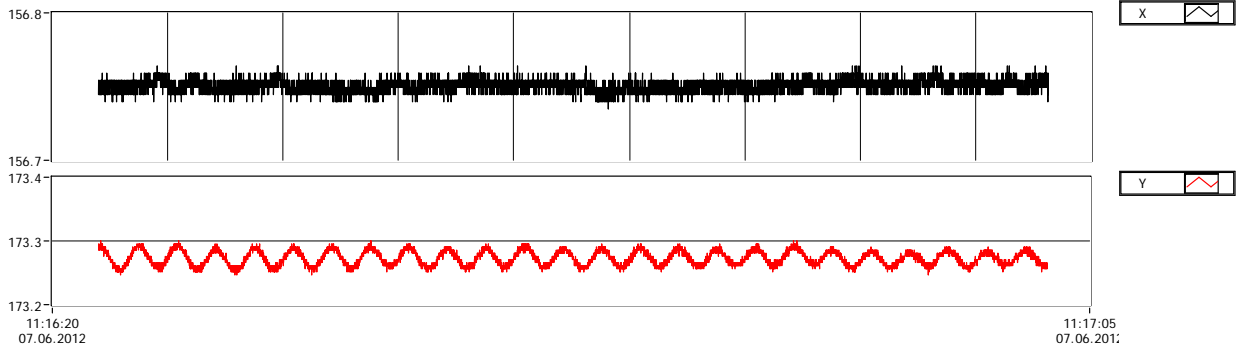
File Index CBF621E6

Position in File 0

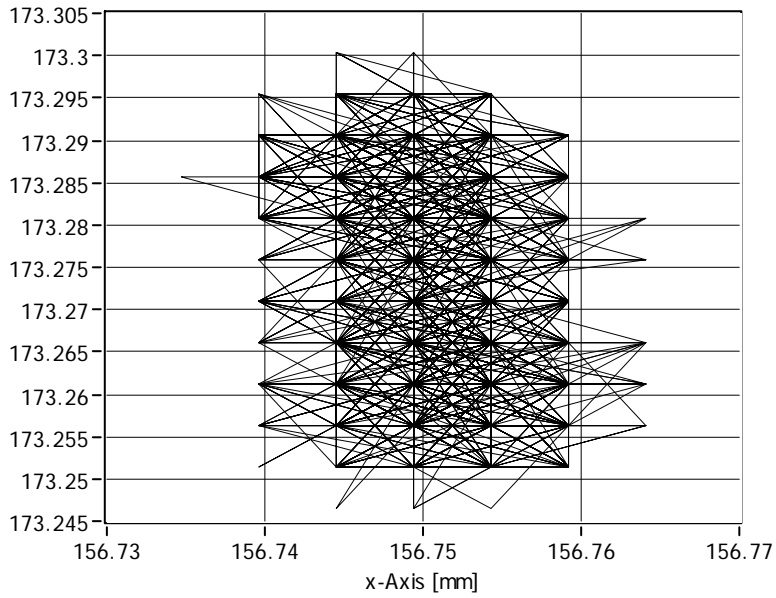
Sample Exponent: 13 (8192 analysis samples, 40.96sec.)

Deflection 1

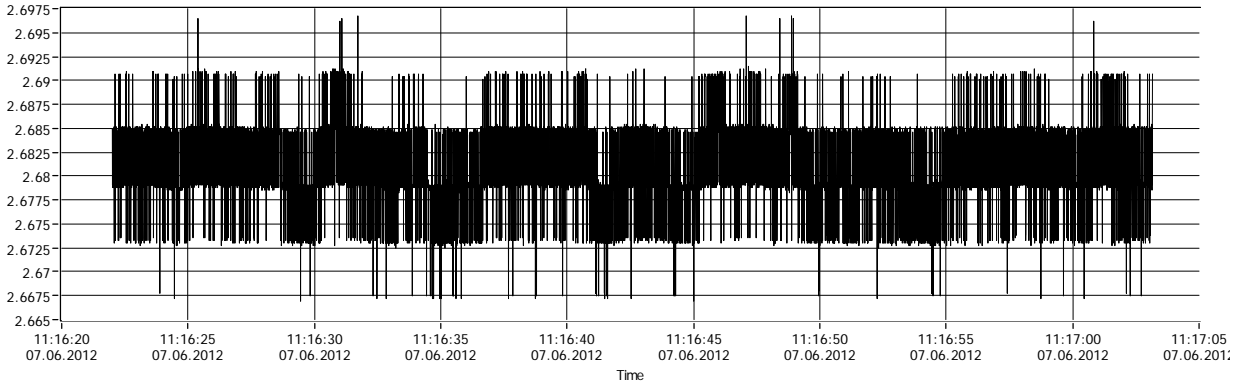
Deflection 1



XY Deflection 1

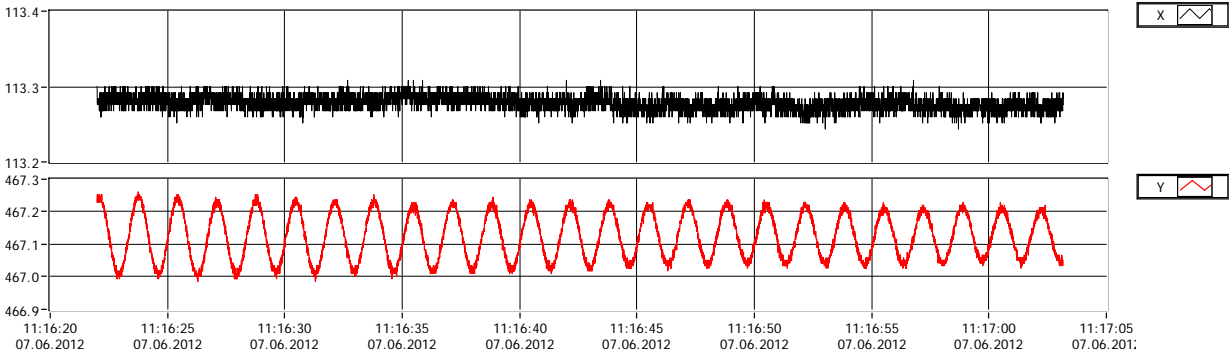


Torsion 1

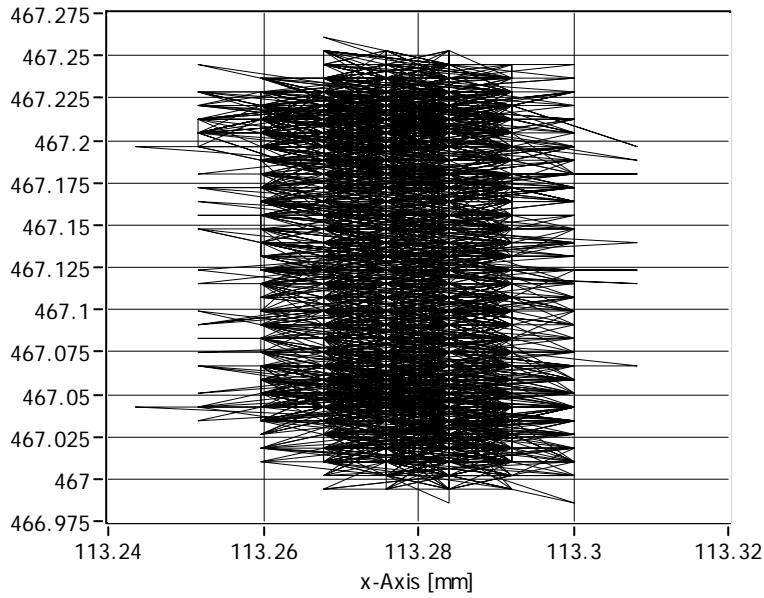


Deflection 2

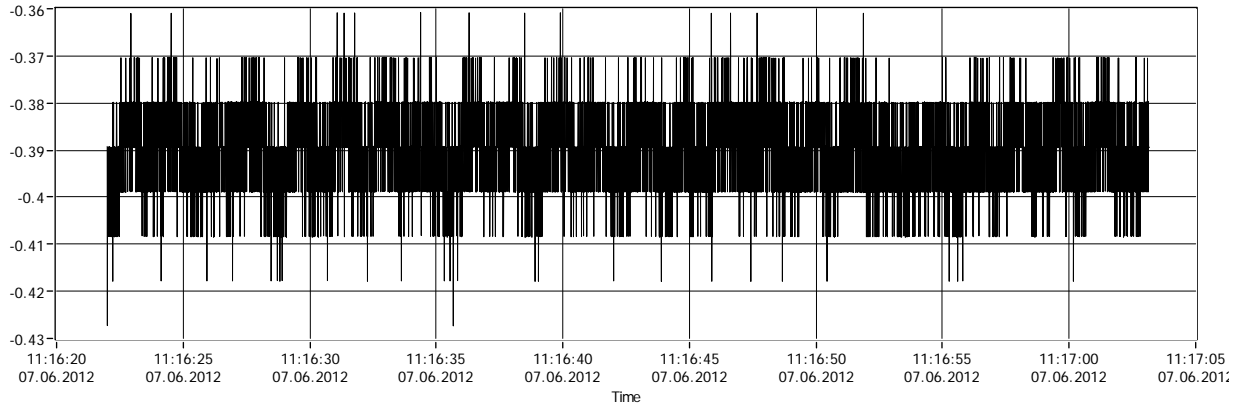
Deflection 2



XY Deflection 2



Torsion 2



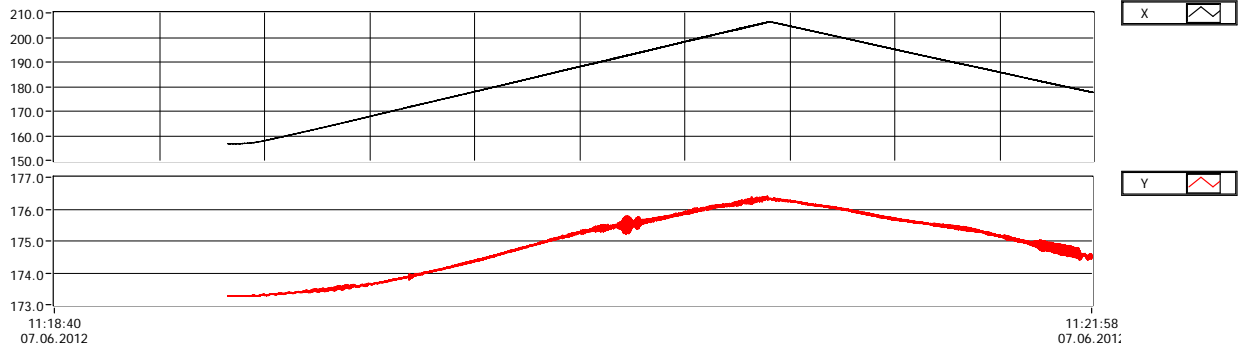
File Index CBF62267

Position in File 8500

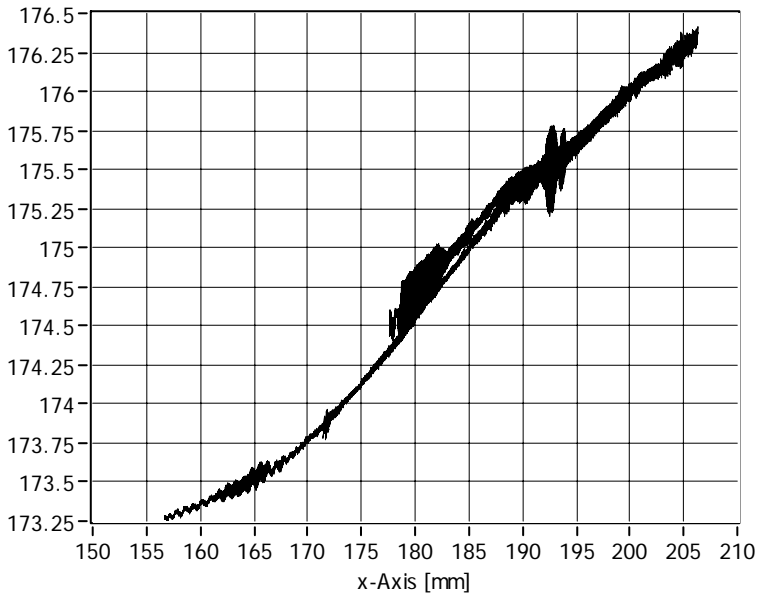
Sample Exponent: 15 (32768 analysis samples, 163.84sec.)

Deflection 1

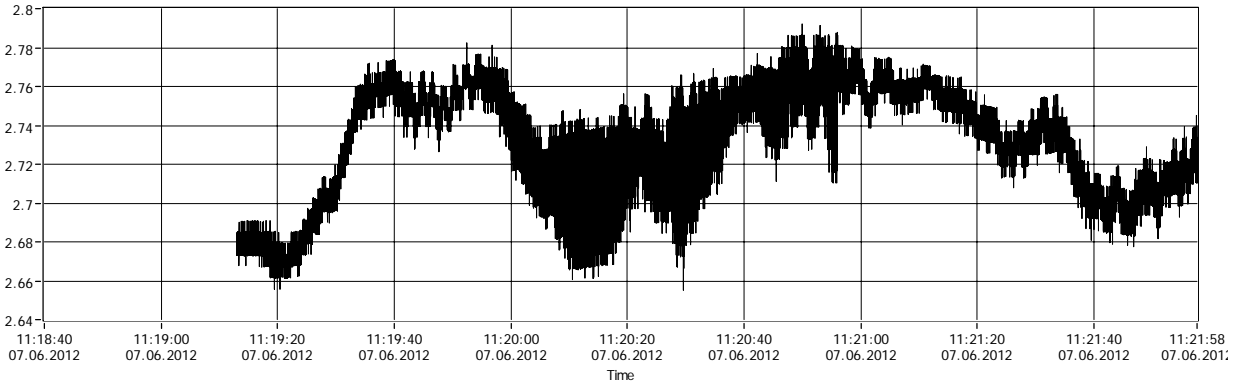
Deflection 1



XY Deflection 1

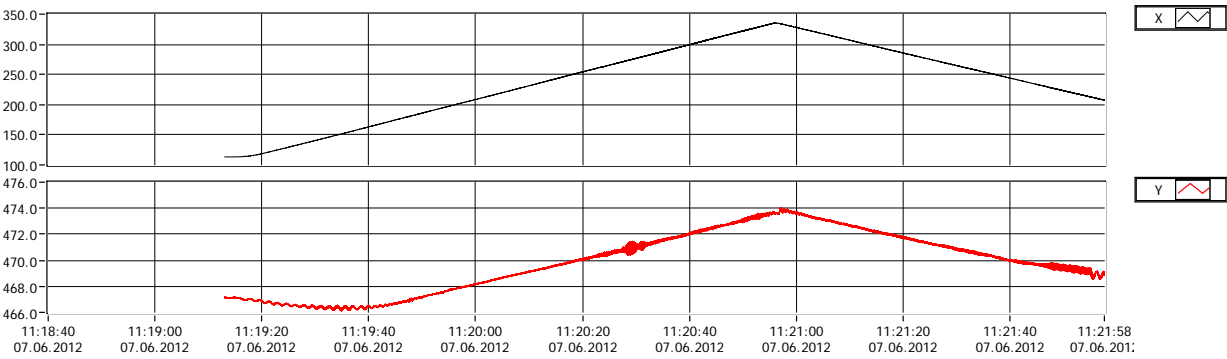


Torsion 1

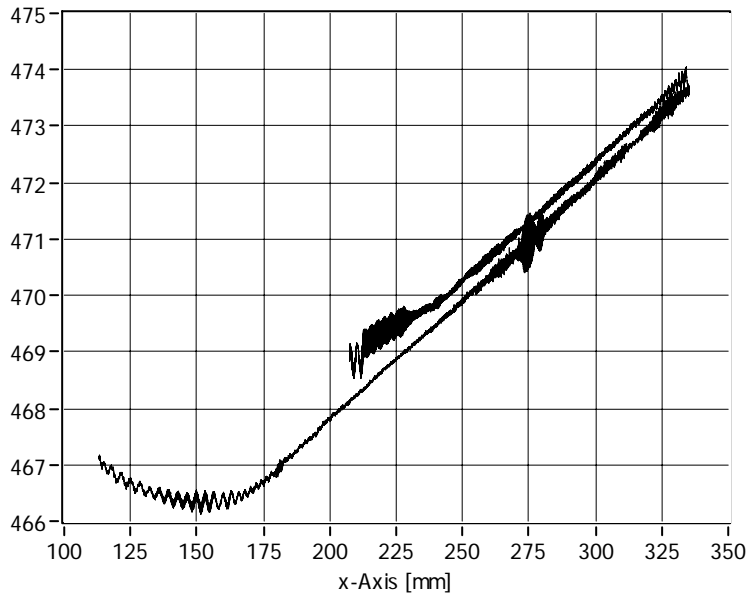


Deflection 2

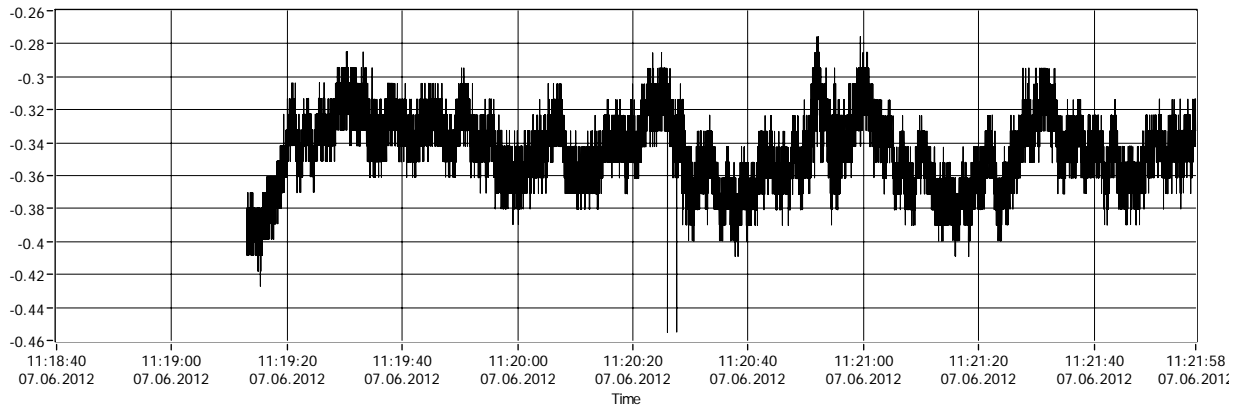
Deflection 2



XY Deflection 2



Torsion 2

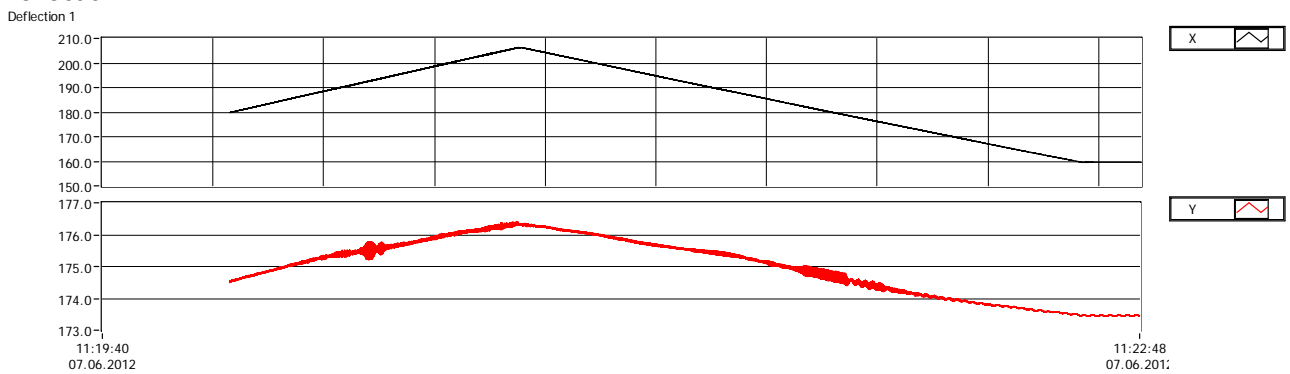


File Index CBF62267

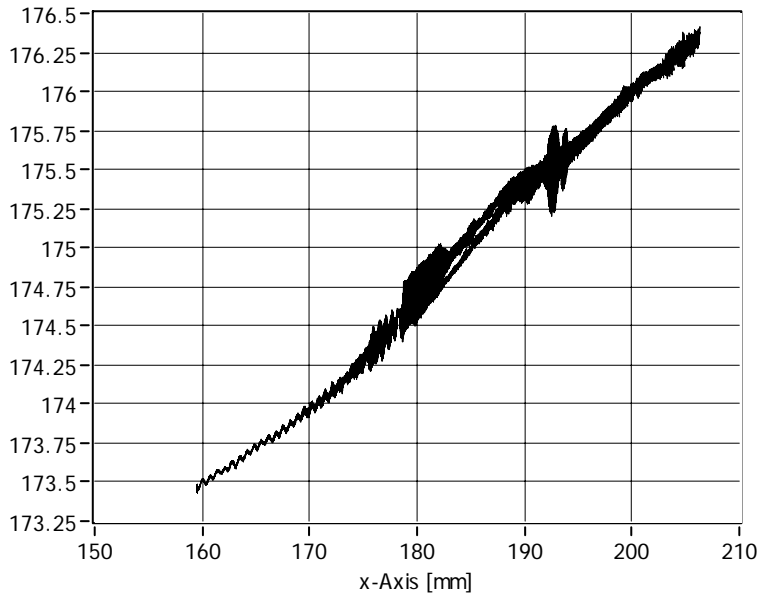
Position in File 18599

Sample Exponent: 15 (32768 analysis samples, 163.84sec.)

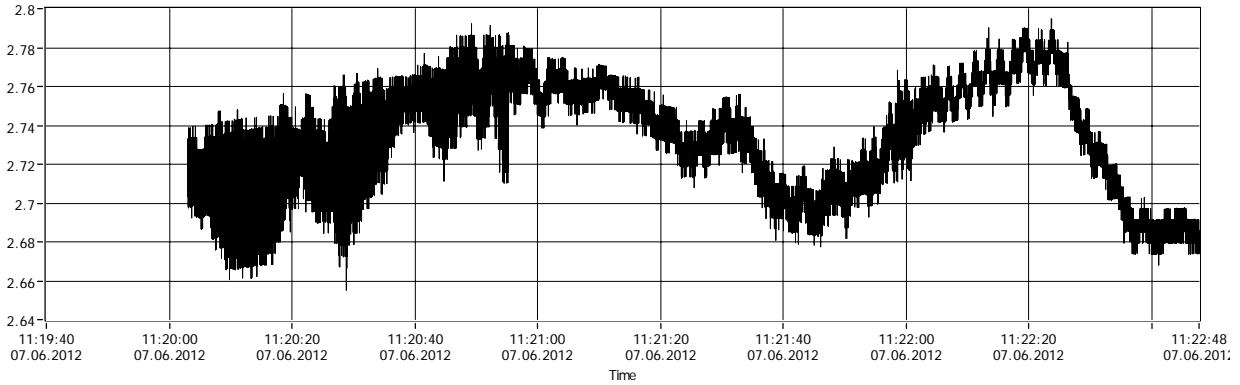
Deflection 1



XY Deflection 1

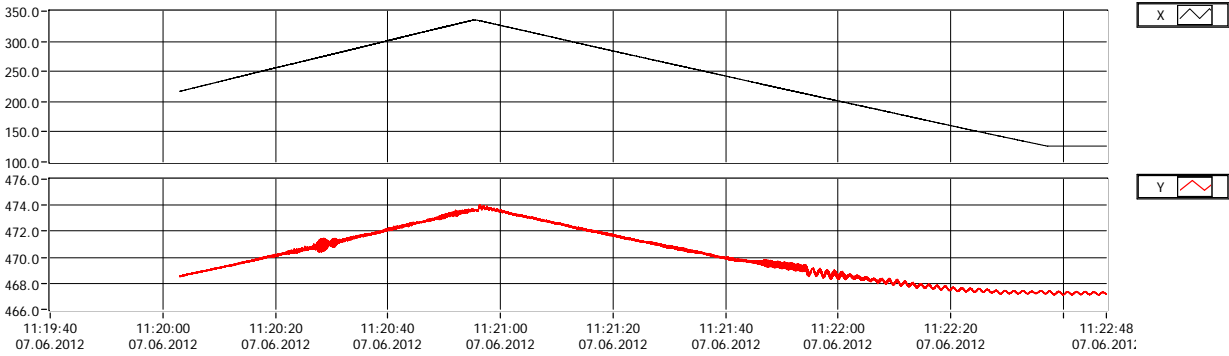


Torsion 1

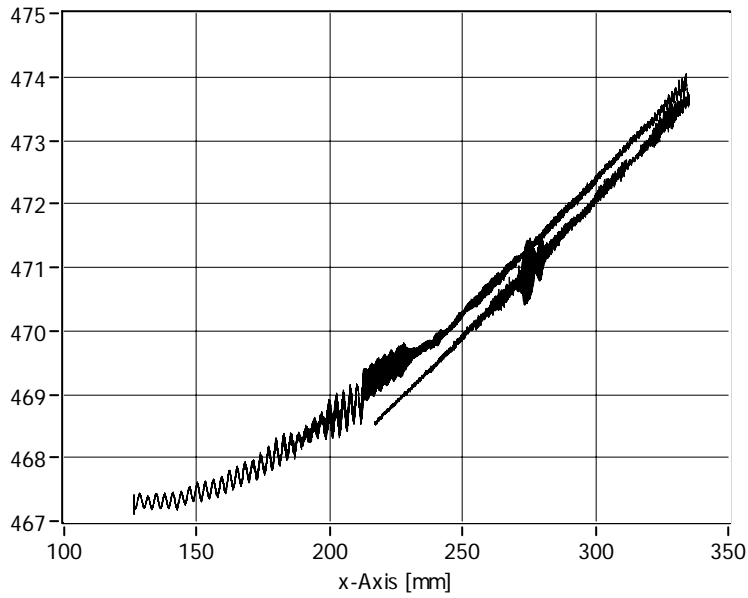


Deflection 2

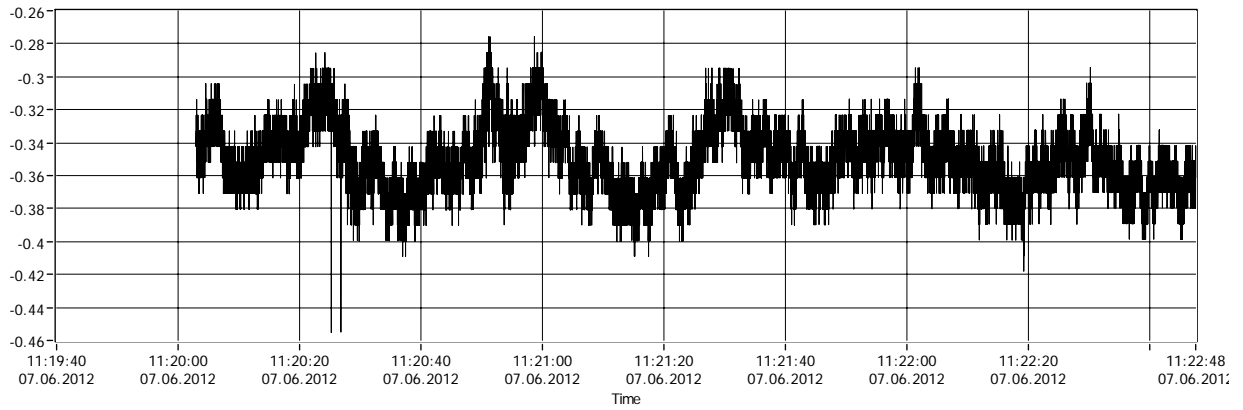
Deflection 2



XY Deflection 2



Torsion 2



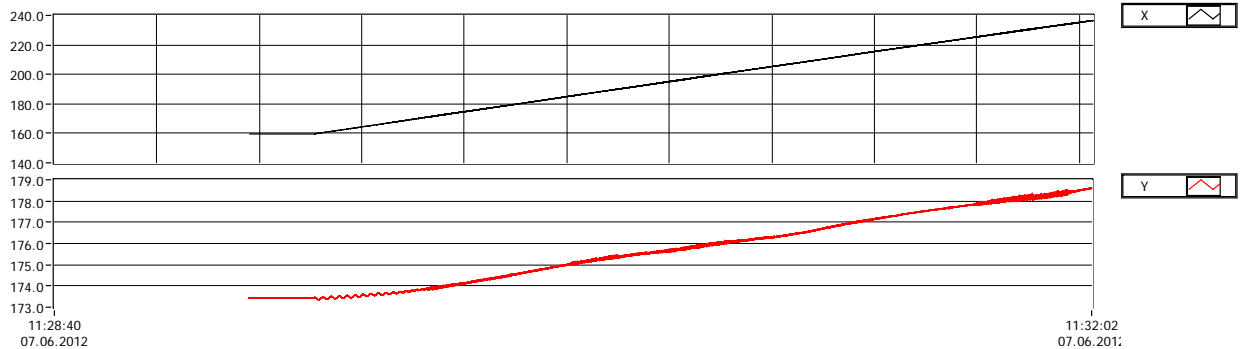
File Index CBF624D5

Position in File 5029

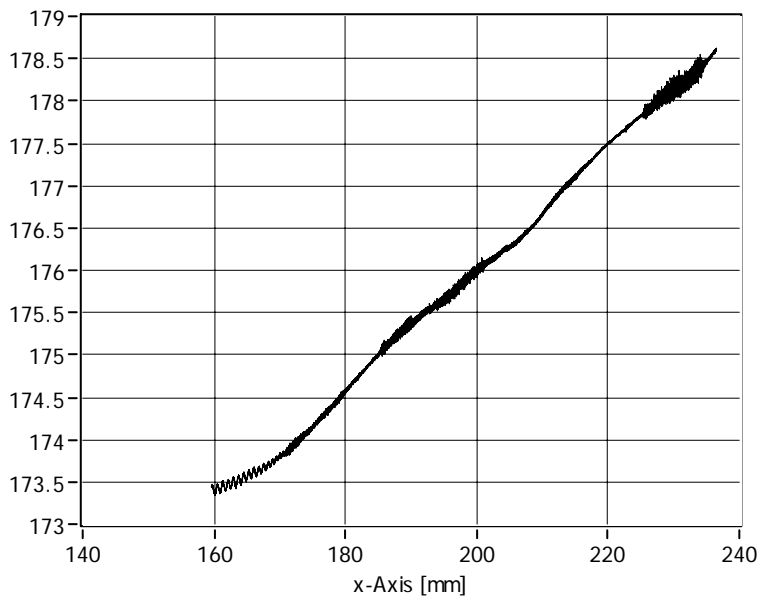
Sample Exponent: 15 (32768 analysis samples, 163.84sec.)

Deflection 1

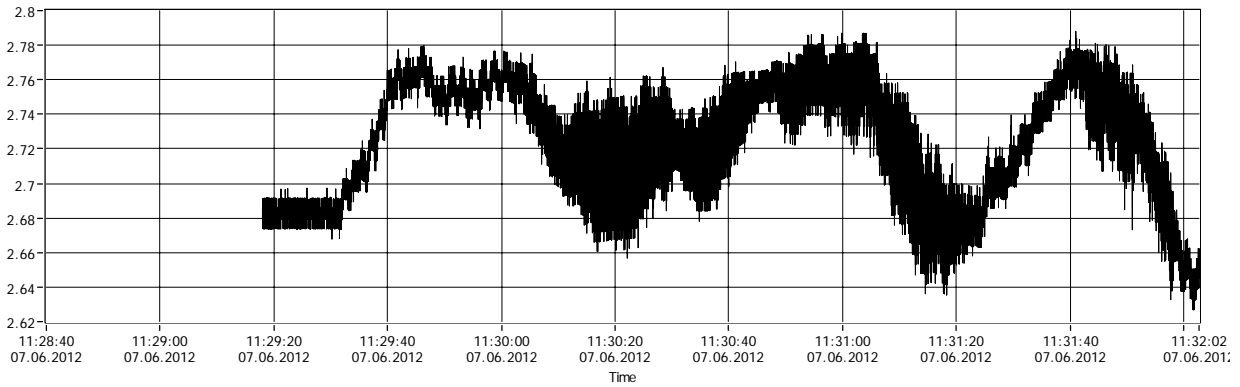
Deflection 1



XY Deflection 1

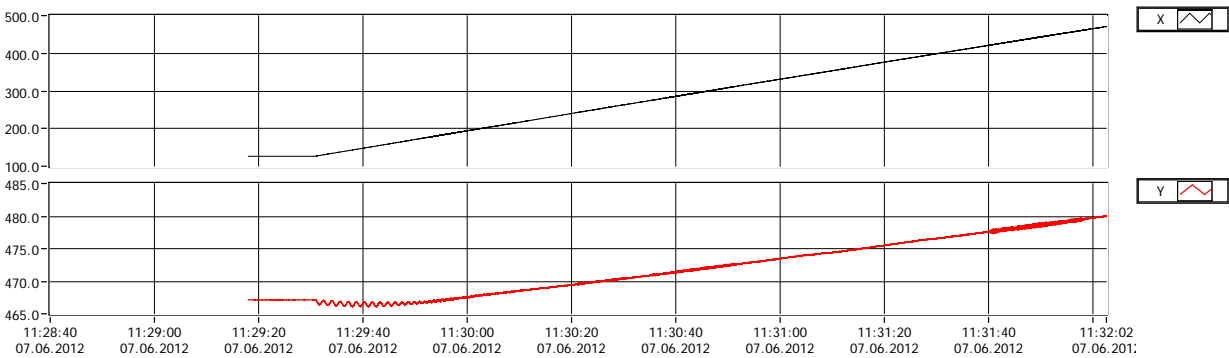


Torsion 1

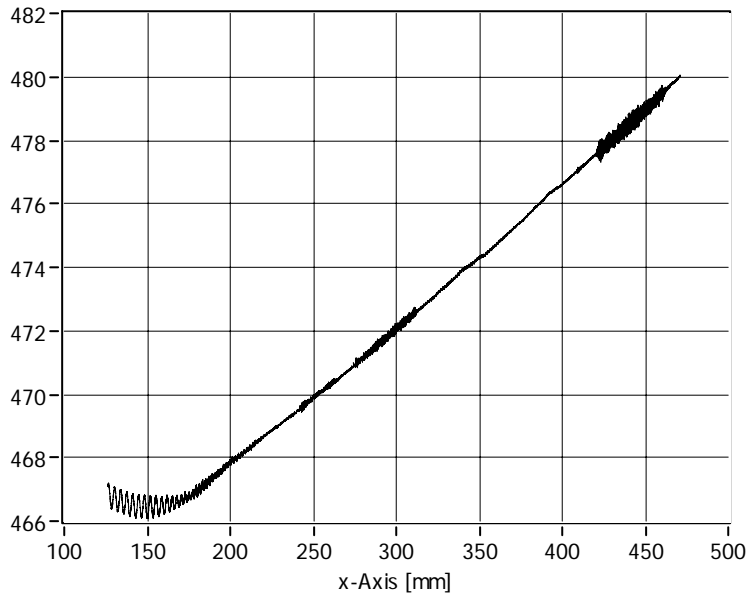


Deflection 2

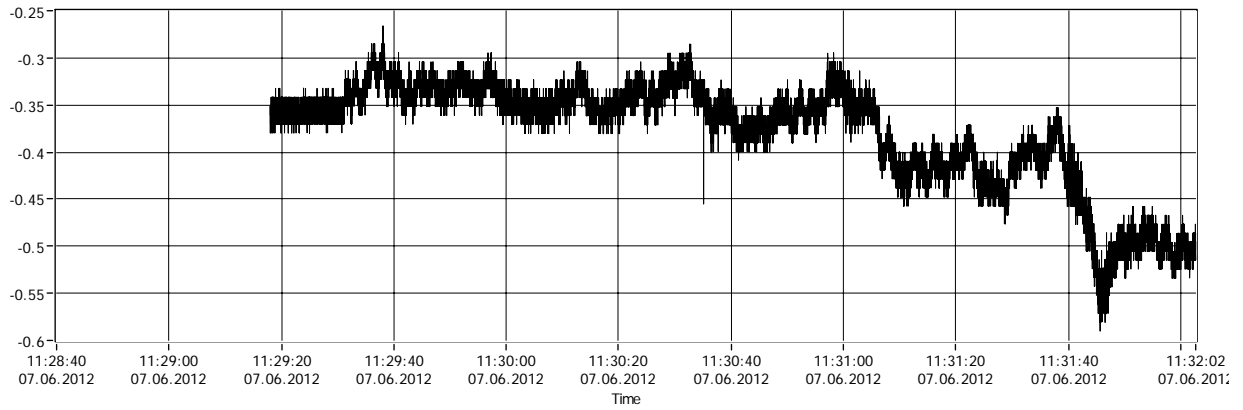
Deflection 2



XY Deflection 2



Torsion 2

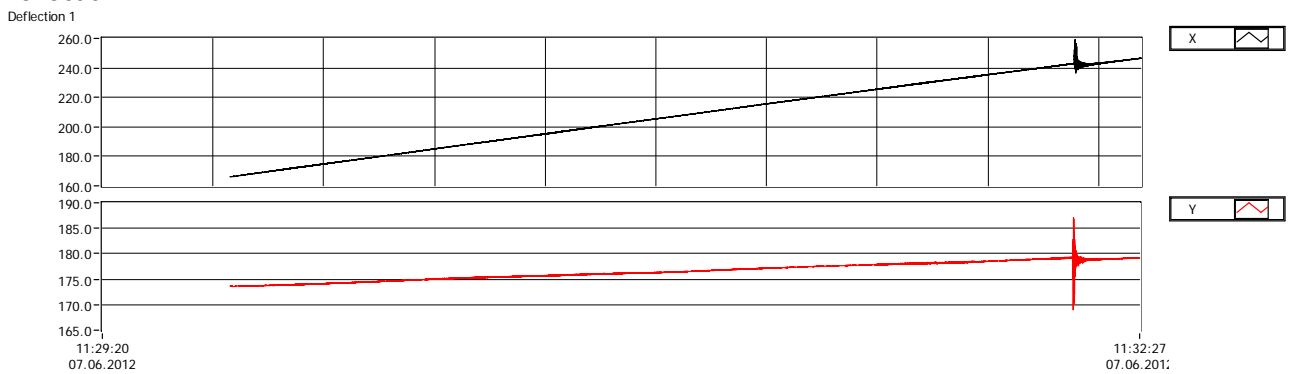


File Index CBF624D5

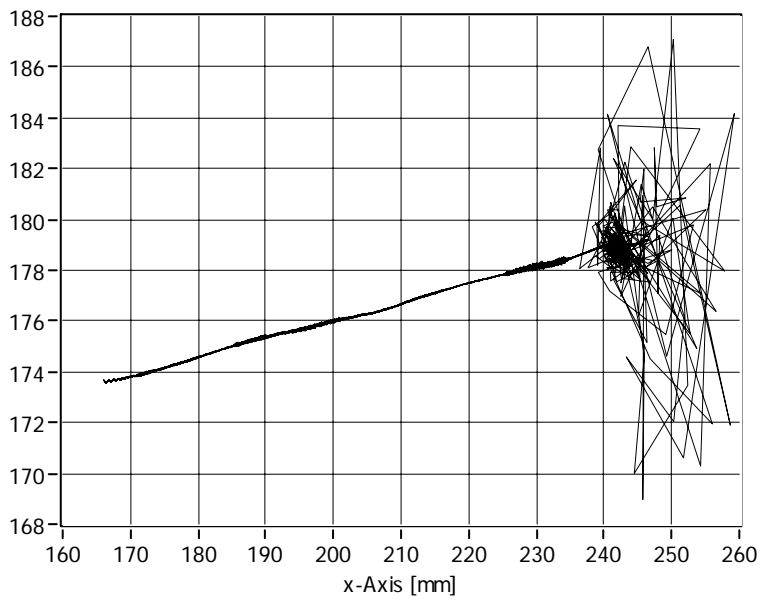
Position in File 10059

Sample Exponent: 15 (32768 analysis samples, 163.84sec.)

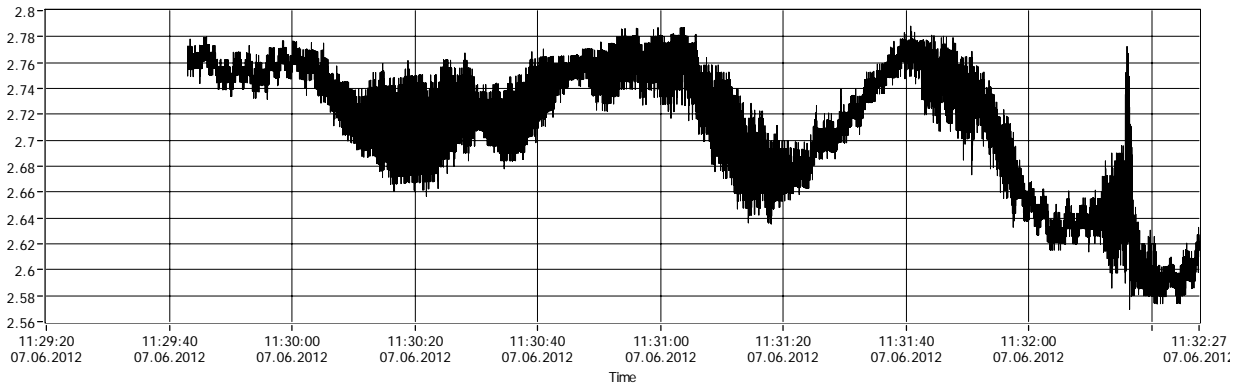
Deflection 1



XY Deflection 1

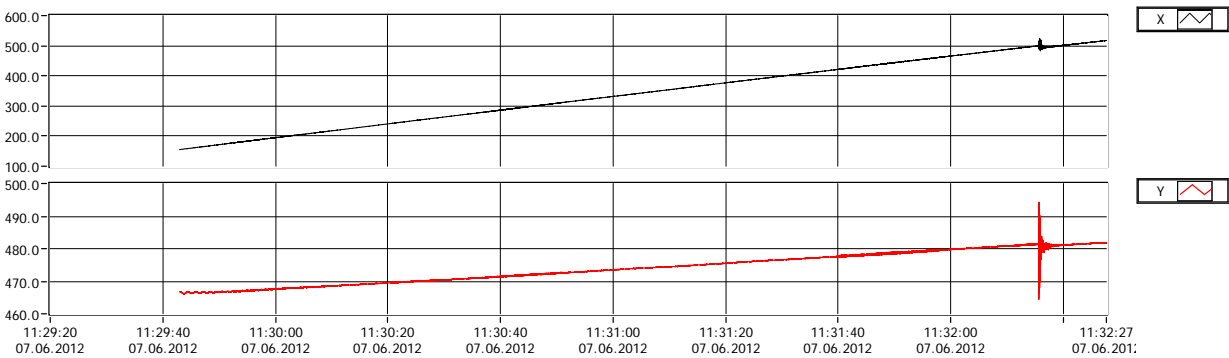


Torsion 1

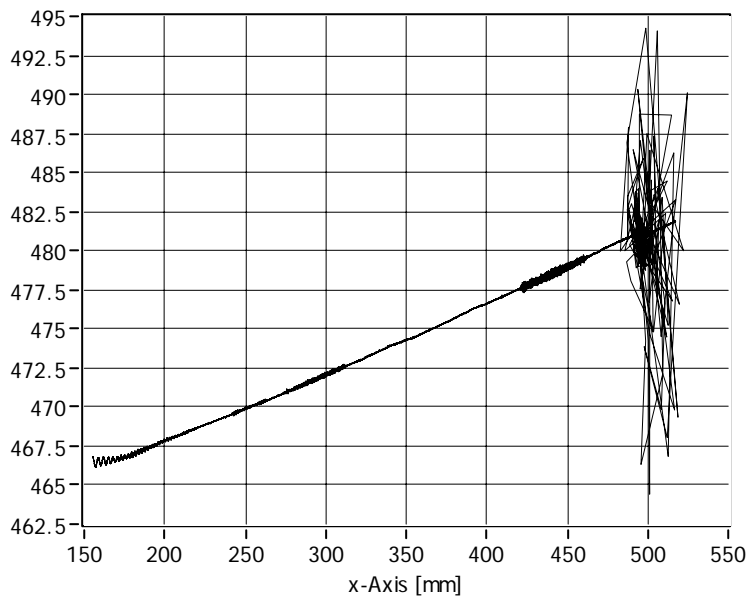


Deflection 1

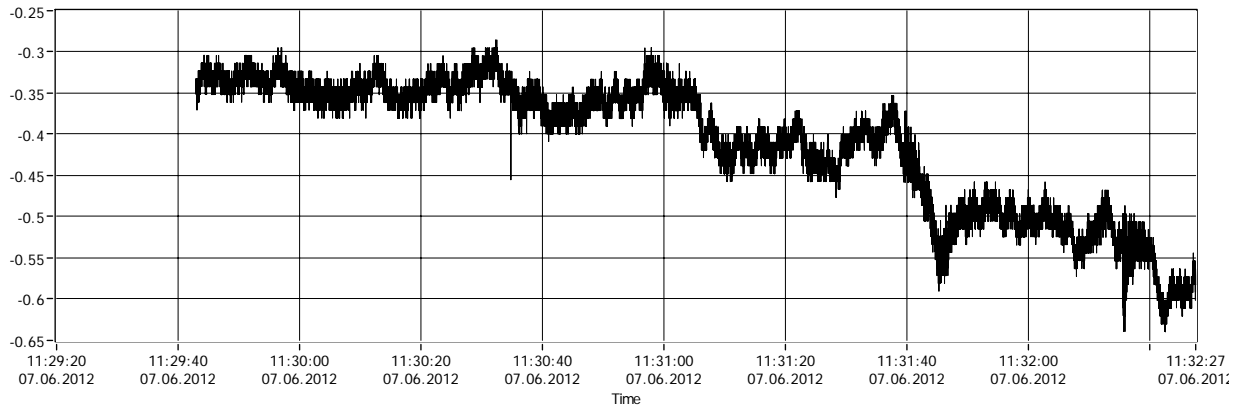
Deflection 2



XY Deflection 2



Torsion 2



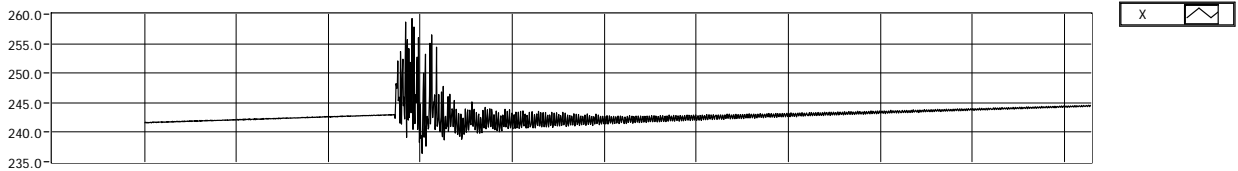
File Index CBF624D5

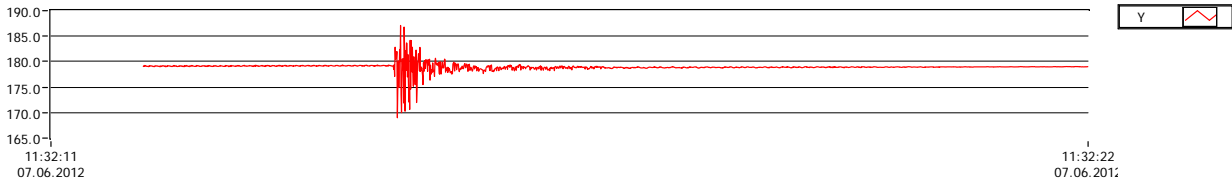
Position in File 39887

Sample Exponent: 11 (2048 analysis samples, 10.24sec.)

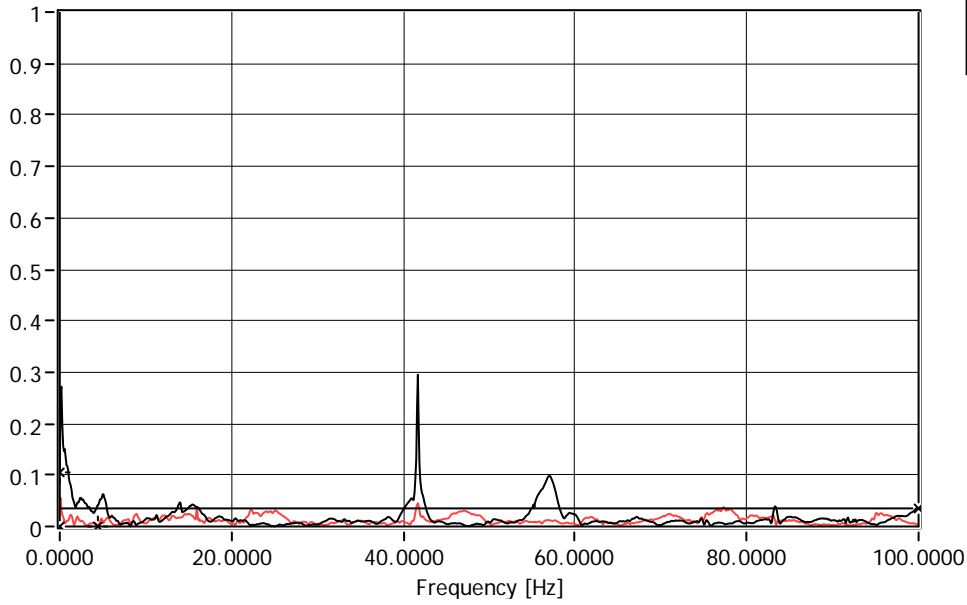
Deflection 1

Deflection 1

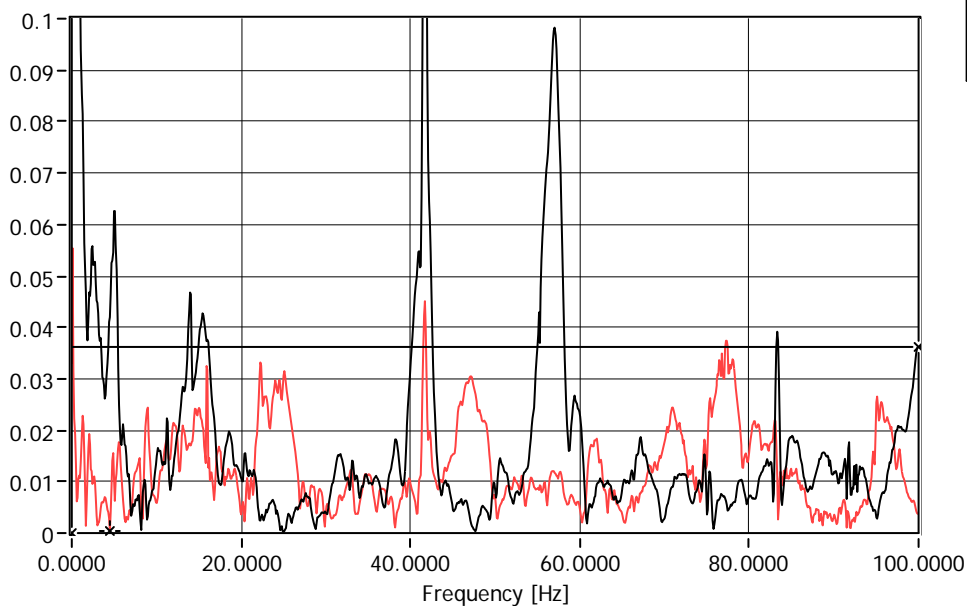




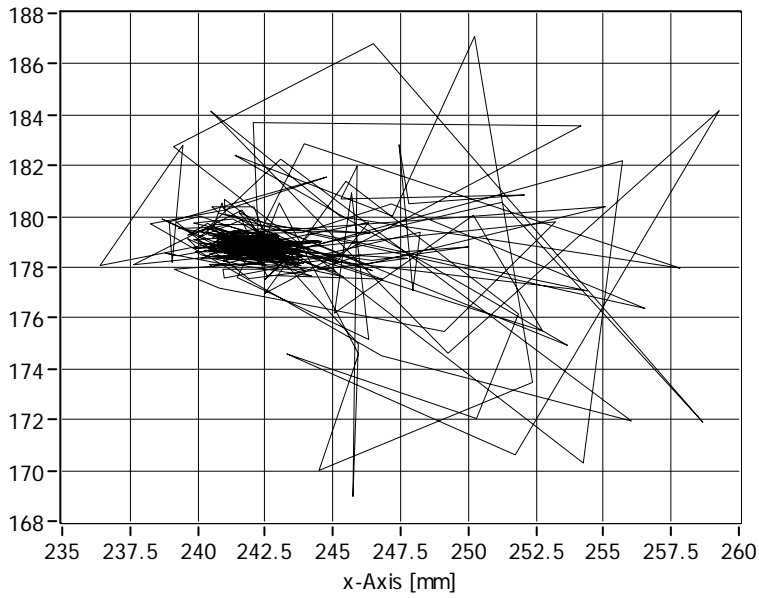
Spectra Deflection 1



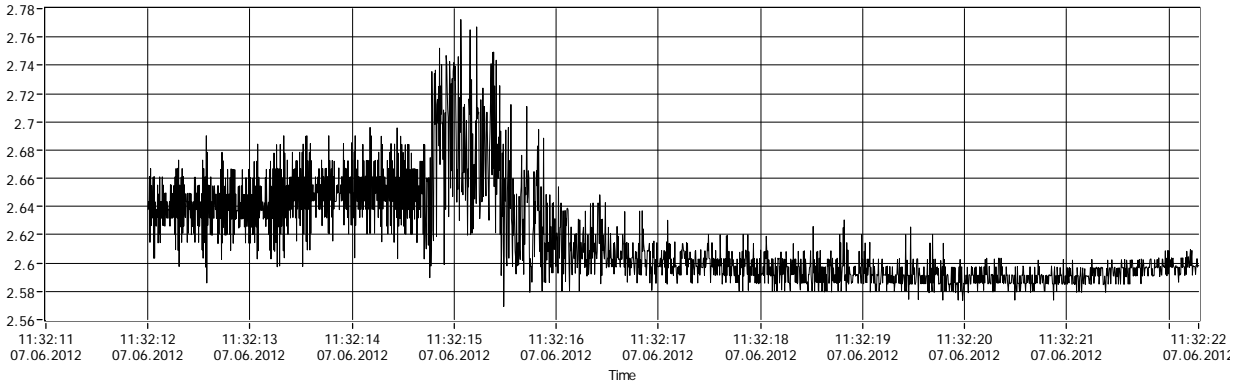
Spectra Deflection 1



XY Deflection 1

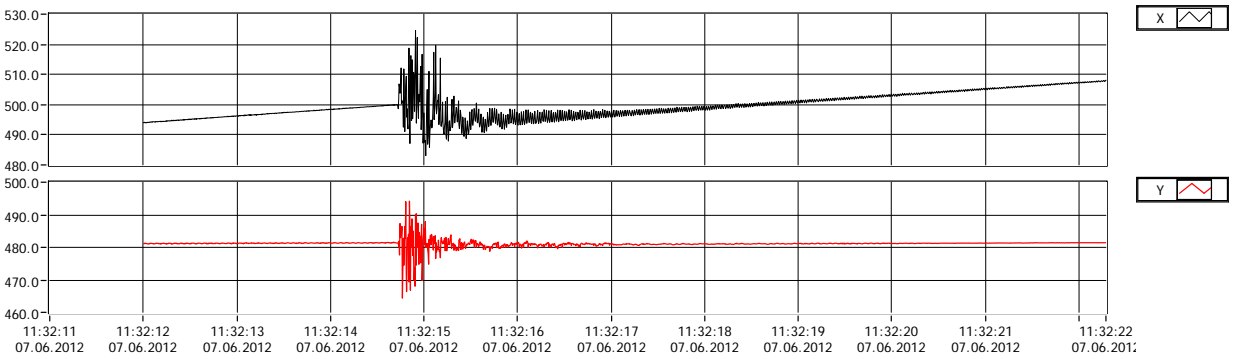


Torsion 1

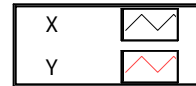
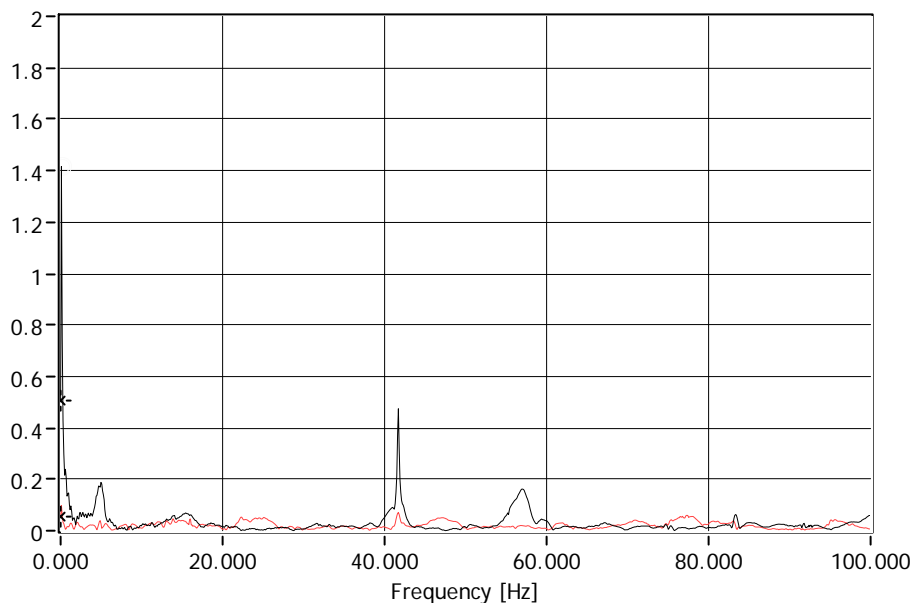


Deflection 2

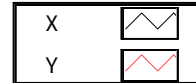
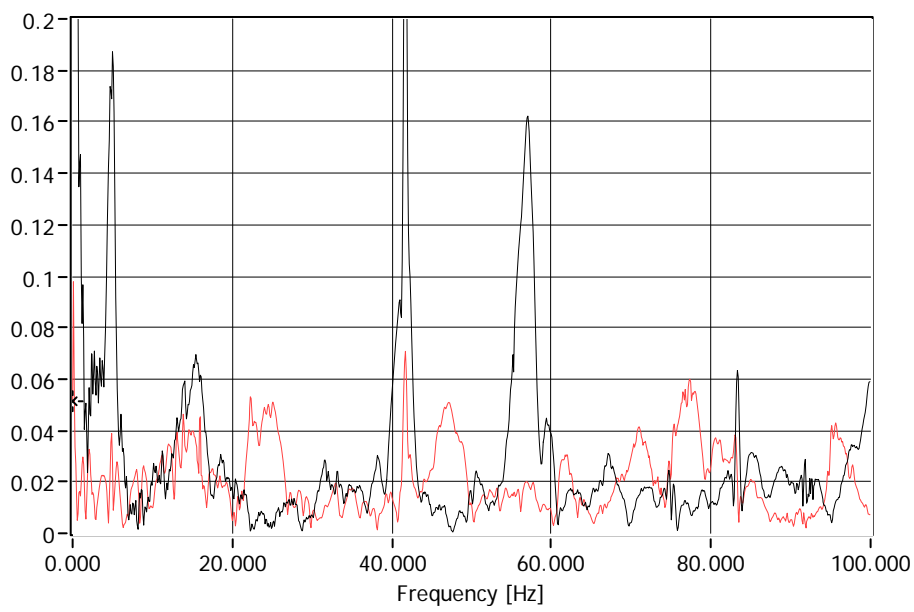
Deflection 2



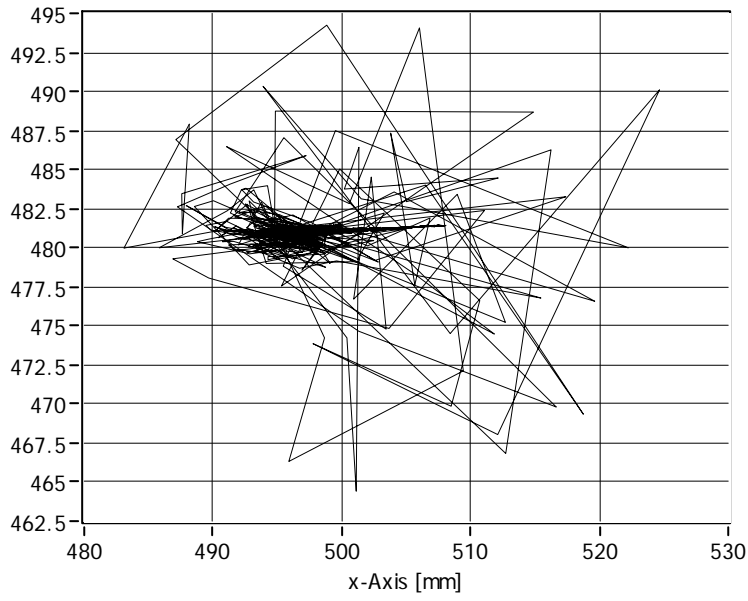
Spectra Deflection 2



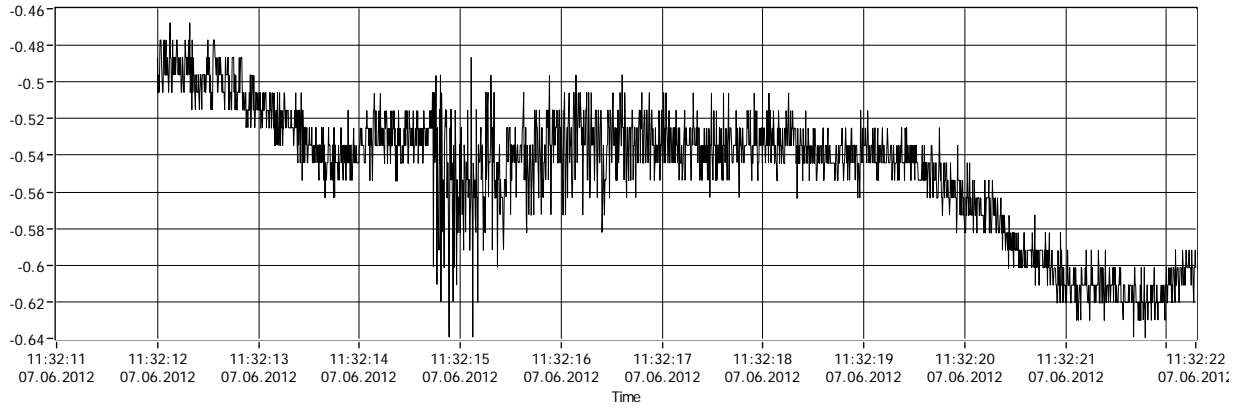
Spectra Deflection 2



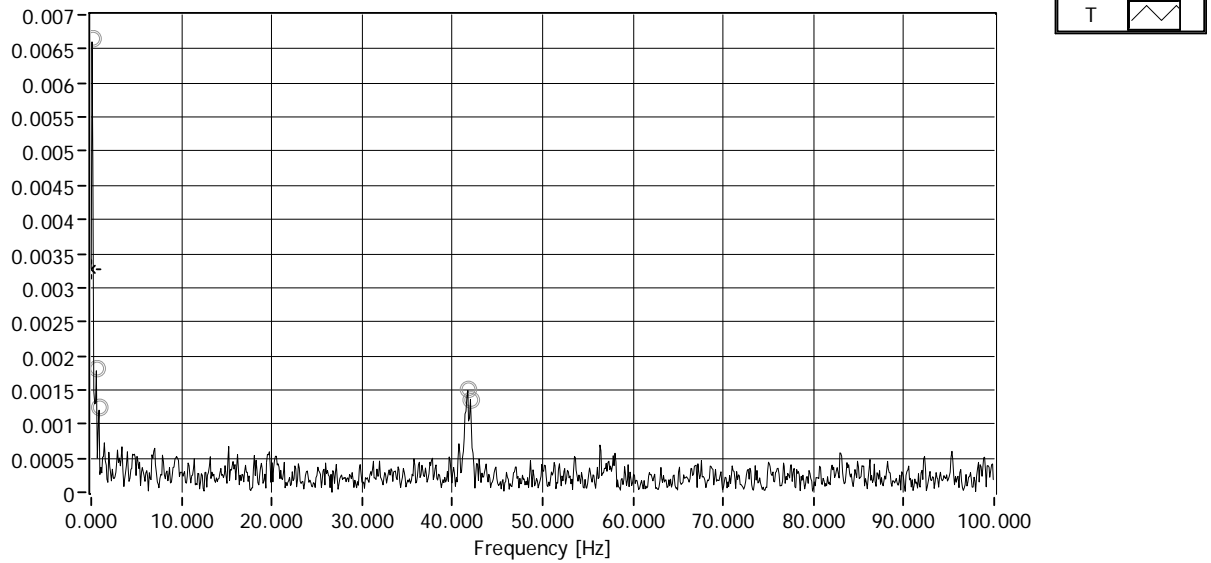
XY Deflection 2



Torsion 2



Spectra Torsion 2



Appendix F Transverse Stiffener Subcomponent Test

Introduction

In the framework of the project “Demonstration of new blade design using manufacturing process simulations” a prototype wind turbine blade box girder was designed and tested. The box girder is meant as a proof of concept for new structural solutions. One of these solutions is a transverse stiffener depicted in Figure 4. The transverse stiffeners are adhesively joined to the cap.

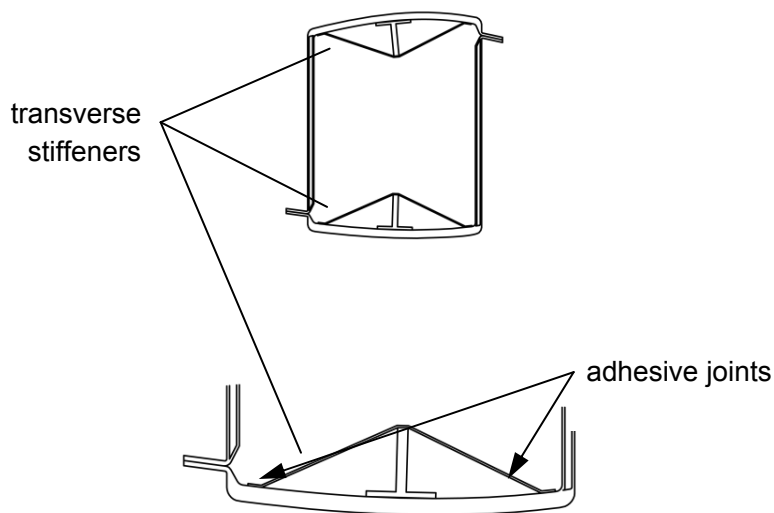


Figure 4: Transverse stiffeners.

As it is difficult to estimate the strength of such a joint, a sub-component test was performed.

An unreinforced and a reinforced (including a “crack stopper”) sample were tested. Figure 5 shows the unreinforced sample. The test setup is shown in Figure 6. Figure 7 and Figure 8 show the failure of the unreinforced and the reinforced sample, respectively.

Due to the 30 degree angle of the transverse stiffener the applied force and the force in each stiffener are identical. Figure 9 shows this force and the strain measured in the center of the transverse stiffeners.

The finite element model of the box girder indicates a force of approximately 65kN (corresponding to 7000 microstrain) in the transverse stiffener for 100% PTS load.

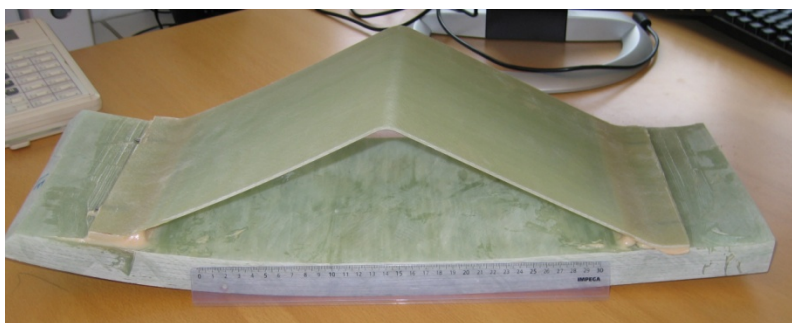


Figure 5: Sample.



Figure 6: Test setup

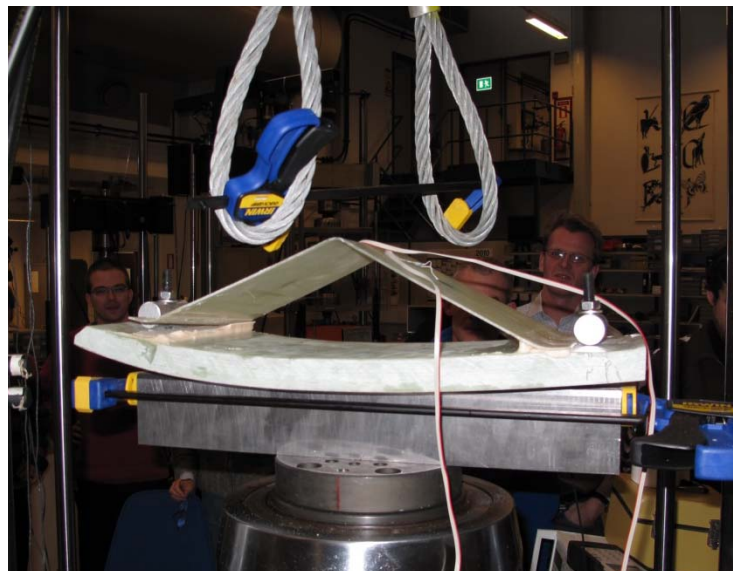


Figure 7: Failure of the unreinforced sample

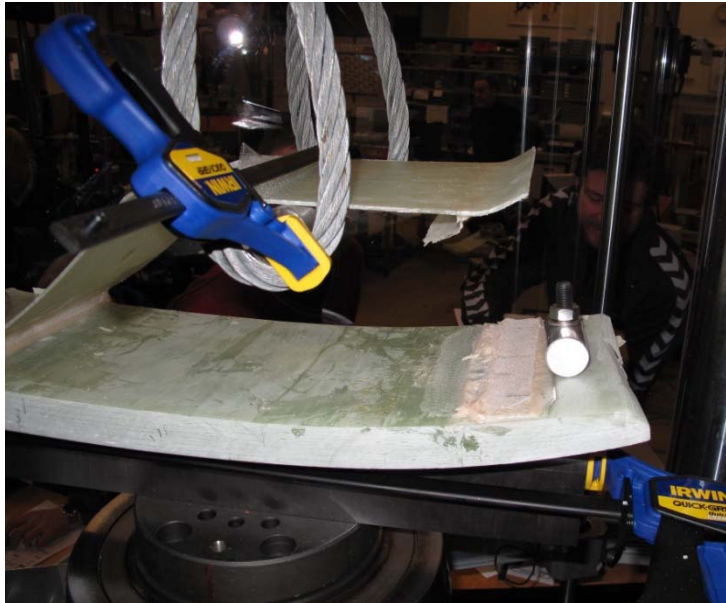


Figure 8: Failure of the reinforced sample

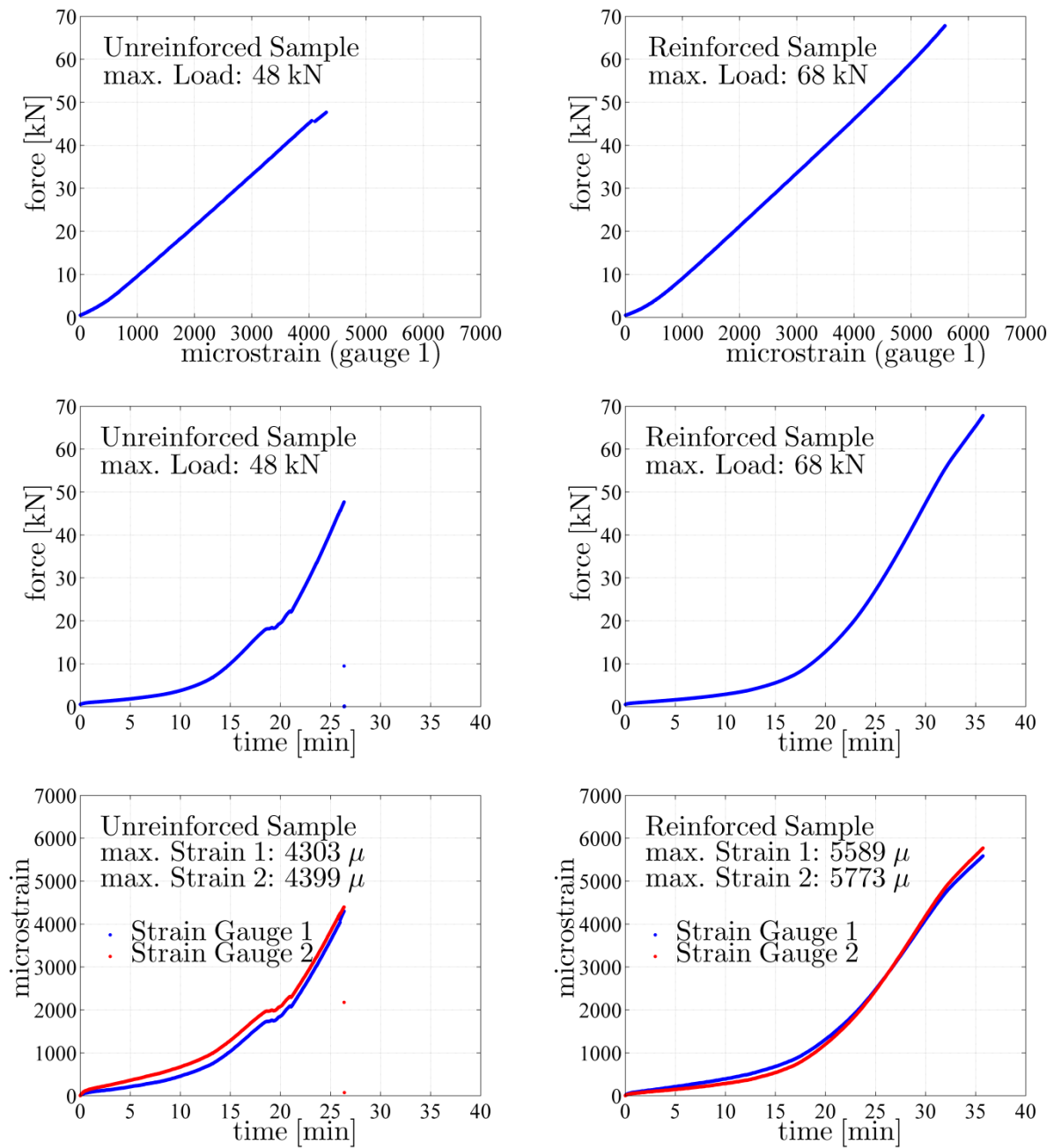


Figure 9: Results



DTU Wind Energy E-0010 (EN); ISBN 978-87-92896-16-2

**Technical University of Denmark
DTU Vindenergi
Frederiksborgvej 399
Bygning 118
4000 Roskilde
Telefon 46 77 50 85
info@vindenergi.dtu.dk
www.vindenergi.dtu.dk**